COSMIC CARTOGRAPHY
Bayesian Reconstruction of the Cosmological Large-Scale Structure

Francisco-Shu Kitaura Joyanes

München 2007

COSMIC CARTOGRAPHY
Bayesian Reconstruction of the Cosmological Large-Scale Structure

Francisco-Shu Kitaura Joyanes

Dissertation
an der Fakultät für Physik
der Ludwig–Maximilians–Universität
München

vorgelegt von
Francisco-Shu Kitaura Joyanes
aus Madrid

München, den 23.11.2007

Erstgutachter: Prof. Simon White
Zweitgutachter: Prof. Gerhard Börner
Tag der mündlichen Prüfung: 20.12.2007

COSMIC CARTOGRAPHY

Bayesian Reconstruction
of the
Cosmological Large-Scale Structure

with

ARGO
an
Algorithm for the **R**econstruction of **G**alaxy-traced **O**ver-densities

by

Francisco-Shu Kitaura Joyanes

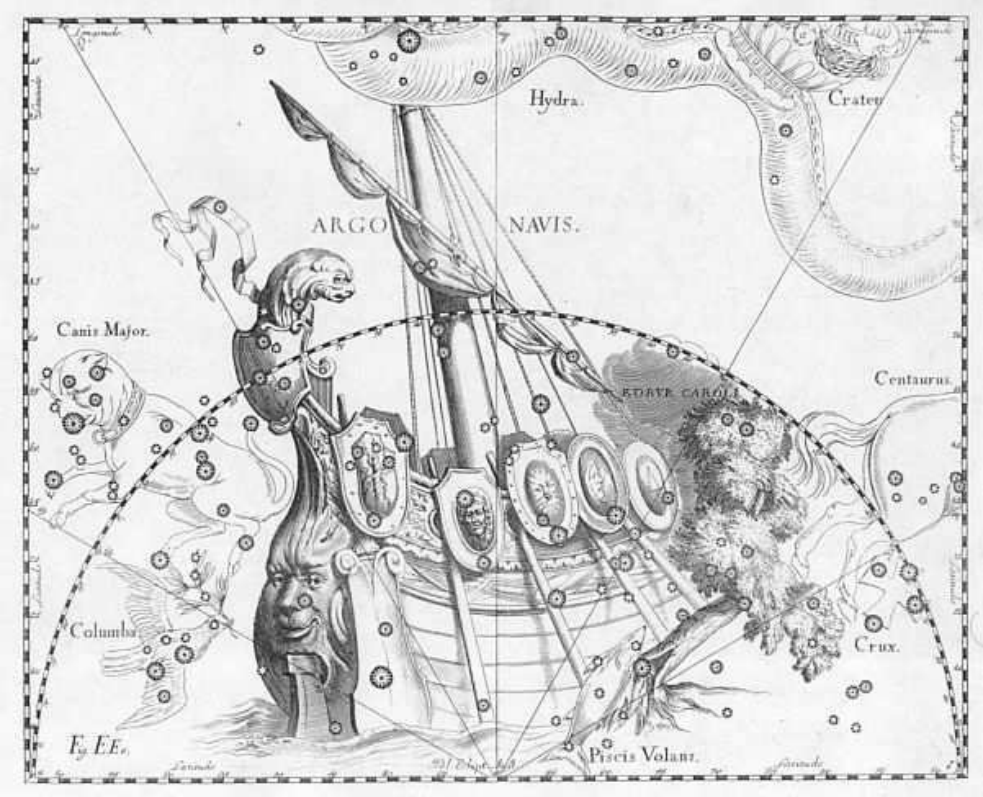

Der Ursprung und die Evolution des Kosmos haben sich der Struktur der groß-skaligen Materieverteilung im Universums aufgeprägt, welche wir mittels unseren astronomischen Himmelsdurchmusterungen in der Galaxienverteilung wahrnehmen können. In den letzten Jahren haben sich Galaxienssurveys mit Rotverschiebungsbestimmung zu einem exzellenten Zugang zu der kosmischen Materiestruktur entwickelt. Diese Surveys sind komplementär zu anderen Informationsquellen wie dem kosmischen Mikrowellenhintergrund, da sie Einblick in andere Epochen der kosmischen Geschichte gewähren. Sie zeigen die Epochen nach der Reionisation des Universums, in der erstmals leuchtkräftige Objekte auftauchten, etwa ab einem Zeitpunkt vor zwölf Milliarden Jahren bis heute. Da das Universum etwa dreizehn Milliarden Jahre alt ist, erlauben Galaxiensurveys prinzipiell immense kosmische Zeiträume zu überblicken, auch wenn die Teleskopsensitivitäten oft nicht ausreichen die entferntesten Lichtquellen des Universums tatsächlich auch zu detektieren. Daher sind Galaxiensurveys extrem interessant für Studien der kosmischen Entwicklung. Die Observablen, wie Galaxienpositionen, -eigenschaften und -rotverschiebung, liefern nur eine unvollständige Repräsentation der Strukturen im Universum, nicht nur aufgrund der Messunsicherheiten und Beschränkungen, sondern auch wegen systematischen Unsicherheiten, wie dem so genannten *Galaxienbias*. Die Galaxien zeichnen das zugrunde liegende kontinuierliche Materiefeld nur partiell nach aufgrund ihrer diskreten Verteilung im Kosmos. Weiterhin haben Galaxienkataloge viele Komplikationen, teilweise physikalisch begründet wie bereits erwähnt, teilweise aber aufgrund der Natur der Beobachtungen. Das Problem das zugrunde liegende Materiefeld zu rekonstruieren um damit kosmologische Studien zu betreiben bedarf daher eines statistischen Zugangs.

Diese Promotionsschrift beschreibt ein kosmisches Karthographieprojekt. Die notwendigen wahrscheilichkeitstheoretischen Konzepte, der mathematische Rahmen, und die numerischen Algorithmen werden ausgiebig untersucht. Auf dieser Basis wird ein Bayesian softwaretool entwickelt. Der resultierende ARGO-code erlaubt die charakteristischen Merkmale der groß-skaligen Strukturen mit noch nie dagewesener Präzision und Flexibilität zu bestimmen. Dies erreicht man durch die gemeinsame Bestimmung der groß-skaligen Dichte zusammen mit einer Anzahl an Parameter, wie dem kosmischen Fluß, den kleinskaligen Eigenbewegungen der Galaxien und dem Leistungsspektrum, anhand der Information, die von den gemessenen Galaxienverteilungen stammt. Der ARGO-code kann dabei viele Beobachtungsproblemen behandeln, wie die Masken des Surveys, die Galaxien Selektionsverfahren, Verwischungseffekte und Rauschen, dank einem Operator basierten Formalismus, daß für diese Zwecke ausgearbeitet wurde. Dank der erreichten Effizienz, kann ARGO die Anwendung iterativer Markov Chain Monte Carlo basierten Sampling-Verfahren angehen. Dies wird letzlich eine volle Beschreibung der Materieverteilung erlauben mit all ihren relevanten Parametern, wie Geschwindigkeiten, Leistungsspektren, *Galaxienbias*, usw., inklusiv deren Unsicherheiten. Einige Anwendungen in denen solche Techniken verwendet werden, sind hier demonstriert. Ein Sampling Algorithmus wird erfolgreich angewendet für die Korrektur der Rotverschiebungseffekte, die besonders stark im nicht-linearen Bereich der Strukturentstehung auftauchen und den sogenannten *Gottesfinger* erzeugen. Letzlich wird auch ein Gibbs-Sampling Algorithmus gezeigt für die Bestimmung des Leistungsspektrums und einige vorläufige Ergebnisse werden präsentiert in denen die richtige Form und Amplitude des Leistungsspektrums ausschließlich aus den Daten rekonstruiert wird.

The cosmic origin and evolution is encoded in the large-scale matter distribution observed in astronomical surveys. Galaxy redshift surveys have become in the recent years one of the best probes for cosmic large-scale structures. They are complementary to other information sources like the cosmic microwave background, since they trace a different epoch of the Universe, the time after reionization at which the Universe became transparent, covering about the last twelve billion years. Regarding that the Universe is about thirteen billion years old, galaxy surveys cover a huge range of time, even if the sensitivity limitations of the detectors do not permit to reach the furthermost sources in the transparent Universe. This makes galaxy surveys extremely interesting for cosmological evolution studies. The observables, galaxy position in the sky, galaxy magnitude and redshift, however, give an incomplete representation of the real structures in the Universe, not only due to the limitations and uncertainties in the measurements, but also due to their biased nature. They trace the underlying continuous dark matter field only partially being a discrete sample of the luminous baryonic distribution. In addition, galaxy catalogues are plagued by many complications. Some have a physical foundation, as mentioned before, others are due to the observation process. The problem of reconstructing the underlying density field, which permits to make cosmological studies, thus requires a statistical approach.

This thesis describes a cosmic cartography project. The necessary concepts, mathematical frame-work, and numerical algorithms are thoroughly analyzed. On that basis a Bayesian software tool is implemented. The resulting ARGO-code allows to investigate the characteristics of the large-scale cosmological structure with unprecedented accuracy and flexibility. This is achieved by jointly estimating the large-scale density along with a variety of other parameters —such as the cosmic flow, the small-scale peculiar velocity field, and the power-spectrum— from the information provided by galaxy redshift surveys. Furthermore, ARGO is capable of dealing with many observational issues like mask-effects, galaxy selection criteria, blurring and noise in a very efficient implementation of an operator based formalism which was carefully derived for this purpose. Thanks to the achieved high efficiency of ARGO the application of iterative sampling algorithms based on Markov Chain Monte Carlo is now possible. This will ultimately lead to a full description of the matter distribution with all its relevant parameters like velocities, power spectra, galaxy bias, etc., including the associated uncertainties. Some applications are shown, in which such techniques are used. A rejection sampling scheme is successfully applied to correct for the observational redshift-distortions effect which is especially severe in regimes of non-linear structure formation, causing the so-called *finger-of-god* effect. Also a Gibbs-sampling algorithm for power-spectrum determination is presented and some preliminary results are shown in which the correct level and shape of the power-spectrum is recovered solely from the data.

We present in an additional appendix the gravitational collapse and subsequent neutrino-driven explosion of the low-mass end of stars that undergo core-collapse Supernovae. We obtain results which are for the first time compatible with the Crab Nebula.

The Bayesian frame-work and numerical development presented in this thesis are partially included in a submitted publication (Kitaura & Enßlin, 2007). The applications on synthetic galaxy catalogues are new (see chapter 5). All the numerical calculations and figures presented in this thesis have been done by the author.

Dedicated to my grand-parents:

Consuelo, Fusao, Hiroko and Francisco,

who will always be a guide in my life,
being persons who constantly fought for their ideals.

Contents

List of Figures

LIST OF FIGURES

List of Tables

LIST OF TABLES

Chapter 1

Introduction

天地に
気結びなして
中に立ち
心構えは
山彦の道

Ametsuchi ni
kimusubi nashite
naka ni tachi
kokoro gamae wa
yamabiko no michi

Being between sky and earth
unifying with them
in the calmness
the state of my heart feels like
following the path of the resounding mountain echo

Morihei Ueshiba

According to our current picture of cosmogenesis, the galaxies, galaxy clusters, galaxy filaments, and giant voids forming the cosmic large-scale structure (LSS) are products of gravitational instability, which pulls increasingly more matter onto the tiny primordial seed density fluctuations generated at the very first epoch of inflation. The shape and size of the cosmic matter distribution reflects the initial conditions set during or shortly after Big Bang, as well as the interplay of the gravitational self-attraction of matter and the diluting action of the Hubble expansion of cosmic space. Valuable information about the properties and the origin of the cosmic inventory are encoded in the LSS, however, on small-scales, that information is being erased through dynamical non-linear processes.

Our goal is to extract as much of this information as possible from astronomical measurements, which introduce uncertainties and, consequently, degeneracies. Therefore, we have to adapt an information-theoretical approach to solve the reconstruction problem of cosmography. The Bayesian framework turns out to be the most general approach as we will discuss

later. In this thesis we present the novel ARGO[1]-software package, which reconstructs the three-dimensional density field from the information provided by galaxy surveys with different Bayesian and inverse methods. Here we focus our study on understanding the Bayesian theoretical background and the required algorithmic aspects. Further extensions of the code in which the power-spectrum and the peculiar velocities can be jointly sampled are presented and tested on mock galaxy catalogues. Some of the preliminary results are presented and future development is outlined.

The large number of telescopes performing galaxy surveys with increasing depth, sky coverage, and accuracy in position and distance (or redshift) determination provide us with superb data on the cosmic matter distribution at an exponentially increasing rate. One problem is that the discrete objects these instruments reveal to us, the galaxies, are the result of a complex non-linear evolution of cosmic matter combined with complicated astrophysical processes such as star formation. A translation of the galaxy data into the much better understood large-scale dark matter (DM) distribution, which would be much easier to analyze for imprints of cosmologically interesting effects, is far from trivial. The discrete nature of galaxies introduces certain noise, usually modeled by shot noise. Moreover, the partially understood galaxy-formation process inserts systematic uncertainties. In addition, the limited volume of surveys adds complications beyond the problems of galaxy-distance determination being contaminated by observational and velocity redshift-distortions. All these complications have to be dealt with simultaneously and in a controlled fashion. Since it cannot be assumed that the correct or optimal values for the various degrees of freedom of the problem (bias factors, redshift-corrections, etc.) will be guessed a priory, repeated and iterative data analysis is mandatory in order to achieve a high-fidelity and well-understood cosmic map. For example, a correction of redshift-distortions of the galaxies requires the gravitational potential generated by the matter distribution to be reconstructed.

Repeated generation of cosmic matter maps increases the urge to face another challenge, the scaling of the performance of the underlying map-generation algorithms with the data size. Since the matter-density information displayed at a location on a map may depend on all input data (galaxy positions), any algorithm optimized to information theory scales super-linear[2]. With increasing survey sizes, increasing requirements for spatial resolution and volume coverage, and the need to frequently re-iterate the map-generation step, the algorithm has to scale closely to linear with data size, otherwise its application is strongly limited. Former applications in cosmography suffered from such inconvenient performance-scaling, and an effort has to be made to develop simultaneously high-performance and accurate methods.

The work presented in this thesis developes the general methodology of Bayesian reconstruction of the cosmic matter distribution, based on the invaluable pioneering work of many other scientists, which will be discussed below, and extends this work to a series of new applications. Existing and novel map making algorithms are summarized in terms of a classification of their Bayesian likelihood and prior functions. The implementation, optimization, and comparison of various numerical schemes are addressed in detail. This provides a starting point

[1] **A**lgorithm for the **R**econstruction of **G**alaxy-traced **O**ver-densities

[2] A map of galaxy counts can be generated by an algorithm with linear scaling to data size however, it is not an optimal representation of the underlying matter field.

for a correct information-theory approach to cosmography. Many additional problems, not addressed in this thesis, such as the galaxy bias, will also have to be solved before accurate maps of the dark matter distribution in our still mysterious Universe can be generated.

Such an undertaking would be highly rewarded in the short and long run. An accurate map of the cosmic matter distribution would be valuable for a manifold of direct scientific applications. These range from structure-formation analysis, to cosmological parameter estimation via power-spectrum measurements, dark energy studies, galaxy-cluster identification and galaxy-bias studies. Accurate cosmic maps would help to determine weak signals associated with the large-scale structure such as the integrated Sachs-Wolf (ISW) effect, or the extended Sunyaev-Zel'dovich (SZ) effect, the detection of which relies on the construction of optimal statistical filters for these signals.

Finally, one could argue that mapping the distribution of matter in the Universe represents a response to mankind's curiosity in its aim to discover *terra incognita* and find an orientation in space and time on cosmological scales and, therefore, should be a goal in itself.

In the remainder of this introduction we give the sources of uncertainties, we present an overview of existent and new Bayesian reconstruction methods, subsequently we briefly describe the algorithmic development presented in this thesis, then we summarize non-Bayesian methods and time-reversal reconstruction methods, and in the final part we give a more detailed overview of the structure of this thesis.

1.1 Classes of uncertainty

Several classes of uncertainties related to the density-field reconstruction from galaxy surveys demand a statistical approach. Some of the uncertainties are intrinsic to the nature of the underlying signal (the dark matter). Other uncertainties are intrinsic to the nature of the observable (the galaxies). And finally there are uncertainties due to degeneracies which appear through the observation and data mining process.

1. **Intrinsic stochastic character: cosmic variance**

   In cosmology it is generally assumed that the structure of the Universe comes from some infinitesimal quantum fluctuations which were frozen out and stretched by an inflationary phase (see Albrecht & Steinhardt, 1982; Bardeen *et al.*, 1983; Guth, 1981; Guth & Pi, 1982; Hawking, 1982; Linde, 1982; Starobinsky, 1982), and later amplified by gravitational instability. According to this picture, the seed fluctuations would have an intrinsic stochastic character and are mainly Gaussian distributed. However, the mechanisms that stretch the quantum fluctuations may also introduce deviations from Gaussianity which would then be imprinted in the seed fluctuations. In general all the moments of the initial fluctuations have to be considered $\langle \boldsymbol{\delta}_{\mathrm{DM}}^{\mathrm{n}} \rangle$. Nevertheless, most of the inflationary scenarios predict the density field to be very closely Gaussian distributed and it is generally sufficient to take the second order moment, the two-point correlation function, or the power-spectrum in Fourier-space. We will discuss below how to determine the power-spectrum and techniques to disentangle intrinsic non-Gaussianities within a Bayesian framework. Note, that there are alternative models to inflation in which e.g. the

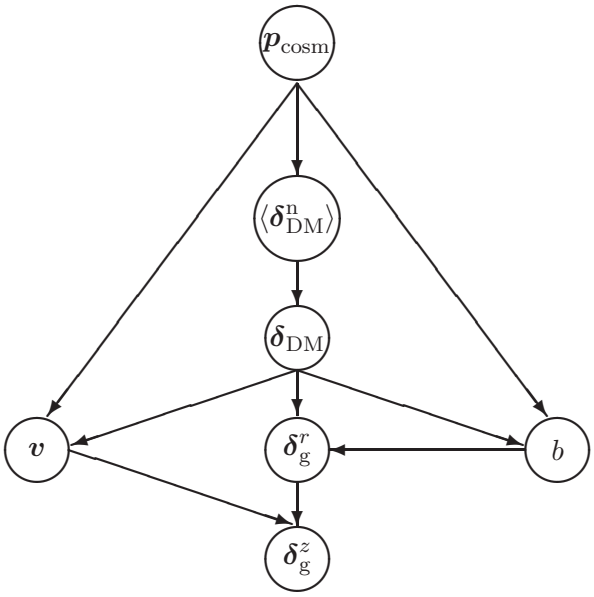

Figure 1.1: Hierarchical Bayes model for a galaxy distribution in redshift space $\boldsymbol{\delta}^{z}_{\rm g}$ is represented here in a directed acyclic graph (DAG). The cosmological parameters $\boldsymbol{p}_{\rm cosm}$ govern the rest of the variables. The initial density field coming from e.g. inflationary scenarios can be statistically described by all its moments $\langle\boldsymbol{\delta}^{\rm n}_{\rm DM}\rangle$. Here the power spectrum is usually taken, since the intitial perturbations are well described by a Gaussian realization of the initial seed fluctuations. The further evolution is described by nearly deterministic processes (given by structure and galaxy formation), which determine the later-time dark matter distribution $\boldsymbol{\delta}_{\rm DM}$ with its peculiar velocity field $\boldsymbol{v}$ and the bias function b that relates the galaxy distribution to the dark matter density field. The dark matter distribution $\boldsymbol{\delta}_{\rm DM}$ with the bias produces the galaxy distribution in real space $\boldsymbol{\delta}^{r}_{\rm g}$. The peculiar velocities $\boldsymbol{v}$ related to the density field through the continuity equation introduce the redshift distortion in $\boldsymbol{\delta}^{r}_{\rm g}$ finally leading to the galaxy distribution in redshift space $\boldsymbol{\delta}^{z}_{\rm g}$.

seed fluctuations are identified with the topological defects that remain as relics of high-energy phase transitions (Kibble, 1976). Accurate reconstructions of the LSS could help to discriminate between the different models.

We review in detail the schemes that allow one to sample the cosmic variance, and present some preliminary results in chapter (5), in which the correct power-spectrum level and shape is extracted from the data.

2. **Physical uncertainties: galaxy bias**

The galaxy formation process is a complicated, non-linear and (probably) non-local process. It is known that on large scales the galaxy power-spectrum fits well to the expected DM spectrum predicted from cosmic microwave background (CMB) observations, if some bias factor b between the amplitude of the galaxy and DM fluctuations is assumed. Detailed studies show that the bias factor is not universal, but depends on galaxy type, galaxy formation time, redshift, etc. (see e.g. Cooray & Sheth, 2002, and references therein). For the purpose of reconstructing the underlying density field, linear biases can easily be tackled within the linear data model described below by including its effects in a selection function. Nevertheless, more complex biases have to be further investigated in a Bayesian framework. Physical processes, which are not perfectly understood

within galaxy formation may be treated in a statistical way, encoding the ignorance about certain physical processes in probability distribution functions. Several works study the stochastic non-linear galaxy biasing (see for example Dekel & Lahav, 1999; Pen, 1998; Tegmark & Bromley, 1999). Some of these models could be implemented in the Bayesian reconstruction process. This issue is out of scope in this thesis, but should be further investigated in this frame-work.

3. **Physical/observational uncertainties: redshift-distortions**

   The peculiar motion of galaxies with respect to the Hubble flow of the Universe: $\boldsymbol{v}$, introduces uncertainties in their redshift measurement, the so-called redshift-distortions (see e.g. Hamilton, 1998, for an introduction to this problem). The measured galaxy over-densities are thus said not to be in real-space $\boldsymbol{\delta}_{\mathrm{g}}^{r}$, but in redshift-space $\boldsymbol{\delta}_{\mathrm{g}}^{z}$. In the linear regime, where galaxies fall into the potential wells of large scale structures, redshift-distortions cause a squashing of the linear over-densities in radial direction. However, in the non-linear regime, galaxies (e.g. in a galaxy cluster) tend to behave like particles in a gas with randomized motions inside the clusters where the potentials are very high. This produces the so-called *finger-of-god* effect, a dispersion along the line of sight. The correction of these distortions is not trivial, since the process of structure formation partially erases the information about the initial fluctuations after entering the non-linear regime. Consequently, determining the real position of galaxies poses a degenerate problem, which has in general many possible solutions. Many efforts have been made to correct for these distortions: in the linear regime these efforts start with Kaiser's pioneering work (see Kaiser, 1987) and are followed by the linear redshift-distortions operator (for a detailed derivation see Hamilton, 1998). In the non-linear regime, these efforts include a velocity dispersion factor (the *dispersion*-model) corresponding to an exponential pairwise velocity distribution function with no mean streaming (see Ballinger *et al.*, 1996). Scoccimarro (2004) presents an exact relationship between real-space and redshift-space two-point statistics through the pairwise velocity distribution function including all non-linearities. More complex methods of correcting for redshift-distortions were classified by Schmoldt *et al.* (1999) into iterative methods, which uses the redshift-space density to calculate a peculiar velocity field, and then iteratively corrects the density field distortions (Kaiser & Stebbins, 1991; Yahil *et al.*, 1991) and more recently Percival (2005). The other class decomposes the redshift-space density in radial and angular basis functions from which the radial redshift-distortion is corrected (see e.g. Nusser & Davis, 1994; Schmoldt *et al.*, 1999). Below, we propose a Bayesian method to correct for the linear and non-linear redshift-distortions in a statistical way (see section 2.6) and present some applications in chapter (5).

4. **Observational uncertainties: measurements**

   The action of measurement introduces uncertainties, either due to the instruments, e.g. blurring by the telescope, or due to the observational strategy, which is included in the noise term, the selection function, and the mask effects (see Zaroubi *et al.*, 1995, for a pioneering work in the LSS field). Ignoring selection functions, windowing, or blurring will lead to strongly biased reconstructions, which are far from the real signal, and thus allow

only very limited interpretation of the true physical picture. A numerical implementation of these effects is presented in chapter (sec:operators). The influence of these effects will then be analyzed separately and tested with our code. The results are presented in chapter (4). Though Argo demonstrates its capability to handle these uncertainties, further work is required in order to apply it to real data. Particular expressions for the selection function according to the redshift survey under study, as well, as masks, etc., have to be implemented.

5. **Mathematical/numerical representation uncertainties: aliasing effects**

   Some uncertainties are not intrinsic to the observable, but originate from the mathematical representation one chooses. Treating galaxies as counts in cells or with other mass-assignment scheme will smear out the information about their measured position for which one has to correct (see sections 3.3.2 and 5.1.3) in order to derive other quantities, like the power-spectrum (see section 5.3.2). The selected data mining schemes can also introduce errors in the reconstruction process, which may be fatal. In particular, using a grid in a box to represent a galaxy survey, introduces empty regions even if the survey covers the whole sky due to the radial limit of the survey. Packing a sphere in a box leaves almost have of the volume empty. We discuss this issue in section (5.3.1) and show its importance for determining the bulk flow. In section (5.3.2), we propose some solutions to this problem based on sampling a fluctuating field in the unobserved regions.

From all the points mentioned above we conclude, that extracting the underlying dark matter density field from the luminous matter distribution given by galaxy redshift surveys poses a classical signal reconstruction problem. A Bayesian network depicting the relation of these uncertainties is shown in fig. (1.1).

1.2 Bayesian reconstruction methods

Any Bayesian statistical approach requires the definition of a likelihood and a prior. The former is the probability distribution function describing the process generating the observational data. It can be interpreted as a distance measure of the observed data to the underlying signal, as we will discuss below. The prior stands for the distribution function modeling our prior knowledge on the signal to be recovered. Mathematically it can be shown that it regularizes the estimator in the presence of noise (see section 2.5.1). Two kinds of priors have to be distinguished, informative priors, in which the previous physical knowledge about the signal is encoded, and non-informative priors, which try to give objective estimators for the underlying signal based on purely information-theoretical arguments. Here, three non-informative priors are considered: flat priors (see section 2.5.5) with a constant probability distribution function (PDF), entropic priors based on Shannon's notion of information (see section 2.5.9), and Jeffrey's prior based on invariant statistical structures under transformation of variables (see section 2.5.8). Finally, a maximization or sampling of the posterior distribution, which is proportional to the product of the likelihood and the prior, has to be done to complete the Bayesian estimation. The maximization of the posterior is called the maximum a posteriori method (MAP). The maximum likelihood (ML) and maximum entropy method (MEM) are particular cases of the MAP with

flat priors and entropic priors, respectively. Complex posterior distribution functions may be sampled iteratively from conditional PDFs in a Markov Chain Monte Carlo fashion (MCMC), see section 2.6. We show how different choices for these distribution functions together with the estimation procedure lead to different reconstruction algorithms, which consequently have distinct application fields (see table 2.1). A review of existing methods is presented and new applications for the large-scale structure reconstruction, which naturally emerge within the Bayesian formalism, are developed.

In this work we consider Poissonian and Gaussian likelihoods for the galaxy distribution. The former has been previously considered in image restoration especially for deconvolution purposes (see Lucy, 1974; Richardson, 1972). For example, the Richardson-Lucy algorithm can be derived as the ML of a Poissonian likelihood (see Shepp & Vardi, 1982, and appendix A.6). Here an image can be regarded as photon counts in cells represented by a Poissonian distribution. However, one should notice that this likelihood does not represent the galaxy-formation process. From a pure image reconstruction perspective, it can still be interesting for LSS estimations, because it naturally represents the discrete nature of a galaxy distribution. The Gaussian likelihood allows the incorporation of arbitrary noise structures through the variance. The CMB map-making algorithms, which aim to convert time-ordered data received from satellites into a map of the CMB signal on the sky as a projection on the sphere, usually use this likelihood. In this case, the ML leads to the simple COBE-filter first derived by Janssen & Gulkis (1992). Nevertheless, the complex scanning strategies and foreground removal can add unlimited complexity to these algorithms (e.g. Doré *et al.*, 2001; Keihänen *et al.*, 2005; Natoli *et al.*, 2001; Stompor *et al.*, 2002; Yvon & Mayet, 2005).

For the LSS the Gaussian prior arises as the natural informative prior due to the arguments discussed above. We propose a novel algorithm: GAPMAP, which maximizes the posterior with a Gaussian prior and a Poissonian likelihood (see section 2.5.4 and appendix A.5). In contrast, the Gaussian likelihood with the Gaussian prior leads to the well-known Wiener-filter, which has been used for the LSS reconstruction (see Erdoğdu *et al.*, 2004, 2006; Fisher *et al.*, 1994, 1995; Hoffman, 1994; Lahav, 1994; Lahav *et al.*, 1994; Schmoldt *et al.*, 1999; Webster *et al.*, 1997; Zaroubi *et al.*, 1995, 1999) and for CMB-mapping (see e.g. Bunn *et al.*, 1994; Tegmark, 1997). It is also known to give optimal results in terms of yielding the least square error, see the pioneering work of Rybicki & Press (1992) and Zaroubi *et al.* (1995). We present in this thesis a fast Wiener-filter extra-regularized with Krylov methods as we will see below.

Intrinsic primordial non-Gaussianities can be imprinted in the seed fluctuations depending on the particular theory responsible for the amplification of the fluctuations coming from the early Universe. To find such deviations, non-informative priors, which give non-linear estimates for the underlying signal are required. Entropic priors are well suited here, and have been previously applied for CMB studies. We extend this work for LSS reconstructions and develop the corresponding maximum entropy method for Gaussian and Poissonian likelihoods (see section 2.5.9 and appendix A.10).

Sampling methods have the advantage of determining the shape of distributions and, thus, leading to a natural estimate of the uncertainty of the estimator. Moreover, the mean can be calculated easily from the sample and is known to give more accurate results than the maximum

in the case of asymmetric PDFs (see e.g. Tanner, 1996).

As an example, Hobson & McLachlan (2003) proposed a SZ-cluster detection algorithm using the Metropolis-Hasting algorithm method based on a Poissonian prior distribution, which is designed to find discrete objects. Recently Sutton & Wandelt (2006) developed a reconstruction method for radio-astronomy that samples from the multiplicity function (see eq. 2.32). Alternative approaches to the maximum likelihood for CMB-mapping algorithms try to jointly reconstruct the CMB-map with its power-spectrum using Gibbs-sampling techniques (Eriksen *et al.*, 2007; O'Dwyer *et al.*, 2004; Wandelt *et al.*, 2004). This approach is especially efficient with respect to other MCMC methods because the transition probability matrix moves the system in each step of the chain. For this special case the importance ratio is always one (see e.g. Neal, 1993). This MCMC method requires, however, the complete knowledge of the full conditional PDFs in order to sample from them. Note, that the Gaussian prior for the signal simultaneously represents the likelihood for the power-spectrum given the signal, which in this case is an inverse Gamma function for the power-spectrum (see section 5.3.2). This distribution naturally samples the power-spectrum, which strongly deviates from Gaussianity.

With the aim of estimating the power-spectrum in an objective way, non-informative priors are used. Usually a flat prior is taken for the power-spectrum. Alternatively, Jeffrey's prior, for which we give a derivation based on Fisher information (see appendix A.9), can be used. Alternatively, an entropic prior could also be taken.

Other attempts have been made to estimate the power-spectrum from the LSS based on the distribution of galaxies. A modified Gaussian PDF with a log-normal mean has been used in this approach (see Percival, 2005). The same kind of concept, using a modified Gaussian distribution to sample deviations from Gaussianity, has been applied to SZ-cluster detection by Pierpaoli & Anthoine (2005).

In this thesis we propose to apply a Gibbs-sampling algorithm to jointly sample the underlying three-dimensional density field with the power-spectrum and the peculiar velocities, which can be used to correct for the redshift-distortions (see chapter 5). Note, that the peculiar velocities can also be used to trace the initial density fluctuations back in time as we will discuss below.

1.3 Algorithmic development

In this thesis we focus our work on the numerical optimization of inverse techniques to show that a joint estimation of the LSS matter density field and its parameters is feasible (see sections 3 & 4).

The calculation of the reconstructions, either through maximization or through sampling, requires the inversion of certain matrices. For the Wiener-filter, for instance, the reconstruction problem consists in one of its steps on the inversion of the correlation matrix of the data. The methods used in this field so far calculated this matrix and inverted it mainly using the Singular Value Decomposition algorithm that scales as $\mathcal{O}(n^3)$ for a $n \times n$ matrix (see e.g. Zaroubi *et al.*, 1995). However, this approach seems to be hopeless in light of the overwhelming amounts of data coming from different surveys and the possibility of combining them. We made special effort to implement an algorithm in which the involved matrices would not need to be stored

taking advantage of an operator formalism, which we worked out here for different reconstruction methods (see table 3.2 and section 3.3). Such a formalism also allows fast iterative numerical methods that speed the inverse step up to a scaling of $\mathcal{O}(n \log_2 n)$ thus reducing the main operations to fast Fourier transforms (FFTs). Some of these numerical schemes have been used in CMB-mapping algorithms, but were lacking a detailed comparison of the efficiency of the different methods. Such a comparison is presented here. We derive the different inverse methods in a unified way starting with a Bayesian motivation for iterative schemes (see appendix B.2) and following with a general formulation of the asymptotic regularization from which the Jacobi, the Steepest Descent, and the Krylov methods are derived. Moreover, non-linear inverse methods are discussed, like the Newton-Raphson, the Lanweber-Fridman and the non-linear Krylov methods. Preconditioning (see appendix B.3) was taken into account in all the derivations and the importance of such a treatment is tested in section (4) (see fig. 4.3). In addition, a previously not discussed Krylov method is derived (see formula 3.37, section 3 and appendix B.1) and its superior efficiency is demonstrated (see section 4).

1.4 Non-Bayesian reconstruction methods

Let us mention here that there are alternative reconstruction methods which recover the underlying density field based on the observed radial peculiar velocity of galaxies, such as the widely known POTENT-code (Bertschinger & Dekel, 1989, 1991; Bertschinger *et al.*, 1990). Kaiser & Stebbins (1991) propose a maximum probability technique to reconstruct the density field from peculiar velocities.

Other works are focused on reconstructing the peculiar velocities from density fields (see e.g. Branchini & Plionis, 1996; Branchini *et al.*, 1996; Kudlicki *et al.*, 2000; Mohayaee & Tully, 2005; Mohayaee *et al.*, 2004). For a review see (Zaroubi, 2002a) and references therein.

In addition, several reconstruction techniques, which we do not discuss here are based on geometrical arguments. These techniques include Voronoi tesselations (see e.g. Doroshkevich *et al.*, 1997; Ebeling & Wiedenmann, 1993; Icke & van de Weygaert, 1991; Kim *et al.*, 2000; Meurs & Wilkinson, 1999; Panko & Flin, 2004; Ramella *et al.*, 2001; Zaninetti, 1995, 2006), Delaunay tesselations (see e.g. Bernardeau & van de Weygaert, 1996; Schaap & van de Weygaert, 2000; van de Weygaert & Schaap, 2001), *friends-of-friends* algorithms (see e.g. Botzler *et al.*, 2004) or *cloud-in-cell* interpolation schemes (see e.g. Gottlöber *et al.*, 2002).

A widely known reconstruction method in various fields is the Pixon method (see e.g. Puetter & Pina, 1993). Unlike Bayesian methods, this method does not assign explicit prior probabilities to image models. Instead, it restricts them by seeking minimum complexity. The Pixon method minimizes complexity by smoothing the image model locally as much as the data allow, thus reducing the number of independent patches, or Pixon elements, in the image. For a recent application in astrophysics see e.g. Eke (2001).

1.5 Time-reversal reconstruction of the initial density field

The reconstruction of the initial density fluctuations is closely related to the reconstruction of the large-scale density field at the observed epoch focused on in this thesis. However, we be-

lieve that fruitful contributions to the field of initial density fluctuations, could be extracted from the work presented here. An accurate over-density field at the observed epoch and the information about the peculiar velocities could be useful to perform such a time reversal reconstruction. Let us thus briefly review the reconstruction schemes developed in this neighboring area of cosmology.

The initial density field is of major interest because it represents the origin of the Universe and many theories can be tested with such information. As a direct application, constrained N-body simulations can be done by taking the reconstructed field as the initial conditions to study structure formation by later comparing the results with the observations (see e.g. Bistolas & Hoffman, 1998; Ganon & Hoffman, 1993; Mathis *et al.*, 2002; Sheth, 1995).

As we have discussed above, the large-scale structure contains information about the seed perturbations and its dynamical evolution is well approximated in the linear regime. Following this idea, Weinberg (1992) proposes to reconstruct the seed fluctuations through the Gaussianization of the observed density field, based on the approximation that the rank order of the initial density field smoothed over scales of a few Mpc is preserved under non-linear gravitational evolution and further assuming the initial field to be Gaussian distributed. This method can be regarded as an Eulerian Gaussian mapping scheme.

Other methods run gravity backward in time taking the position and peculiar velocities of objects at a certain redshift. Here, different schemes have been proposed: a huge class relies on Lagrangian dynamical schemes; another class is based on the minimal action principle; and another class is based on optimal mass transportation schemes have been applied for the initial density field reconstruction.

Lagrangian dynamical schemes mainly use the Zel'dovich approximation (Zel'Dovich, 1970) in which the comoving trajectories of the particles are straight lines. In this formalism, the variable under consideration is the displacement of a particle. Several reconstruction schemes are based on this approximation, including the Zel'dovich-Bernoulli equation derived by Nusser *et al.* (1991), the Zel'dovich-continuity equation presented in Gramann (1993) or the path interchange Zel'dovich approximation scheme (PIZA) used by Croft & Gaztanaga (1997), among others (see for example Dekel *et al.*, 1990; Narayanan & Weinberg, 1998; Nusser & Dekel, 1992; Valentine *et al.*, 2000). Several of these methods are compared in Narayanan & Croft (1999). More recently, it was proposed to determine the inverse Lagrangian map (defined as the transformation of the present (Eulerian) positions to the respective initial (Lagrangian) positions) by minimizing a quadratic cost-function, which searches the optimal mass-transport solution of the Monge-Ampère-Kantorovich problem (Brenier *et al.*, 2003; Frisch *et al.*, 2002; Mohayaee *et al.*, 2003, 2006)

The minimal action principle method was pioneered by Peebles (1989, 1990). One of its first applications was presented in Shaya *et al.* (1995). Here the gravitational instability problem is treated as a two-point boundary problem and the trajectories of the mass particles are solved by minimizing the action integral. This method was extended by Goldberg (2001a,b); Goldberg & Spergel (2000a,b).

1.6 Structure formation

Here we present a brief introduction to structure formation on large scales. The presented equations are mainly based on the books by Peebles (1980) and Peacock (1999).

The structure formation of the Universe is governed by an interplay of many coupled physical processes. However, one can establish delimited regimes and neglect many of the processes, depending on which physical effects are the object of study. In general the physical state of a statistical ensemble of particles is described by the particle distribution function $f(\boldsymbol{r},\boldsymbol{p},t)$ in phase space (position $\boldsymbol{r}$, and momentum $\boldsymbol{p}$, time t) and its evolution is given by the Boltzmann equation

$$\frac{\partial}{\partial t}f + \frac{\partial \boldsymbol{r}}{\partial t}\nabla_{\boldsymbol{r}} f + \frac{\partial \boldsymbol{p}}{\partial t}\nabla_{\boldsymbol{p}} f = \left(\frac{\mathrm{d}f}{\mathrm{d}t}\right)^{\mathrm{coll.}}. \tag{1.1}$$

The term in the rhs is only present when particles collide, which happens whenever baryons get involved. This is the case for self-interacting cosmic rays, cosmic rays or photon radiation interacting with molecular clouds, or neutrinos depositing energy in the stellar plasma triggering Supernova explosions (see appendix of supernova work). On large scales the gravitational clustering is believed to be dominated by collision-less dark matter, which permits us to neglect the collision term and write (Vlasov's equation)

$$\frac{\partial}{\partial t}f + \frac{1}{m}\boldsymbol{p}\nabla_{\boldsymbol{r}} f - m\nabla_{\boldsymbol{r}}\Phi\nabla_{\boldsymbol{p}} f = 0, \tag{1.2}$$

where the potential is given by Poisson's equation

$$\nabla^2_{\boldsymbol{r}}\Phi(\boldsymbol{r},t) = 4\pi G m \int \mathrm{d}\boldsymbol{p}\, f(\boldsymbol{r},\boldsymbol{p},t), \tag{1.3}$$

with the density defined as $\rho(\boldsymbol{r},t) \equiv m\int \mathrm{d}\boldsymbol{p}\, f(\boldsymbol{r},\boldsymbol{p},t)$ and the streaming velocity as $\boldsymbol{v}(\boldsymbol{r},t) \equiv \int \mathrm{d}\boldsymbol{p}\,(\boldsymbol{p}/m) f(\boldsymbol{r},\boldsymbol{p},t)/\int \mathrm{d}\boldsymbol{p}\, f(\boldsymbol{r},\boldsymbol{p},t)$. The Newtonian approach assumes that the gravitational perturbations are much smaller than the scale of the system given by the cosmological horizon: $d_{\mathrm{H}} = c/H_0$, with c being the speed of light, and H_0 the Hubble constant at present day. This system has theoretically a well defined solution. However, finding such a solution turns out to be in general very difficult. A wide extended alternative approach consists in performing N-body simulations in which the phase space density is sampled by a large number of particles. Another approach models the Universe as an ideal fluid assuming that the mean free path of matter is short. This is the picture of the homogeneous Universe which is valid on large scales. The evolution of this (non-relativistic) fluid is given by the equations of fluid dynamics, the continuity equation, the Euler equation, and Poisson's equation[1]

$$\frac{\partial \rho}{\partial t} + \nabla_{\boldsymbol{r}}(\rho \boldsymbol{v}) = 0, \tag{1.4}$$

$$\frac{\partial \boldsymbol{v}}{\partial t} + (\boldsymbol{v}\cdot\nabla_{\boldsymbol{r}})\boldsymbol{v} = -\frac{\nabla p}{\rho} - \nabla_{\boldsymbol{r}}\Phi, \tag{1.5}$$

$$\nabla^2_{\boldsymbol{r}}\Phi = 4\pi G\rho. \tag{1.6}$$

[1] For an example with coupled fluid-radiation dynamics see appendix of supernova work.

Note, that the pressure term in the Euler-energy equation is usually neglected when studying the dark matter evolution. Allowing for small departures from homogeneity we define

$$\rho(\boldsymbol{x},t) = \rho_0(t) + \delta\rho(\boldsymbol{x},t), \tag{1.7}$$
$$\boldsymbol{v}(\boldsymbol{x},t) = \boldsymbol{v}_0(t) + \delta\boldsymbol{v}(\boldsymbol{x},t), \tag{1.8}$$
$$p(\boldsymbol{x},t) = p_0(t) + \delta p(\boldsymbol{x},t), \tag{1.9}$$
$$\Phi(\boldsymbol{x},t) = \Phi_0(t) + \delta\Phi(\boldsymbol{x},t). \tag{1.10}$$

The resulting linear order equations are describing the evolution of density fluctuations in an expanding Universe governed by gravity

$$\frac{\mathrm{d}\delta}{\mathrm{d}t} + \nabla_{\boldsymbol{r}}\delta\boldsymbol{v} = 0, \tag{1.11}$$
$$\frac{\mathrm{d}\delta\boldsymbol{v}}{\mathrm{d}t} + (\delta\boldsymbol{v}\cdot\nabla_{\boldsymbol{r}})\boldsymbol{v}_0 = -\frac{\nabla\delta p}{\rho_0} - \nabla_{\boldsymbol{r}}\delta\Phi, \tag{1.12}$$
$$\nabla^2_{\boldsymbol{r}}\delta\Phi = 4\pi G\rho_0\delta, \tag{1.13}$$

where we introduced the convective time derivative: $\mathrm{d}/\mathrm{d}t \equiv \partial/\partial t + \boldsymbol{v}\cdot\nabla$ and the fractional density perturbation: $\delta \equiv \delta\rho/\rho_0$.

In an expanding Universe it is convenient to introduce the comoving coordinates $\boldsymbol{x}$: $\boldsymbol{r}(t) = a(t)\boldsymbol{x}(t)$, with the proper time t, and $a(t)$ being the scale factor, describing the general expansion of the Universe. Then the velocity can be written as

$$\boldsymbol{v} = \dot{\boldsymbol{r}} = \dot{a}\boldsymbol{x} + a\dot{\boldsymbol{x}}, \tag{1.14}$$

where $\delta\boldsymbol{v} \equiv a\dot{\boldsymbol{x}} \equiv a\boldsymbol{u}$ is called the peculiar velocity. Translating the spatial derivatives into comoving coordinates,e.g by replacing: $\nabla_{\boldsymbol{r}} = 1/a\nabla_{\boldsymbol{x}}$, we obtain the following linearized equations for conservation of mass and momentum as experienced by an observer moving with the Hubble flow

$$\dot{\delta} = -\nabla_{\boldsymbol{x}}\cdot\boldsymbol{u}, \tag{1.15}$$
$$\boldsymbol{u} + 2\frac{\dot{a}}{a}\boldsymbol{u} = -\frac{\nabla_{\boldsymbol{x}}\delta p}{\rho_0} - \frac{\nabla_{\boldsymbol{x}}\delta\Phi}{a^2}. \tag{1.16}$$

Let us now express the density field in a Fourier expansion

$$\hat{\delta}(\boldsymbol{k},a) = \int \mathrm{d}\boldsymbol{x}\exp(i\boldsymbol{k}\cdot\boldsymbol{x})\delta(\boldsymbol{x},a). \tag{1.17}$$

We can then combine eqs. (1.15) and (1.16) by eliminating $\boldsymbol{u}$ to the following equation

$$\ddot{\hat{\delta}} + 2\frac{\dot{a}}{a}\dot{\hat{\delta}} = \hat{\delta}\Big(4\pi G\rho_0 - \frac{c_{\mathrm{s}}^2k^2}{a^2}\Big), \tag{1.18}$$

where the sound speed: $c_{\mathrm{s}}^2 \equiv \partial p/\partial\rho$ was introduced to close the system. This equation has in general, two solutions: a decaying mode $D_-(z)$ and a growing mode $D_+(z)$. The latter being

the only relevant one for structure formation. We therefore can express the evolution of density perturbations as

$$\hat{\delta}(\boldsymbol{k}, z) = \frac{D_+(z)}{D_+(z_0)}\hat{\delta}(\boldsymbol{k}, z_0), \tag{1.19}$$

with $D_+(z)$ being the growth factor at redshift $z = 1/a(t) - 1$ ($z_0 : z = 0$). For particular expressions of the growth factor under different cosmologies see e.g. Peacock (1999). As already discussed in section (1.1), the initial fluctuations accord to a Gaussian random field to great accuracy. This also applies to the large-scale structure, which in linear approximation, only modifies the amplitude of the initial perturbations. The field is then completely specified by the power-spectrum $P(k, z)$ under the assumption of a statistically isotropic and homogeneous density field:

$$\langle\hat{\delta}(\boldsymbol{k}, z)\overline{\hat{\delta}(\boldsymbol{k}', z)}\rangle = (2\pi)^3\delta_{\mathrm{D}}(\boldsymbol{k} - \boldsymbol{k}')P(k, z). \tag{1.20}$$

We will use different expressions for the power-spectrum. A linear power-spectrum as given by Peacock & Dodds (1994), and a non-linear power-spectrum that describes also the effects of virialized structures, given by Smith *et al.* (2003). The growth of density fluctuations happens via self-gravitation, which is reduced by radiation pressure and small-scale fluctuations are dissipated by free streaming. The cumulative effects are described by the so-called transfer function

$$T(k) \equiv \frac{\hat{\delta}(k, z_0)}{\hat{\delta}(k, z)D_+(z)}. \tag{1.21}$$

Accurate results require solving the Boltzmann equation of the coupled plasma of matter and relativistic particles (see Seljak & Zaldarriaga, 1996, for a numerical solution). There exist several fitting formulae. In this work we use the BBKS (see Bardeen *et al.*, 1986) and the Bond & Efstathiou (1984) transfer-functions. The time evolution of the power-spectrum is then given by

$$P(k, z) = P_0(k)T^2(k)\frac{D_+(z)}{D_+(z_0)}, \tag{1.22}$$

with $P_0(k)$ being the initial power-spectrum.

Note, that the theory presented in this section is only valid in the linear and quasi-linear regime of structure formation. However, the problems that appear in the matter reconstruction from galaxy redshift surveys requires a deep study of non-linear effects. In this thesis we present a Bayesian frame-work, which can deal separately with the different uncertainties presented above, and find statistical solutions to the complex system described at the beginning of this section. For further details see chapter (5).

1.7 Structure of the thesis

This thesis is structured as follows: in chapter (2) we state the problem of signal reconstruction, then we define the data model. Subsequently, we introduce a general statistical perspective within a Bayesian framework from which different solutions to the reconstruction problem are presented, including Wiener-filtering, the COBE-filter, a novel GAPMAP algorithm with a

Poissonian likelihood and a Gaussian prior, Jeffrey's prior and the Maximum Entropy method (MEM). Markov Chain Monte Carlo methods (MCMC) that sample the global probability distribution function of the signal and all underlying parameters are presented as the ideal approach to achieve a full Bayesian solution of the reconstruction problem. In the numerical method chapter (3), different iterative inverse schemes which have been implemented in ARGO are presented, including a very efficient novel scheme. The operator formalism is worked out for four novel algorithms in large-scale structure reconstruction. The efficiency of the different inverse schemes is tested with the Wiener-filter under different reconstruction cases with synthetic data, including structured noise, blurring, selection function effects, and windowing in chapter (4). Finally, we apply in chapter (5) some of the methods developed in this thesis to reconstructions of the LSS based on mock galaxy redshift surveys. In this last chapter, we discuss the physical and statistical problems, study the quality and efficiency of the reconstructions, and present novel methods for redshift-distortions corrections and power-spectrum estimation. Particular detailed derivations are presented in the appendix.

Chapter 2

Bayesian approach to signal reconstruction

In nature you can find all future styles.

Auguste Rodin

The reconstruction of a signal (here: DM distribution) given a set of measurements (here: galaxy catalogues) is usually a highly degenerate problem, as we have discussed above, where the signal is under-sampled and modified by systematic and intrinsic errors due to the nature of the observable. This is indeed the situation that we are facing, since most of the galaxy redshift surveys have partial sky coverage and the discrete nature of galaxies introduces shot noise.

An expression for the data as a function of the real signal has to be modeled in a first step. The reconstruction problem is classically seen as the inverse of this functional dependence. The solution to this problem is far from being trivial and essential issues, like solution existence, solution uniqueness, and instability of the solving process, have to be considered. Regarding the solution existence, there will be no model that exactly fits the data, since the mathematical model of the physics of the system is approximate and the data contain noise. That forces us to look for optimal solutions, rather than exact solutions. We will have to deal especially with the last two points mentioned above, uniqueness and stability, because an infinite set of possible solutions can fit the data and because of the ill-conditioned character of the system we are treating. A regularization method that stabilizes the inverse process by imposing additional constraints will be required. We show below how the Bayesian framework permits us to do a regularization in a *natural* way and furthermore to jointly estimate the signal and its parameters. The calculation of the Bayesian estimators will require extra-regularization techniques, which will be presented in section (3). We will start posing the inverse problem by defining the model of the data.

2.1 Data model

The galaxy formation process is known to be a complicated, non-linear and probably non-local process, as mentioned in the introduction. Thus, attempts to invert the galaxy distribution into the original DM distribution suppose a great challenge. It is known that, given some bias factor between the amplitude of the galaxy and the DM fluctuations, the galaxy power-spectrum on large scales fits well to the expected DM spectrum predicted from CMB observations. Detailed studies reveal that the bias factor is not universal, but depends on galaxy type, galaxy formation time, redshift, etc. The data model connecting the signal (DM distribution) to our observable (galaxy counts) is in consequence complex, non-linear and non-local. The main goal of this thesis is to develop a Bayesian frame-work that permits one to split the dependencies into separated problems, which can then be jointly tackled with physical and statistical techniques. Such an example is given in chapter (5), where the non-linear structure formation effects are solved by performing a sampling procedure based on a physical model. In principle, also the bias of the galaxies can be sampled in this way (see discussion in the introduction). However, this is out of the scope of this thesis.

Here we present a linear data model which, however, can easily be extended to a simple non-linear data model by a non-linear weighting scheme (e.g. by weighting the galaxies according to their apparent luminosity). Nevertheless, many of the uncertainties we are facing, such as the convolution effects due to the blurring of a telescope, the pixelization scheme, the mask effects due to the observation strategy, or the selection effects due to the limited sensitivity of the detectors, can be described with a linear model. This linear model will contain non-linear information in the noise term as will be shown in section (5.1.3).

2.1.1 Linear data model

The general linear reconstruction problem formally can be written as the inverse problem of recovering the signal $\boldsymbol{s}$ from the observations $\boldsymbol{d}$ related in the following way

$$d(\boldsymbol{x}) = \int \mathrm{d}\boldsymbol{y} R(\boldsymbol{x}, \boldsymbol{y}) s^{\epsilon}(\boldsymbol{y}), \tag{2.1}$$

where R represents the kernel of the Fredholm integral equation of the first kind defined by (2.1), with noise on the signal s being expressed by the superscript ϵ. Discretizing eq. (2.1) and assuming additive noise, we can formulate the signal degradation model by

$$\boldsymbol{d} = \boldsymbol{R}\boldsymbol{s} + \boldsymbol{\epsilon}. \tag{2.2}$$

where the $m \times 1$ vector $\boldsymbol{d}$ represents the data points resulting from the measurements (here: galaxy counts), the statistical noise and the underlying signal are a $m \times 1$ vector $\boldsymbol{\epsilon}$, and a $n \times 1$ vector $\boldsymbol{s}$ respectively. The object that operates on the signal is $\boldsymbol{R}$ a $m \times n$ matrix which commonly describes blurring effects caused by the atmosphere, the point-spread function (PSF) of the telescope or the response function of the detectors of the instrument.

Let us denote the physical observation process encoded in the $\boldsymbol{R}$-matrix as $\boldsymbol{R}_{\mathrm{P}}$. We are interested in the selection function of the survey f_{S} with the corresponding masks f_{M}, which

can also be included in $\boldsymbol{R}$. One has to be careful with the data model defined in eq. 2.2. As several authors point out, there is a correlation between the underlying signal $\boldsymbol{s}$ and the level of shot noise produced by the discrete distribution of galaxies (see e.g. Seljak, 1998). Since, by definition, additive noise assumes no correlation with the signal –otherwise we would have signal content in the noise – we define the effective noise $\boldsymbol{\epsilon}$ as the product of a structure function $f_{\rm SF}$, which could be correlated with the signal, with a random noise component ($\epsilon_{\rm N}$) that is uncorrelated with the signal. Given the above definitions, the effective noise ϵ is uncorrelated with the signal. We may then rewrite eq. (2.2) in continuous representation as

$$d(\boldsymbol{x}) = \int \mathrm{d}\boldsymbol{y} R_{\rm P}(\boldsymbol{x},\boldsymbol{y}) f_{\rm S}(\boldsymbol{y}) f_{\rm M}(\boldsymbol{y}) s(\boldsymbol{y}) + f_{\rm SF}(s(\boldsymbol{x}))\epsilon_{\rm N}(\boldsymbol{x}), \tag{2.3}$$

where $R(\boldsymbol{x},\boldsymbol{y}) = R_{\rm P}(\boldsymbol{x},\boldsymbol{y}) f_{\rm S}(\boldsymbol{y}) f_{\rm M}(\boldsymbol{y})$ and $\epsilon(\boldsymbol{x}) = f_{\rm SF}(\boldsymbol{s}(\boldsymbol{x}))\epsilon_{\rm N}(\boldsymbol{x})$. In practice, we will assume white noise (i.e. constant noise in Fourier space), $\epsilon_{\rm N} = \epsilon_{\rm WN}$. However, none of the presented techniques in this thesis depend on this simplification. Some of the previous studies of large-scale structure reconstruction also included the inverse of the linear redshift-distortions operator as a matrix multiplying $\boldsymbol{R}$ (see e.g. Lahav *et al.*, 1994). Such an operator cannot easily be found for the non-linear regime. Earlier works try to correct the non-linear redshift-distortions with an additional factor in the power-spectrum analogous to Kaiser's factor (see Ballinger *et al.*, 1996; Erdoğdu *et al.*, 2004; Kaiser, 1987). Here, we propose a Bayesian solution to the signal reconstruction problem as it will be discussed later.

In most cases, the signal will be strongly under-constrained due to under-sampling, i.e. $n \gg m$, which is nearly unavoidable due to partial sky coverage of surveys. The linear equation (eq. 2.2) to be inverted is a rank-deficient system. Such systems are characterized by non-uniqueness, since the matrix $\boldsymbol{R}$ has a nontrivial null space. By superposition, any linear combination of the null space models (models $\boldsymbol{s}_0$ that satisfy $\boldsymbol{R}\boldsymbol{s}_0 = 0$) can be added to a particular solution leading to infinite solutions. Consequently, we cannot discriminate between situations where the solution is truly zero (see for example Aster *et al.*, 2005). As is well known, a direct inversion of eq. (2.2) ($\boldsymbol{R}^{-1}\boldsymbol{d}$) will amplify the statistical noise and lead to an unstable solution (see e.g. Zaroubi *et al.*, 1995). Instead, a regularization method, which often follows several steps, has to be applied . The first step consists of finding an expression for an estimator of the signal $\boldsymbol{s}$ that approximately satisfies the data model (eq. 2.2) and copes with the noise. Further regularization methods are usually required in a second step to actually calculate the estimator. This happens whenever some ill-posed linear or non-linear operators have to be inverted. We shall distinguish between noise regularization and inverse regularization according to the first and the second step, respectively. As Zaroubi *et al.* (1995) pointed out, using a mean variance estimator alone does not completely solve the inverse problem. Therefore, they proposed the singular value decomposition algorithm (SVD) to extra-regularize these problems. However, this method requires one to calculate the correlation matrix of the data implying a slow algorithm, scaling as $\mathcal{O}(n^3)$, and needs large storage facilities. We will show that a Bayesian approach is a *natural* regularizer for the noise, which then can be regularized further for the inverse purpose with efficient methods that scale as $\mathcal{O}(n \log_2 n)$ (see section 3). Let us address the problem of signal reconstruction from a statistical inference perspective.

2.2 Inversion via statistical estimator

In parametric modeling it is assumed that observational data have been generated by random processes with probability density distributions, depending on the model parameters (see for example Robert, 2001). Statistical analysis in this context is essentially an inverse method, which aims at retrieving the causes (here reduced to the parameters of the probabilistic generating mechanism) from the effects (here summarized by the observations).

Traditionally, one tries to find a way where the available information is optimally used and a unique estimator is selected from an infinite set of solutions. One of the classical approaches consists of minimizing the variance of the residuals, which is the variance of the discrepancy between the estimator and the set of possible realizations consistent with the data (see Rybicki & Press, 1992). This conjecture is reasonable because the least deviation from the set of *true* signals is searched. The estimator obtained in this way is called the least squares quadratic (LSQ) estimator. However, a transparent statement of the statistical assumptions is missing in this method, contrary to the Bayesian approach used in this work as will be shown below. Moreover, Bayesian statistics allows sampling the PDF of the system under consideration in a natural way. Strictly speaking, one does not look for a unique estimator in this framework. Nevertheless, a summary of the PDF can be given by the mean of the sample (see section 2.6).

The most general approach to determine an estimator, however, should be based on the global (joint) PDF over all relevant quantities, like the signal $\boldsymbol{s}$ and all model parameters $\boldsymbol{p}$, without neglecting any possible dependences. Let us assume that $P(\boldsymbol{s}, \boldsymbol{p} \mid \boldsymbol{d})$, the joint PDF of the system under consideration, depends on the signal $\boldsymbol{s}$ and a series of additional parameters $\boldsymbol{p}$, given the observations $\boldsymbol{d}$. One solution would then be to calculate the expectation of the signal over the joint PDF space

$$\mathrm{E}_{\mathrm{joint}}(\boldsymbol{s}) \equiv \int \mathrm{d}\boldsymbol{s}\, \mathrm{d}\boldsymbol{p} \left[P(\boldsymbol{s}, \boldsymbol{p} \mid \boldsymbol{d})\, \boldsymbol{s} \right] \equiv \langle \boldsymbol{s} \rangle_{(\boldsymbol{s},\boldsymbol{p}|\boldsymbol{d})}, \tag{2.4}$$

where we have introduced the ensemble average $\langle\rangle_{(\boldsymbol{s},\boldsymbol{p}|\boldsymbol{d})}$ with the subscript representing the PDF over which the integral is done $P(\boldsymbol{s}, \boldsymbol{p} \mid \boldsymbol{d}) \rightarrow (\boldsymbol{s}, \boldsymbol{p} \mid \boldsymbol{d})$[1]. Expression (2.4) can consequently be read as the ensemble average over all possible signals and parameters. The joint PDF is unfortunately quite hard to calculate directly, and the integral in eq. (2.4) is computationally too expensive for realistic cases as it involves many parameters and a large amount of data. To disentangle the uncertainties in parameter and signal spaces, let us apply the product rule of statistics[2] to eq. (2.4)

$$\begin{aligned} \mathrm{E}_{\mathrm{joint}}(\boldsymbol{s}) &= \int \mathrm{d}\boldsymbol{p}\, P(\boldsymbol{p} \mid \boldsymbol{d}) \left[\int \mathrm{d}\boldsymbol{s} \left[P(\boldsymbol{s} \mid \boldsymbol{p}, \boldsymbol{d})\, \boldsymbol{s} \right] \right] \\ &= \mathrm{E}_{\boldsymbol{p}} \Big[\mathrm{E}_{\boldsymbol{s}} \left(\boldsymbol{s} \mid \boldsymbol{p}, \boldsymbol{d} \right) \mid \boldsymbol{d} \Big] = \langle \langle \boldsymbol{s} \rangle_{(\boldsymbol{s}|\boldsymbol{p},\boldsymbol{d})} \rangle_{(\boldsymbol{p}|\boldsymbol{d})}. \end{aligned} \tag{2.5}$$

[1] Sometimes, however, the ensemble angles will denote the estimator of some signal or parameter in a more general sense, like the maximum likelihood or the maximum a posteriori (see sections 2.4 and 2.5, respectively). Note that a bracket formalism could be introduced at this point, in which eq. (2.4) would be represented in the following way: $(\boldsymbol{s}|\boldsymbol{s}|\boldsymbol{p}, \boldsymbol{d})$.

[2] $P(\boldsymbol{s}, \boldsymbol{p} \mid \boldsymbol{d}) = P(\boldsymbol{s} \mid \boldsymbol{p}, \boldsymbol{d}) P(\boldsymbol{p} \mid \boldsymbol{d})$

This means that the expectation of the signal $\boldsymbol{s}$ corresponds to the average of the conditional mean of $\boldsymbol{s}$ over the marginal distribution of $\boldsymbol{p}$ (see for example Gelman *et al.*, 2004), where the conditional mean is given by

$$\mathrm{E}_{\mathrm{cond}}(\boldsymbol{s}) = \mathrm{E}_{\boldsymbol{s}}(\boldsymbol{s} \mid \boldsymbol{p}, \boldsymbol{d}) = \int \mathrm{d}\boldsymbol{s} \left[P(\boldsymbol{s} \mid \boldsymbol{p}, \boldsymbol{d})\, \boldsymbol{s} \right] = \langle \boldsymbol{s} \rangle_{(\boldsymbol{s}|\boldsymbol{p},\boldsymbol{d})}. \tag{2.6}$$

Traditionally, the conditional PDF has been used to determine the estimator of the signal assuming that all the parameters are known (e.g. Zaroubi *et al.*, 1995).

As the reconstruction step of the density field is computationally expensive, a joint estimation of the parameters is out of scope. Therefore, the reduced approach of basing the estimators on conditional PDFs provides a computationally more feasible way to tackle problems of this kind. In particular, we will demonstrate that an operator formalism allows efficient sampling of the conditional PDFs, enabling us to sample the joint PDF in a Bayesian framework.

2.3 Bayesian approach

Given a data model, one can usually find an expression for the sampling distribution, i.e. the probability of obtaining the data given the signal and some additional parameters $\boldsymbol{p}$, $P(\boldsymbol{d} \mid \boldsymbol{s}, \boldsymbol{p})$. This is much less difficult than a direct calculation of the posterior $P(\boldsymbol{s} \mid \boldsymbol{d}, \boldsymbol{p})$. We need an expression which relates both the sampling and the posterior distribution given by Bayes theorem. The derivation of Bayes theorem is straightforward from the joint PDF of the signal and the data, using the product rule and the fact that the joint PDF is invariant under permutations of its arguments[1]. Bayes theorem can be expressed by the following equation

$$P(\boldsymbol{s} \mid \boldsymbol{d}, \boldsymbol{p}, I) = \frac{P(\boldsymbol{d} \mid \boldsymbol{s}, \boldsymbol{p}, I) P(\boldsymbol{s} \mid \boldsymbol{p}, I)}{P(\boldsymbol{d} \mid \boldsymbol{p}, I)}, \tag{2.7}$$

where $P(\boldsymbol{s} \mid \boldsymbol{p}, I)$ represents the prior knowledge about the signal, as it models the signal before any observations occur. The PDF given by $P(\boldsymbol{d} \mid \boldsymbol{p}, I)$ stands for the so-called evidence that is treated as the normalization of the posterior

$$P(\boldsymbol{d} \mid \boldsymbol{p}, I) = \int \mathrm{d}\boldsymbol{s}\, P(\boldsymbol{d} \mid \boldsymbol{s}, \boldsymbol{p}, I) P(\boldsymbol{s} \mid \boldsymbol{p}, I). \tag{2.8}$$

It is worth mentioning that all the probabilities are conditional to the underlying physical picture, or prior information I. This has to be explicitly considered in case of model comparisons. In the following sections, we will present the steps for completing a Bayesian analysis, starting with the likelihood, then discussing the importance of the prior, and finishing with sampling through the joint signal and parameter space. Note that different choices for these three components (likelihood, prior, and sampling) lead to different classes of reconstruction algorithms.

[1]

$$\begin{aligned} P(\boldsymbol{s}, \boldsymbol{d}, \boldsymbol{p}, I) &= P(\boldsymbol{s} \mid \boldsymbol{d}, \boldsymbol{p}, I) P(\boldsymbol{d} \mid \boldsymbol{p}, I) = \\ P(\boldsymbol{d}, \boldsymbol{s}, \boldsymbol{p}, I) &= P(\boldsymbol{d} \mid \boldsymbol{s}, \boldsymbol{p}, I) P(\boldsymbol{s} \mid \boldsymbol{p}, I) \end{aligned}$$

An overview of the different reconstruction scheme implementations based on this classification can be found in table (2.1).

2.4 The likelihood

The likelihood function is formally any function of the parameters $\boldsymbol{\theta}$ proportional to the sample density

$$\mathcal{L}(\boldsymbol{\theta} \mid \boldsymbol{d}) \propto P(\boldsymbol{d} \mid \boldsymbol{\theta}). \tag{2.9}$$

Many inference approaches are based on the likelihood function, justified by the likelihood principle, which states that the information obtained by an observation $\boldsymbol{d}$ about $\boldsymbol{\theta}$ is entirely contained in the likelihood function $\mathcal{L}(\boldsymbol{\theta} \mid \boldsymbol{d})$. To be specific, if d_1 and d_2 are two observations depending on the same parameter θ such that there exists a constant c satisfying $\mathcal{L}_1(\theta \mid d_1) = c\mathcal{L}_2(\theta \mid d_2)$ for every θ, d_1 and d_2 then bring the same information about θ and must hence lead to identical inferences.

Maximum likelihood (ML) methods, for example, rely on the likelihood principle with an estimator of the parameters given by

$$\langle \boldsymbol{\theta} \rangle_{\mathrm{ML}} = \arg\sup_{\boldsymbol{\theta}} \mathcal{L}(\boldsymbol{\theta} \mid \boldsymbol{d}), \tag{2.10}$$

i.e., the value of $\boldsymbol{\theta}$ that maximizes the probability density at $\boldsymbol{d}$. Bayesian methods take also advantage of the likelihood principle incorporating the decision-related requirement of the inferential problem through the definition of a prior distribution (see section 2.5). The definition of the likelihood is the first step in a Bayesian framework to determine the posterior distribution (see eq. 2.7). In using galaxy redshift surveys to trace the matter distribution, we have to deal with the discrete nature of the data sample. Thus the likelihood may be derived here for Poissonian statistics.

2.4.1 Poissonian likelihood

The likelihood of our galaxy distribution may be approximately represented by a Poissonian distribution (the real statistics should describe the much more complex galaxy formation process). Under the assumption of independent and identically distributed (*iid*) observations, this yields

$$\mathcal{L}(\boldsymbol{s} \mid \boldsymbol{d}, \boldsymbol{p}) \propto P(\boldsymbol{d} \mid \boldsymbol{s}, \boldsymbol{p}) \quad = \quad \prod_{i=1}^{m} \exp\left(-\left[(\boldsymbol{R}\boldsymbol{s}')_i + c_i\right]\right) \frac{\left[(\boldsymbol{R}\boldsymbol{s}')_i + c_i\right]^{(d_i' + c_i)}}{(d_i' + c_i)!},$$

where d_i' are the galaxy counts per cell i and the real, positive signal of the expectation value of the number of galaxies is given by $\boldsymbol{s}_i' = \overline{n_{\mathrm{g}}}(1 + b\boldsymbol{s}_i)$, with $s_i = \delta_{\rho i} = \frac{\rho_i - \overline{\rho}}{\overline{\rho}}$ the DM over-density, our target signal. The quantity n_{g} stands for the mean number of galaxies, $\overline{\rho}$ represents the mean density and b the bias factor. All these quantities are redshift-dependent. The additional parameters $\boldsymbol{p}$ in this case would be represented by some background c_i and would enter into the operator $\boldsymbol{R}$ that modifies the signal $\boldsymbol{s}$.

For a similar application in astronomy see Lahav & Gull (1989) and Robinson (1991). If d_i' is not converted to an integer, a Gamma function may be used instead of the factorial, $(d_i' + c_i)! \rightarrow \Gamma(d_i' + c_i + 1)$.

2.4.2 Gaussian likelihood

When the number of counts is large the Poisson distribution can be approximated by the normal distribution. In that case, the likelihood can be given by a Gaussian distributed noise

$$\begin{aligned} \mathcal{L}(\boldsymbol{s} \mid \boldsymbol{d}, \boldsymbol{p}) \propto P(\boldsymbol{d} \mid \boldsymbol{s}, \boldsymbol{p}) &= \frac{1}{[(2\pi)^m \det(\boldsymbol{N})]^{1/2}} \exp\left(-\frac{1}{2}\boldsymbol{\epsilon}^\dagger \boldsymbol{N}^{-1}\boldsymbol{\epsilon}\right) \\ &\propto \exp\left[-\frac{1}{2}\chi^2(\boldsymbol{s})\right], \end{aligned} \tag{2.11}$$

where $\boldsymbol{N} = \langle \boldsymbol{\epsilon}\boldsymbol{\epsilon}^\dagger \rangle_{(\boldsymbol{\epsilon}|\boldsymbol{p})}$ is the covariance matrix of the noise $\boldsymbol{\epsilon} \equiv \boldsymbol{d} - \boldsymbol{R}\boldsymbol{s}$, and

$$\chi^2(\boldsymbol{s}) = (\boldsymbol{d} - \boldsymbol{R}\boldsymbol{s})^\dagger \boldsymbol{N}^{-1} (\boldsymbol{d} - \boldsymbol{R}\boldsymbol{s}). \tag{2.12}$$

The parameters $\boldsymbol{p}$ determine the structure of the noise $\boldsymbol{\epsilon}$ (and therefore the structure of the covariance matrix $\boldsymbol{N}$), and also enter into the operator $\boldsymbol{R}$. We give different expressions for the noise covariance matrix $\boldsymbol{N}$ in section (3.3).

Note that χ^2 coincides with the square of the Mahalanobis distance[1] between $\boldsymbol{d}$ and $\boldsymbol{R}\boldsymbol{s}$, and also coincides with the squared $\boldsymbol{N}^{-1}$-norm of the error

$$\chi^2(\boldsymbol{s}) = D^2_{\rm Mah}(\boldsymbol{d}, \boldsymbol{R}\boldsymbol{s})_{\boldsymbol{N}^{-1}} = ||\boldsymbol{\epsilon}||^2_{\boldsymbol{N}^{-1}}. \tag{2.13}$$

In this case, the ML will correspond to the least squares of the error. It will minimize the $\chi^2(\boldsymbol{s})$ and hence minimize the Mahalanobis distance between the data and the noise-free data model. Therefore, the ML is equivalent to searching the estimator that fits the data better without constraining the model for the signal. Let us study the prior that precisely sets constraints on the signal $\boldsymbol{s}$.

2.5 The prior

A second step in Bayesian analysis is to specify the prior distribution for the signal, which contains the prior knowledge about the signal before the measurements were carried out. For little informative data it can strongly affect the posterior distribution and thus modify any inference based on it. For this reason, frequentists criticize Bayesian methods as being subjective. Other definitions of probability, like the frequentist, however, can be shown in most of the situations to be particular cases of the Bayesian approach (see e.g. Tanner, 1996), implying the use of an implicit prior. The advantage of defining the prior knowledge about the system under consideration is that the interpretation of the results is straightforward, especially because assumptions

[1] We introduce here a generalized definition of the Mahalanobis distance as: $D^2_{\rm Mah}(\boldsymbol{x}, \boldsymbol{y})_{\boldsymbol{M}} = (\boldsymbol{x} - \boldsymbol{y})^\dagger \boldsymbol{M} (\boldsymbol{x} - \boldsymbol{y})$, with $\boldsymbol{x}$ and $\boldsymbol{y}$ being two vectors in the N-dimensional space and $\boldsymbol{M}$ a $N \times N$ matrix.

Classification of reconstruction methods

	Non-informative priors		Informative priors (MAP)	
Prior	**Flat (ML)**	**Entropic (MEM)**	**Gaussian**	**Poissonian**
Likelihood				
Gaussian			WIENER (Tikhonov, Ridge)	
–Radio		Sutton & Wandelt (2006)[#]		
–CMB	COBE: Janssen & Gulkis (1992) Tegmark (1997,1997b) ROMA: Natoli *et al.* (2001) MAPCUMBA: Doré *et al.* (2001) MAXIMA: Stompor *et al.* (2002) MAGIC[#]: Wandelt *et al.* (2004) MIRAGE: Yvon & Mayet (2005) MADAM: Keihänen *et al.* (2005)	Maisinger *et al.* (1997) Hobson *et al.* (1998)	Bunn & Sugiyama (1995) Tegmark (1997,1997b) MAGIC[#]: Wandelt *et al.* (2004) O'Dwyer *et al.* (2004)[#] Eriksen *et al.* (2007)[#] Larson *et al.* (2007)[#]	Hobson & McLachlan (2003)[#]
–LSS			Fisher *et al.* (1994) Hoffman (1994) Lahav *et al.* (1994), Lahav (1994) Zaroubi *et al.* (1995) Fisher *et al.* (1995) Webster *et al.* (1997) Zaroubi *et al.* (1999) Schmoldt *et al.* (1999) Erdoğdu *et al.* (2004,2006)	
		ARGO: MEMG[*] (section 2.5.9, appendix A.10)	**ARGO**: WIENER[**#] (sections 2.5.3, 2.6, 4, appendix A.2)	
Poissonian	Richardson (1972) Lucy (1974)	**ARGO**: MEMP[*] (section 2.5.9, appendix A.10)	**ARGO**: GAPMAP[*] (section 2.5.4, appendix A.5)	
Inverse Gamma				
–CMB	MAGIC[#]: Wandelt *et al.* (2004) O'Dwyer *et al.* (2004)[#] Larson *et al.* (2007)[#] Eriksen *et al.* (2007)[#]			
–LSS	**ARGO**[*#] (section 5.3.2)			
Modified Gaussian				
–CMB	Pierpaoli & Anthoine (2005)[#]			
–LSS	Percival (2005)[#]			

[*]developed and presented in this thesis; [**]developed, tested and presented in this thesis; [#]able to sample PDFs

Table 2.1: In the previous page the classification of reconstruction methods in astrophysics based on the prior (columns) and likelihood (rows) is shown. Note that most of the reconstruction algorithms in other research areas, such as tomography, where Tikhonov-regularization is widely used, or the algebraic reconstruction technique (ART), which is based on the asymptotic regularization, fall into the class of Wiener-filtering schemes as we show in section (2.5.1) and appendix B.2. The differences in the ML CMB-map-making algorithms reside mainly in the modeling of the complex noise structure that arises due to the scanning strategies of the satellites and in the various foreground removal methods. The LSS Wiener-filtering methods on the other hand present improvements in the redshift distortions treatment, or are based on the different input data, either galaxy-positions or peculiar velocities. The discrete object detection (Hobson & McLachlan, 2003) algorithm was developed to find Sunyaev-Zeldovich clusters. This is also the case for the modified Gaussian by Pierpaoli et al. (2005). The reconstruction of the power-spectrum is also listed here. In CMB the joint map and power-spectrum estimation is done by MAGIC. Percival (2005) samples the power-spectrum with a modified Gaussian likelihood given by a log-normal mean. We propose to follow the steps done in CMB and sample the density field and the power-spectrum jointly (see section 5.3.2). This thesis covers three new areas in LSS (GAPMAP, MEMG, MEMP) and presents four novel algorithms with which reconstructions can be done very fast. We have left out the reconstruction methods that are focused on the cosmological initial conditions, since they address a different problem and, in general, cannot be classified in terms of the PDFs listed in this table. Neither can other reconstruction algorithms based on geometrical arguments, like Voronoi, Delaunay tessellations, *friends-of-friends* schemes or *cloud-in-cell* interpolation schemes, be classified here.

flowing into the inference procedure are clearly stated. Once the prior is defined, we can obtain the maximum a posteriori (MAP) estimator, by maximizing the posterior distribution, which is proportional to the likelihood multiplied by the prior,

$$\langle \boldsymbol{\theta} \rangle_{\mathrm{MAP}} = \arg\sup_{\boldsymbol{\theta}} P(\boldsymbol{\theta} \mid \boldsymbol{d}). \tag{2.14}$$

Note that there is a crucial difference to the maximum likelihood estimator (eq. 2.10) due to the incorporation of the prior information.

2.5.1 Bayes and regularization methods: the prior as a regularizer

Looking at the $\log$-probabilities, we see that the MAP estimator maximizes the following quantity using Bayes theorem ($\log P(\boldsymbol{\theta} \mid \boldsymbol{d}) \propto \log(P(\boldsymbol{d} \mid \boldsymbol{\theta}) P(\boldsymbol{\theta}))$)

$$Q = \log P(\boldsymbol{d} \mid \boldsymbol{\theta}) + \log P(\boldsymbol{\theta}). \tag{2.15}$$

If we assume that the error is Gaussian distributed, (which is a fair assumption if there is no prior information about the noise), and we parameterize the prior of the parameter, say the signal $\boldsymbol{s}$, we can rewrite eq. (2.15) as ($2Q \to Q$)

$$Q = -\chi^2(\boldsymbol{s}) + \alpha f_{\mathrm{p}}(\boldsymbol{s}), \tag{2.16}$$

where we absorbed the factor 2 in the Lagrangian multiplier α, and f_{p} represents the penalty function that obliges the estimator to fulfill some constraint on the parameter $\boldsymbol{s}$, to the detriment of the $\chi^2(\boldsymbol{s})$ that strongly relies on the data. If we further assume that $\boldsymbol{N}^{-1} = \boldsymbol{I}$ (say we have

white noise), the Mahalanobis distance reduces to the Euclidean distance ($D^2_{\rm Mah}(\boldsymbol{d}, \boldsymbol{Rs})|_{\boldsymbol{N}^{-1}=\boldsymbol{I}} = D^2_{\rm Euc}(\boldsymbol{d}, \boldsymbol{Rs})$), and the quantity one wants to minimize reads

$$||\boldsymbol{\epsilon}||^2 + \alpha f_{\rm p}(\boldsymbol{s}), \tag{2.17}$$

where we have absorbed the minus sign in α. Expression (2.17) is equivalent to least squares with a regularization term, and belongs to Ridge-regression problems (Hoerl, 1962; Hoerl & Kennard, 1970). Assuming that the penalty function takes the following form $f_{\rm p}(\boldsymbol{s}) = ||\boldsymbol{s}||^2$, we can write expression (2.17) as

$$||\boldsymbol{\epsilon}||^2 + \alpha||\boldsymbol{s}||^2, \tag{2.18}$$

which then becomes the Tikhonov regularization method (Tikhonov, 1963). The parameter α is called the regularization parameter. These methods lead to linear filters and are essentially identical to Wiener-filtering (Foster, 1961), which will be presented in the next section. Note that Tikhonov regularization is equivalent to MAP of a Gaussian likelihood with noise covariance matrix $\boldsymbol{N} = \boldsymbol{I}$ and Gaussian prior, with signal covariance matrix $\boldsymbol{S} = \alpha^{-1}\boldsymbol{I}$. Nevertheless, the penalty function $f_{\rm p}$ in general can be a non-linear function of the parameter to be estimated (say the signal $\boldsymbol{s}$) leading to non-linear estimators. We will introduce MEM as such an example. Tikhonov regularization can also be generalized to non-linear problems by introducing a non-linear kernel operator $\boldsymbol{R}(\boldsymbol{s})$.

Summarizing the exposed theory of signal reconstruction, we might interpret the likelihood as some distance measure between the data and the noise-free model of the data, and the prior as some constraint that tightens the estimator to the model of the signal. We have shown here that the classical methods of signal reconstruction, like the Tikhonov regularization, are particular cases of the Bayesian approach. The inclusion of a prior can be regarded as a *natural* regularization, in the sense that the regularization term is provided by a (physical) model of the *true* signal. In appendix B.2, we discuss the relation between other regularization methods and the Bayesian approach. In the following sections we introduce different priors that are relevant for large-scale structure reconstruction and are implemented in ARGO.

2.5.2 Gaussian prior

The distribution of the primordial density field should be very close to Gaussianity according to most of the inflationary scenarios (Albrecht & Steinhardt, 1982; Guth, 1981; Linde, 1982). In fact, the measurements of the CMB show very small deviations from Gaussianity (see e.g. Komatsu *et al.*, 2003). Non-Gaussianities in the matter distribution arose mainly from non-linear gravitational collapse. The non-linear regime of structure formation is responsible for the strong radial redshift-distortions, the *finger-of-god* effect, limiting the accuracy of reconstructions. Previous attempts to correct for these distortions have modified the power-spectrum by introducing a Lorentzian factor (see e.g. Ballinger *et al.*, 1996; Erdoğdu *et al.*, 2004). In section (2.6) we propose an alternative way to do this in a Bayesian framework, where peculiar velocities are sampled together with the three dimensional map of the matter distribution. For the underlying DM density fluctuation we will assume a Gaussian prior. This is a crude approximation for the density field at the present epoch of the Universe, especially on small-scales. It is, however, a valid description on large-scales and allows to incorporate non-linear corrections

in a MCMC fashion, as will be discussed in section (2.6). Following Bardeen *et al.* (1986) we may thus write the PDF of the signal as a multivariate Gaussian distribution

$$P(\boldsymbol{s} \mid \boldsymbol{p}) = \frac{1}{[(2\pi)^n \det(\boldsymbol{S})]^{1/2}} \exp\left(-\frac{1}{2}\boldsymbol{s}^\dagger \boldsymbol{S}^{-1}\boldsymbol{s}\right), \tag{2.19}$$

with $\boldsymbol{S}$ being the covariance matrix of the signal ($\boldsymbol{S} = \boldsymbol{S}(\boldsymbol{p}) = \langle \boldsymbol{s}\boldsymbol{s}^\dagger \rangle_{(\boldsymbol{s}|\boldsymbol{p})}$). This formula emphasizes the high dimensional character of the problem (n dimensions of the signal reconstruction, with n being typically between 10^3 and 10^9).

2.5.3 Gaussian prior and Gaussian likelihood: the Wiener-filter

The Gaussian prior together with the Gaussian likelihood lead to the Wiener-filter, completing the square for the signal in the exponent of the posterior distribution (see Zaroubi *et al.* (1995) and appendix A.1),

$$\begin{aligned} P(\boldsymbol{s} \mid \boldsymbol{d}, \boldsymbol{p}) &\propto \exp\left(-\frac{1}{2}\left[\boldsymbol{s}^\dagger \boldsymbol{S}^{-1}\boldsymbol{s} + (\boldsymbol{d} - \boldsymbol{R}\boldsymbol{s})^\dagger \boldsymbol{N}^{-1}(\boldsymbol{d} - \boldsymbol{R}\boldsymbol{s})\right]\right) \\ &\propto \exp\left(-\frac{1}{2}\left[(\boldsymbol{s} - \langle \boldsymbol{s}\rangle_{\rm WF})^\dagger (\boldsymbol{\sigma}_{\rm WF}{}^2)^{-1}(\boldsymbol{s} - \langle \boldsymbol{s}\rangle_{\rm WF})\right]\right), \end{aligned} \tag{2.20}$$

where the Wiener-filter used to calculate the estimator from the data $\langle \boldsymbol{s}\rangle_{\rm WF} = \boldsymbol{F}_{\rm WF}\boldsymbol{d}$ is given by

$$\boldsymbol{F}_{\rm WF} = (\boldsymbol{S}^{-1} + \boldsymbol{R}^\dagger \boldsymbol{N}^{-1}\boldsymbol{R})^{-1}\boldsymbol{R}^\dagger \boldsymbol{N}^{-1}, \tag{2.21}$$

and the corresponding covariance is

$$\boldsymbol{\sigma}^2_{\rm WF} = \langle \boldsymbol{r}\boldsymbol{r}^\dagger \rangle_{\rm WF} = (\boldsymbol{S}^{-1} + \boldsymbol{R}^\dagger \boldsymbol{N}^{-1}\boldsymbol{R})^{-1}, \tag{2.22}$$

with $\boldsymbol{r} = \boldsymbol{s} - \langle \boldsymbol{s}\rangle_{\rm WF}$ being the residual. The Wiener-filter can also be obtained as the LSQ estimator [1] (for an explicit derivation see Zaroubi *et al.*, 1995, and appendix A.2) leading to the following expression

$$\langle \boldsymbol{s}\rangle_{\rm WF} = \langle \boldsymbol{s}\rangle_{\rm LSQ} = \langle \boldsymbol{s}\boldsymbol{d}^\dagger \rangle \langle \boldsymbol{d}\boldsymbol{d}^\dagger \rangle^{-1}\boldsymbol{d}, \tag{2.23}$$

where the correlation matrix of the signal and the data ($\langle \boldsymbol{s}\boldsymbol{d}^\dagger \rangle$) is multiplied by the inverse of the autocorrelation matrix of the data ($\langle \boldsymbol{d}\boldsymbol{d}^\dagger \rangle^{-1}$). Given that the signal and the noise are uncorrelated ($\langle \boldsymbol{s}\boldsymbol{\epsilon}^\dagger \rangle = 0$), the correlation matrix of the signal and the data reduces to: $\langle \boldsymbol{s}\boldsymbol{d}^\dagger \rangle = \boldsymbol{S}\boldsymbol{R}^\dagger$. Thus, eq. (2.23) can be reformulated as

$$\boldsymbol{F}_{\rm WF} = \boldsymbol{S}\boldsymbol{R}^\dagger (\boldsymbol{R}\boldsymbol{S}\boldsymbol{R}^\dagger + \boldsymbol{N})^{-1}. \tag{2.24}$$

We show in appendix (A.3) that both expressions for the Wiener-filter (eqs. 2.21 and 2.24) are equivalent. From now on, we will call eq. (2.24) the direct representation of the Wiener-filter, and eq. (2.21) the inverse representation of the Wiener-filter.

[1] Note that in this case, the least squares are referred to the residuals $\boldsymbol{r}$, i.e. the difference between the real signal $\boldsymbol{s}$ and the estimated signal $\langle \boldsymbol{s}\rangle_{\rm LSQ}$: $||\boldsymbol{r}||^2 = ||\boldsymbol{s} - \langle \boldsymbol{s}\rangle_{\rm LSQ}||^2$, where the prior on $\boldsymbol{s}$ is given in a more implicit way by assuming a linear relation between the estimator and the data and statistical homogeneity.

The following notation can be introduced for the posterior PDF

$$P(\boldsymbol{s} \mid \boldsymbol{d}, \boldsymbol{p}) \propto G(\boldsymbol{s} - \langle \boldsymbol{s} \rangle_{\mathrm{WF}}, \boldsymbol{\sigma}^2_{\mathrm{WF}}), \tag{2.25}$$

i.e. given a dataset $\boldsymbol{d}$ derived from a Gaussian process, the possible signals are Gaussian distributed around the Wiener-filter reconstruction $\langle \boldsymbol{s} \rangle_{\mathrm{WF}}$ with a covariance $\boldsymbol{\sigma}^2_{\mathrm{WF}}$. The parameters $\boldsymbol{p}$ enter the operator $\boldsymbol{R}$, including also the cosmological parameters that determine the signal covariance matrix $\boldsymbol{S}$. We will discuss in section (2.6) how to sample $\boldsymbol{S}$ and to determine cosmological parameters.

A remarkable characteristic of the Wiener-filter is that it suppresses the signal in the presence of a high noise level resulting in the null estimator and gives just the deblurred data when noise is negligible. In this sense it is a biased estimator, since its covariance matrix has less power than the original one. Some attempts have been made to derive an equivalent unbiased estimator (see Zaroubi, 2002b). However, one might be especially interested in obtaining a conservative estimator. Sampling the joint PDF will fill the missing modes (see e.g. Wandelt *et al.*, 2004) and in this way complete the signal in regions where it is under-sampled or the signal to noise ratio is low. It is interesting to note that the Wiener Filter coincides with the MAP estimator in the case of a Gaussian prior on $\boldsymbol{s}$ and a Gaussian likelihood ($\langle \boldsymbol{s} \rangle_{\mathrm{WF}} = \langle \boldsymbol{s} \rangle_{\mathrm{MAP}}$). Performing the integral of the conditional PDF (see eq. 2.6) one obtains the same estimator again, thus $\langle \boldsymbol{s} \rangle_{\mathrm{WF}} = \langle \boldsymbol{s} \rangle_{(\boldsymbol{s}|\boldsymbol{d},\boldsymbol{p})}$. This is a very important result, since it permits one to sample the conditional PDF. We propose to exploit this property for the joint estimation of the signal and its power-spectrum as is done in the CMB (see Wandelt *et al.* (2004) and section 5.3.2).

2.5.4 Gaussian prior and Poissonian likelihood: the GAPMAP estimator

The Gaussian likelihood constitutes a valid approximation when the Poissonian character of the distribution is appropriately modeled in the noise correlation matrix $\boldsymbol{N}$. However, one would rather describe a discrete sampling process like a galaxy survey with a Poissonian likelihood. Unfortunately, there is no filter available for such a case. Thus, we present a novel iterative equation for the MAP estimator with a Gaussian prior and a Poissonian likelihood, which we call GAPMAP (see appendix A.5 for a derivation)

$$\boldsymbol{s}^{j+1} = \boldsymbol{S}\boldsymbol{R}^{\dagger} b\overline{n_{\mathrm{g}}} \left(-\vec{1} + \mathrm{diag}\left(\boldsymbol{R}\overline{n_{\mathrm{g}}}(\vec{1} + b\boldsymbol{s}^{j}) + \boldsymbol{c} \right)^{-1} (\boldsymbol{d}' + \boldsymbol{c}) \right). \tag{2.26}$$

2.5.5 Flat prior

With the aim of deriving objective posterior distributions, non-informative prior distributions are introduced. A non-informative prior would suggest that any value is reasonable. Flat priors where the probability distribution is assumed to be constant $\boldsymbol{P}(\boldsymbol{s}) = \mathrm{const}$ are thus very often applied. Note, however, that these are improper priors, since the integral of these distributions diverges to infinity. In this case, the posterior is proportional to the likelihood. The maximum likelihood solution coincides in this way with the MAP estimator assuming a flat prior ($\langle \boldsymbol{s} \rangle_{\mathrm{ML}} = \langle \boldsymbol{s} \rangle_{\mathrm{MAP}|\mathrm{flat}}$).

2.5.6 Flat prior and Gaussian likelihood: the COBE-filter

In CMB map-making algorithms it is common to use the so-called COBE-filter (see Janssen & Gulkis, 1992; Tegmark, 1997), which can easily be derived by maximizing the likelihood given in eq. (2.11)

$$\boldsymbol{F}_{\mathrm{COBE}} = (\boldsymbol{R}^\dagger \boldsymbol{N}^{-1} \boldsymbol{R})^{-1} \boldsymbol{R}^\dagger \boldsymbol{N}^{-1}. \tag{2.27}$$

This filter has the property that among all unbiased linear estimators (with a noise of zero mean), it leads to the minimum variance (Natoli *et al.*, 2001). Here unbiased means that the statistical mean of the estimator is equal to the *true* signal. This is, however, only fulfilled when the inverse of $\boldsymbol{R}^\dagger \boldsymbol{N}^{-1} \boldsymbol{R}$ exists (see appendix A.7). The covariance for the COBE-filter can found to be

$$\boldsymbol{\sigma}^2_{\mathrm{COBE}} = \langle \boldsymbol{r}\boldsymbol{r}^\dagger \rangle_{\mathrm{COBE}} = (\boldsymbol{R}^\dagger \boldsymbol{N}^{-1} \boldsymbol{R})^{-1}. \tag{2.28}$$

Note that, in general, the following relation holds: $\boldsymbol{\sigma}^2_{\mathrm{WF}} \leq \boldsymbol{\sigma}^2_{\mathrm{COBE}}$, as a comparison to eq. (2.22) shows.

Tegmark (1997) claims that several linear filters like the COBE or the Wiener-filter conserve information by comparing the Fisher information matrix corresponding to the filtered signal to the one of the un-filtered time ordered data. This property apparently permits one to perform cosmological parameter estimation from the reconstructed signal after filtering the data. However, linear filters conserve information only if they are invertible, which is not provided for realistic cases as we show in appendix A.8. A consistent estimation of cosmological parameters has to be done in a full Bayesian framework by estimating the joint PDF of the signal and the parameters, as we will see in section (2.6) (Wandelt *et al.*, 2004).

2.5.7 Flat prior and Poissonian likelihood: the Richardson-Lucy algorithm

A widely used deblurring algorithm in astronomy and medical tomography is the Richardson-Lucy algorithm (Lucy, 1974; Richardson, 1972), which was shown to be the maximum likelihood solution with a Poissonian likelihood by Shepp & Vardi (1982). We show the derivation in appendix A.6, as a simplified case with respect to eq. (2.26). The Richardson-Lucy algorithm cannot prevent serious noise amplifications in the restoration process (see e.g. Carasso, 1999). This is a natural consequence when a prior that regularizes the solution is missing. A toy application is presented in fig. (4.5).

2.5.8 Jeffrey's prior

Other non-informative priors have been suggested based on invariant statistical structures under transformation of variables in a Bayesian formalism. Considering a one-to-one transformation in the one-dimensional case of the parameter: $\phi = f(\theta)$, the equivalence between the respective prior densities is expressed by

$$P(\phi) = P(\theta) \left| \frac{\mathrm{d}\theta}{\mathrm{d}\phi} \right| = P(\theta) \left| f'(\theta) \right|^{-1}. \tag{2.29}$$

This relation is satisfied by Jeffrey's prior $P(\theta) \propto [J(\theta)]^{1/2}$, where $J(\theta)$ is the Fisher information[1]

$$J(\theta) \equiv \langle \left(\frac{\partial \log P(d|\theta)}{\partial \theta} \right)^2 \rangle_{(d|\theta)} = -\langle \frac{\partial^2 \log P(d|\theta)}{\partial \theta^2} \rangle_{(d|\theta)}, \tag{2.30}$$

and where we have assumed the following regularity condition $\int \mathrm{d}d \frac{\partial^2}{\partial \theta^2} P(d \mid \theta) = 0$. Relation (2.29) can be proved easily by doing the evaluation $J(\phi) = -\langle \frac{\partial^2 \log P(d|\phi)}{\partial \phi^2} \rangle_{(d|\theta)} = J(\theta) \left| \frac{\mathrm{d}\theta}{\mathrm{d}\phi} \right|^2$ (see e.g. Gelman *et al.*, 2004). Note, however, that in the multidimensional case, Jeffrey's prior may lead to incoherences or even paradoxes (see e.g. Berger & Bernardo, 1992; Robert, 2001). Jeffrey's prior is applied adequately, when not even the order of magnitude of the parameter to be estimated is known a priori. We derive Jeffrey's ignorance prior for the 3-D power-spectrum ($\boldsymbol{S} = \mathrm{diag}(P_{\mathrm{S}}(\boldsymbol{k}))$)[1] in appendix A.9 (see section 5.3.2 for an application of this prior).

2.5.9 Entropic prior and Maximum Entropy method

Another approach searches the least informative model compatible with the data using a prior based on Boltzmann's definition of entropy S^{E} [2] (or equivalently, Shannon's notion of information, see Shannon, 1948),

$$P(\boldsymbol{s} \mid \boldsymbol{p}) = \exp(\alpha S^{\mathrm{E}}), \tag{2.31}$$

and maximizing the resulting posterior distribution, being α some constant, and $\boldsymbol{s}$ the so-called hidden image (or signal). This inference procedure is called the Maximum Entropy method (MEM) (Frieden, 1972; Gull, 1989; Gull & Daniell, 1978; Hobson *et al.*, 1998; Jaynes, 1963, 1968; Maisinger *et al.*, 1997; Skilling, 1989). For a review see Narayan & Nityananda (1986). From now on we will represent the underlying signal by $\boldsymbol{s}$ in the framework of MEM. The MEM can be considered as MAP estimation with an entropic prior.

The particular expression for the entropy depends on the statistical formulation of the non-informative prior. Let us think of a positive signal as a grid with q cells, with each cell i having a certain intensity value s_i, $i = 1, \ldots, q$, with an uncertainty on each value given by $\pm\alpha^{-1}$. Then we define some discrete *quanta* n_i on each cell related to the intensity through the uncertainty: $n_i = \alpha s_i$. The signal can be guessed by distributing the n_i *quantas* in the grid. In this way, the image is modeled in this way analogously to the energy configuration space of a thermo-dynamical system. If we further demand each cell to be *iid*, the number of ways this object can occur is given by the multiplicity

$$W = \frac{N_{\mathrm{q}}!}{n_1! n_2! \ldots n_q!}, \tag{2.32}$$

[1] The generalization to the multidimensional case leads to the following matrix form: $\boldsymbol{J}_{ij}(\boldsymbol{\theta}) \equiv \langle \frac{\partial \log P(\boldsymbol{d}|\boldsymbol{\theta})}{\partial \boldsymbol{\theta}_i} \frac{\partial \log P(\boldsymbol{d}|\boldsymbol{\theta})}{\partial \boldsymbol{\theta}_j} \rangle_{(\boldsymbol{d}|\boldsymbol{\theta})}$ (see appendix A.8).

[1] Here the autocorrelation matrix $\boldsymbol{S}$ is represented in k-space. We will discuss this in further detail in section (3.3).

[2] Not to be confused by the signal autocorrelation $\boldsymbol{S}$.

with $N_{\rm q}$ being the total amount of *quantas* to be distributed in all cells ($N_{\rm q} = \sum_i n_i$). The probability of any particular result is then given by the multinomial distribution

$$P(\boldsymbol{s}' \mid \boldsymbol{p}) = W q^{-N_{\rm q}}. \tag{2.33}$$

Sutton & Wandelt (2006) propose to sample from the multiplicity function directly to perform reconstructions in radioastronomy. By using Stirling's formula for the factorials ($n! \sim n^n e^{-n}$) we can write

$$\log P(\boldsymbol{s}' \mid \boldsymbol{p}) = -\alpha \sum_i s'_i \log s'_i + const. \tag{2.34}$$

Comparing this expression with eq. (2.31), we recover Shannon's definition of entropy ($S^{\rm E}_{+} = \sum_i s'_i \log s'_i$)[3]. The expression that is commonly used for the entropy is a generalization of Shannon's formula by Skilling that can be derived based only on consistency arguments within probabilistic information theory for positive and additive distributions (PADs) (Skilling, 1989).

This generalization implies the definition of a Lebesgue measure ($\boldsymbol{m}$) for the integral of some function of the hidden image to represent the entropy

$$S^{\rm E}_{+}(\boldsymbol{s}' \mid \boldsymbol{p}) = \sum_i \left[s'_i - m_i - s'_i \log\left(s'_i/m_i\right) \right], \tag{2.35}$$

here in its discretized form. Skilling's expression for the entropy can also be derived by considering a *team of monkeys* throwing balls at q cells at random with Poissonian expectation μ_i: $P(\boldsymbol{n}|\mu) = \prod_i \mu_i^{n_i} e^{-\mu_i}/n_i!$, where $n_i = \alpha s_i$ and $\mu = \alpha m_i$ (Skilling, 1989). For a review on further expressions for the entropy see Molina *et al.* (2001).

The global maximum of $S^{\rm E}$ over $\boldsymbol{s}$ in the absence of further constraints is found to be $\boldsymbol{s}' = \boldsymbol{m}$. Consequently, $\boldsymbol{m}$ can also be thought of as a prior model for the image. However, this expression for the entropy will allow reconstructing positive signals only. Zaroubi *et al.* (1995) propose to define $\boldsymbol{s}' = \boldsymbol{\rho}$ and $\boldsymbol{m} = \boldsymbol{\rho}_0$, to avoid the possibility of having a negative distribution for $\boldsymbol{s}$.

According to Gull & Skilling (1990) the MEM can be extended to reconstruct distributions, which can be either positive or negative, as in the case of density fluctuations. Such distributions can be described as the difference between two subsidiary positive distributions (PADs)

$$\boldsymbol{s} = \boldsymbol{u} - \boldsymbol{v}, \tag{2.36}$$

relative to a common model $\boldsymbol{m}$ [1]

$$S^{\rm E}_{\pm}(\boldsymbol{u}, \boldsymbol{v} \mid \boldsymbol{p}) = \sum_i \left[u_i - 2m_i - u_i \log(u_i/m_i) \right] + \sum_i \left[v_i - 2m_i - v_i \log(v_i/m_i) \right]. \tag{2.37}$$

One can see from eq. (2.36) that $\partial S^{\rm E}_{\pm}/\partial \boldsymbol{u} = -\partial S^{\rm E}_{\pm}/\partial \boldsymbol{v}$, hence yielding

$$\boldsymbol{u}\boldsymbol{v} = \boldsymbol{m}^2. \tag{2.38}$$

[3] The "+" symbol in $S^{\rm E}_{+}$ denotes that the definition is only valid for positive signals $\boldsymbol{s}'$.

[1] The "$\pm$" symbol in $S^{\rm E}_{\pm}$ denotes that the definition is valid for positive and negative signals $\boldsymbol{s}$.

From the relations given by eqs. (2.36) and (2.38), it is easy to derive

$$\boldsymbol{u} = \frac{1}{2}(\boldsymbol{w} + \boldsymbol{s}), \tag{2.39}$$

$$\boldsymbol{v} = \frac{1}{2}(\boldsymbol{w} - \boldsymbol{s}), \tag{2.40}$$

with $w_i = (s_i^2 + 4m_i^2)^{1/2}$. Using these expressions, the total entropy can be rewritten as

$$S_{\pm}^{\mathrm{E}}(\boldsymbol{s} \mid \boldsymbol{p}) = \sum_i \Big[w_i - 2m_i - s_i \log\Big((w_i + s_i)/2m_i \Big) \Big]. \tag{2.41}$$

The Maximum Entropy method gives a non-linear estimator of the underlying signal that one wants to reconstruct. This method is especially interesting to study deviations from Gaussianity (Hobson *et al.*, 1998; Maisinger *et al.*, 1997). It is equivalent to maximize χ^2 with a Lagrangian multiplier, which includes a penalty function given by the entropy. Maximum Entropy in this context searches the hidden image that adds the least additional information to the data.

The quantity we need to maximize is given by

$$Q^{\mathrm{E}}(\boldsymbol{s} \mid \boldsymbol{p}) = \alpha S^{\mathrm{E}}(\boldsymbol{s} \mid \boldsymbol{p}) + \log \mathcal{L}(\boldsymbol{s} \mid \boldsymbol{d}, \boldsymbol{p}), \tag{2.42}$$

where the $\log \mathcal{L}$ is given by eq. (2.12) or eq. (A.29). The equation we want to solve is

$$\nabla Q^{\mathrm{E}}(\boldsymbol{s} \mid \boldsymbol{p}) = 0. \tag{2.43}$$

In section (3.2), different iterative algorithms to solve this non-linear problem will be discussed. The required expressions for the gradient of Q^{E} and its curvature for positive and positive/negative expressions of the entropy (eqs. 2.35 and 2.41) and for both Gaussian and Poissonian likelihoods are presented in appendix A.10.

Note that in the limit of low density fluctuations, i.e. in the linear regime, the expression of the entropy reduces to the quadratic entropy (eventually with an offset of the origin of $\boldsymbol{s}$), $S^{\mathrm{E}}(\boldsymbol{s} \mid \boldsymbol{p}) \simeq -\sum_i s_i^2/2m_i$. This expression is very similar to a Gaussian prior for the signal with a variance given by $\boldsymbol{m}$. In that case Maximum Entropy leads to the Wiener-filter.

2.6 Markov Chain Monte Carlo: sampling the joint PDF

The drawback of the maximization methods hitherto mentioned, is that they find a unique estimator that is most probably subject to the chosen values for the required parameters. As already mentioned, the complete characterization of a system is contained in the joint PDF in the product space of possible signals and parameters. Thus, it would be desirable to sample from this PDF to find the region of highest confidence for our estimator. This is possible using Markov Chain Monte Carlo (MCMC). The importance of sampling from the joint PDF and the viability of doing that with MCMCs has already been discussed in other contexts in astronomy (Hobson & McLachlan, 2003; Jewell *et al.*, 2004; Wandelt *et al.*, 2004). With the MCMC method, the whole system can be moved in its configuration space by updating all variables

successively in a Monte Carlo fashion, until the system relaxes (*burns-in*) and reaches the highest density region.

The expectation of the i-th parameter (θ_i) can be calculated by the so-called ergodic average, which is given by the mean of the sample

$$\langle \theta_i \rangle_{(\boldsymbol{\theta}|\boldsymbol{d})} \simeq \frac{1}{N_\mathrm{b}} \sum_{t=0}^{N_\mathrm{b}-1} {\theta_i}^t, \tag{2.44}$$

with N_b being the size of the sample drawn once the Markov Chain has *burned-in*. In general, the mean estimator is more reliable than the maximum of the distribution, especially in cases with deviations from Gaussianity (see e.g. Gelman *et al.*, 2004). The MCMC method permits one to approximately solve the integral in eq. (2.4) through expression (2.44).

2.6.1 Gibbs sampling

The most straightforward MCMC method is the Gibbs sampler (Geman & Geman, 1984), also known as the *heatbath* algorithm. The Gibbs algorithm samples from the joint PDF by repeatedly replacing each component with a value drawn from its distribution conditional on the current values of all other components. This process can be seen as a Markov Chain with transition probabilities $\boldsymbol{\pi}_k$ for $k = 1, ..., n$,

$$\boldsymbol{\pi}_k(\boldsymbol{\theta}, \boldsymbol{\theta}') = P(\theta'_k \mid \{\theta_i : i \neq k\}) \cdot \prod_{i \neq k} \delta_\mathrm{K}(\theta_i, \theta'_i), \tag{2.45}$$

where $\{\theta_i : i \neq k\} = (\theta_1, ..., \theta_{k-1}, \theta_{k+1}, ..., \theta_n)$ (see e.g. Neal, 1993) and δ_K is the Kroenecker delta-function. The Gibbs sampler starts with some initial values $\boldsymbol{\theta}^{(0)} = (\theta_1^{(0)}, ..., \theta_n^{(0)})$ and obtains new updates $\boldsymbol{\theta}^{(j)} = (\theta_1^{(j)}, ..., \theta_n^{(j)})$ from the previous step $\boldsymbol{\theta}^{(j-1)}$ through successive generation of values

$$\begin{aligned}
\theta_1^{(j)} &\sim P(\theta_1 \mid \{\theta_i^{(j-1)} : i \neq 1\}) \\
\theta_2^{(j)} &\sim P(\theta_2 \mid \theta_1^{(j)}, \{\theta_i^{(j-1)} : i > 2\}) \\
&\vdots \\
\theta_n^{(j)} &\sim P(\theta_n \mid \{\theta_i^{(j)} : i \neq n\})
\end{aligned} \tag{2.46}$$

In this way a random walk on the vector $\boldsymbol{\theta}$ is performed by making subsequent steps in low-dimensional subspaces, which span the full product space. This is similar to individual collisions of particles in a mechanical system that drives a many-body system to an equilibrium distribution for all degrees of freedom. We are especially interested in this sampling method because of its efficiency that permits us to tackle large dimensional problems in contrast to other algorithms, which include acceptance and rejection rules. See Wandelt *et al.* (2004) for applications in CMB-mapping and power-spectrum estimation. However, in the case where the particular distribution function is unknown or cannot be explicitely expressed rejection sampling methods will be necessary (see section 5.3.1), like the Metropolis-Hastings algorithm (Hastings, 1970; Metropolis *et al.*, 1953).

The MCMC method can be applied to perform simultaneously the reconstruction of the density field and the estimation of other parameters, such as the power-spectrum, the peculiar velocities, the bias, or the comological parameters (see fig. 1.1). We present in chapter (5) two novel applications of this method to power-spectrum estimation and redshift-distortion corrections, which can also be used in a joint algorithm. Note, that a higher degree of complexity can be achieved in the schemes we present in chapter (5) by going beyond linear perturbation theory or considering higher moments of the density field.

Chapter 3

Numerical method

El modo de dar una vez en el clavo es dar cien veces en la herradura.

Miguel de Unamuno

In order to efficiently sample the joint PDF, as it is required in MCMC methods (see section 2.6), fast inverse algorithms need to be considered to regularize the solution. General iterative inverse methods scale as $\mathcal{O}(n^3)$ since they imply matrix multiplications of a $n \times n$ matrix in an iterative fashion (at most n-steps until convergence). This makes the study of the joint PDFs as presented in section (2.6), at a first glance, un-feasible. However, a proper formulation of the problem in an operator formalism allows treating the matrices as operators that have to be neither calculated nor stored. Within this operator formalism, the inversion methods we present here sped up to a scaling of $\mathcal{O}(n \log_2 n)$. We start with a general formulation of iterative methods and subsequently present the different schemes that we have implemented in ARGO. Since a preconditioning treatment can dramatically enhance the performance of iterative schemes (see our numerical experiments in section 4), we pay special attention to this point in the derivation of the different schemes.

3.1 Iterative inverse and regularization methods: a unified formulation of different linear methods

Let us consider a region D in the n-dimensional Euclidean space E_n and denote $L_2(D)$ the Hilbert space of all complex measurable square integrable functions $\int_D \mathrm{d}^n \boldsymbol{z} |\boldsymbol{g}|^2(\boldsymbol{z}) < \infty$ with inner product [1]

$$\langle \boldsymbol{g} | \boldsymbol{s} \rangle = \int_D \mathrm{d}^n \boldsymbol{z} \overline{\boldsymbol{g}(\boldsymbol{z})} \boldsymbol{s}(\boldsymbol{z}), \tag{3.1}$$

and norm of $\boldsymbol{g} \in L_2(D)$

$$||\boldsymbol{g}|| = \langle \boldsymbol{g} | \boldsymbol{g} \rangle^{1/2}. \tag{3.2}$$

[1] Here a Dirac type notation is introduced. It should not be confused with the ensemble average notation, which does not have a balk in-between.

Let Ψ be a subspace of the Hilbert space $L_2(D)$ with the conditions that every element $\boldsymbol{\psi} \in \Psi$ must satisfy being smoothness, limit behavior at the boundary D, etc. Let us now consider the linear operator $\boldsymbol{A}$, defined on the linear manifold Ψ, and suppose that $\boldsymbol{A}$ is a positive definite, i.e. $\langle \boldsymbol{A}\boldsymbol{\psi}|\boldsymbol{\psi}\rangle \geq 0$ [1] for all $\boldsymbol{\psi} \in \boldsymbol{\Psi}$. The kind of inverse problem we are interested in belongs to the stationary problems of the form

$$\boldsymbol{A}\boldsymbol{\psi} = \boldsymbol{f}, \tag{3.3}$$

since, for example, for the COBE-filter we have to invert $\boldsymbol{A}\langle \boldsymbol{s}\rangle_{\rm COBE} = \boldsymbol{R}^\dagger \boldsymbol{N}^{-1}\boldsymbol{d}$, with $\boldsymbol{\psi} = \langle \boldsymbol{s}\rangle_{\rm COBE}$, $\boldsymbol{A} = \boldsymbol{R}^\dagger \boldsymbol{N}^{-1}\boldsymbol{R}$ and $\boldsymbol{f} = \boldsymbol{R}^\dagger \boldsymbol{N}^{-1}\boldsymbol{d}$, and for the Wiener-filtering we have $\boldsymbol{\psi} = (\boldsymbol{S}\boldsymbol{R}^\dagger)^{-1}\langle \boldsymbol{s}\rangle_{\rm WF}$, $\boldsymbol{A} = (\boldsymbol{R}^\dagger \boldsymbol{S}\boldsymbol{R} + \boldsymbol{N})$ and $\boldsymbol{f} = \boldsymbol{d}$. Eq. (3.3) has the same structure as eq. (2.2), but without a noise term. Hence, a regularization method is again required.

3.1.1 Minimization of the quadratic form

Another way of approaching the linear inverse problem is the minimization of a quadratic form given by

$$Q_{\boldsymbol{A}}(\boldsymbol{\psi}) = \frac{1}{2}\langle \boldsymbol{A}\boldsymbol{\psi}|\boldsymbol{\psi}\rangle - \langle \boldsymbol{f}|\boldsymbol{\psi}\rangle + c. \tag{3.4}$$

The gradient of $Q_{\boldsymbol{A}}$ leads to

$$\frac{{\rm d}Q_{\boldsymbol{A}}}{{\rm d}\boldsymbol{\psi}}(\boldsymbol{\psi}) \equiv Q'_{\boldsymbol{A}}(\boldsymbol{\psi}) = \boldsymbol{A}\boldsymbol{\psi} - \boldsymbol{f}, \tag{3.5}$$

assuming that the operator $\boldsymbol{A}$ is self-adjoint. Setting the gradient to zero, one obtains eq. (3.3). The surface defined by a quadratic form with a positive definite matrix $\boldsymbol{A}$ is shaped like a paraboloid bowl (see e.g. Shewchuk, 1994). This ensures the existence of a unique minimum or, equivalently, the convergence of appropriate algorithms.

3.1.2 Solution of the non-stationary problem: asymptotic regularization

Here, a unified framework for the regularization methods that we have implemented in ARGO is given based on the asymptotic regularization. Nevertheless, an original Bayesian motivation to the asymptotic solution is presented in appendix B.2.

The stationary problem (eq. 3.3) can be replaced by a non-stationary equation, which relaxes to the equilibrium solution

$$\frac{\partial \boldsymbol{\psi}}{\partial t} + \boldsymbol{A}\boldsymbol{\psi} = \boldsymbol{f}. \tag{3.6}$$

We seek solutions of the form

$$\boldsymbol{\psi} = \sum_l \psi_l \boldsymbol{u}_l, \tag{3.7}$$

with a spectrum for the operator $\boldsymbol{A}$

$$\boldsymbol{A}\boldsymbol{u}_l = \lambda_l \boldsymbol{u}_l. \tag{3.8}$$

[1] This expression can be written in matrix notation as $\boldsymbol{\psi}^\dagger \boldsymbol{A}\boldsymbol{\psi} \geq 0$, where $\boldsymbol{\psi}^\dagger$ is the conjugate and transpose of the vector $\boldsymbol{\psi}$.

Expanding $\boldsymbol{f}$ in this basis, yields

$$\boldsymbol{f} = \sum_l f_l \boldsymbol{u}_l. \tag{3.9}$$

Then we get the following relations for the Fourier coefficients in the stationary case

$$\lambda_l \psi_l = f_l, \tag{3.10}$$

and for the non-stationary case

$$\frac{\partial \psi_l(t)}{\partial t} + \lambda_l \psi_l(t) = f_l, \ \psi_l(0) = 0, \tag{3.11}$$

which lead to the following solutions

$$\boldsymbol{\psi} = \sum_l \frac{f_l}{\lambda_l} \boldsymbol{u}_l, \tag{3.12}$$

and

$$\boldsymbol{\psi}(t) = \sum_l \frac{f_l}{\lambda_l} (1 - e^{-\lambda_l t}) \boldsymbol{u}_l, \tag{3.13}$$

for the stationary and non-stationary cases, respectively. Since the spectrum of a positive definite operator $\boldsymbol{A}$ is real, $\lambda_l > 0$, it follows that $\lim_{t\to\infty} \boldsymbol{\psi}|_{\mathrm{non-stationary}} = \boldsymbol{\psi}|_{\mathrm{stationary}}$.

The non-stationary problem can be solved using difference methods with respect to t

$$\boldsymbol{\psi}^{j+1} = \boldsymbol{\psi}^j + \tau^j \boldsymbol{M}^j (\boldsymbol{f} - \boldsymbol{A}\boldsymbol{\psi}^j), \tag{3.14}$$

with $\{\boldsymbol{M}^j\}$ being a set of non-singular matrices [1] and $\{\tau_j\}$ being a sequence of real parameters. Here we concentrate on a constant, self-adjoint matrix $\boldsymbol{M}$. Let us rewrite eq. (3.14) as

$$\boldsymbol{\psi}^{j+1} = \boldsymbol{\psi}^j + \tau^j \boldsymbol{M} \boldsymbol{\xi}^j, \tag{3.15}$$

with the residuals given by

$$\boldsymbol{\xi}^j = \boldsymbol{f} - \boldsymbol{A}\boldsymbol{\psi}^j. \tag{3.16}$$

The error vectors are defined as

$$\boldsymbol{\eta}^j = \boldsymbol{\psi}^j - \boldsymbol{\psi}^*, \tag{3.17}$$

where $\boldsymbol{\psi}^* = \boldsymbol{A}^{-1}\boldsymbol{f}$ is the exact solution. The matrix $\boldsymbol{M}$ and the real number $\{\tau_j\}$ are chosen to speed up the convergence. $\boldsymbol{M}$ usually represents the preconditioning of eq. (3.14) and τ_j can be interpreted as the time step (see appendix B.3), and is also called relaxation parameter. Here truncation regularization occurs by quitting the iteration loop. Some stopping rules are therefore required. In the case where no noise regularization was conducted in the first step, they crucially define the noise regularization. In the other cases, they mostly determine algorithmic performance and accuracy. At this point we are interested in the regularization for the inverse purpose, since we have already found expressions which regularize the noise

[1] We implicitly generalized eq. (3.6) to $\partial\boldsymbol{\psi}(t)/\partial t = \boldsymbol{M}(t)(\boldsymbol{f} - \boldsymbol{A}\boldsymbol{\psi})$, where the auxiliary matrix $\boldsymbol{M}$ is chosen to speed up convergence.

(e.g. Wiener-filter, or MEM). However, the results presented in section 4 show that in some cases truncation leads to better results (see discussion in section 4.2.6). In the following sections, we will show how different iterative schemes are based on the general formula given by eq. (3.14). It is worth mentioning that other methods that we do not discuss in this thesis, like the algebraic reconstrcution technique (ART, see Gordon, 1974), can also be expressed through this formula.

3.1.3 Jacobi method

The Jacobi iteration method splits the operator $\boldsymbol{A}$ in two matrices

$$\boldsymbol{A} = \boldsymbol{D} + \boldsymbol{B}, \tag{3.18}$$

where $\boldsymbol{D}$ contains the diagonal elements of $\boldsymbol{A}$ and $\boldsymbol{B}$ contains the off-diagonal elements. From eq. (3.3) one follows

$$\boldsymbol{\psi} = \boldsymbol{D}^{-1}(\boldsymbol{f} - \boldsymbol{B}\boldsymbol{\psi}). \tag{3.19}$$

Substituting $\boldsymbol{B}$ by $\boldsymbol{A} - \boldsymbol{D}$ one gets the following iteration scheme

$$\boldsymbol{\psi}^{j+1} = \boldsymbol{\psi}^{j} + \boldsymbol{D}^{-1}(\boldsymbol{f} - \boldsymbol{A}\boldsymbol{\psi}^{j}). \tag{3.20}$$

The Jacobi method turns out to be a particular case of the iteration scheme given by eq. (3.14) with a preconditioning matrix given by $\boldsymbol{M} = \boldsymbol{D}^{-1}$ and $\tau^j = 1$. This method can, must be optimized by increasing the timestep τ^j by a certain percentage if the solution converges and decreasing the timestep if the solution diverges. An optimal timestep is hard to find, because the spectrum of the operator $\boldsymbol{A}$ has to be known (see appendix B.3).

3.1.4 Steepest Descent method

The steepest descent method searches the minimum of the quadratic form by choosing the direction in which $Q_{\boldsymbol{A}}$ decreases most rapidly. This direction is given by the residual

$$-Q'_{\boldsymbol{A}}(\boldsymbol{\psi}^j) = \boldsymbol{f} - \boldsymbol{A}\boldsymbol{\psi}^j = \boldsymbol{\xi}^j. \tag{3.21}$$

The form of the iteration scheme is thus given by eq. (3.15), with the length of the step in the direction of the residual given by τ^j. Steepest descent looks for the optimal length which minimizes the quadratic form with respect to τ^j

$$0 = \frac{\mathrm{d}Q_{\boldsymbol{A}}}{\mathrm{d}\tau^j}(\boldsymbol{\psi}^{j+1}) = \langle Q'_{\boldsymbol{A}}(\boldsymbol{\psi}^{j+1}) | \frac{\mathrm{d}\boldsymbol{\psi}^{j+1}}{\mathrm{d}\tau^j} \rangle = \langle \boldsymbol{\xi}^{j+1} | \boldsymbol{M}\boldsymbol{\xi}^{j} \rangle. \tag{3.22}$$

This implies that subsequent searching directions must be orthogonal (say $\boldsymbol{M} = \boldsymbol{I}$). Starting from this condition it is straightforward to derive the expression for τ^j. It is only necessary to use the definition of residual for $\boldsymbol{\xi}^{j+1}$ and substitute $\boldsymbol{\psi}^{j+1}$ from eq. (3.15).

$$\tau^j = \frac{\langle \boldsymbol{\xi}^j | \boldsymbol{M}\boldsymbol{\xi}^j \rangle}{\langle \boldsymbol{A}\boldsymbol{M}\boldsymbol{\xi}^j | \boldsymbol{M}\boldsymbol{\xi}^j \rangle}. \tag{3.23}$$

$\mathbf{D}_m$ \ $\mathbf{N}_l$	$\langle \boldsymbol{\xi}^{j+1} \vert \boldsymbol{M}\boldsymbol{\xi}^{j+1}\rangle$	$\langle \boldsymbol{\xi}^{j+1} \vert \boldsymbol{M}\Delta\boldsymbol{\xi}\rangle$	$\langle \Delta\boldsymbol{\xi} \vert \boldsymbol{M}\Delta\boldsymbol{\xi}\rangle$ $-\langle \boldsymbol{\xi}^{j} \vert \boldsymbol{M}\boldsymbol{\xi}^{j}\rangle$	$-\langle \boldsymbol{M}\boldsymbol{\xi}^{j+1} \vert \boldsymbol{M}\boldsymbol{\mu}^{j}\rangle_{\boldsymbol{A}}$
$\langle \boldsymbol{\xi}^{j} \vert \boldsymbol{M}\boldsymbol{\xi}^{j}\rangle$	**FR**	**PR**	N3/D1	—
$\langle \boldsymbol{\mu}^{j} \vert \boldsymbol{M}\boldsymbol{\xi}^{j}\rangle$	N1/D2	N2/D2	N3/D2	—
$-\langle \boldsymbol{\xi}^{j} \vert \boldsymbol{M}\Delta\boldsymbol{\xi}\rangle$	N1/D3	N2/D3	N3/D3	—
$-\langle \boldsymbol{\mu}^{j} \vert \boldsymbol{M}\Delta\boldsymbol{\xi}\rangle$	N1/D4	**HS**	N3/D4	—
$-(\langle \Delta\boldsymbol{\xi} \vert \boldsymbol{M}\Delta\boldsymbol{\xi}\rangle$ $-\langle \boldsymbol{\xi}^{j+1} \vert \boldsymbol{M}\boldsymbol{\xi}^{j+1}\rangle)$	N1/D5	N2/D5	N3/D5	—
$\langle \boldsymbol{M}\boldsymbol{\mu}^{j} \vert \boldsymbol{M}\boldsymbol{\mu}^{j}\rangle_{\boldsymbol{A}}$	—	—	—	**EXP**

Table 3.1: Formulae for the β-factor: $\beta_{lm}^{j+1} = \frac{\mathbf{N}_l}{\mathbf{D}_m}$, where we have used the following definition: $\Delta\boldsymbol{\xi} \equiv \boldsymbol{\xi}^{j+1} - \boldsymbol{\xi}^{j}$. Three of the methods are discussed in the literature: **FR** (Fletcher-Reeves), **PR** (Polak-Ribière, and **HS** (Hestenes-Stiefels). The rest of the formulae are derived in this thesis using equivalence relations derived in appendices B.1.1-B.1.3. The **FR** and the **PR** methods are tested against the **EXP** algorithm in section (4).

Both the calculation of the factors τ^j and the residuals $\boldsymbol{\xi}^j$ imply applying the operator $\boldsymbol{A}$, each time on different vectors. It is possible, however, to reduce the operation of $\boldsymbol{A}$ to the same vector for every iteration, but the residuals, must be calculated in a different way. Multiplying both sides of eq. (3.15) by $-\boldsymbol{A}$ and adding $\boldsymbol{f}$, one obtains the following relation for the residuals

$$\boldsymbol{\xi}^{j+1} = \boldsymbol{\xi}^{j} - \tau^{j}\boldsymbol{A}\boldsymbol{M}\boldsymbol{\xi}^{j}. \tag{3.24}$$

Notice that the vector $\boldsymbol{A}\boldsymbol{M}\boldsymbol{\xi}^j$ already appears in the expression for τ^j, and consequently saves one operation. However, expression (3.16) has to be periodically used with the feedback of $\boldsymbol{\psi}^j$, to avoid the accumulation of floating-point roundoff error. The disadvantage of this method is that it ends up searching repeatedly in the same direction. This is especially severe when the quadratic form is highly deformed, which occurs when the matrix $\boldsymbol{A}$ deviates from the unity matrix. We will see, however, that steepest descent competes with any other method when the preconditioning is effective, and thus the stretched shape of the quadratic form is brought close to a spherical symmetric shape. Preconditioning should not imply too many operations; that is the reason why the inverse of the matrix, which contains only the diagonal elements of $\boldsymbol{A}$, is usually taken for preconditioning. This will work especially fine when the operator $\boldsymbol{A}$ is diagonally dominant, which in our case occurs when nearly full-sky data are available.

3.1.5 Krylov methods: Conjugate Gradients

To make the iteration scheme more efficient, Conjugate Gradients proposes to search each time in a different direction. This is achieved by imposing $\boldsymbol{A}$-orthogonality to two different ($i \neq j$) searching vectors $\boldsymbol{\mu}^i$ and $\boldsymbol{\mu}^j$

$$\langle \boldsymbol{\mu}^{j} \vert \boldsymbol{\mu}^{i}\rangle_{\boldsymbol{A}} \equiv \langle \boldsymbol{A}\boldsymbol{\mu}^{j} \vert \boldsymbol{\mu}^{i}\rangle = 0, \tag{3.25}$$

which are then said to be conjugated. In the preconditioned case, the searching vectors are multiplied by $\boldsymbol{M}$ so that the conjugacy has to be formulated in the following way:
$\langle \boldsymbol{M}\boldsymbol{\mu}^{j} \vert \boldsymbol{M}\boldsymbol{\mu}^{i}\rangle_{\boldsymbol{A}} = 0$ (for $i \neq j$).

The iteration scheme is given by substituting the residuals in eq. (3.15) by the new searching vectors $\{\boldsymbol{\mu}^j\}$

$$\boldsymbol{\psi}^{j+1} = \boldsymbol{\psi}^j + \tau^j \boldsymbol{M}\boldsymbol{\mu}^j. \tag{3.26}$$

By subtracting $\boldsymbol{\psi}^*$ we obtain an equation for the errors,

$$\boldsymbol{\eta}^{j+1} = \boldsymbol{\eta}^j + \tau^j \boldsymbol{M}\boldsymbol{\mu}^j. \tag{3.27}$$

Taking into account the relation between the residuals and the errors

$$\boldsymbol{\xi}^{j+1} = -\boldsymbol{A}\boldsymbol{\eta}^{j+1}, \tag{3.28}$$

we can derive the recurrent formula for the residuals

$$\boldsymbol{\xi}^{j+1} = -\boldsymbol{A}(\boldsymbol{\eta}^j + \tau^j \boldsymbol{M}\boldsymbol{\mu}^j) = \boldsymbol{\xi}^j - \tau^j \boldsymbol{A}\boldsymbol{M}\boldsymbol{\mu}^j. \tag{3.29}$$

Here again, expression (3.16) has to be used periodically with the feedback of $\boldsymbol{\psi}^j$ to avoid the accumulation of floating-point roundoff error. The optimal length of the step is found by minimizing the quadratic form

$$0 = \frac{\mathrm{d}Q_{\boldsymbol{A}}}{\mathrm{d}\tau^j}(\boldsymbol{\psi}^{j+1}) = -\langle \boldsymbol{\xi}^{j+1} | \boldsymbol{M}\boldsymbol{\mu}^j \rangle = \langle \boldsymbol{\eta}^{j+1} | \boldsymbol{M}\boldsymbol{\mu}^j \rangle_{\boldsymbol{A}}. \tag{3.30}$$

Substituting expression (3.27) in (3.30) we then obtain

$$\tau^j = -\frac{\langle \boldsymbol{\eta}^j | \boldsymbol{M}\boldsymbol{\mu}^j \rangle_{\boldsymbol{A}}}{\langle \boldsymbol{M}\boldsymbol{\mu}^j | \boldsymbol{M}\boldsymbol{\mu}^j \rangle_{\boldsymbol{A}}} = \frac{\langle \boldsymbol{\xi}^j | \boldsymbol{M}\boldsymbol{\mu}^j \rangle}{\langle \boldsymbol{M}\boldsymbol{\mu}^j | \boldsymbol{M}\boldsymbol{\mu}^j \rangle_{\boldsymbol{A}}}. \tag{3.31}$$

It can be shown that this formula is equivalent to the following expression

$$\tau^j = \frac{\langle \boldsymbol{\xi}^j | \boldsymbol{M}\boldsymbol{\xi}^j \rangle}{\langle \boldsymbol{M}\boldsymbol{\mu}^j | \boldsymbol{M}\boldsymbol{\mu}^j \rangle_{\boldsymbol{A}}}, \tag{3.32}$$

using $\langle \boldsymbol{\xi}^j | \boldsymbol{M}\boldsymbol{\mu}^j \rangle = \langle \boldsymbol{\xi}^j | \boldsymbol{M}\boldsymbol{\xi}^j \rangle$ (see appendix B.1).

To generate $\boldsymbol{A}$-orthogonal searching vectors one could think of Gram-Schmidt-conjugation

$$\boldsymbol{\mu}^j = \boldsymbol{\xi}^j + \sum_{k=0}^{j-1} \beta^{jk} \boldsymbol{\mu}^k. \tag{3.33}$$

Here it was assumed that the residuals $\{\boldsymbol{\xi}^j\}$ form a set of linearly independent vectors (see appendix B.1). The expression for the factors β^{jk} can be derived by calling $\boldsymbol{A}$-orthogonality in eq. (3.33)

$$\begin{aligned} \langle \boldsymbol{M}\boldsymbol{\mu}^j | \boldsymbol{M}\boldsymbol{\mu}^i \rangle_{\boldsymbol{A}} &= \langle \boldsymbol{M}\boldsymbol{\xi}^j | \boldsymbol{M}\boldsymbol{\mu}^i \rangle_{\boldsymbol{A}} + \sum_{k=0}^{j-1} \beta^{jk} \langle \boldsymbol{M}\boldsymbol{\mu}^k | \boldsymbol{M}\boldsymbol{\mu}^i \rangle_{\boldsymbol{A}} \\ 0 &= \langle \boldsymbol{M}\boldsymbol{\xi}^j | \boldsymbol{M}\boldsymbol{\mu}^i \rangle_{\boldsymbol{A}} + \beta^{ji} \langle \boldsymbol{M}\boldsymbol{\mu}^i | \boldsymbol{M}\boldsymbol{\mu}^i \rangle_{\boldsymbol{A}}. \end{aligned} \tag{3.34}$$

One obtains the following formula for the factors

$$\beta^{ji} = -\frac{\langle \boldsymbol{M}\boldsymbol{\xi}^j | \boldsymbol{M}\boldsymbol{\mu}^i \rangle_{\boldsymbol{A}}}{\langle \boldsymbol{M}\boldsymbol{\mu}^i | \boldsymbol{M}\boldsymbol{\mu}^i \rangle_{\boldsymbol{A}}}, \tag{3.35}$$

where $i < j$ according to eq. (3.33)[1].

This method seems to require too much memory, as apparently all previous searching vectors must be stored to calculate the new one. However, only one β-factor remains in the sum in eq. (3.33), as we show in appendix B.1.3. Hence, Gram-Schmidt orthogonalization can be simplified to the following expression

$$\boldsymbol{\mu}^{j+1} = \boldsymbol{\xi}^{j+1} + \beta^{j+1}\boldsymbol{\mu}^j, \tag{3.36}$$

where

$$\beta^{j+1}_{\mathrm{EXP}} \equiv \beta^{j+1} \equiv \beta^{j+1\,j} = -\frac{\langle \boldsymbol{M}\boldsymbol{\xi}^{j+1} | \boldsymbol{M}\boldsymbol{\mu}^j \rangle_{\boldsymbol{A}}}{\langle \boldsymbol{M}\boldsymbol{\mu}^j | \boldsymbol{M}\boldsymbol{\mu}^j \rangle_{\boldsymbol{A}}}, \tag{3.37}$$

with EXP meaning expensive, since the nominator of β apparently requires an extra $\boldsymbol{A}$ operation. This additional operation can be saved by taking the vector $\boldsymbol{A}\boldsymbol{M}\boldsymbol{\mu}^j$ from τ^j or with alternative methods (see appendix B.1), like the Fletcher-Reeves method (Fletcher & Reeves, 1964)

$$\beta^{j+1}_{\mathrm{FR}} = \frac{\langle \boldsymbol{\xi}^{j+1} | \boldsymbol{M}\boldsymbol{\xi}^{j+1} \rangle}{\langle \boldsymbol{\xi}^j | \boldsymbol{M}\boldsymbol{\xi}^j \rangle}, \tag{3.38}$$

the Polak-Ribière formula (Polak & Ribière 1969)

$$\beta^{j+1}_{\mathrm{PR}} = \frac{\langle \boldsymbol{\xi}^{j+1} | \boldsymbol{M}(\boldsymbol{\xi}^{j+1} - \boldsymbol{\xi}^j) \rangle}{\langle \boldsymbol{\xi}^j | \boldsymbol{M}\boldsymbol{\xi}^j \rangle}, \tag{3.39}$$

or the Hestenes-Stiefel expression (Hestenes & Stiefel, 1952)

$$\beta^{j+1}_{\mathrm{HS}} = -\frac{\langle \boldsymbol{\xi}^{j+1} | \boldsymbol{M}(\boldsymbol{\xi}^{j+1} - \boldsymbol{\xi}^j) \rangle}{\langle \boldsymbol{\mu}^j | \boldsymbol{M}(\boldsymbol{\xi}^{j+1} - \boldsymbol{\xi}^j) \rangle}. \tag{3.40}$$

However, β_{EXP} turns out to be a very efficient scheme, which behaves far more stably than the rest (see section 4). Since the β-formulae (eq. 3.37-3.40) are mathematically equivalent, one could think of combining them in a single scheme finding numerically different solutions. However, this kind of hybrid scheme remains to be thouroughly studied.

Formula (3.36) shows that new searching vectors are built from a linear combination of the current residual and the previous searching vector. Since the subsequent residuals are given by the linear combination of the previous residual and the $\boldsymbol{A}$-operator applied to the searching vector, the manifold where the solution is being searched is spanned by the residuals and the so-called Krylov space. The latter is built by applying the $\boldsymbol{A}$ operator to the basis vector successively. In this manifold, curved quadratic forms appear to be spherical and thus the

[1]Note that the sign of β depends on the definition of the Gram-Schmidt conjugation. An alternative definition with the negation of the residuals would cancel the minus sign in eq. (3.35). The sign of β can be regarded as a free parameter.

searching process becomes more effective. It is possible to derive the Conjugate Gradients method by minimizing the $\boldsymbol{A}$-norm of the error: $\min||\boldsymbol{\eta}||_{\boldsymbol{A}}$ (see e.g. Marchuk, 1982). In this sense an optimal solution to the inverse problem can be found even if no unique solution exists. Conjugate Gradients works, even if the operator $\boldsymbol{A}$ is not a positive definite (for a discussion see e.g. Shewchuk, 1994). It can easily be shown that Conjugate Gradients converges at most in n-steps, with n being the number of pixels/vector columns (see e.g. Shewchuk, 1994).

3.2 Non-linear inverse methods

Non-linear inverse methods are especially required in reconstruction algorithms that do not assume a Gaussian distribution. The iterative method given in eq. (2.26), which makes use of a Poissonian likelihood, can alternatively be solved with the methods presented in this section. The same applies to the MEM, where zeros of the non-linear eq. (2.43) have to be found.

The generalization of the regularization methods to non-linear inverse problems is possible with methods like Tikhonov regularization as mentioned in section (2.5) or like asymptotic regularization as will be shown below (a relation between both methods is shown in appendix B.2). However, the proofs of the convergence properties are different since the spectral theoretical foundation is missing here. We refer the reader to e.g. O'Sullivan (1990).

Let us generalize eq. (3.3) to non-linear equations of the form

$$\boldsymbol{A}(\boldsymbol{\psi}) = \boldsymbol{f}, \tag{3.41}$$

with $\boldsymbol{A}$ being a non-linear operator, and solve the non-linear and non-stationary equation given by

$$\frac{\partial \boldsymbol{\psi}}{\partial t} + \boldsymbol{A}(\boldsymbol{\psi}) = \boldsymbol{f}, \tag{3.42}$$

with the forward Euler method. Discretizing the solution yields

$$\boldsymbol{\psi}^{j+1} = \boldsymbol{\psi}^{j} + \tau^{j}\boldsymbol{T}(\boldsymbol{\psi}^{j})(\boldsymbol{f} - \boldsymbol{A}(\boldsymbol{\psi}^{j})), \tag{3.43}$$

with $\boldsymbol{T}$ being also a non-linear operator, typically given by $\nabla \boldsymbol{A}^{\dagger}$ or $\nabla \boldsymbol{A}^{-1}$, though more complicated expressions exist (see the Levenberg-Marquardt method or the regularized Gauss-Newton method, Hanke 1997 or Bakushinskii 1992 and Blaschke *et al.* 1997, respectively).

3.2.1 Newton-Raphson method

One of the most extended non-linear inverse methods is the so-called Newton-Raphson method (for an application in MEMs see Hobson *et al.*, 1998; Maisinger *et al.*, 1997), which can easily be derived by doing a Taylor expansion of the function under study and truncating it at the first order

$$\boldsymbol{\psi}^{j+1} = \boldsymbol{\psi}^{j} + (\nabla \boldsymbol{A}(\boldsymbol{\psi}^{j}))^{-1}(\boldsymbol{f} - \boldsymbol{A}(\boldsymbol{\psi}^{j})). \tag{3.44}$$

This method requires the inverse of the gradient of $\boldsymbol{A}$, which for the cases we are interested in is the inverse of a Hessian matrix. Recalling the problem of finding extrema of a function

as presented in section (3.1.1) and taking into account eq. (3.21), the previous equation can be rewritten as

$$\boldsymbol{\psi}^{j+1} = \boldsymbol{\psi}^{j} - (\nabla\nabla Q_{\boldsymbol{A}}(\boldsymbol{\psi}^{j}))^{-1}\nabla Q_{\boldsymbol{A}}(\boldsymbol{\psi}^{j}), \tag{3.45}$$

where $\nabla\nabla Q_{\boldsymbol{A}} \equiv \partial Q_{\boldsymbol{A}}/\partial\boldsymbol{\psi}^{l}\partial\boldsymbol{\psi}^{m}$ is the Hessian matrix of $Q_{\boldsymbol{A}}$. For a direct derivation of this equation, we require a Taylor expansion until the second order of $Q_{\boldsymbol{A}}$, which is where the non-linearity arises. The MEM can be solved (eq. 2.43) with expression (3.45) by doing the substitutions: $Q_{\boldsymbol{A}} \rightarrow Q^{\mathrm{E}}$ and $\boldsymbol{\psi}^{j} \rightarrow \boldsymbol{s}^{j}$. Here the quantity Q^{E} is implicitly approximated by its quadratic expansion $Q_{\boldsymbol{A}}$. Calculating the inverse of the Hessian $(\nabla\nabla Q_{\boldsymbol{A}}(\boldsymbol{\psi}^{j}))^{-1}$ implies solving a linear ill-posed problem in each iteration of the scheme (3.45). Some solutions have been found to regularize this scheme, like the Levenberg-Marquardt method (see Hanke, 1997) or the regularized Gauss-Newton method (see e.g. Bakushinskii, 1992; Blaschke *et al.*, 1997).

3.2.2 Landweber-Fridman method

Alternative algorithms to the above mentioned Newton-Raphson class of methods do not need to invert the Hessian matrix and can thus simultaneously speed up and stabilize the inversion process. The Landweber-Fridman algorithm belongs to the class of methods based on steepest descent

$$\boldsymbol{\psi}^{j+1} = \boldsymbol{\psi}^{j} + (\nabla\boldsymbol{A}(\boldsymbol{\psi}^{j}))^{\dagger}(\boldsymbol{f} - \boldsymbol{A}(\boldsymbol{\psi}^{j})). \tag{3.46}$$

Making the same substitutions as for eq. (3.45), we obtain

$$\boldsymbol{\psi}^{j+1} = \boldsymbol{\psi}^{j} - (\nabla\nabla Q_{\boldsymbol{A}}(\boldsymbol{\psi}^{j}))^{\dagger}\boldsymbol{\nabla} Q_{\boldsymbol{A}}(\boldsymbol{\psi}^{j}). \tag{3.47}$$

Here just the adjoint of the Hessian must be taken $(\nabla\nabla Q_{\boldsymbol{A}}(\boldsymbol{\psi}^{j}))^{\dagger}$. For a convergence analysis of this method see Hanke *et al.* (1995).

3.2.3 Non-linear Krylov methods

Another class of methods that do not require one to invert the Hessian matrix are the Krylov-based methods, which we have exposed in the previous section. The difference with respect to the linear case mainly resides in the calculation of the residuals $\boldsymbol{\xi}^{j}$ and the step size τ^{j}. The residuals are updated now by the negation of the gradient of the quadratic form that approximates the function under consideration $\boldsymbol{\xi}^{j} = -\nabla Q_{\boldsymbol{A}}(\boldsymbol{\psi}^{j})$ (see eq. 3.21). The step size is given by

$$\tau^{j} = -\frac{\langle \nabla Q_{\boldsymbol{A}}(\boldsymbol{\psi}^{j}) | \boldsymbol{M}\boldsymbol{\mu}^{j}\rangle}{\langle \boldsymbol{M}\boldsymbol{\mu}^{j} | \boldsymbol{M}\boldsymbol{\mu}^{j}\rangle_{\nabla\nabla Q_{\boldsymbol{A}}(\boldsymbol{\psi}^{j})}}. \tag{3.48}$$

The derivation of this expression (see appendix B.1.4) is based on the second order Taylor expansion of $Q_{\boldsymbol{A}}$. That is why Krylov algorithms which use this formula are called Newton-Krylov methods. There are alternative expressions for the time step τ^{j} where the Hessian is approximated and does not need to be explicitly calculated, like those using a secant approximation. For various implementations of non-linear Krylov methods see, for example, Shewchuk (1994).

	$\boldsymbol{R}$	$\boldsymbol{R}^\dagger$	$\boldsymbol{S}$	$\boldsymbol{S}^{-1}$	$\boldsymbol{S}^{-1/2}$	$\boldsymbol{N}$	$\boldsymbol{N}^{-1}$	$\boldsymbol{S}\boldsymbol{R}^\dagger$	$\boldsymbol{R}^\dagger\boldsymbol{N}^{-1}$	$\boldsymbol{R}^\dagger\boldsymbol{N}^{-1/2}$	$\boldsymbol{R}^\dagger\boldsymbol{N}^{-1}\boldsymbol{R}$	$\boldsymbol{R}\boldsymbol{S}\boldsymbol{R}^\dagger$
C							X		X		X	
W	X	X	X	X$^\#$	X$^\#$	X	X$^\#$	X		X$^\#$	X$^\#$	X
GM	X	X	X					X				
MG	X	X					X		X		X	
MP	X	X										

$^\#$ additional operators required for sampling processes (see eq. 5.22)

Table 3.2: Operators in columns needed for the different estimators in rows, the COBE-filter (2.27), the Wiener-filter (2.24), the GAPMAP estimator (2.26), and the MEMs (sections 2.5.9 & 3.2, and appendix A.10). Note that the trivial diagonal matrices have been left out of this table. The first two estimators are linear estimators, whereas the rest are non-linear. MEMG and MEMP stand for the Maximum Entropy method with a Gaussian likelihood and with a Poissonian likelihood, respectively. Note that some of the operators have to be further inverted either directly, like $(\boldsymbol{R}^\dagger\boldsymbol{N}\boldsymbol{R})^{-1}$ for the COBE-filter, or in combination with other operators, like $(\boldsymbol{R}\boldsymbol{S}\boldsymbol{R}^\dagger + \boldsymbol{N})^{-1}$ for the Wiener-filter. The methods presented in section (3) show how to do this implicitly by applying the operators in an iterative fashion.

3.3 Operator formalism

The iterative methods presented so far require an operator formalism to become efficient. In this formalism, matrices should be represented in such a way that their action can be expressed as simple operations, like sums and multiplications. In order to achieve this, one has to carefully choose the adequate representation, in which the individual matrix components are diagonal, though the whole matrix may not be. In this section, we present the different operators under consideration (see table 3.2) in k-space and real-space and discuss their optimal representation. In this way, we can take advantage of the fast Fourier-transform methods (FFTs) that scale as $n \log_2 n$, with n being the length of the arrays, and which ultimately determine the speed of the algorithm.

3.3.1 Fourier-transform definitions and dimensionality of the problem

Let us introduce the following definitions of the $N_{\rm D}$-dimensional forward and inverse Fourier-transforms

$$\hat{x}(\boldsymbol{k}) \equiv \mathrm{FT}\big[x(\boldsymbol{r})\big] \equiv \int \mathrm{d}^{N_{\rm D}}\boldsymbol{r}\, \exp(i\boldsymbol{k}\cdot\boldsymbol{r})x(\boldsymbol{r}), \tag{3.49}$$

and

$$x(\boldsymbol{r}) \equiv \mathrm{IFT}\big[\hat{x}(\boldsymbol{k})\big] \equiv \int \frac{\mathrm{d}^{N_{\rm D}}\boldsymbol{k}}{(2\pi)^{N_{\rm D}}} \exp(-i\boldsymbol{k}\cdot\boldsymbol{r})\hat{x}(\boldsymbol{k}), \tag{3.50}$$

respectively.

In general, the reconstruction problem has three spatial dimensions ($N_{\rm D} = 3$), with the corresponding discrete array lengths for the real-space and k-space vectors given by $\boldsymbol{r} = (r_x, r_y, r_z)$ and $\boldsymbol{k} = (k_x, k_y, k_z)$. Each component has the following range: $r_x = \frac{L_x}{n_x}[0, n_x - 1], r_y = \frac{L_y}{n_y}[0, n_y - 1], r_z = \frac{L_z}{n_z}[0, n_z - 1]$ and $k_x = \frac{2\pi}{L_x}[0, n_x - 1], k_y = \frac{2\pi}{L_y}[0, n_y - 1], k_z = \frac{2\pi}{L_z}[0, n_z - 1]$, where the volume of the Universe under consideration is given by $V = L_x \times L_y \times L_z$ in [(Mpc/h)^3], and the box containing that volume is divided into $n = n_x \times n_y \times n_z$

cells, with n being the length of the array x. In the following, we will treat the operators as being continuous. However, the discrete implementation can be derived in a straightforward way (for a discussion on the relation between discrete and continuous representations see Martel, 2005). Note that the methods presented here can be applied in arbitrary dimensions. The number of dimensions $N_{\rm D}$ is thus kept as a free parameter.

In our convention, vectors defined in real-space have plain notation (x) and in k-space they are denoted with hats ($\hat{x}$). Matrices, however, have two hats in k-space. We represent convolutions with circles "$\circ$" and multiplications with dots "$\cdot$". Due to the convolution theorem, where convolutions are shown to be multiplications in the counter space, we can either omit hats if they are present or include them if they are not, and replace circles with dots and vice versa "$\cdot \leftrightarrow \circ$" to change from one representation to the other. All the numerical iterative inversion schemes (see section 3) of the different reconstruction algorithms (section 2) require only a small number of basic operators, listed in table (3.2). To show how the operators listed in table (3.2) can efficiently be applied we derive their action on an arbitrary vector.

3.3.2 Data model: the response operator

Let us first remember the data model given in eq. (2.3), and suppose that the operator $\boldsymbol{R}_{\rm P}$ is given by a convolution in real-space with some blurring function $f_{\rm B}$

$$d(\boldsymbol{r}) \equiv \int \mathrm{d}^{N_{\rm D}}\boldsymbol{r}'\, f_{\rm B}(\boldsymbol{r}-\boldsymbol{r}')f_{\rm S}(\boldsymbol{r}')f_{\rm M}(\boldsymbol{r}')s(\boldsymbol{r}') + f_{\rm SF}(\boldsymbol{r})\epsilon_{\rm N}(\boldsymbol{r}). \tag{3.54}$$

The operator $\boldsymbol{R}$ acting on an arbitrary vector $\{x\}$ is thus given by

$$\boldsymbol{R}\{\boldsymbol{x}\}(\boldsymbol{r}) \equiv \int \mathrm{d}^{N_{\rm D}}\boldsymbol{r}'\, f_{\rm B}(\boldsymbol{r}-\boldsymbol{r}')f_{\rm S}(\boldsymbol{r}')f_{\rm M}(\boldsymbol{r}')\{x(\boldsymbol{r}')\}. \tag{3.55}$$

The selection function and the masks should conveniently be multiplied in real-space to save convolutions

$$f_{\rm SM}(\boldsymbol{r}) \equiv f_{\rm S}(\boldsymbol{r})f_{\rm M}(\boldsymbol{r}). \tag{3.56}$$

Accordingly, the same operation as in eq. (3.55) leads to

$$\hat{\boldsymbol{R}}\{\hat{\boldsymbol{x}}\}(\boldsymbol{k}) = \underbrace{\hat{f}_{\rm B}(\boldsymbol{k})\underbrace{\int \frac{\mathrm{d}^{N_{\rm D}}\boldsymbol{q}}{(2\pi)^{N_{\rm D}}}\hat{f}_{\rm SM}(\boldsymbol{k}-\boldsymbol{q})\{\hat{x}(\boldsymbol{q})\}}_{\hat{f}_{\rm SM}\circ\{\hat{x}\}}}_{\hat{f}_{\rm B}\cdot\left[\hat{f}_{\rm SM}\circ\{\hat{x}\}\right]}, \tag{3.57}$$

in k-space. Here we have introduced the operator notation in which the equations have to be read from right to left. The braces show the sequence in which the subsequent operations have to be performed in the algorithm. The analogous operation for the adjoint $\boldsymbol{R}^{\dagger}$ can be derived from the definition of the response operator in real space (see eq. 3.55) leading to

$$\boldsymbol{R}^{\dagger}\{\boldsymbol{x}\}(\boldsymbol{r}) = f_{\rm S}(\boldsymbol{r})f_{\rm M}(\boldsymbol{r})\int \mathrm{d}^{N_{\rm D}}\boldsymbol{r}'\, f_{\rm B}(\boldsymbol{r}'-\boldsymbol{r})\{x(\boldsymbol{r}')\}. \tag{3.58}$$

$$\begin{aligned}\boldsymbol{R}\hat{\hat{\boldsymbol{S}}}\boldsymbol{R}^\dagger\{\hat{\boldsymbol{x}}\}(\boldsymbol{k}) &= \int \frac{\mathrm{d}^{N_\mathrm{D}}\boldsymbol{k}'}{(2\pi)^{N_\mathrm{D}}}\langle\hat{\alpha}(\boldsymbol{k})\overline{\hat{\alpha}(\boldsymbol{k}')}\rangle_{(\boldsymbol{s},\boldsymbol{\epsilon}|\boldsymbol{p})}\{\hat{x}(\boldsymbol{k}')\} \\
&= \hat{f}_\mathrm{B}(\boldsymbol{k})\int\frac{\mathrm{d}^{N_\mathrm{D}}\boldsymbol{q}}{(2\pi)^{N_\mathrm{D}}}\hat{f}_\mathrm{SM}(\boldsymbol{k}-\boldsymbol{q})\int\frac{\mathrm{d}^{N_\mathrm{D}}\boldsymbol{q}'}{(2\pi)^{N_\mathrm{D}}}P_\mathrm{S}(\boldsymbol{q}')(2\pi)^{N_\mathrm{D}}\delta_\mathrm{D}(\boldsymbol{q}-\boldsymbol{q}')\int\frac{\mathrm{d}^{N_\mathrm{D}}\boldsymbol{k}'}{(2\pi)^{N_\mathrm{D}}}\overline{\hat{f}_\mathrm{SM}(\boldsymbol{k}'-\boldsymbol{q}')\hat{f}_\mathrm{B}(\boldsymbol{k}')}\{\hat{x}(\boldsymbol{k}')\} \\
&= \hat{f}_\mathrm{B}(\boldsymbol{k})\int\frac{\mathrm{d}^{N_\mathrm{D}}\boldsymbol{q}}{(2\pi)^{N_\mathrm{D}}}\hat{f}_\mathrm{SM}(\boldsymbol{k}-\boldsymbol{q})P_\mathrm{S}(\boldsymbol{q})\int\frac{\mathrm{d}^{N_\mathrm{D}}\boldsymbol{k}'}{(2\pi)^{N_\mathrm{D}}}\overline{\hat{f}_\mathrm{SM}(\boldsymbol{k}'-\boldsymbol{q})\hat{f}_\mathrm{B}(\boldsymbol{k}')}\cdot\{\hat{x}(\boldsymbol{k}')\} \\
&= \underbrace{\hat{f}_\mathrm{B}(\boldsymbol{k})\underbrace{\int\frac{\mathrm{d}^{N_\mathrm{D}}\boldsymbol{q}}{(2\pi)^{N_\mathrm{D}}}\hat{f}_\mathrm{SM}(\boldsymbol{k}-\boldsymbol{q})\,\underbrace{P_\mathrm{S}(\boldsymbol{q})\underbrace{\int\frac{\mathrm{d}^{N_\mathrm{D}}\boldsymbol{k}'}{(2\pi)^{N_\mathrm{D}}}\hat{f}_\mathrm{SM}(\boldsymbol{q}-\boldsymbol{k}')\,\underbrace{\overline{\hat{f}_\mathrm{B}(\boldsymbol{k}')}\cdot\{\hat{x}(\boldsymbol{k}')\}}_{\overline{\hat{f}_\mathrm{B}}\cdot\{\hat{x}\}}}_{\hat{f}_\mathrm{SM}\circ\left[\overline{\hat{f}_\mathrm{B}}\cdot\{\hat{x}\}\right]}}_{P_\mathrm{S}\cdot\left[\hat{f}_\mathrm{SM}\circ\left[\overline{\hat{f}_\mathrm{B}}\cdot\{\hat{x}\}\right]\right]}}_{\hat{f}_\mathrm{SM}\circ\left[P_\mathrm{S}\cdot\left[\hat{f}_\mathrm{SM}\circ\left[\overline{\hat{f}_\mathrm{B}}\cdot\{\hat{x}\}\right]\right]\right]}}_{\hat{f}_\mathrm{B}\cdot\left[\hat{f}_\mathrm{SM}\circ\left[P_\mathrm{S}\cdot\left[\hat{f}_\mathrm{SM}\circ\left[\overline{\hat{f}_\mathrm{B}}\cdot\{\hat{x}\}\right]\right]\right]\right]}\end{aligned} \tag{3.51}$$

$$\begin{aligned}&\boldsymbol{R}^\dagger\hat{\hat{\boldsymbol{N}}}_\mathrm{N}^{-1}\boldsymbol{R}\{\hat{\boldsymbol{x}}\}(\boldsymbol{k}) \\
&\quad= \left(\hat{f}_\mathrm{B}(\boldsymbol{k})\int\frac{\mathrm{d}^{N_\mathrm{D}}\boldsymbol{q}}{(2\pi)^{N_\mathrm{D}}}\hat{f}_\mathrm{SM}(\boldsymbol{k}-\boldsymbol{q})\right)^\dagger\int\frac{\mathrm{d}^{N_\mathrm{D}}\boldsymbol{q}'}{(2\pi)^{N_\mathrm{D}}}{P_\mathrm{N}}^{-1}(\boldsymbol{q}')(2\pi)^{N_\mathrm{D}}\delta_\mathrm{D}(\boldsymbol{q}-\boldsymbol{q}')\hat{f}_\mathrm{B}(\boldsymbol{q}')\int\frac{\mathrm{d}^{N_\mathrm{D}}\boldsymbol{k}'}{(2\pi)^{N_\mathrm{D}}}\hat{f}_\mathrm{SM}(\boldsymbol{q}'-\boldsymbol{k}')\{\hat{x}(\boldsymbol{k}')\} \\
&\quad= \int\frac{\mathrm{d}^{N_\mathrm{D}}\boldsymbol{q}}{(2\pi)^{N_\mathrm{D}}}\hat{f}_\mathrm{SM}(\boldsymbol{k}-\boldsymbol{q})\overline{\hat{f}_\mathrm{B}(\boldsymbol{q})}\int\frac{\mathrm{d}^{N_\mathrm{D}}\boldsymbol{q}'}{(2\pi)^{N_\mathrm{D}}}{P_\mathrm{N}}^{-1}(\boldsymbol{q}')(2\pi)^{N_\mathrm{D}}\delta_\mathrm{D}(\boldsymbol{q}-\boldsymbol{q}')\hat{f}_\mathrm{B}(\boldsymbol{q}')\int\frac{\mathrm{d}^{N_\mathrm{D}}\boldsymbol{k}'}{(2\pi)^{N_\mathrm{D}}}\hat{f}_\mathrm{SM}(\boldsymbol{q}'-\boldsymbol{k}')\{\hat{x}(\boldsymbol{k}')\} \\
&\quad= \underbrace{\int\frac{\mathrm{d}^{N_\mathrm{D}}\boldsymbol{q}}{(2\pi)^{N_\mathrm{D}}}\hat{f}_\mathrm{SM}(\boldsymbol{k}-\boldsymbol{q})\,\underbrace{\overline{\hat{f}_\mathrm{B}(\boldsymbol{q})}\,\underbrace{{P_\mathrm{N}}^{-1}(\boldsymbol{q})\,\underbrace{\hat{f}_\mathrm{B}(\boldsymbol{q})\underbrace{\int\frac{\mathrm{d}^{N_\mathrm{D}}\boldsymbol{k}'}{(2\pi)^{N_\mathrm{D}}}\hat{f}_\mathrm{SM}(\boldsymbol{q}-\boldsymbol{k}')\{\hat{x}(\boldsymbol{k}')\}}_{f_\mathrm{SM}\circ\{\hat{x}\}}}_{\hat{f}_\mathrm{B}\cdot\left[f_\mathrm{SM}\circ\{\hat{x}\}\right]}}_{{P_\mathrm{N}}^{-1}\cdot\left[\hat{f}_\mathrm{B}\cdot\left[f_\mathrm{SM}\circ\{\hat{x}\}\right]\right]}}_{\overline{\hat{f}_\mathrm{B}}\cdot\left[{P_\mathrm{N}}^{-1}\cdot\left[\hat{f}_\mathrm{B}\cdot\left[\hat{f}_\mathrm{SM}\circ\{\hat{x}\}\right]\right]\right]}}_{\hat{f}_\mathrm{SM}\circ\left[\overline{\hat{f}_\mathrm{B}}\cdot\left[{P_\mathrm{N}}^{-1}\cdot\left[\hat{f}_\mathrm{B}\cdot\left[\hat{f}_\mathrm{SM}\circ\{\hat{x}\}\right]\right]\right]\right]}\end{aligned} \tag{3.52}$$

$$\begin{aligned}&\boldsymbol{R}^\dagger\hat{\hat{\boldsymbol{N}}}_\mathrm{WN}^{-1}\boldsymbol{R}\{\hat{\boldsymbol{x}}\}(\boldsymbol{k}) \\
&\quad= \underbrace{\int\frac{\mathrm{d}^{N_\mathrm{D}}\boldsymbol{q}}{(2\pi)^{N_\mathrm{D}}}\hat{f}_\mathrm{SM}(\boldsymbol{k}-\boldsymbol{q})\,\underbrace{\overline{\hat{f}_\mathrm{B}(\boldsymbol{q})}\underbrace{\int\frac{\mathrm{d}^{N_\mathrm{D}}\boldsymbol{q}'}{(2\pi)^{N_\mathrm{D}}}{N_\mathrm{WN}}^{-1}(\boldsymbol{q}-\boldsymbol{q}')\,\underbrace{\hat{f}_\mathrm{B}(\boldsymbol{q}')\,\underbrace{\int\frac{\mathrm{d}^{N_\mathrm{D}}\boldsymbol{k}'}{(2\pi)^{N_\mathrm{D}}}\hat{f}_\mathrm{SM}(\boldsymbol{q}'-\boldsymbol{k}')\{\hat{x}(\boldsymbol{k}')\}}_{f_\mathrm{SM}\circ\{\hat{x}\}}}_{\hat{f}_\mathrm{B}\cdot\left[f_\mathrm{SM}\circ\{\hat{x}\}\right]}}_{{N_\mathrm{WN}}^{-1}\circ\left[\hat{f}_\mathrm{B}\cdot\left[f_\mathrm{SM}\circ\{\hat{x}\}\right]\right]}}_{\overline{\hat{f}_\mathrm{B}}\cdot\left[{N_\mathrm{WN}}^{-1}\circ\left[\hat{f}_\mathrm{B}\cdot\left[\hat{f}_\mathrm{SM}\circ\{\hat{x}\}\right]\right]\right]}}_{\hat{f}_\mathrm{SM}\circ\left[\overline{\hat{f}_\mathrm{B}}\cdot\left[{N_\mathrm{WN}}^{-1}\circ\left[\hat{f}_\mathrm{B}\cdot\left[\hat{f}_\mathrm{SM}\circ\{\hat{x}\}\right]\right]\right]\right]}\end{aligned} \tag{3.53}$$

Table 3.3: In the previous page the action on an arbitrary vector $\hat{\boldsymbol{x}}$ of the most complex operators that appear in table (3.2) is shown. The upper one is required for Wiener-filtering and represents the signal term in the covariance matrix of the data. The middle and lower ones stand for the inverse of the ML variance (eq. 2.28) and are required for the COBE-filter, the MEMG and for sampling purposes with the Wiener-filter. The equations have to be read from right to left. The braces show the order in which the operations have to be done from top to bottom. One has to be very careful with the correct conjugation of the different functions. Note that, contrary to naiv expectations, the conjugation of the first selection function $\hat{f}_{\rm SM}$ to be applied in the upper operation disappears.

In k-space it yields

$$\hat{\hat{\boldsymbol{R}}}^{\dagger}\{\hat{\boldsymbol{x}}\}(\boldsymbol{k}) = \hat{f}_{\rm SM} \circ \left[\overline{\hat{f}_{\rm B}} \cdot \{\hat{\boldsymbol{x}}\}\right](\boldsymbol{k}). \tag{3.59}$$

Note, that this expression can be naturally obtained by calculating the signal term of the data-autocorrelation matrix (see the upper operator in fig. 3.3). In section (4.2.4) we will consider a Gaussian smoothing of the signal, as could happen through an observational process, where we test the deconvolution with our scheme. However, the blurring function that we will consider in the rest of our work is given by the mass assignment function, or pixel window, which describes the effect of representing point sources (such as galaxies) on a grid. The most popular assignment functions are the nearest grid point (NGP), the clouds-in-cell (CIC), and the triangular-shaped cloud functions (TSC). For these schemes, we have (see Hockney & Eastwood, 1981)

$$\hat{f}_{\rm B}(\boldsymbol{k}) = \left[\frac{\sin\left(\pi k_x/2k_{Nyx}\right)\sin\left(\pi k_y/2k_{Nyy}\right)\sin\left(\pi k_z/2k_{Nyz}\right)}{(\pi k_x/2k_{Nyx})(\pi k_y/2k_{Nyy})(\pi k_z/2k_{Nyz})}\right]^p, \tag{3.60}$$

with $p = 1$ for NGP, $p = 2$ for CIC, and $p = 3$ for TSC, and where the Nyquist frequences are given by $k_{Nyx} = \pi/dLx$, $k_{Nyy} = \pi/dLy$, and $k_{Nyz} = \pi/dLz$. We use in our work the NGP- and the CIC-scheme implemented by Jasche (2007).

3.3.3 Covariance matrix of the data

The data model consists of two terms

$$\alpha(\boldsymbol{r}) = \int \mathrm{d}^{N_{\rm D}}\boldsymbol{r}'\, f_{\rm B}(\boldsymbol{r}-\boldsymbol{r}')f_{\rm SM}(\boldsymbol{r}')s(\boldsymbol{r}'), \tag{3.61}$$

and

$$\epsilon(\boldsymbol{r}) = f_{\rm SF}(\boldsymbol{r})\epsilon_{\rm N}(\boldsymbol{r}). \tag{3.62}$$

The same quantities in k-space are given by

$$\hat{\alpha}(\boldsymbol{k}) = \hat{f}_{\rm B}(\boldsymbol{k}) \int \frac{\mathrm{d}^{N_{\rm D}}\boldsymbol{q}}{(2\pi)^{N_{\rm D}}} \hat{f}_{\rm SM}(\boldsymbol{k}-\boldsymbol{q})\hat{s}(\boldsymbol{q}), \tag{3.63}$$

and

$$\hat{\epsilon}(\boldsymbol{k}) = \int \frac{\mathrm{d}^{N_{\rm D}}\boldsymbol{q}}{(2\pi)^{N_{\rm D}}} \hat{f}_{\rm SF}(\boldsymbol{k}-\boldsymbol{q})\hat{\epsilon}_{\rm N}(\boldsymbol{q}). \tag{3.64}$$

Consequently, the covariance matrix of the data is given by the following sum

$$\langle \hat{d}(\boldsymbol{k})\overline{\hat{d}(\boldsymbol{k'})}\rangle_{(\boldsymbol{s},\boldsymbol{\epsilon}|\boldsymbol{p})} = \langle \hat{\alpha}(\boldsymbol{k})\overline{\hat{\alpha}(\boldsymbol{k'})}\rangle_{(\boldsymbol{s},\boldsymbol{\epsilon}|\boldsymbol{p})} + \langle \hat{\epsilon}(\boldsymbol{k})\overline{\hat{\epsilon}(\boldsymbol{k'})}\rangle_{(\boldsymbol{s},\boldsymbol{\epsilon}|\boldsymbol{p})}, \tag{3.65}$$

where we have assumed that the noise is uncorrelated to the signal, which is consistent with our data model. Even though the structure function may be correlated with the signal $\langle \hat{s}(\boldsymbol{k})\overline{\hat{f}_{\mathrm{SF}}(\boldsymbol{k'})}\rangle_{(\boldsymbol{s},\boldsymbol{f}_{\mathrm{SF}}|\boldsymbol{p})} \neq 0$, the random noise part is not $\langle \hat{s}(\boldsymbol{k})\overline{\hat{\epsilon}_{\mathrm{N}}(\boldsymbol{k'})}\rangle_{(\boldsymbol{s},\boldsymbol{\epsilon}|\boldsymbol{p})} = 0$. We will calculate the different terms of the data covariance matrix and other related operators in the next sections.

3.3.4 Covariance matrix of the data: the signal term

Here it becomes necessary to choose the Fourier representation, since it is there that the signal-autocorrelation matrix appears to be diagonal in the form of a power spectrum (eq. 3.66). Taking into account statistical homogeneity for the signal $\boldsymbol{s}$

$$\langle \hat{s}(\boldsymbol{k})\overline{\hat{s}(\boldsymbol{k'})}\rangle_{(\boldsymbol{s}|\boldsymbol{p})} = (2\pi)^{N_{\mathrm{D}}}\delta_{\mathrm{D}}(\boldsymbol{k}-\boldsymbol{k'})P_{\mathrm{S}}(\boldsymbol{k'}), \tag{3.66}$$

with δ_{D} being the Dirac-delta function, we can derive the expression for the signal covariance matrix term

$$\begin{aligned}
\hat{\hat{\boldsymbol{S}}}\boldsymbol{R}^{\dagger}(\boldsymbol{k},\boldsymbol{k'}) &= \langle \hat{\alpha}(\boldsymbol{k})\overline{\hat{\alpha}(\boldsymbol{k'})}\rangle_{(\boldsymbol{s}|\boldsymbol{p})} \\
&= \hat{f}_{\mathrm{B}}(\boldsymbol{k})\int \frac{\mathrm{d}^{N_{\mathrm{D}}}\boldsymbol{q}}{(2\pi)^{N_{\mathrm{D}}}}\hat{f}_{\mathrm{SM}}(\boldsymbol{k}-\boldsymbol{q})P_S(\boldsymbol{q})\overline{\hat{f}_{\mathrm{SM}}(\boldsymbol{k'}-\boldsymbol{q})\hat{f}_{\mathrm{B}}(\boldsymbol{k'})} \\
&= \hat{f}_{\mathrm{B}}(\boldsymbol{k})\int \frac{\mathrm{d}^{N_{\mathrm{D}}}\boldsymbol{q}}{(2\pi)^{N_{\mathrm{D}}}}\hat{f}_{\mathrm{SM}}(\boldsymbol{k}-\boldsymbol{q})P_S(\boldsymbol{q})\hat{f}_{\mathrm{SM}}(\boldsymbol{q}-\boldsymbol{k'})\overline{\hat{f}_{\mathrm{B}}(\boldsymbol{k'})},
\end{aligned}$$

For its action on a vector (see fig. 3.3), we get

$$\hat{\hat{\boldsymbol{S}}}\boldsymbol{R}^{\dagger}\{\hat{\boldsymbol{x}}\}(\boldsymbol{k}) = \hat{f}_{\mathrm{B}}\cdot\left[\hat{f}_{\mathrm{SM}}\circ\left[P_{\mathrm{S}}\cdot\left[\hat{f}_{\mathrm{SM}}\circ\left[\overline{\hat{f}_{\mathrm{B}}}\cdot\{\hat{x}\}\right]\right]\right]\right](\boldsymbol{k}), \tag{3.67}$$

and consequently

$$\begin{aligned}
\hat{\hat{\boldsymbol{S}}}\boldsymbol{R}^{\dagger}\{\hat{\boldsymbol{x}}\}(\boldsymbol{k}) &= \int \frac{\mathrm{d}^{N_{\mathrm{D}}}\boldsymbol{k'}}{(2\pi)^{N_{\mathrm{D}}}}\langle \hat{s}(\boldsymbol{k})\overline{\hat{d}(\boldsymbol{k'})}\rangle_{(\boldsymbol{s}|\boldsymbol{p})}\{\hat{x}(\boldsymbol{k'})\} \\
&= P_{\mathrm{S}}(\boldsymbol{k})\underbrace{\underbrace{\int \frac{\mathrm{d}^{N_{\mathrm{D}}}\boldsymbol{k'}}{(2\pi)^{N_{\mathrm{D}}}}\hat{f}_{\mathrm{SM}}(\boldsymbol{k}-\boldsymbol{k'})\underbrace{\overline{\hat{f}_{\mathrm{B}}(\boldsymbol{k'})}\cdot\{\hat{x}(\boldsymbol{k'})\}}_{\overline{\hat{f}_{\mathrm{B}}}\cdot\{\hat{x}\}}}_{\hat{f}_{\mathrm{SM}}\circ\left[\overline{\hat{f}_{\mathrm{B}}}\cdot\{\hat{x}\}\right]}}_{P_{\mathrm{S}}\cdot\left[\hat{f}_{\mathrm{SM}}\circ\left[\overline{\hat{f}_{\mathrm{B}}}\cdot\{\hat{x}\}\right]\right]}.
\end{aligned} \tag{3.68}$$

The inverse of the signal-autocorrelation matrix can be solved trivially in Fourier-space: $\hat{\hat{\boldsymbol{S}}}^{-1} = \mathrm{diag}(P_{\mathrm{S}}(\boldsymbol{k})^{-1})$. Hence, the inverse square root yields $\hat{\hat{\boldsymbol{S}}}^{-1/2} = \mathrm{diag}(P_{\mathrm{S}}(\boldsymbol{k})^{-1/2})$.

3.3.5 Covariance matrix of the data: the noise term

We assume, analogous to the case of the signal, statistical homogeneity for ϵ_{N}

$$\langle \hat{\epsilon_{\mathrm{N}}}(\boldsymbol{k})\overline{\hat{\epsilon_{\mathrm{N}}}(\boldsymbol{k'})}\rangle_{(\boldsymbol{\epsilon}|\boldsymbol{p})} = (2\pi)^{N_{\mathrm{D}}}\delta_{\mathrm{D}}(\boldsymbol{k}-\boldsymbol{k'})P_{\mathrm{N}}(\boldsymbol{k'}), \tag{3.69}$$

and then derive the expression for the noise covariance matrix

$$\begin{aligned}\hat{\hat{\boldsymbol{N}}}(\boldsymbol{k},\boldsymbol{k'}) &= \langle \hat{\epsilon}(\boldsymbol{k})\overline{\hat{\epsilon}(\boldsymbol{k'})}\rangle_{(\boldsymbol{s},\boldsymbol{\epsilon}|\boldsymbol{p})} \\ &= \int \frac{\mathrm{d}^{N_{\mathrm{D}}}\boldsymbol{q}}{(2\pi)^{N_{\mathrm{D}}}}\hat{f}_{\mathrm{SF}}(\boldsymbol{k}-\boldsymbol{q})P_{\mathrm{N}}(\boldsymbol{q})\hat{f}_{\mathrm{SF}}(\boldsymbol{q}-\boldsymbol{k'}).\end{aligned} \tag{3.70}$$

Its action on a vector yields

$$\begin{aligned}\hat{\hat{\boldsymbol{N}}}\{\hat{\boldsymbol{x}}\}(\boldsymbol{k}) &= \int \frac{\mathrm{d}^{N_{\mathrm{D}}}\boldsymbol{k'}}{(2\pi)^{N_{\mathrm{D}}}}\langle \hat{\epsilon}(\boldsymbol{k})\overline{\hat{\epsilon}(\boldsymbol{k'})}\rangle_{(\boldsymbol{s},\boldsymbol{\epsilon}|\boldsymbol{p})}\{\hat{x}(\boldsymbol{k'})\} \\ &= \underbrace{\int \frac{\mathrm{d}^{N_{\mathrm{D}}}\boldsymbol{q}}{(2\pi)^{N_{\mathrm{D}}}}\hat{f}_{\mathrm{SF}}(\boldsymbol{k}-\boldsymbol{q})\,P_{\mathrm{N}}(\boldsymbol{q})\,\underbrace{\int \frac{\mathrm{d}^{N_{\mathrm{D}}}\boldsymbol{k'}}{(2\pi)^{N_{\mathrm{D}}}}\hat{f}_{\mathrm{SF}}(\boldsymbol{q}-\boldsymbol{k'})\{\hat{x}(\boldsymbol{k'})\}}_{\hat{f}_{\mathrm{SF}}\circ\{\hat{x}\}}}_{P_{\mathrm{N}}\cdot\left[\hat{f}_{\mathrm{SF}}\circ\{\hat{x}\}\right]} \\ &\qquad \hat{f}_{\mathrm{SF}}\circ\left[P_{\mathrm{N}}\cdot\left[\hat{f}_{\mathrm{SF}}\circ\{\hat{x}\}\right]\right],\end{aligned} \tag{3.71}$$

In the case where there is no structure function, the noise autocorrelation reduces to

$$\hat{\hat{\boldsymbol{N}}}_{\mathrm{N}}(\boldsymbol{k},\boldsymbol{k'}) = (2\pi)^{N_{\mathrm{D}}}\delta_{\mathrm{D}}(\boldsymbol{k}-\boldsymbol{k'})P_{\mathrm{N}}(\boldsymbol{k'}). \tag{3.72}$$

Then, its action is given by

$$\hat{\hat{\boldsymbol{N}}}_{\mathrm{N}}\{\hat{\boldsymbol{x}}\}(\boldsymbol{k}) = P_{\mathrm{N}}\cdot\{\hat{x}\}(\boldsymbol{k}). \tag{3.73}$$

The corresponding inverse operation is

$$\hat{\hat{\boldsymbol{N}}}_{\mathrm{N}}^{-1}\{\hat{\boldsymbol{x}}\}(\boldsymbol{k}) = {P_{\mathrm{N}}}^{-1}\cdot\{\hat{x}\}(\boldsymbol{k}). \tag{3.74}$$

Consequently, we obtain (see fig. 3.3)

$$\boldsymbol{R}^{\dagger}\hat{\hat{\boldsymbol{N}}}_{\mathrm{N}}^{-1}\boldsymbol{R}\{\hat{\boldsymbol{x}}\}(\boldsymbol{k}) = \hat{f}_{\mathrm{SM}}\circ\left[\overline{\hat{f}_{\mathrm{B}}}\cdot\left[{P_{\mathrm{N}}}^{-1}\cdot\left[\hat{f}_{\mathrm{B}}\cdot\left[\hat{f}_{\mathrm{SM}}\circ\{\hat{x}\}\right]\right]\right]\right](\boldsymbol{k}), \tag{3.75}$$

and

$$\boldsymbol{R}^{\dagger}\hat{\hat{\boldsymbol{N}}}_{\mathrm{N}}^{-1}\{\boldsymbol{x}\}(\boldsymbol{k}) = \hat{f}_{\mathrm{SF}}\circ\left[\overline{\hat{f}_{\mathrm{B}}}\cdot\left[{P_{\mathrm{N}}}^{-1}\cdot\{\hat{x}\}\right]\right](\boldsymbol{k}). \tag{3.76}$$

The inverse square root of $\hat{\hat{\boldsymbol{N}}}_{\mathrm{N}}$ can now be calculated and leads to

$$\hat{\hat{\boldsymbol{N}}}_{\mathrm{N}}^{-1/2}(\boldsymbol{k}) = \mathrm{diag}({P_{\mathrm{N}}}^{-1/2}(\boldsymbol{k})). \tag{3.77}$$

The operation $\boldsymbol{R}^\dagger \hat{\hat{\boldsymbol{N}}}_{\mathrm{N}}^{-1/2}\{\hat{\boldsymbol{x}}\}$ can then be obtained by doing the following substitution $\hat{\hat{\boldsymbol{N}}}_{\mathrm{N}}^{-1} \rightarrow \hat{\hat{\boldsymbol{N}}}_{\mathrm{N}}^{-1/2}$ in eq. (3.76)

$$\boldsymbol{R}^\dagger \hat{\hat{\boldsymbol{N}}}_{\mathrm{N}}^{-1/2}\{\boldsymbol{x}\}(\boldsymbol{k}) = \overline{\hat{f}_{\mathrm{B}}} \cdot \big[\overline{\hat{f}_{\mathrm{SF}}} \circ \big[{P_{\mathrm{N}}}^{-1/2} \cdot \{\hat{x}\}\big]\big](\boldsymbol{k}). \tag{3.78}$$

We are especially interested in the case of white noise ($P_{\mathrm{N}} = P_{\mathrm{WN}} = const$) with a structure function (given by the Poissonian shot noise)

$$\hat{\hat{\boldsymbol{N}}}_{\mathrm{WN}}(\boldsymbol{k}, \boldsymbol{k}') = P_{\mathrm{WN}} \int \frac{\mathrm{d}^{N_{\mathrm{D}}}\boldsymbol{q}}{(2\pi)^{N_{\mathrm{D}}}} \hat{f}_{\mathrm{SF}}(\boldsymbol{k}-\boldsymbol{q})\overline{\hat{f}_{\mathrm{SF}}(\boldsymbol{k}'-\boldsymbol{q})}. \tag{3.79}$$

The corresponding action yields

$$\begin{aligned}\hat{\hat{\boldsymbol{N}}}_{\mathrm{WN}}\{\hat{\boldsymbol{x}}\}(\boldsymbol{k}) \;=\; & P_{\mathrm{WN}} \underbrace{\int \frac{\mathrm{d}^{N_{\mathrm{D}}}\boldsymbol{q}}{(2\pi)^{N_{\mathrm{D}}}} \hat{f}_{\mathrm{SF}}(\boldsymbol{k}-\boldsymbol{q}) \underbrace{\int \frac{\mathrm{d}^{N_{\mathrm{D}}}\boldsymbol{k}'}{(2\pi)^{N_{\mathrm{D}}}} \hat{f}_{\mathrm{SF}}(\boldsymbol{q}-\boldsymbol{k}')\{\hat{x}(\boldsymbol{k}')\}}_{\hat{f}_{\mathrm{SF}}\circ\{\hat{x}\}}}_{\hat{f}_{\mathrm{SF}}\circ\left[\hat{f}_{\mathrm{SF}}\circ\{\hat{x}\}\right]}. \\ & P_{\mathrm{WN}} \cdot \big[\hat{f}_{\mathrm{SF}} \circ \big[\hat{f}_{\mathrm{SF}} \circ \{\hat{x}\}\big]\big] = P_{\mathrm{WN}} \cdot \big[\hat{f}_{\mathrm{SF}}^2 \circ \{\hat{x}\}\big]\end{aligned} \tag{3.80}$$

It can be seen from this equation, that the preferential representation now is in real-space, where $\boldsymbol{N}$ is diagonal

$$\boldsymbol{N}_{\mathrm{WN}}(\boldsymbol{r}, \boldsymbol{r}') = \delta_{\mathrm{D}}(\boldsymbol{r}-\boldsymbol{r}')C_{\mathrm{WN}} f_{\mathrm{SF}}^2(\boldsymbol{r}'), \tag{3.81}$$

with $C_{\mathrm{WN}} = \mathrm{IFT}\big[P_{\mathrm{WN}}\big]$ being a constant. The inverse operation yields

$$\boldsymbol{N}_{\mathrm{WN}}^{-1}\{\boldsymbol{x}\}(\boldsymbol{r}) = (C_{\mathrm{WN}} f_{\mathrm{SF}}^2)^{-1} \cdot \{x\}(\boldsymbol{r}). \tag{3.82}$$

Hence, the inverse square root yields

$$\boldsymbol{N}_{\mathrm{WN}}^{-1/2}(\boldsymbol{r}), \boldsymbol{r}' = \delta_{\mathrm{D}}(\boldsymbol{r}-\boldsymbol{r}'){C_{\mathrm{WN}}}^{-1/2} f_{\mathrm{SF}}^{-1}(\boldsymbol{r}), \tag{3.83}$$

and its action in k-space reads

$$\hat{\hat{\boldsymbol{N}}}_{\mathrm{WN}}^{-1/2}\{\hat{\boldsymbol{x}}\}(\boldsymbol{k}) = {P_{\mathrm{WN}}}^{-1/2} \cdot \big[\hat{f}_{\mathrm{SF}}^{-1} \circ \{\hat{x}\}\big](\boldsymbol{k}). \tag{3.84}$$

$$\boldsymbol{R}^\dagger \hat{\hat{\boldsymbol{N}}}_{\mathrm{WN}}^{-1}\boldsymbol{R}\{\hat{\boldsymbol{x}}\}(\boldsymbol{k}) = \hat{f}_{\mathrm{SF}} \circ \big[\overline{\hat{f}_{\mathrm{B}}} \cdot \big[\hat{\hat{N}}_{\mathrm{WN}}^{-1} \circ \big[\hat{f}_{\mathrm{B}} \cdot \big[\hat{f}_{\mathrm{SF}} \circ \{\hat{x}\}\big]\big]\big]\big](\boldsymbol{k}), \tag{3.85}$$

and consequently

$$\boldsymbol{R}^\dagger \hat{\hat{\boldsymbol{N}}}_{\mathrm{WN}}^{-1}\{\hat{\boldsymbol{x}}\}(\boldsymbol{k}) = \hat{f}_{\mathrm{SF}} \circ \big[\overline{\hat{f}_{\mathrm{B}}} \cdot \big[\hat{\hat{N}}_{\mathrm{WN}}^{-1} \circ \{\hat{x}\}\big]\big](\boldsymbol{k}). \tag{3.86}$$

To calculate $\boldsymbol{R}^\dagger \hat{\hat{\boldsymbol{N}}}_{\mathrm{WN}}^{-1/2}\{\hat{\boldsymbol{x}}\}$ one has to do the following substitution $\hat{\hat{\boldsymbol{N}}}_{\mathrm{WN}}^{-1} \rightarrow \hat{\hat{\boldsymbol{N}}}_{\mathrm{WN}}^{-1/2}$ in eq. (3.86)

$$\boldsymbol{R}^\dagger \hat{\hat{\boldsymbol{N}}}_{\mathrm{WN}}^{-1/2}\{\hat{\boldsymbol{x}}\}(\boldsymbol{k}) = \hat{f}_{\mathrm{SF}} \circ \big[\overline{\hat{f}_{\mathrm{B}}} \cdot \big[\hat{\hat{N}}_{\mathrm{WN}}^{-1/2} \circ \{\hat{x}\}\big]\big](\boldsymbol{k}). \tag{3.87}$$

In summary, we showed that the action of the different operators on a vector required for the different reconstruction estimators (see table 3.2) can be calculated in a straightforward way, as an ordered series of products and convolutions. Note that whenever we need to perform a convolution, we change to the counter space representation with FFTs and do multiplications[1] there.

[1] In order to avoid aliasing effects one has to adequately perform *zero-padding* (see e.g. Press *et al.*, 1992).

Chapter 4

Efficiency and quality validation of the inverse methods with the Wiener-filter

Qué es la vida? Un frenesí.
Qué es la vida? Una ilusión,
una sombra, una ficción.
Y el mayor bien es pequeño,
que toda la vida es sueño,
y los sueños, sueños son.

Calderón de la Barca, La vida es sueño

In this section the Wiener-filter implemented in ARGO is tested with the different linear inverse algorithms presented in the section of numerical methods (3) under several conditions determined by structured noise, blurring, selection function effects and windowing.

The inverse methods that we test here are the Jacobi (J), the Steepest Descent (SD), and several Krylov methods, like the Fletcher-Reeves (FR), the Polak-Ribière (PR), and the EXP Conjugate Gradients method (see section 3.1.5 and appendix B.1.3). This scheme has not been previously discussed in the literature and turns out to be very efficient as will be discussed below. Many other Krylov methods (see table 3.1) can be built from simple equivalence relations, as we show in appendix B.1. However, only the methods mentioned above are taken into account here, as we consider them to be sufficiently representative. The extra-regularization we propose with these Krylov methods converts the Wiener-filtering in a hybrid Tikhonov-Krylov space regularization method. In addition, we also test the Wiener-filter that uses hermitian redundancy as derived in appendix A.2. We call the Wiener-filter defined by the mapping equation (A.12) the conjugated Wiener-filter (CJ), whereas the Wiener-filter defined by eq. (A.14) has no extra suffix.

With the aim of having full control over the synthetic data, we generate Gaussian random fields[1] with the Peacock & Dodds (1994) formula for the power spectrum. The resulting *real*

[1] We use GARFIELDS: **GA**ussian **R**andom **FIELDS**, a program we developed to generate Gaussian random fields from a given power spectrum. The method can be found in detail in Martel (2005).

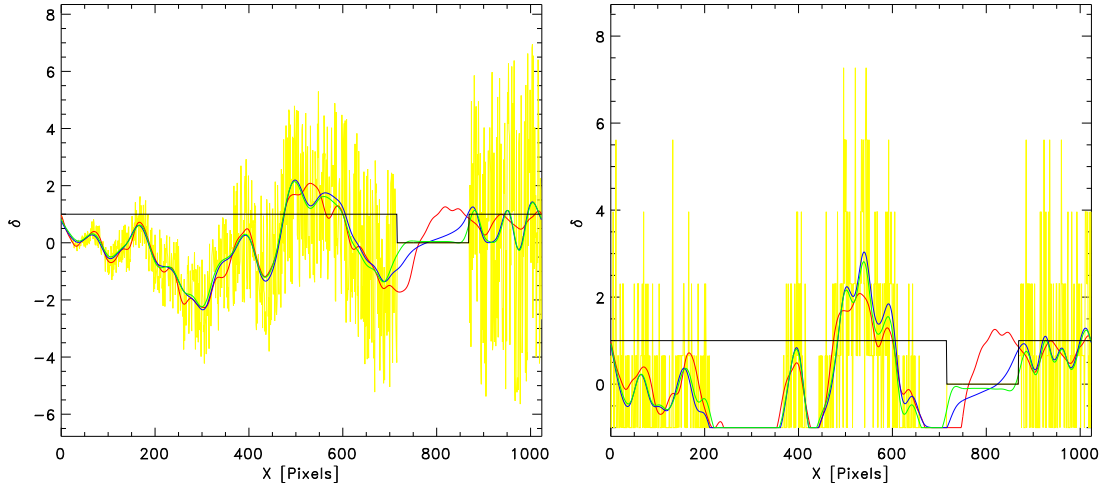

Figure 4.1: **1D Reconstruction with structured noise & window:** The left plot shows the reconstruction of a one-dimensional noisy signal. The red curve is the *true* underlying signal. The yellow lines represent the measured data in each grid cell. The data are windowed by a function given by the black line. A random noise with a structure function that increases with the distance with respect to the origin has been added to the *true* signal. The green and the blue lines show different reconstructions. In the blue case the windowing is formally treated, whereas in the green case the unseen region is modeled by a mean signal, which is zero in this case. We see that the unsampled region is estimated by the blue curve better than by the green curve, where the edge effects were neglected. The proper treatment of edge-effects gives even better results in the sampled regions close to the the borders of the unsampled regions. This improvement can clearly be seen in fig. (4.8). **Poisson noise:** In the right plot, two sampling processes are underlying the yellow signal. First the Gaussian random field that generates the red signal, which is then Poisson sampled leading to the yellow data. Again, the blue and the green curves represent the reconstructions with and without proper window treatment, respectively.

density field is denoted by $\delta_{\rm real} \equiv \delta_\rho$, and the reconstruction by $\delta_{\rm rec} \equiv \psi$. The signals are discretized and arranged as vectors given by $[k + n_z \times (j + n_y \times i)]$, where $i \in [0, n_x - 1]$, $j \in [0, n_y - 1]$, and $k \in [0, n_z - 1]$. The algorithmic part of the reconstruction methods shown in section (3) does not change with the dimensionality, but solely the length of the vectors given by $n = n_x \times n_y \times n_z$ change and thus also the dimension of the involved matrices. The formulation of the matrices is explained in detail in section (3.3). The Fourier transforms must be accordingly called with the dimensions under consideration, which occurs in ARGO by switching between the different FFTs given by FFTW[1]. In addition, the power spectrum that is used for the reconstruction has to be set up with the corresponding length and the data have to be correctly rearranged to their original dimensions ($[i][j][k] \leftarrow [k + n_z \times (j + n_y \times i)]$) after their manipulation.

[1]FFTW is a C subroutine library for computing fast discrete Fourier transforms in one or more dimensions of arbitrary input size and of both real and complex data: http://www.fftw.org/

4.1 One-dimensional example

We can see in fig. (4.1) an example of a Gaussian realization in one-dimension (red curve) that can represent a time-line. A structured noise that increases with the distance ($f_{\mathrm{SF}}(r) \propto r$) and with a random noise component ($\epsilon_{\mathrm{WN}} = G(0,1)$[1]) was added to the signal. Finally a region was excluded simulating windowing effects. The resulting curve was taken as the input signal (yellow curve). The reconstruction given by ARGO is in blue and green, where the boundary effects were considered in the first case, but not in the second. There the signal was assumed to be zero in the UN-sampled region. We can see that the blue curve better resembles the *real* signal guided by the trend at the boundary. This effect is much larger in multiple dimensions as is shown in fig. (4.8). In the right plot in fig. (4.1), two sampling processes are underlying the yellow signal. First, the Gaussian random field that generates the red signal, which is then Poisson sampled thus leading to the yellow data. Again the blue and the green curves represent the reconstructions with and without proper window treatment, respectively. In this case, the blue curve also approaches the *true* signal better.

4.2 Multi-dimensional test cases

ARGO has been implemented such that the global dimension N_{D} (see section 3.3.1), and even the length in each dimension (n_x, n_y, n_z), can be chosen arbitrarily. Our tests in one-, two- and three dimensions show that the results do not differ qualitatively. The convergence behavior changes with the length of the arrays ($n = n_x \times n_y \times n_z$) as $n \log_2 n$ fully determined by the FFTs, as we showed in section (3). For the demonstration cases in this thesis, we have selected the two-dimensional tests with $128 \times 128 = 16384$ pixels. However, three dimensional tests were also carried out leading to the same conclusions.

4.2.1 Qualitative and quantitative measurement of the quality of the reconstruction

To give a quantitative measurement of the quality of the reconstructions, we define the correlation coefficient r between the reconstructed and the real density field by

$$r \equiv \frac{\sum_i^n \delta_{\rho i} \psi_i}{\sqrt{\sum_i^n \delta_{\rho i}^2} \sqrt{\sum_j^n \psi_j^2}}. \tag{4.1}$$

This statistical quantity is not very sensitive to the overall distribution and yields good values (close to unity) in some cases even with poor reconstructions (see figure 4.7). The pixel to pixel plot of the *real* density field against the reconstruction is highly informative because the scatter in the alignment of the pixels around the line of perfect correlation (45° slope) gives a qualitative goodness of the reconstruction. In general, the quality of the recovered density map is better represented by the Euclidean distance between the real and the reconstructed signals. The ensemble average of this quantity can also be regarded as an action or loss function that

[1] $G(0,1)$: zero mean and variance 1.

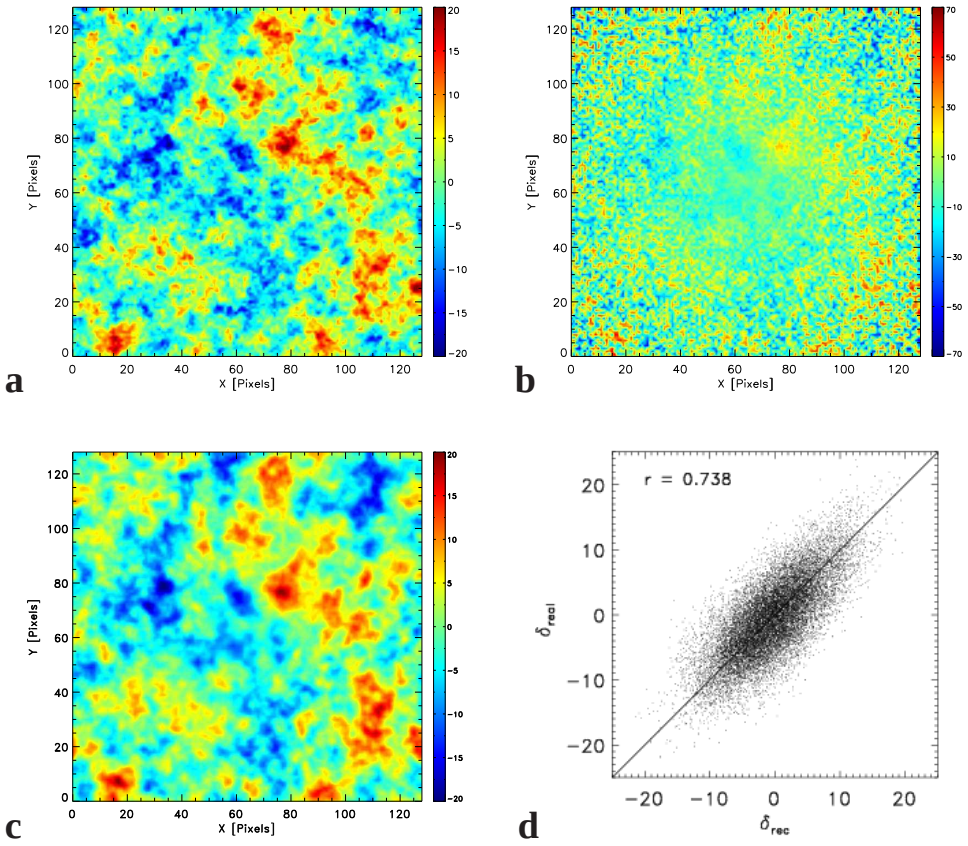

Figure 4.2: **Structured noise treatment:** The upper left picture shows the real signal. The upper right picture is the input signal, where some random noise that increases radially was added. Note that the scale of the colourbar changes from a maximum overdensity of 20 to 70. The lower left picture **c** shows the reconstruction. The reconstructions using different numerical methods implemented in ARGO are indistinguishable. In the lower right image **d**, the real density field is plotted against the reconstructed density field pixel by pixel without any smoothing. The numerical performance of this reconstrcution case is shown in the next figure.

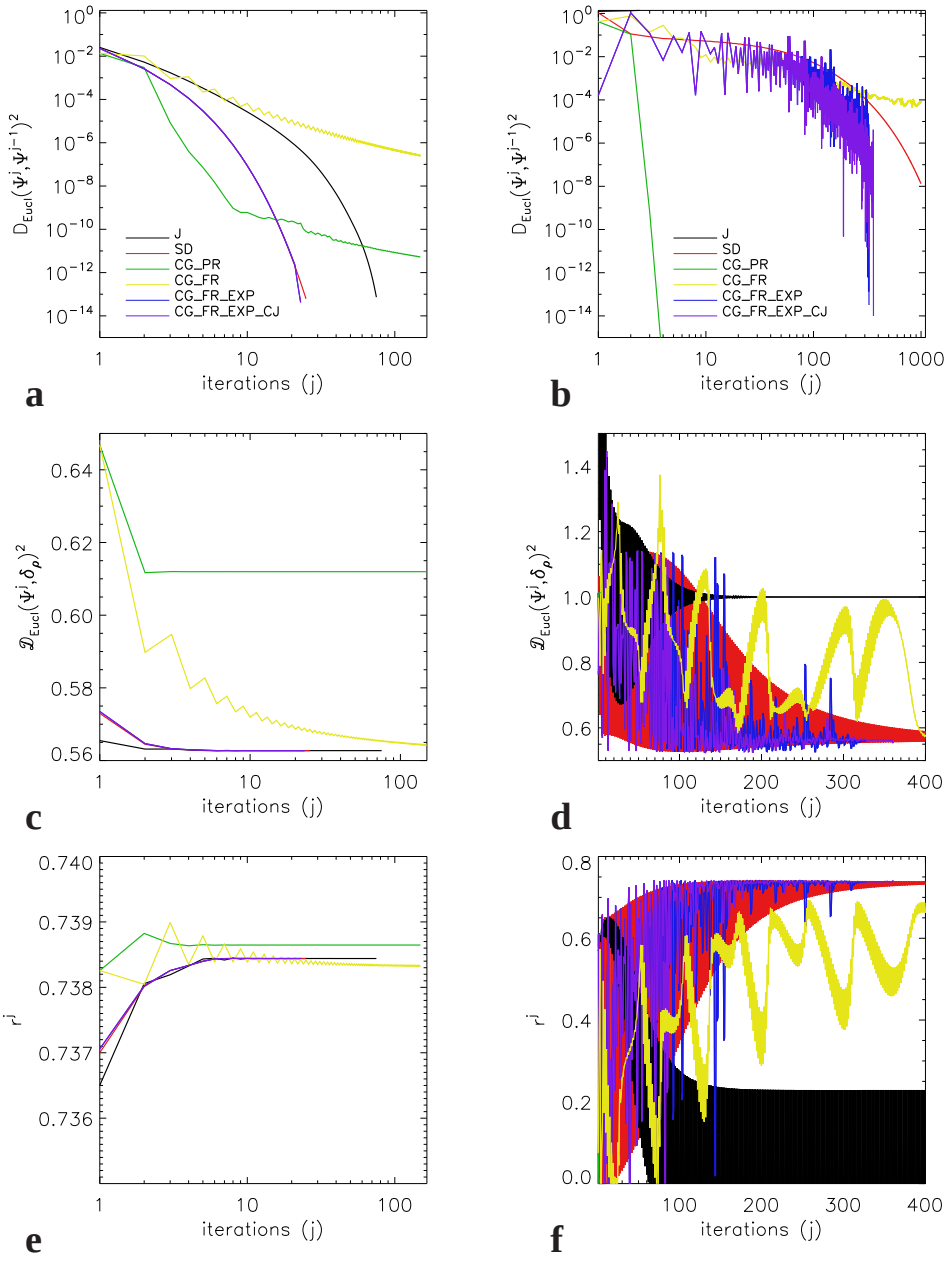

Figure 4.3: **Numerical performance with and without preconditioning:** Here the convergence behaviour and the goodness of the reconstructions using different inversion algorithms can be seen. The pictures on the left show the methods using preconditioning, whereas the pictures on the right do not use preconditioning. The upper plots show the squared Euclidean distance between succesive reconstructions. The plots in the middle show the normalized Euclidean distance between the different reconstructions and the true signal. The lower plots show the evolution of the statistical correlation coefficient between reconstruction and signal. We see from panel **c** and panel **e** that after less than 10 iterations the reconstructions do not significantly improve with most of the inversion algorithms. The different inversion algorithms used are: Jacobi (J), Steepest Descent (SD), Conjugate Gradients (CG), Fletcher Reeves (FR), and Polak Riviere (PR). We also tested a more expensive variant that uses one additional operation of the involved matrix (EXP) and one other variant (CJ), where a degree of freedom in the mapping equation for the Wiener-filter is used.

leads to the Wiener-filter through minimization (see appendix A.2). Here we introduce the volume-averaged squared Euclidean distance[1]

$$\mathrm{D}^2_{\mathrm{Eucl}}(\psi, \delta_\rho) \equiv \frac{1}{V} \int \mathrm{d}^{N_\mathrm{D}} \boldsymbol{r} \left[\psi(\boldsymbol{r}) - \delta_\rho(\boldsymbol{r})\right]^2, \tag{4.2}$$

with $V = L_x \times L_y \times L_z$. We further normalize the Euclidean distance through the following definition

$$\mathcal{D}^2_{\mathrm{Eucl}}(\psi, \delta_\rho) \equiv \frac{\mathrm{D}^2_{\mathrm{Eucl}}(\psi, \delta_\rho)}{\mathrm{D}^2_{\mathrm{Eucl}}(\psi_0, \delta_\rho)}, \tag{4.3}$$

where ψ_0 is the zero vector. We define the convergence tolerance criterion based on the squared Euclidean distance between subsequent reconstructions

$$\mathrm{tol}^{\mathrm{j}+1}_{\mathrm{crit}} \equiv \mathrm{D}^2_{\mathrm{Eucl}}(\psi^{j+1}, \psi^j). \tag{4.4}$$

We prefer this criterion with respect to the squared residuals $||\xi||^2$ (see eq. 3.16) because all the tests show that no further statistical quality improvement in the reconstructions is reached after $\mathrm{tol}^{\mathrm{j}+1}_{\mathrm{crit}}$, as can be inferred from the correlation coefficients r and the normalized squared Euclidean distances $\mathcal{D}^2_{\mathrm{Eucl}}(\psi, \delta_\rho)$.

4.2.2 Numerical performance with and without preconditioning

Here we analyze the convergence behavior of the different inverse schemes with and without preconditioning. We start by considering a Gaussian random field with some structured noise that increases radially and is modulated by a random noise component. As a preconditioning expression, the diagonal part of the data covariance matrix is chosen, which is given by the sum of

$$\begin{aligned} \hat{\hat{\boldsymbol{S}}}\boldsymbol{R}^\dagger(\boldsymbol{k}, \boldsymbol{k}) &= \hat{f}_\mathrm{B}(\boldsymbol{k}) \int \frac{\mathrm{d}^{N_\mathrm{D}}\boldsymbol{q}}{(2\pi)^{N_\mathrm{D}}} \hat{f}_\mathrm{SM}(\boldsymbol{k}-\boldsymbol{q}) P_S(\boldsymbol{q}) \hat{f}_\mathrm{SM}(\boldsymbol{q}-\boldsymbol{k}) \overline{\hat{f}_\mathrm{B}(\boldsymbol{k})} \\ &= \underbrace{P_\mathrm{B}(\boldsymbol{k}) \int \frac{\mathrm{d}^{N_\mathrm{D}}\boldsymbol{q}}{(2\pi)^{N_\mathrm{D}}} P_\mathrm{SM}(\boldsymbol{k}-\boldsymbol{q}) P_S(\boldsymbol{q})}_{P_\mathrm{B} \cdot \left[P_\mathrm{SM} \circ P_\mathrm{S}\right],} \end{aligned} \tag{4.5}$$

and

$$\begin{aligned} \hat{\hat{\boldsymbol{N}}}(\boldsymbol{k}, \boldsymbol{k}) &= \int \frac{\mathrm{d}^{N_\mathrm{D}}\boldsymbol{q}}{(2\pi)^{N_\mathrm{D}}} \hat{f}_\mathrm{SF}(\boldsymbol{k}-\boldsymbol{q}) P_\mathrm{N}(\boldsymbol{q}) \hat{f}_\mathrm{SF}(\boldsymbol{q}-\boldsymbol{k}) \\ &= \underbrace{\int \frac{\mathrm{d}^{N_\mathrm{D}}\boldsymbol{q}}{(2\pi)^{N_\mathrm{D}}} P_\mathrm{SF}(\boldsymbol{k}-\boldsymbol{q}) P_N(\boldsymbol{q})}_{P_\mathrm{SF} \circ P_\mathrm{N},} \end{aligned} \tag{4.6}$$

where we have used the following definitions: $P_\mathrm{B} \equiv ||\hat{f}_\mathrm{B}||^2$, $P_\mathrm{SM} \equiv ||\hat{f}_\mathrm{SM}||^2$ and $P_\mathrm{SF} \equiv ||\hat{f}_\mathrm{SF}||^2$. We can thus calculate the preconditioning matrix M required for the different schemes

[1] Note that $\mathrm{D}^2_{\mathrm{Eucl}}(\psi, \delta_\rho) = \frac{1}{V} D^2_{\mathrm{Eucl}}(\psi, \delta_\rho)$.

(section 3) by just inverting each diagonal component. The results summarized in fig. (4.3) show important differences between the reconstructions done with (on the left side) and without (on the right side) preconditioning. Some of the methods just speed up, like the various EXP methods or the SD scheme. Others, however, are stabilized and manage to converge to the solution only after preconditioning, like the J, the FR and the CPR methods. Without preconditioning, the latter converges extremely quickly to a wrong solution. This is due to the fact that we did not impose the following stabilization: $\beta_{\mathrm{PR}} = \max(\beta_{\mathrm{PR}}, 0)$ in this calculation (see Shewchuk, 1994, for a discussion). However, our tests show that upon imposing this stabilization the PR-method becomes significantly slower than the rest. On the other hand, the EXP-Krylov methods behave most stably and converge very quickly. In the preconditioned case, we see that all methods converge to the same statistical result, as we can infer from the correlation coefficient r and $\mathcal{D}^2_{\mathrm{Eucl}}(\psi, \delta_\rho)$, except for the PR scheme that yields slightly less optimal results (see the green line in comparison to the rest in panel **c**). We have tested preconditioning in the rest of the examples and could confirm the results presented in this section. Preconditioning turns out to be necessary to achieve fast algorithms.

4.2.3 Poissonian distribution

In this study case, we investigate the reconstruction of a Gaussian field based on a Poissonian distribution. This model is far from reality, where much more complex processes are known to occur (see discussion in section 2.1.1). However, we can model a non-Gaussian process in this way and test how good the Wiener-filter reconstruction works under such circumstances. Here the assumed data model does not coincide with the one that has generated the data. However, the Poissonian noise can be modeled in the noise matrix of the Wiener-filtering through the structure function f_{S}.

The results presented in fig. (4.4) show very good agreement between the reconstruction and the *real* underlying density field (compare panels **a** and **c**). The convergence behaviour and statistical goodness is plotted in the left side of fig. (4.6), panels **a**, **c** and **e**. There we can see that the FR and PR methods do not converge rapidly (see yellow and green curves in panel **a**). On the contrary, the J, SD, and EXP schemes are very efficient (panel **c**) and lead to very similar results (panels **c** and **e**).

4.2.4 Blurring effects: deconvolution

In this numerical experiment we tested the blurring effects by convolving the density field with a Gaussian. The result is shown in fig. (4.5), panel **b**. We see how the small structures are smoothed out and only the larger ones prevail. Some noise with a structure function was added to the signal. However, the noise was kept low with the aim of investigating primarily the blurring effect. The results of the reconstruction that considers only the noise does not change much with respect to the input signal, as can be expected. However, the extra-regularized Wiener-filtering deblurs the image applying eqs. (3.67) and (3.68), and yields the figure shown in panel **c**. We see how much of the small scale structure is restored and the peaks become enhanced. The correlation between this reconstruction and the original signal (panel **e**) is significantly better than for the case where the blurring is ignored (panel **f**). We can see in

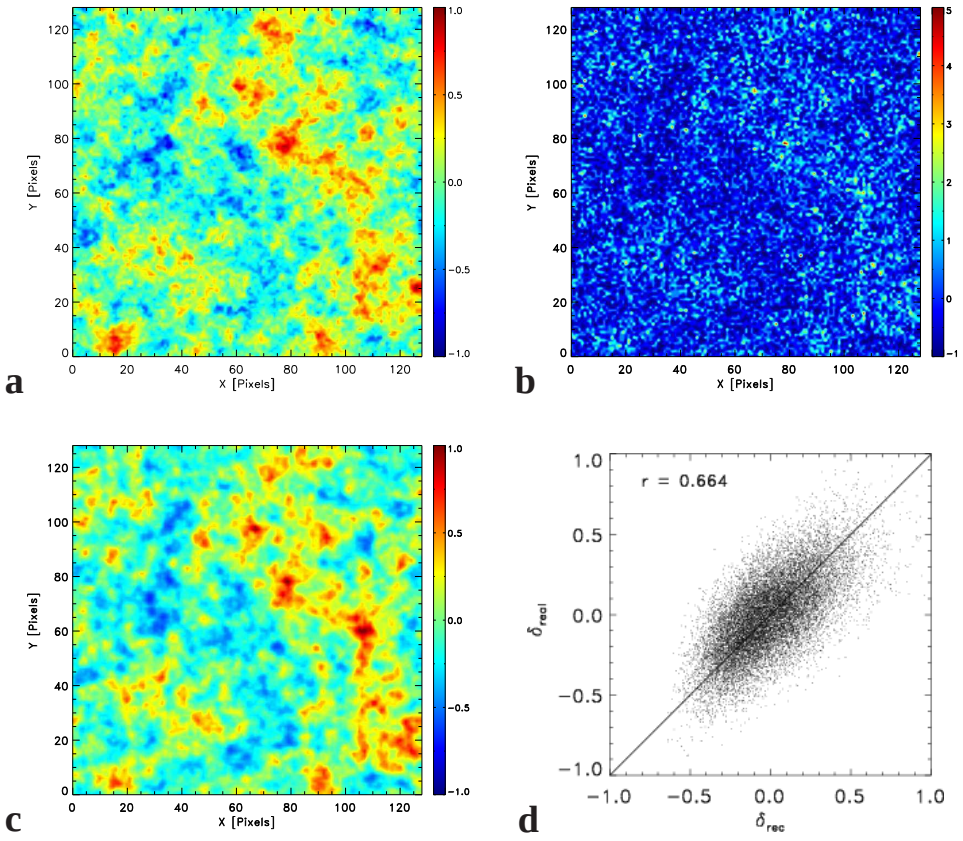

Figure 4.4: **Poissonian noise:** Here two stochastic processes are underlying the input signal. First the Gaussian random field that generates the signal in panel **a**, which is then Poisson sampled leading to the signal in panel **b**. The reconstruction in panel **c** is shown to be in good agreement with the underlying signal. The pixel values are correctly distributed as can be seen in panel **d**.

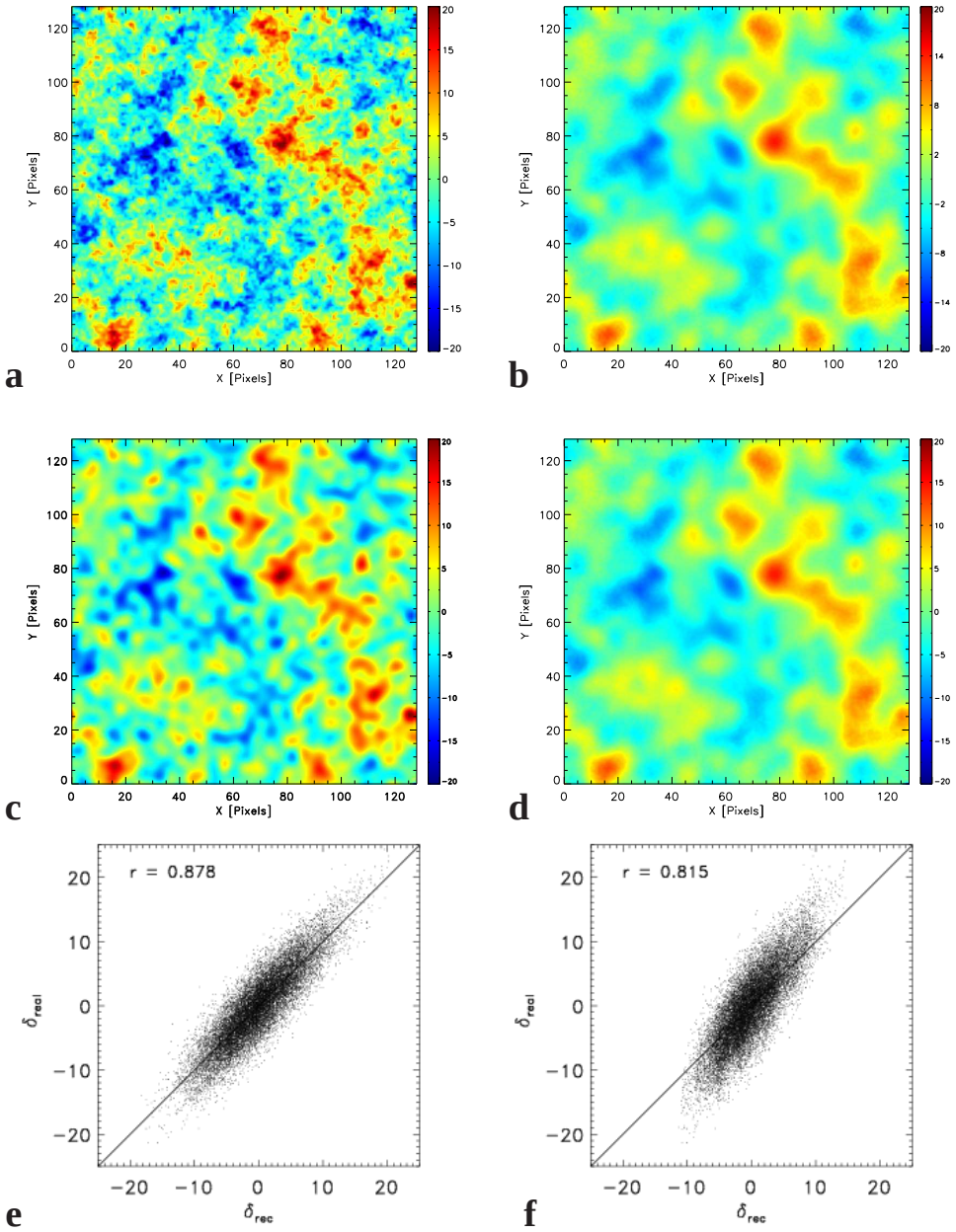

Figure 4.5: **Blurring treatment:** Here the signal (panel **a**) was convolved with a gaussian modeling blurring effects, as shown in panel **b**. Some low noise with a structure function was added. Panel **c** shows the deblurred result. Panel **d** takes only the noise into account. We see in panel **f** the correlation between the input signal and the *true* signal, because the noise is negligible. The correlation coefficient is thus very high, however, the alignment of the pixels in the plot is not correct. Overdensities and underdensities tend to be underestimated, which is consistent with the blurring effect. The reconstruction given in panel **e** corrects this effect and consequently a higher correlation coefficient is achieved.

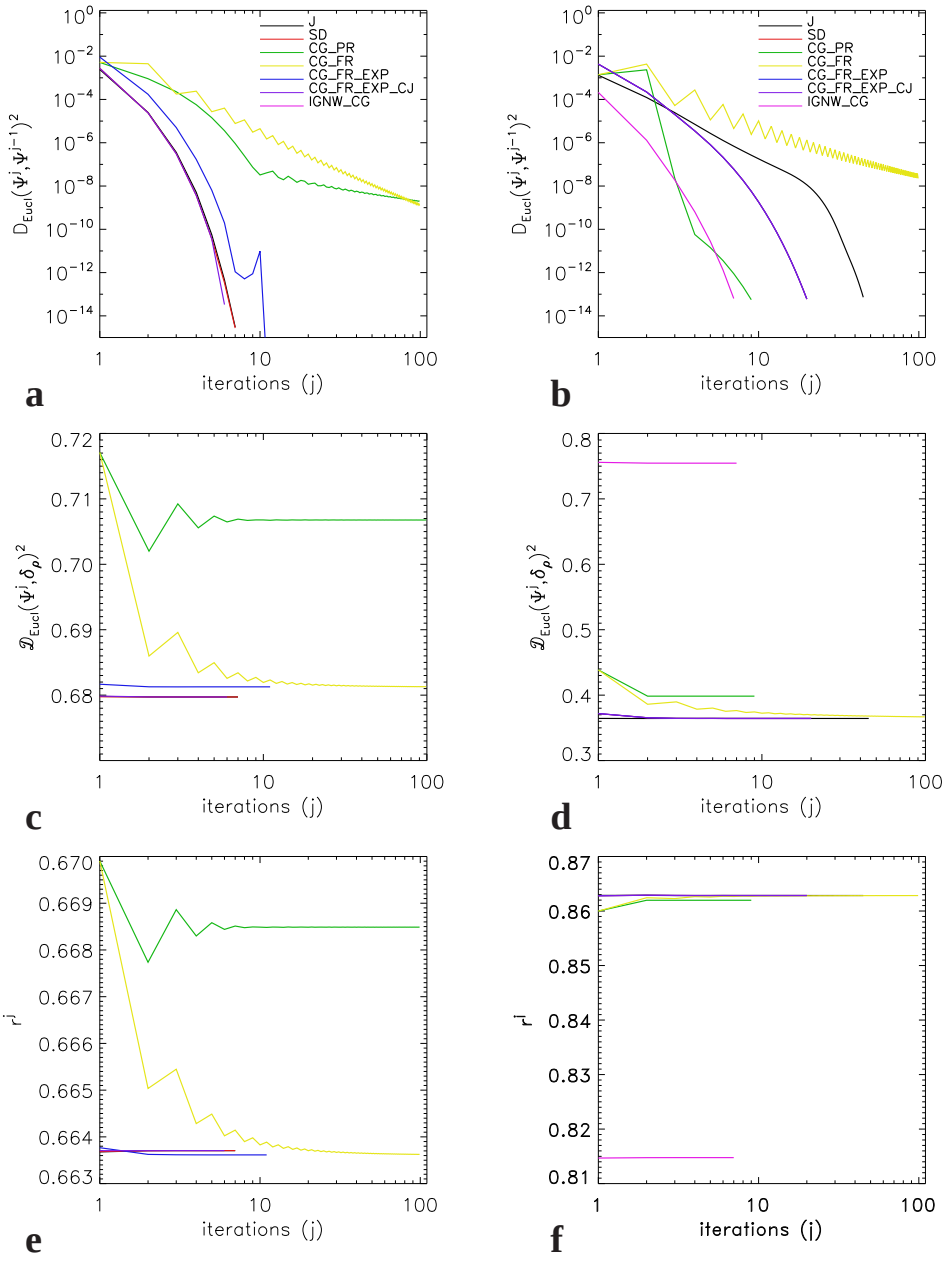

Figure 4.6: **Poissonian noise and numerical performance (panels a, c, e):** Here the convergence behaviour and quality of the reconstruction is comparable for the J, SD, EXP methods. The FR and PR schemes do not present a fast convergence (panel **a**). Nevertheless, the FR scheme (yellow curve) seems to lead to the correct solution (panels **c** and **e**). The PR formula, on the contrary, stagnates at reconstructions that have much lower quality compared to the rest of the schemes. **Blurring treatment and numerical performance (panels b, d, f):** In this study case, the EXP algorithm seems to work better than the rest of the schemes. Although the PR formula converges very rapidly (green curve in panel **b**), it leads to a lower quality reconstruction (panels **d** and **f**). The FR scheme converges to the same solution as the J, SD, and EXP algorithms, however, with a slower convergence (yellow curve in panel **b**). The J and SD methods have an overall good behaviour in this case, but still converge significantly slower than the EXP scheme (their convergence is identical black and red curves are overplotted). The reconstruction considering just the noise is very poor, because the noise is negligible in this case (pink curves).

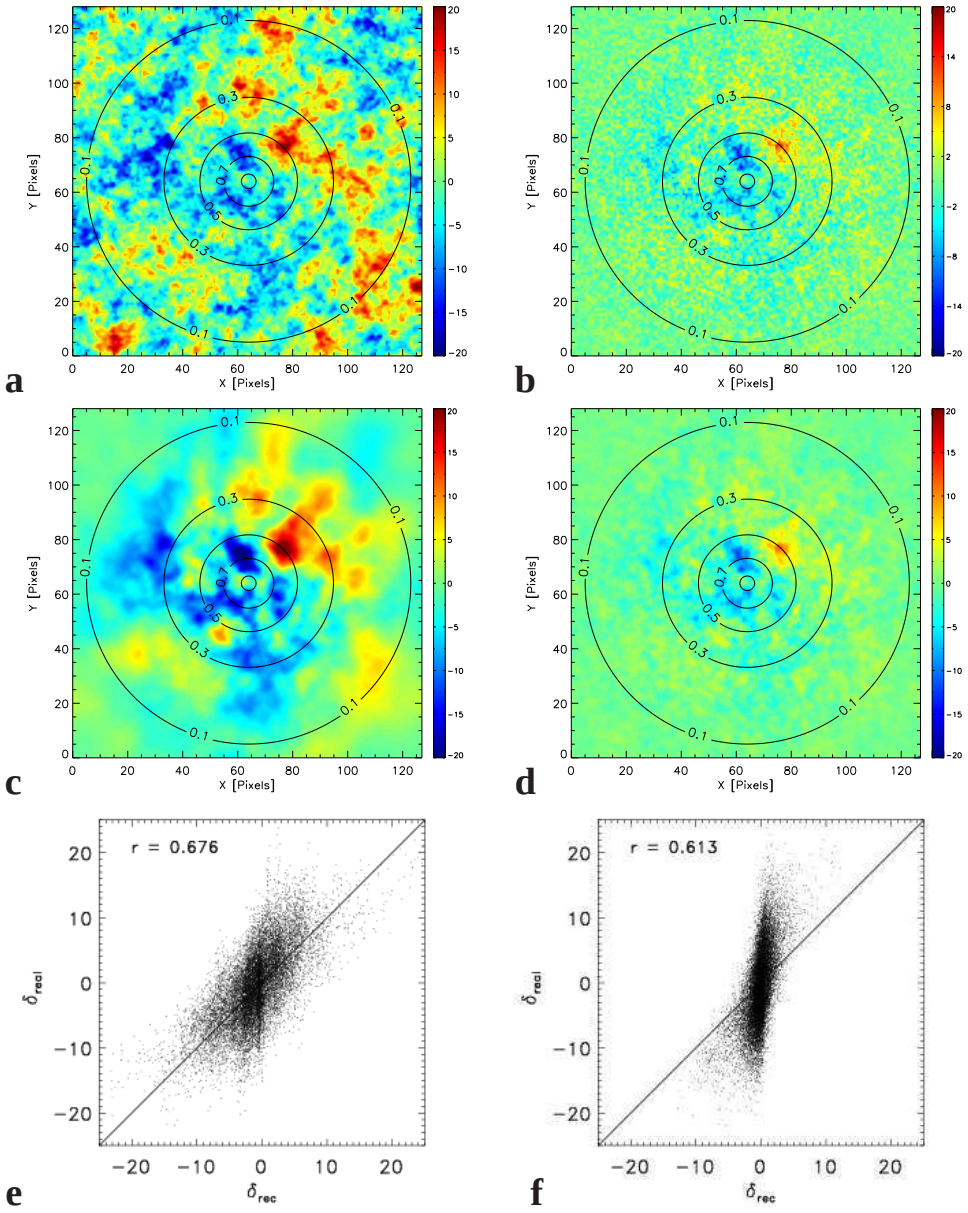

Figure 4.7: **Selection function treatment:** Here selection function effects were simulated with a function that takes values between zero and one, decreasing exponentially in radial direction. The contours show different values of this function. Panel **a** shows the real density field. Panel **b** shows the input data, where the true signal was multiplied in real space with the selection function and a radially increasing noise was added. The reconstruction and its correlation with the true signal are represented in panel **c** and **e**, respectively. The reconstruction ignoring selection effects by taking only the noise into account leads to panels **d** and **f**. The reconstruction given in panel **d** is very conservative and smooths the overdensities out due to noise supression. This leads to a high correlation coefficient, though the individual pixels are clearly not correctly aligned (panel **f**). Panel **c**, on the contrary, shows more structures that are enhanced due to consideration of the selection function effects. This correctly distributes the pixels, as can be seen in panel **e**. The correlation coefficient seems to be significantly better than in panel **f**, however, a better measure of the overall quality of the reconstruction can be seen in next figure.

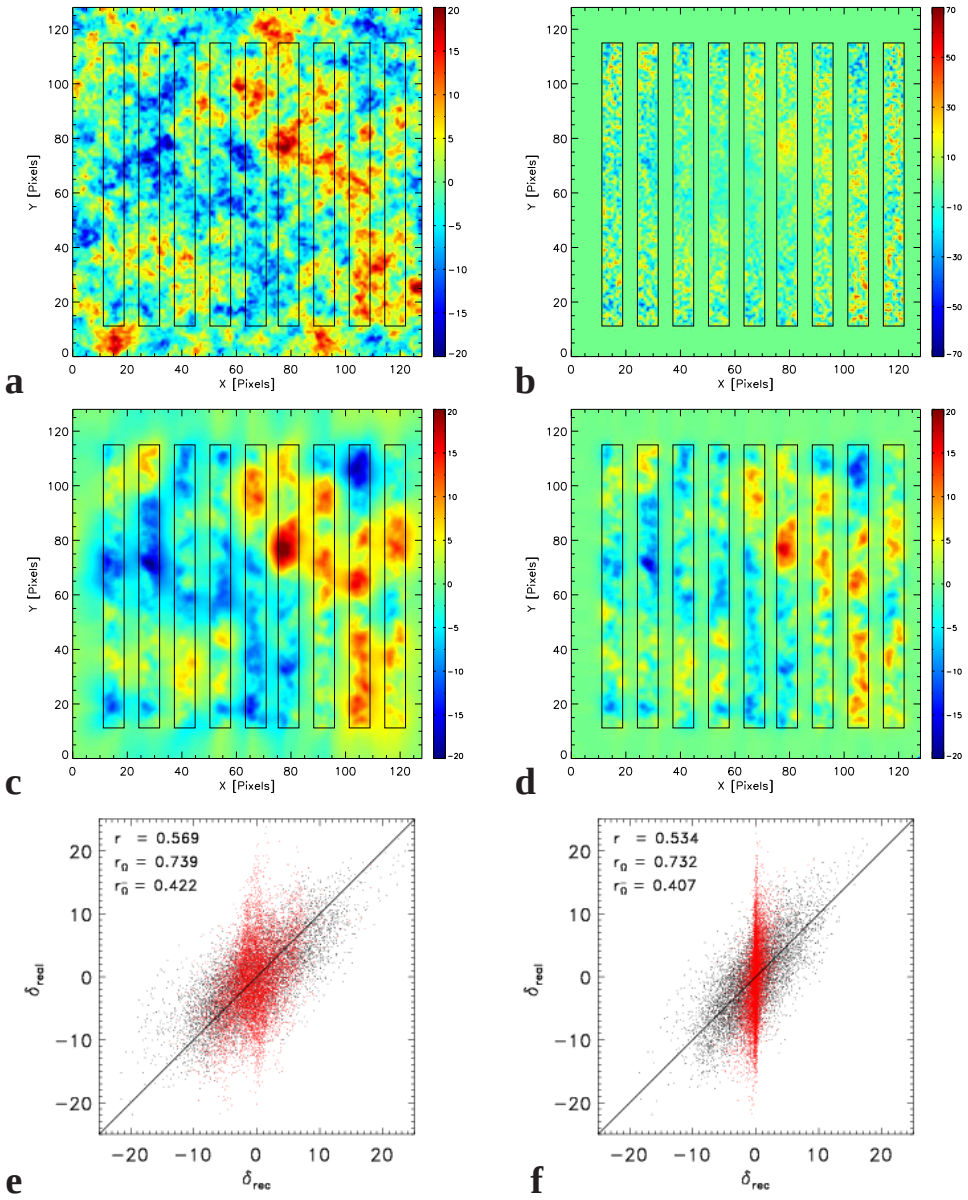

Figure 4.8: **Windowing treatment:** Here the edge effects are shown in two dimensions. The true signal was multiplied by a windowing function that is one in the observed region (Ω) and zero in the unknown region ($\bar{\Omega}$). The sampled regions are given by the vertical stripes. In addition, a radially increasing noise was added (see panel **b**). Panel **c** shows the reconstruction handling the edge effects. Panel **d** represents the result taking only the noise into account. We see in panel **c** how the information is propagated into the unsampled regions leading to a closer resemblance of the real signal, whereas the noise is just suppressed in panel **d**. Panels **e** and **f** show the correlation coefficients for the whole reconstructed region, split into the sampled (black dots) and the unsampled regions (red dots). Note that the red dots are strongly aligned around the zero value in panel **f**, whereas they are correctly spread in panel **e**, statistically representing the information propagation process mentioned above.

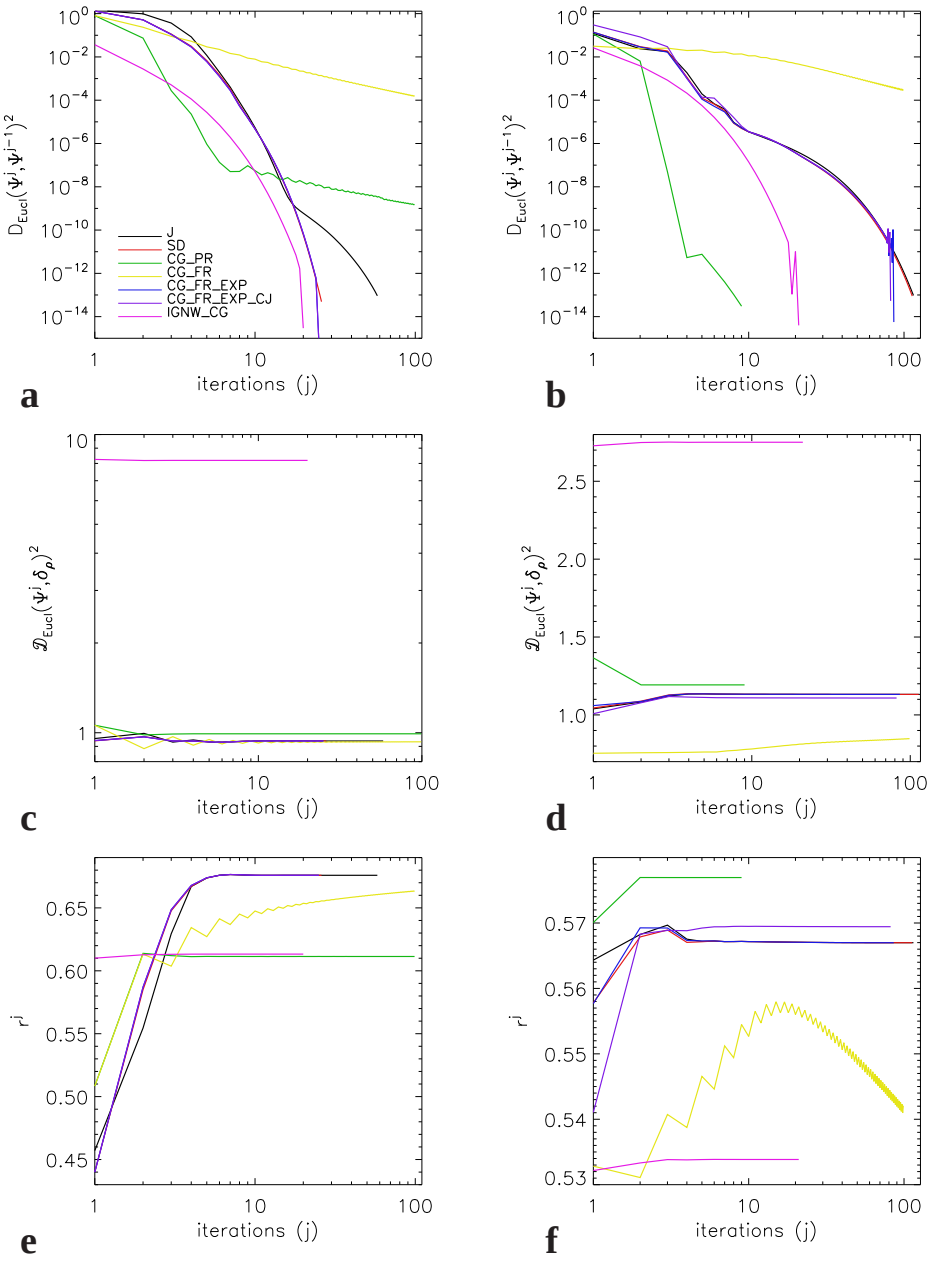

Figure 4.9: **Selection function treatment and numerical performance (panels a, c, e):** The same color coding is used as in fig. (4.3) panel **a**, except for additional curve (represented in pink) that indicates the reconstruction in which the selection effects are ignored. Panel **a** shows the squared Euclideanstatistical correlation r is also much better for the case where the selection effects are properly treated (panel **e**). One concludes from the three plots, that the SD and EXP methods (red, blue and violet curves) clearly converge faster to a more or equally optimal solution in comparison with the rest of the methods. The J scheme shows a significantly slower convergence (black curve in panel **a**). The PR algorithm stagnates at poorer reconstructions as can be seen from panel **c** and **e**.

Figure 4.9: **Windowing treatment and numerical performance (panels b, d, f):** In this case, the PR shows extremely good results: fast convergence (panel **b**) and a high correlation coeficient (panel **d**). However, the Euclidean distance is slightly bigger than for the rest of the methods, except for the pink curve (ignoring windowing effects). The FR method is disastrous in this study case and diverges from the solution as can be seen in panel **f**. The J, SD, and EXP methods show good and stable results. The J and SD algorithms give extremely similar results. Although their convergence behaviour is similar to the EXP schemes, the latter give slightly better results: smaller values for the Euclidean distance and higher values for the correlation coefficient (violet curves in panels **d** and **f**, respectively).

fig. (4.6) that the deconvolution algorithm is very fast for all the methods except for the FR-scheme. The PR-method is the fastest, but it leads to slightly worse results (see the green curve in panels **c** and **e**). The EXP turns out to be more efficient than the J and SD methods in this case.

4.2.5 Selection function effects

For this case we use a modified data model in which the selection function also affects the noise

$$d = f_{\rm S} \cdot (s + f_{\rm SF} \cdot \epsilon_{\rm WN}), \tag{4.7}$$

with $f_{\rm S} \in [0, 1]$, simulating the fading strength of the signal with increasing distance. The results are plotted in fig. (4.7), where the structure of the signal can be seen to become indistinguishable in radial direction (see panel **b**). Taking only the noise into account leads to very poor reconstructions (see panel **d**). On the contrary, by also considering the selection function effects, the structures are resolved even at contours where only 10 % of the signal plus noise is left (see panel **c**). As can be appreciated in panels **e** and **f** there is an improvement in the correlation between the *real* density field and the reconstructed signal. Panel **e** shows a higher correlation coefficient, but the quality enhancement of the reconstruction can be seen better in the distribution of the density values for each pixel. How the points are correctly spread along the diagonal line can be verified there. The longer Euclidean distance to the *real* density field shows the quantitative difference very clearly, by just comparing the pink curve with the rest (fig. 4.9 and panel **c**). It is worth mentioning that although the PR test seems to give a comparable result to the calculation that ignores the selection function. The final correlation coefficient in panel **e** shows that the reconstructions actually strongly differ and panel **c** shows that the quality of the recovered signal is notably better for the former experiment.

In addition, we tested the same selection function affecting only the underlying signal with a model given by

$$d = f_{\rm S} \cdot s + f_{\rm SF} \cdot \epsilon_{\rm WN}, \tag{4.8}$$

and obtained the same qualitative results.

4.2.6 Windowing effects

In this section we investigate the mask effects that introduce coupling between different modes in Fourier-space so that the data covariance matrix is no longer diagonal. The input signal is

given in panel **b** of fig. (4.8). The noisy signal from panel **b** in fig. (4.2) was cut in stripes to simulate *observed* regions. We compare two reconstructions here, the first one ignores windowing effects given in panel **d** and a second reconstruction employs the proper treatment of the boundary through f_{M} in the algorithm (see eqs. 3.67 and 3.68). The statistical correlation is given in panels **e** and **f**, respectively. Our experiments show better results not only for the latter reconstruction in the un-sampled region ($\overline{\Omega}$), represented by the red dots in panels **e** and **f** in fig. (4.8), but also in the sampled regions (Ω). The global correlation r is significantly improved. Whereas the distribution of the black dots, the values of the densities in the *observed* regions, does not apparently change, the distribution of the un-sampled red dots clearly does. These are distributed around the zero value for the case where windowing is ignored because a zero signal is assumed by ARGO in the $\overline{\Omega}$ region. In contrast we see that the red dots are distributed along the diagonal line when edge effects are considered. This is equivalent to a propagation of the information to the un-sampled regions or the appropriate interpolation and extrapolation of signals. Looking at the numerical performance in fig. (4.6) reveals that most of the methods behave very similarly, except for the PR and FR schemes that deviate from the rest. The former converges rapidly to a good solution that has a higher correlation (see green curve in panel **f**), but a slightly worse Euclidean distance to the *true* signal. The FR on the other hand converges extremely slowly. The correlation coefficient is at a stage where it becomes dramatically worse (see yellow curve in panel **f**). The smaller Euclidean distance is no measure for the quality in this case because these low values can be achieved when the reconstruction is very conservative (closer to zero) and has no structure. Notice how many schemes start with better values for that distance measure (see panel **d**). The EXP methods converge faster and the CJ version leads to even slightly better results (see violet curve in panels **d** and **f**).

It is also worth mentioning that the best reconstructions in terms of high correlation coefficients and low Euclidean distances to the underlying signal are achieved only after three iterations for the J, SD, and EXP methods, prior to numerical convergence. We furthermore tested ARGO under extreme noise conditions in which the inversion diverges and produces density values that approach infinity. At early iterations, extremely good reconstructions were produced. These examples underline the regularization character of the inversion schemes under consideration in this thesis. However, for the cases we are interested in, where the noise is mainly determined by the discrete sampling of galaxies, no additional stopping rules are required and the inversion algorithms can be run until full convergence.

Chapter 5

Bayesian reconstructions from galaxy redshift surveys

Was ist geschehen, mit mir? Warum bin ich über Nacht in ein Insekt verwandelt?

Franz Kafka, Die Verwandlung

In this chapter we investigate the Bayesian reconstruction of the matter distribution from a galaxy redshift survey. We show that the methodology presented in the previous sections permits us to perform very fast high-resolved reconstructions of the density field, and consequently to sample the joint space spanned by the signal and its parameters, such as the velocity field and the power-spectrum.

A proper reconstruction turns out to require a global and simultaneous treatment of different effects due to structure formation —such as linear structure formation and virialization— together with the observational and sampling uncertainties. However, corrections of the structure formation velocity distortions are done very approximately, if at all (see section 5.2.3). In order to overcome such limitations, we suggest a novel rejection-sampling method to correct for linear as well as non-linear velocity distortion based on physical-statistical models (see section 5.3.1).

Furthermore, a Bayesian reconstruction builds on a known matter power-spectrum. However, the power-spectrum itself should be determined from the data. We approach this via a novel Gibbs-sampling algorithm for the power-spectrum determination and sampling in three dimensions. This method was proposed by Kitaura & Enßlin (2007) and developed in collaboration with Jens Jasche, who implemented the power-spectrum sampling module, Benjamin Wandelt, Jeremy Blaizot, and Torsten Enßlin (see section 5.3.2).

The chapter is divided in three sections. In the first section we define the physical and statistical problem and motivate the Bayesian approach. In the second section we describe single Bayesian reconstruction steps. In the last section we present novel Bayesian sampling schemes in the large-scale structure reconstruction field.

5.1 Physical and statistical problem

Let us motivate the algorithmic development we present in this chapter by first defining the physical and observational system and then analyze the statistical nature of the problem. We start presenting the redshift-distortions problem, then we discuss the statistical character of the signal and finally we develop the noise model with a Poissonian likelihood.

5.1.1 Redshift-distortions

The measured redshift of a galaxy, or its so-called recession velocity can be expressed by Hubble's law, that describes the bulk flow of the Universe. However, the peculiar velocity of the galaxies along the line-of-sight introduces so-called redshift-distortions. This has to be considered while translating redshifts into positions using Hubble's law. Hence, a galaxy's redshift-distance or redshift-space position cz (conveniently expressed in velocity units) is given by its true distance or real-space position $r = H_0 d$ plus its peculiar velocity $\boldsymbol{v}$ along the line-of-sight in direction $\hat{\boldsymbol{r}}$

$$cz = H_0 d + \hat{\boldsymbol{r}} \cdot \boldsymbol{v}. \tag{5.1}$$

Using a notation with $c \equiv 1$ and defining $v_r \equiv \hat{\boldsymbol{r}} \cdot \boldsymbol{v}$ we can rewrite last equation as

$$z = r + v_r. \tag{5.2}$$

For low over-densities, linear theory gives good estimates of the peculiar velocity

$$\boldsymbol{v}_{\mathrm{LT}} = -\beta \nabla \nabla^{-2} \delta_\rho, \tag{5.3}$$

where ∇^{-2} is the inverse Laplacian[1]. For high over-densities, the structures tend to be virialized. This means that the galaxies will behave like a Boltzmann gas, introducing dispersions in redshift-space along the line-of-sight, the so-called *finger-of-god* effect. It is obvious from this, that a proper reconstruction of the density field depends on the knowledge of the velocity field, and vice-versa, the velocity field will be determined by the density field. Though the physical system of a matter distribution interacting gravitationally has a well defined theoretical solution that can in principle be found by solving Vlasov's equation, the observational process destroys uniqueness. After shell-crossing the relationship between the real-position and the redshift-position stops being unique. A statistical approach is thus very appropriate in this case. Within a Bayesian framework the joint probability distribution of the density field and the velocity field compatible with the redshift observations can be found.

5.1.2 Statistical variance

Finding the joint distribution requires sampling the density field also. One needs to know the uncertainty in the reconstruction for that purpose. There are many sources of uncertainty as we discussed in the introduction.

[1] One has to take care here with the mass-assignment function chosen, since this will change the expression of the Laplacian.

Some observational effects, such as the selection function and the mask are very relevant (see section 4.2.5 and 4.2.6). We will ignore, however, these effects in most of the studies in this chapter. Nevertheless, we present various methods to include these effects in the generation of the fluctuating term corresponding to the reconstruction (see section 5.3.2).

In addition, the galaxy bias needs to be treated. We will also ignore this problem, for the moment, and assume a bias of one. The bias parameter, however, could be introduced as part of the sampling scheme analogous to the power-spectrum (see the hierarchical Bayes model 1.1).

Another source of uncertainty comes from the cosmic variance which is usually described by the second moment of the density field distribution, the power-spectrum. The power-spectrum can be partially extracted from the data in a Gibbs-sampling scheme as we describe in section (5.3.2). However, the modes that are not contained in the data will have to be drawn from a prior probability distribution. Or in other words, only modes contained in the data can be used for the reconstruction. The statitics determined by these modes, however, permits one to reconstruct regions that are not covered by the observed data.

The mass-assignment schemes used to interpolate the discrete sample of galaxies on a grid also introduces aliasing effects in the reconstructions that can become very important in iterative schemes like the ones we propose here. For this reason we have to carefully investigate them. As we already showed in section (4.2.4), blurring effects are well treated in ARGO. We include the blurring effects due to the pixel window in the response function (see section 3.3.2). This is only considered in the signal term (see section 3.3.4), but not in the noise term so far (see section 3.3.5). The latter is usually introduced arbitrarily, without clearly motivating its origin. Here, we make the effort to include this explicitely.

For the case of a distribution of galaxies, it is usually assumed that there is shot noise. Many of the derivations are based on Peebles approach of introducing a hyper-fine grid in which only one or zero galaxies are left in each cell, hiding the underlying implicit assumption of a galaxy formation model given by the Poisssonian distribution (see e.g. Jing (2005) and appendix C.21). This is certainly a strong, but common simplification in matter reconstructions. It is also a frequently and successfully used in power-spectrum estimation because more complex models, like the halo-model (see e.g. Cooray & Sheth, 2002) mainly affect the small scales ($\lesssim 2$ Mpc/h). Such small scales are, for now, out of scope in this work.

In the next section we discuss the noise model required for a Bayesian reconstruction under the simple assumption of a Poissonian distribution making special effort in establishing the link to the mass-assignment problem.

5.1.3 Model assumptions for the shot noise of the galaxy distribution

The matter density is assumed to be fixed and known, and not subject to statistical uncertainties, since we are interested in reconstructing a single realization and sample the cosmic variance by performing many reconstructions. Note, that two essential sampling processes underly a galaxy distribution. The first is due to the variance of the gravitational field and the second is due to the discrete sampling process on top of that field (see appendix C.21 for a relation between both sampling process). Let us focus here on the latter process. Given the matter density, we further assume a Poissonian process to approximately describe galaxy formation.

The number of galaxies n_g within a Volume ΔV around position $\boldsymbol{r}$ is then distributed as

$$P(n_\mathrm{g}(\boldsymbol{r})|\lambda(\boldsymbol{r})) = \frac{\lambda(\boldsymbol{r})^{n_\mathrm{g}(\boldsymbol{r})}}{n_\mathrm{g}(\boldsymbol{r})!}\exp(-\lambda(\boldsymbol{r})), \tag{5.4}$$

where the expected number of galaxy counts is given by the Poissonian ensemble average: $\lambda(\boldsymbol{r}) = \langle n_\mathrm{g}(\boldsymbol{r})\rangle_{n_\mathrm{g}}$ (see eq. C.1 in appendix C.1) and is directly related to the expected galaxy density at that position: $\langle n_\mathrm{g}(\boldsymbol{r})\rangle_{n_\mathrm{g}} \equiv \Delta V \rho_\mathrm{g}(\boldsymbol{r})$ (with ΔV being a small volume).

The matter density is assumed to be known and not subject to a statistical distribution function for the calculation of the noise term, since we are interested in single reconstruction steps which will simulate cosmic variance by a data augmentation procedure (see section 5.3.2). We link this formalism to the theoretical ensemble averaged noise expression in appendix (C.21).

In addition, we have to consider the gridding of the discrete galaxy sample that permits us to use FFTs to compute other quantities like the density field, the gravitational potential, or the velocity field. The process of putting the galaxies on a regular grid is equivalent to a convolution in real-space followed by a grid-point selection step. The noise covariance-matrix that we derive under these considerations can be written as (see appendix C.2)

$$\boldsymbol{N}(\boldsymbol{r}_1, \boldsymbol{r}_2) = \frac{1}{\overline{n}^2}\,\Pi\big(\frac{\boldsymbol{r}_1}{H}\big)\Pi\big(\frac{\boldsymbol{r}_2}{H}\big)\int \mathrm{d}\boldsymbol{r}_1'\, W(\boldsymbol{r}_1 - \boldsymbol{r}_1')W(\boldsymbol{r}_2 - \boldsymbol{r}_1')\langle n_\mathrm{g}(\boldsymbol{r}_1')\rangle_{n_\mathrm{g}}, \tag{5.5}$$

with W being the gridding-kernel[1], and $\Pi(\boldsymbol{r}) \equiv \sum_{\boldsymbol{n}\in\mathbb{Z}}\delta_\mathrm{D}(\boldsymbol{r} - \boldsymbol{n})$ with H being the grid-spacing.

The noise term in the data model (eq. 2.2) that can be deduced from the noise covariance matrix is given by

$$\boldsymbol{\epsilon}(\boldsymbol{r}) = \frac{1}{\overline{n}}\,\Pi\big(\frac{\boldsymbol{r}}{H}\big)\int \mathrm{d}\boldsymbol{r}'\, W(\boldsymbol{r} - \boldsymbol{r}')\sqrt{\langle n_\mathrm{g}(\boldsymbol{r}')\rangle_{n_\mathrm{g}}}\,\chi(\boldsymbol{r}'), \tag{5.6}$$

with $\chi(\boldsymbol{r})$ being a stochastic white noise field with the following properties: $\langle\chi(\boldsymbol{r})\rangle = 0$ and $\langle\chi(\boldsymbol{r})\chi(\boldsymbol{r}')\rangle = \delta_\mathrm{D}(\boldsymbol{r} - \boldsymbol{r}')$. Note, that the noise has the form that we introduced in section (2.1.1) with a structure function multiplied by a random white noise term: $\epsilon(\boldsymbol{r}) = f_\mathrm{SF}(\boldsymbol{r})\epsilon_\mathrm{WN}(\boldsymbol{r})$, but additionally introduces the convolution produced by the grid-sorting scheme.

This modifies the noise term in the Wiener-filter (see section 2.5.3) and has not been taken into account in previous works. Our tests show that the pixelization scheme has an important effect on small scales when performing power-spectrum sampling (see section 5.3.2). Since, for now, we are focusing on different effects, we consider a simplified noise covariance-matrix of the form: $\boldsymbol{N} = \mathrm{diag}(\langle n_\mathrm{g}\rangle/\overline{n_\mathrm{g}}^2)$. Note, however, that the blurring effects of the pixelization are taken into account in the signal term, as we already showed in section (3.3). They are very critical, and need to be treated especially when dealing with low-resolution grids.

The noise covariance expression requires an estimate for the expected number of galaxies $\lambda_\mathrm{g} = \langle n_\mathrm{g}^g\rangle$, which so far we had assumed to be known. However, all we know with certainty is the number of galaxies observed. To guess λ_g, we propose to assume a flat prior for it and apply Bayes theorem (see appendix C.3) leading to: $\langle\lambda_\mathrm{g}^g\rangle = n_\mathrm{g}^g + 1$. This result is reasonable,

[1] Expressions for the different gridding kernels in Fourier-space are given in section (3.3).

grid	FFT-grid	n	resolution	time
32	64	$\sim 3 \cdot 10^4$	~ 12.8 Mpc/h	~ 30 s
64	128	$\sim 3 \cdot 10^5$	~ 6.4 Mpc/h	~ 1.5 min
128	256	$\sim 2 \cdot 10^6$	~ 3.2 Mpc/h	~ 20 min
256	512	$\sim 2 \cdot 10^7$	~ 1.6 Mpc/h	~ 1.5 hr

Table 5.1: Computing time for different resolutions. The physical box is on a grid with a number of cells in each side given by the first column. Zero-padding is performed to avoid aliasing effects. The FFTs work thus on a larger grid given in the second column. The dimension of the problem is given by the number of cells n in the third column. The matrices to be inverted are: $n \times n$ large. The corresponding resolution is given in the fourth column with a comoving box side-length of 410 Mpc/h. Finally, the computing time is given in the fifth column, which will vary depending on the structure of the mask. However, in cases when large regions were cut out, the convergence behavior did not change much, being less than two times slower in our worst test-case. The convergence criterion was defined by the square of the residuals $\boldsymbol{\xi}$ and had to fulfill: $|\boldsymbol{\xi}|^2 \equiv \sum_{i \in pix} |\xi_i|^2 < 10^{-7}$.

because it implies non-zero noise even in cells with no single galaxy count ($n^g = 0$), which could have resulted by chance or due to the limited observational sensitivity from an otherwise positive $\lambda_{\rm g}^g$. Thus, there is no need to assume artificial noise in those empty cells, which we would otherwise have to introduce to ensure numerical stability. Our noise expression $\boldsymbol{N} = \mathrm{diag}((n_{\rm g}^g + 1)/\overline{n_{\rm g}}^2)$ is therefore naturally derived from the assumption of a Poissonian model for the galaxy distribution.

5.2 Single Bayesian-reconstruction step

Here we investigate the quality and the efficiency of single reconstruction steps. We start presenting the mock galaxy survey that we use as input data and give a brief description of the assumed cosmology. Finally, we present results for reconstructions assuming a linear power-spectrum and reconstructions with a non-linear power-spectrum and an effective redshift-distortions treatment as is done in the literature.

5.2.1 Setup: input data and input cosmology

For our reconstruction studies we use the mock galaxy redshift catalogue provided by Blaizot (2007) that resembles the SDSS-survey[1] in many respects (selection function, sensitivity, etc.), however, the mock catalogue covers the whole sky (see Blaizot *et al.*, 2005, for a description of the method). This catalogue is extracted from the Millenium simulation (see Springel *et al.*, 2005). In this way a direct comparison to the *true* underlying dark matter distribution is possible (see figs. 5.3 and 5.11). Though the synthetic catalogue has been built on the interpolation of different snapshots for different redshift bins, we consider only the snapshot at redshift zero and the corresponding power-spectrum. This can be done due to the small redshift volume we

[1] Sloan Digital Sky Survey: www.sdss.org

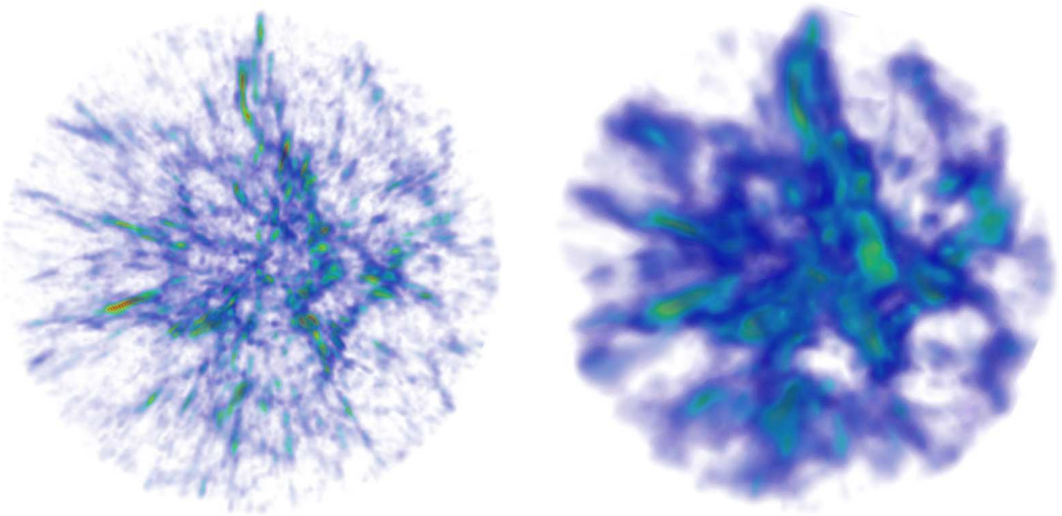

Figure 5.1: Projection of the 3D reconstructions with and without redshift-distortions treatment. On the left the reconstruction with a linear power spectrum is shown. On the right the reconstruction with a non-linear power-spectrum and an effective redshift-distortions treatment is represented.

use in this study. However, the redshift variation of the power-spectrum needs to be taken into account in studies with wide redshift ranges. This is the case for deep redshift surveys.

Here we take all the galaxies (744912 objects equally weighted) inside a sphere of a redshift $z \leq 0.05$ with their positions indicated by rectascension, declination and redshift. The box we consider has thus about 410 Mpc/h comoving length in each coordinate assuming a Hubble constant of $H_0 = 73$ km/Mpc/s in concordance with the Millenium run. The galaxies are then distributed onto a grid with the CIC-scheme (see section 3.3.2). We use two kind of power-spectra in our studies: either the Peacock & Dodds (1994) linear power spectrum and the BBKS transfer-function (see Bardeen *et al.*, 1986) or the Bond & Efstathiou (1984) transfer-function with the non-linear Smith *et al.* (2003) power-spectrum. The latter contains a quasi-linear term and a halo model term that reproduce very nicely the non-linear structure formation *bump* in the power-spectrum (see fig. 5.11). The cosmological parameters chosen are: $\Omega_{\rm m} = 0.3$, $\Omega_\Lambda = 0.7$, $\Gamma = 0.21$, $\sigma_8 = 0.9$, $\beta_{\rm p} = 1.5$, and $n_{\rm s} = 1.0$.

5.2.2 Wiener-reconstruction with a linear power-spectrum

We start with a Wiener-reconstruction using the linear power-spectrum given by Peacock & Dodds (1994) and the BBKS transfer-function (see Bardeen *et al.*, 1986). This power-spectrum is used in the expression for the Wiener-filter that we recall here

$$\langle \boldsymbol{s} \rangle_{\rm WF} = \langle \boldsymbol{s}\boldsymbol{d}^\dagger \rangle \langle \boldsymbol{d}\boldsymbol{d}^\dagger \rangle^{-1} \boldsymbol{d}, \tag{5.7}$$

see section (2.5.3).

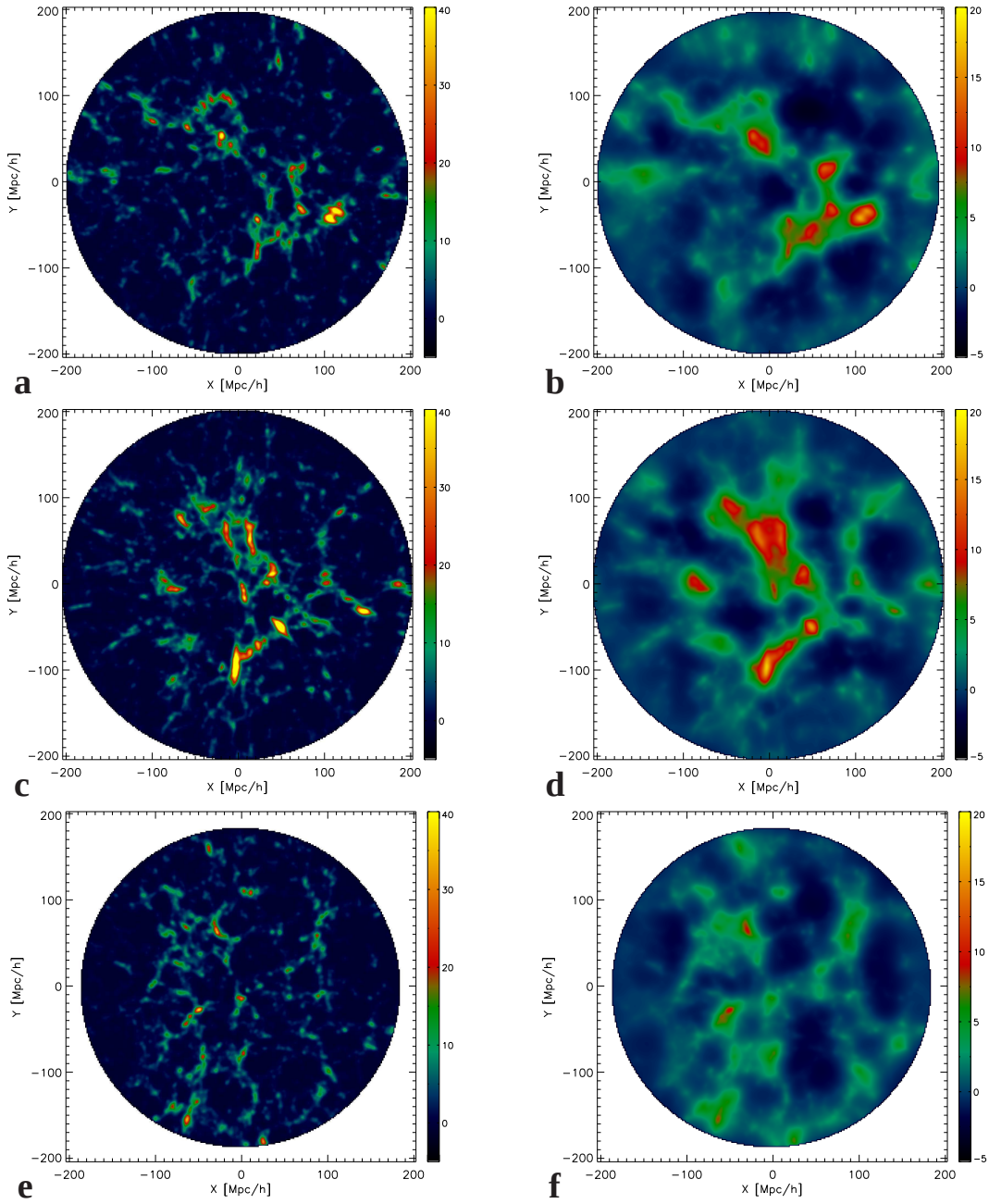

Figure 5.2: Slices through the reconstruction with and without effective redshift distortions treatment. On the lhs the reconstruction taking a linear power-spectrum without any redshift-distortions treatment is represented for the slices through the 256^3 box beginning from the top: 100 (panel **a**), 128 (panel **c**) and 180 (panel **e**), corresponding to slices at ~ -45 Mpc/h, ~ 0 Mpc/h, and ~ 80 Mpc/h in z-direction. On the rhs the reconstruction with an effective redshift-distortions correction treatment are shown for the same slices (panels **b**, **d**, and **f**). The slices have a thickness of about 1.6 Mpc/h.

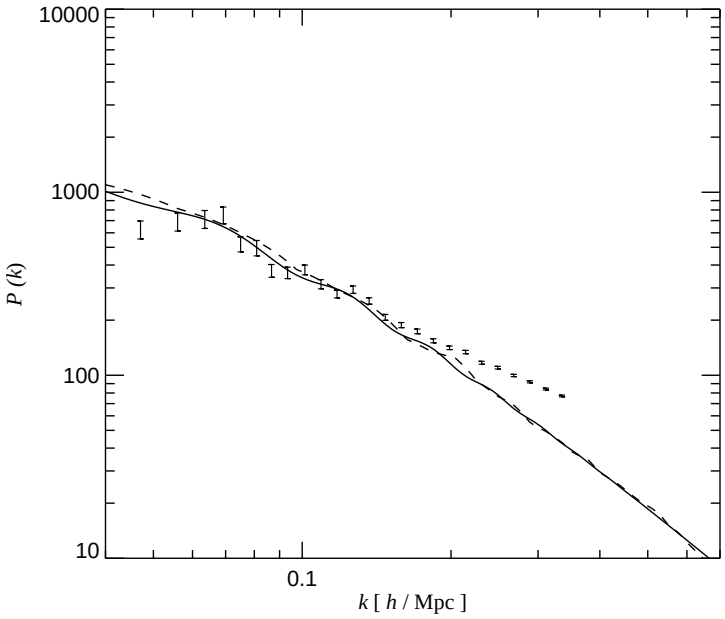

Figure 5.3: Measured power-spectrum from the linear reconstruction. The error bars indicate the power-spectrum measured from the Millenium run at redshift zero (see Springel *et al.*, 2005). The dark line represents the predicted power-spectrum at redshift zero from linear theory. The dashed line shows the power-spectrum measured from a reconstruction plus data augmentation step (see section 5.3.2) which themselves used a linear power-spectrum assumption. The volume of the reconstruction was normalized to the volume of the millenium run for a better comparison.

We perform reconstructions with grids of different resolutions and cell numbers (see table 5.1). For the case of a grid with 256^3 cells, which implies a resolution of ~ 1.6 Mpc/h side-length, the matrix we have to invert has a size of $\sim 10^7 \times 10^7$. Our Krylov-scheme permits us to perform such an inversion with a single processor in about 1.5 hours, requiring a RAM memory of only ~ 32 Mb due to the developed operator formalism, which does not express the matrices in an explicit way as described in section (3.3). Note, that former works, based on a singular value decomposition matrix inversion scheme were limited to $\sim 10^4$ cells, while using days/weeks of super-computing facilities.

The resulting over-density distribution can be seen in figs. (5.1) and (5.2). The measured power-spectrum from the reconstruction is plotted in fig. (5.3) (dashed line) and shows a remarkably good agreement with the linear theory prediction (black line), but does not follow the non-linear *bump*.

The projected three-dimensional distribution represented in the left panel of fig. (5.1) clearly shows an elongation of the structures along the line-of-sight due to the virialization of structures. Nevertheless, another imperceptible effect to the eye is present, which acts on large scales. It is a slight radial compression of extended structures due to the large-scale galaxy motions caused by the linear regime of structure formation in which the galaxies tend to fall

towards deeper gravitational potentials.

Before we introduce our new frame-work of redshift-distortions correction via Bayesian sampling, let us discuss in the next section how to effectively treat these effects as it is done so far as described in the literature of Wiener-reconstructions (see table 2.1).

5.2.3 Effective redshift-distortions treatment

The Wiener-filter can be expressed in such a way that it also transforms the data from redshift-space into the reconstructed signal in real-space. The corresponding expression given by Zaroubi *et al.* (1995) is

$$\langle s(\boldsymbol{r})\rangle_{\mathrm{WF}} = \langle s(\boldsymbol{r})d^{\dagger}(\boldsymbol{z})\rangle\langle d(\boldsymbol{z})d^{\dagger}(\boldsymbol{z})\rangle^{-1}d(\boldsymbol{z}). \tag{5.8}$$

The non-linear power spectrum in redshift-space can be expressed as the non-linear power-spectrum in real-space multiplied by some correction factors that depend on the mode k and the direction $\mu = \cos(\boldsymbol{k}\cdot\boldsymbol{r})$

$$P^{z}_{\mathrm{NL}}(k,\mu) = P^{r}_{\mathrm{NL}}(k,\mu)K(\mu)D(k,\mu), \tag{5.9}$$

being $K(\mu) = (1+\beta\mu^2)^2$ the so-called linear Kaiser-factor and $D(k,\mu) = 1/1+(k^2\sigma_{\mathrm{p}}^2\mu^2)/2$ the non-linear Lorentzian factor. The redshift-distortion parameter is defined here as: $\beta \equiv \Omega_{\mathrm{m}}^{0.6}/b$[1], where we used $\Omega_{\mathrm{m}} = 0.3$, $b = 1.0$ and the dispersion $\sigma_{\mathrm{p}} = 506$ km/s/H_0 according to Hawkins *et al.* (2003). The linear Kaiser-factor can be derived from linear perturbation theory (Kaiser, 1987). The Lorentzian factor is the Fourier-transform of the exponential distribution for the velocities and was introduced by Ballinger *et al.* (1996). Erdoğdu *et al.* (2004) suggest taking the angular-averaged correlation matrices in eq. (5.8) (see section D.1).

Our results after applying this estimation procedure with the non-linear Smith *et al.* (2003) and the Bond & Efstathiou (1984) transfer-function are represented on the right-hand-side (rhs) of figs. (5.1) and (5.2). The reconstructed density fields turn out to be strongly smoothed. The Lorentzian factor that appears twice —in the data autocorrelation matrix and in the signal to data correlation matrix— damps the power at scales: $k \lesssim 0.3$ h Mpc^{-1} (see fig. 11 in Erdoğdu *et al.*, 2004). The approximation of averaging over all angles and assuming the same dispersion velocity for all clusters is obviously very crude. However, this treatment tells us at which scales the non-linear effects become negligible. The method itself does not correct the effects caused by the non-linear redshift-distortions. A closer comparison of the reconstruction with and without the effective redshift-distortions treatment shows the degree of information that is lost. The plots in the left-hand-side (lhs) of fig. (5.2) clearly show the filamentary structure, whereas they appear to be completely washed out in the plots on the rhs, due to the effective correction.

A Bayesian approach finding a solution to this problem demands a joint estimation of the density field and the peculiar velocity field. This will be discussed in the next section.

[1] β is in general the linear growth rate at the present day (f_0) divided by the bias factor b: $\beta \equiv f_0/b$.

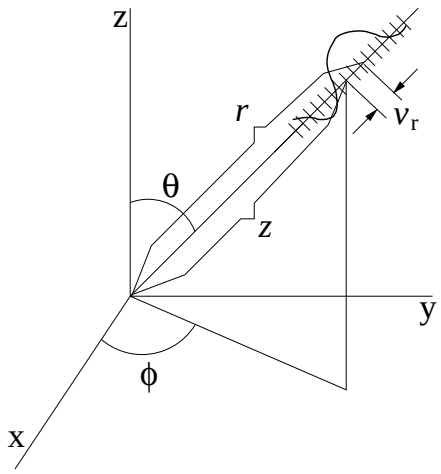

Figure 5.4: Geometric illustration of the redshift distortion and the velocity sampling scheme. Each galaxy is treated independently along its line-of-sight, sampling the velocity for different guess positions.

5.3 Bayesian-sampling methods

In this section, we describe methods to sample the joint space of the signal and its parameters with MCMC techniques. In particular, we develop methods to sample the density field together with the velocity field and the density field together with the power-spectrum. Some preliminary results are shown in which the redshift-distortions are corrected by sampling of the velocity field. In these tests the density field is corrected iteratively by sampling new guess positions for the real-space distribution. In the final section of this chapter we present the different methods used to sample the signal, even with non-Gaussian distributions, together with its power-spectrum in a Gibbs-sampling process. We show the first successful results using ARGO-code together with the inverse-Gamma function sampling module implemented by Jasche (2007). The obtained results are very promising and show the overall validity of the Bayesian approach, but should be regarded more qualitatively rather than quantitatively, and should be further analyzed in future works.

5.3.1 Joint signal and peculiar velocities estimation: redshift-distortions correction

We propose to sample the peculiar velocities in a MCMC fashion (see section 2.6), analogous to the case of the power-spectrum (see Wandelt *et al.* (2004) and section 5.3.2). We draw realizations of the matter field given the data, a power-spectrum and assumed galaxy peculiar velocities

$$\boldsymbol{s}^{(j+1)} \sim P(\boldsymbol{s} \mid \boldsymbol{v}^{(j)}, \boldsymbol{S}, \boldsymbol{d}). \tag{5.10}$$

The velocities are subsequently sampled too:

$$\boldsymbol{v}^{(j+1)} \sim P(\boldsymbol{v} \mid \boldsymbol{s}^{(j+1)}). \tag{5.11}$$

In each step where we sample the peculiar velocity, the redshift-distortion can be corrected using eq. (5.1)

$$r^{(j+1)} = z - v_r^{(j+1)} \tag{5.12}$$

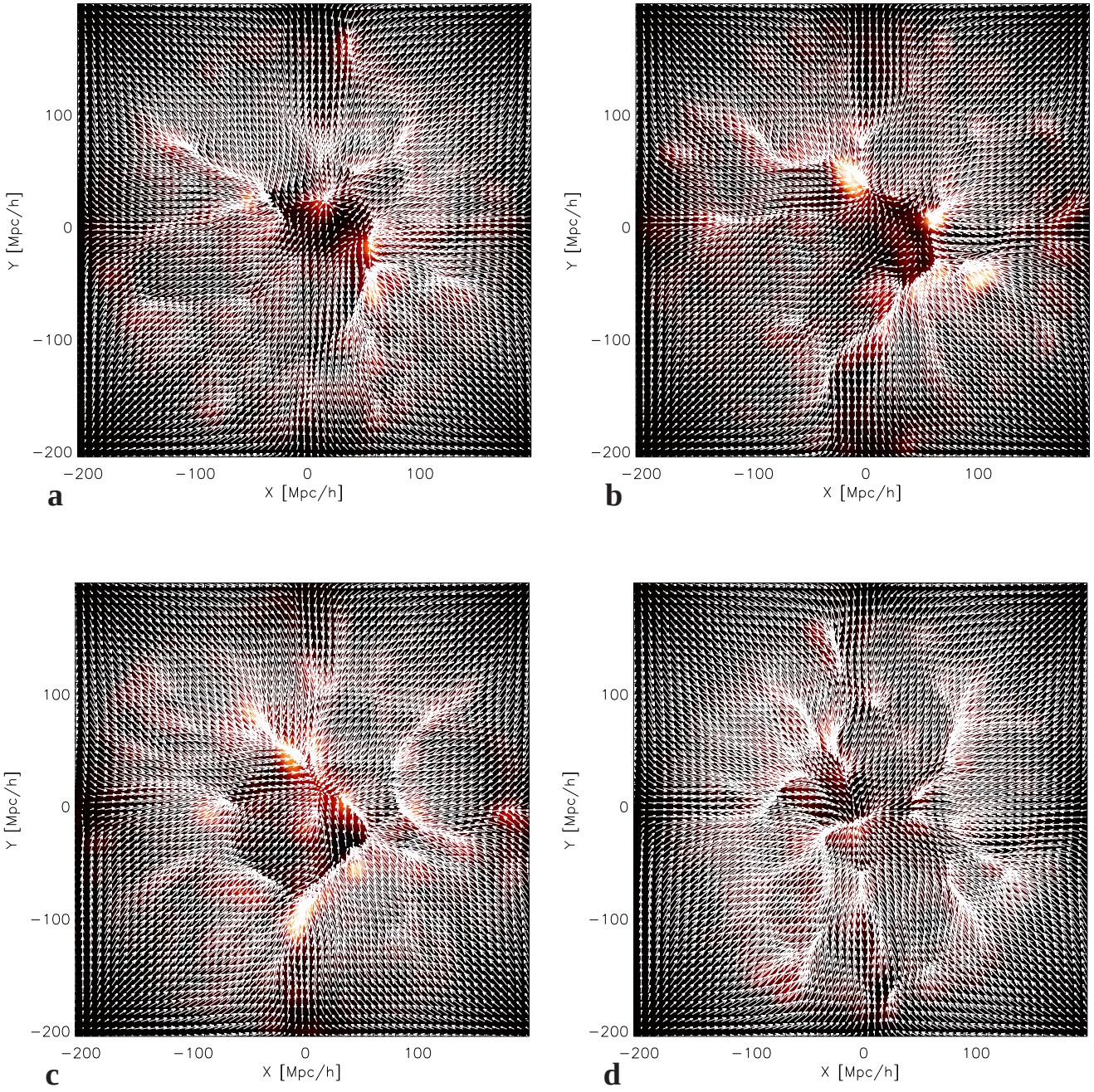

Figure 5.5: Slices through the reconstruction with the projected linear vector field. The effect of the empty corners can be seen here. Slices through the 64^3 box beginning from the top: 20 (panel **a**), 25 (panel **b**), 32(panel **c**), and 45(panel **d**) corresponding to slices at ~ -77 Mpc/h, ~ -45 Mpc/h, ~ 0 Mpc/h, and ~ 80 Mpc/h in z-direction. The slices have a thickness of about 6.4 Mpc/h.

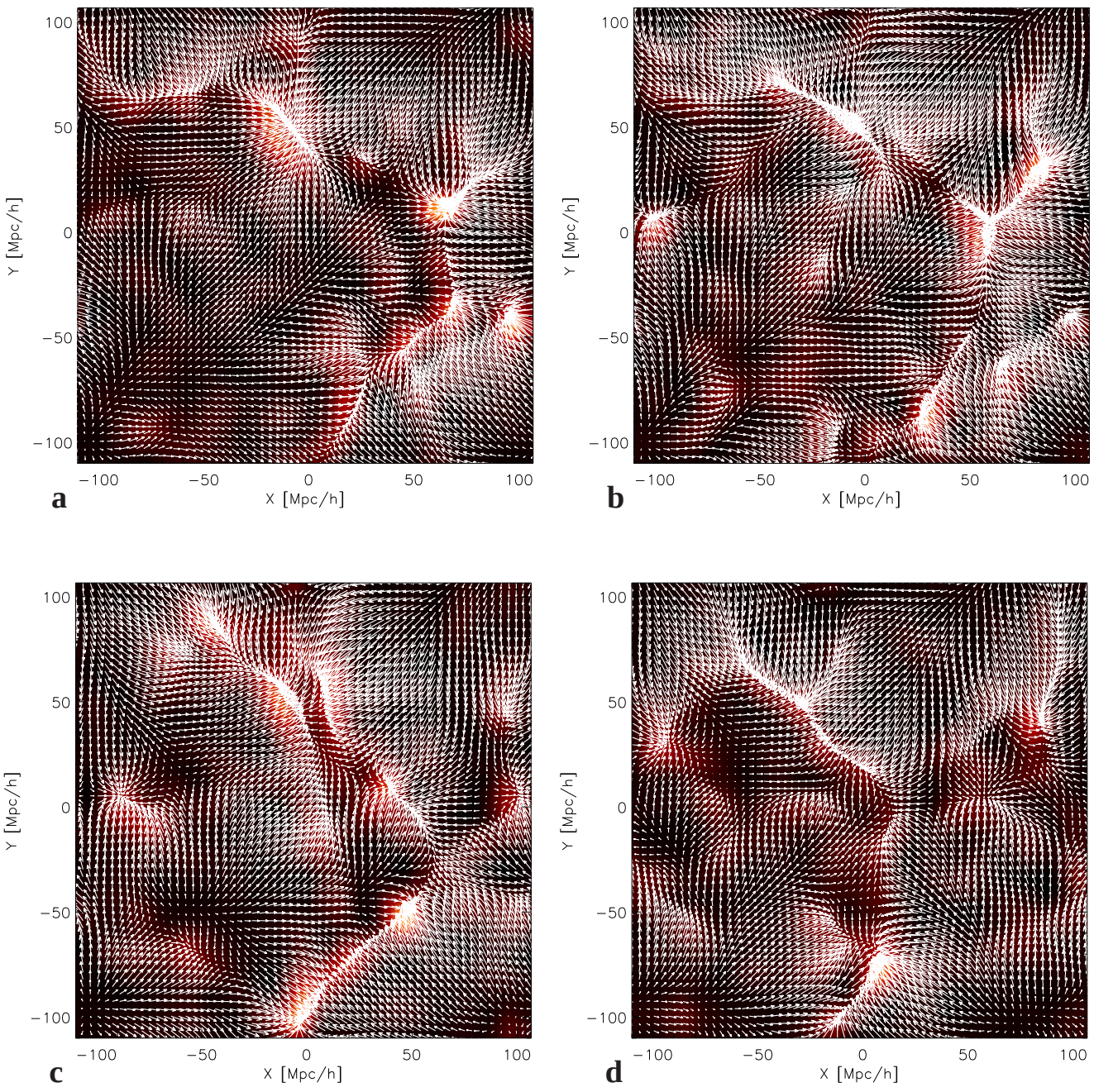

Figure 5.6: Slices through the reconstruction with the projected linear vector field. The periodic boundary condition can be seen here. Slices through the 64^3 box beginning from the top: 20 (panel **a**), 25 (panel **b**), 32(panel **c**), and 45(panel **d**) corresponding to slices at ~ -41 Mpc/h, ~ -24 Mpc/h, ~ 0 Mpc/h, and ~ 45 Mpc/h in z-direction. The slices have a thickness of about 3.4 Mpc/h.

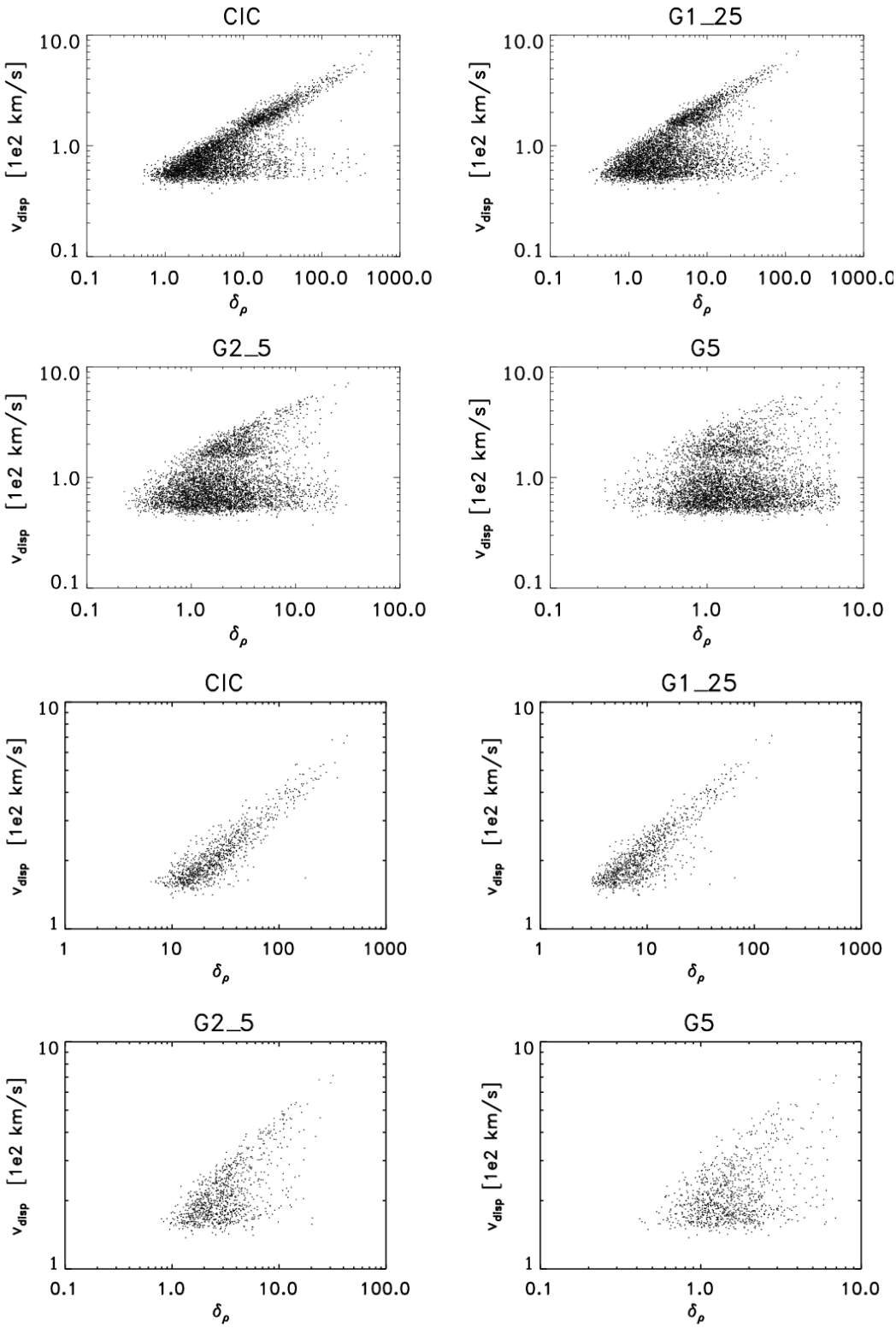

Figure 5.7: Velocity dispersion in the SDSS mock halos for cells with a given overdensity containing more than 200 particles (top) and for more than 1000 particles (bottom) of the Millenium simulation at different resolutions. The velocity dispersion-density correlation visible in this plot is used for the correction of the finger-of-god effect.

We propose to sample the peculiar velocities from a PDF with a mean $\langle v \rangle_{\rm M}$ given by the linear theory $\boldsymbol{v}_{\rm LT}$ and a velocity dispersion σ_v depending on the local value of the over-density,

$$P(\boldsymbol{v} \mid \boldsymbol{s}^{(j)}) \propto G\left(\boldsymbol{v} - \langle \boldsymbol{v} \rangle_{\rm M}(\boldsymbol{s}^{(j)}), \sigma_v^2(\boldsymbol{s}^{(j)})\right), \tag{5.13}$$

where we take a Gaussian distribution in our studies, but this could be extended to other PDFs. We use a power-law to sample the dispersion velocity taken from simulations as described in the next section.

Velocity dispersion as a function of the over-density

In order to study the physical relationship between the density field and the velocity dispersion we look at correlations in numerical simulations. Figure (5.7) shows the velocity dispersion in the SDSS mock halos for cells with a given DM over-density from the Millenium run. The over-density in the cells was calculated by the CIC mass-assignment scheme for the DM particles (see panel a in fig.5.7). Only cells with more than 200 particles where chosen in the upper panel. The velocity dispersion distribution after convolving the density field with a Gaussian of: 1.25 Mpc/h (G1_25), 2.5 Mpc/h (G2_5), and 5 Mpc/h (G5) are also plotted. This shows that the non-linear velocity sampling must be calibrated in differently depending on the chosen resolution; it obviously gets worse with lower resolution. Our queries in the GAVO virtual observatory[1] showed that the nature of the velocity dispersion is bimodal. Looking for the relationship by taking cells with more than 1000 particles (see lower panel) shows a strong power-law behavior with a slope in the logarithmic plot of ~ 0.4 and describes the internal structure of halos with many galaxies. The slope is close to the theoretically expected value of 0.5 that is derived by solving for the velocity assuming the virial theorem relation. The weaker slope is consistent with the fact that the cosmic structures are in general not fully virialized.

The other distribution shows a constant relation for the velocity dispersion at any value for the over-density. This describes halos with just one very massive galaxy. Here, the internal dispersion of the halos does not make sense, but rather the dispersion of the halos themselves. We will assume that these halos move with a velocity dispersion given by the power-law of the more populated halos. In conclusion, we have found a power-law that describes the internal structure of halos with many galaxies.

We use this relationship to sample all the galaxies in high-density regions in each iteration. The bulk flow motion should also be corrected with linear theory. However, the current status of our investigation does not permit us to include these corrections due to several problems that we discuss below. Solutions to these problems are outlined, which require calibration with mock galaxy catalogues. An alternative detailed-balance rejection sampling algorithm was developed in collaboration with Enßlin (2007) and is presented in appendix (D.2). We also present some successful reconstructions in which the non-linear effects were corrected by a velocity sampling scheme described below.

[1] www.g-vo.org

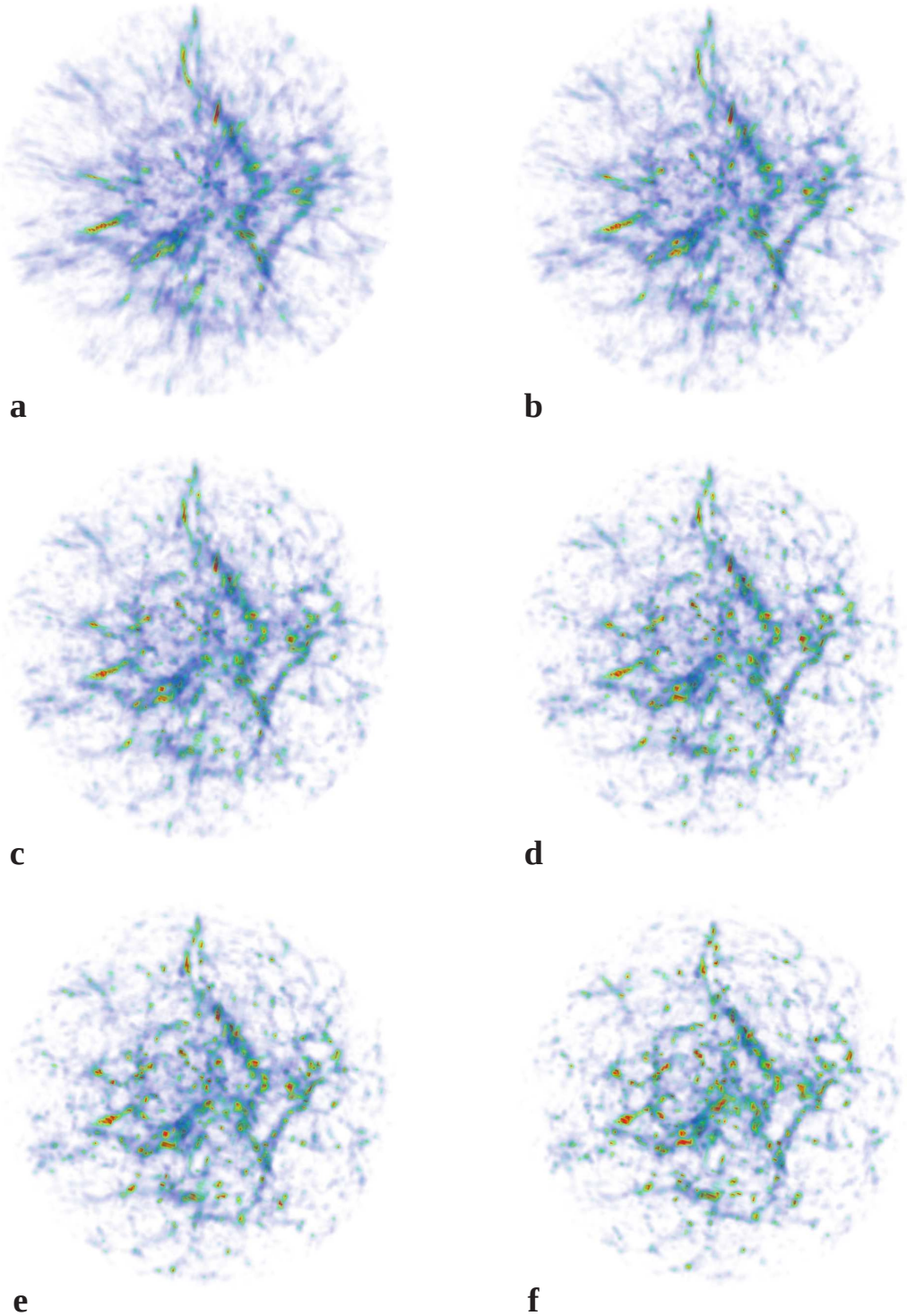

Figure 5.8: Joint signal and velocity reconstruction. We show here the successive projections of the 3D reconstructions for the full-sky SDSS-mock galaxy catalogue with redshift-distortions correction. The peculiar velocities of each galaxy are sampled in each iteration. Panel **a** shows the first iteration, and panels **b**, **c**, **d**, **e**, and **f** after 5, 10, 15, 20, and 30 iterations, respectively.

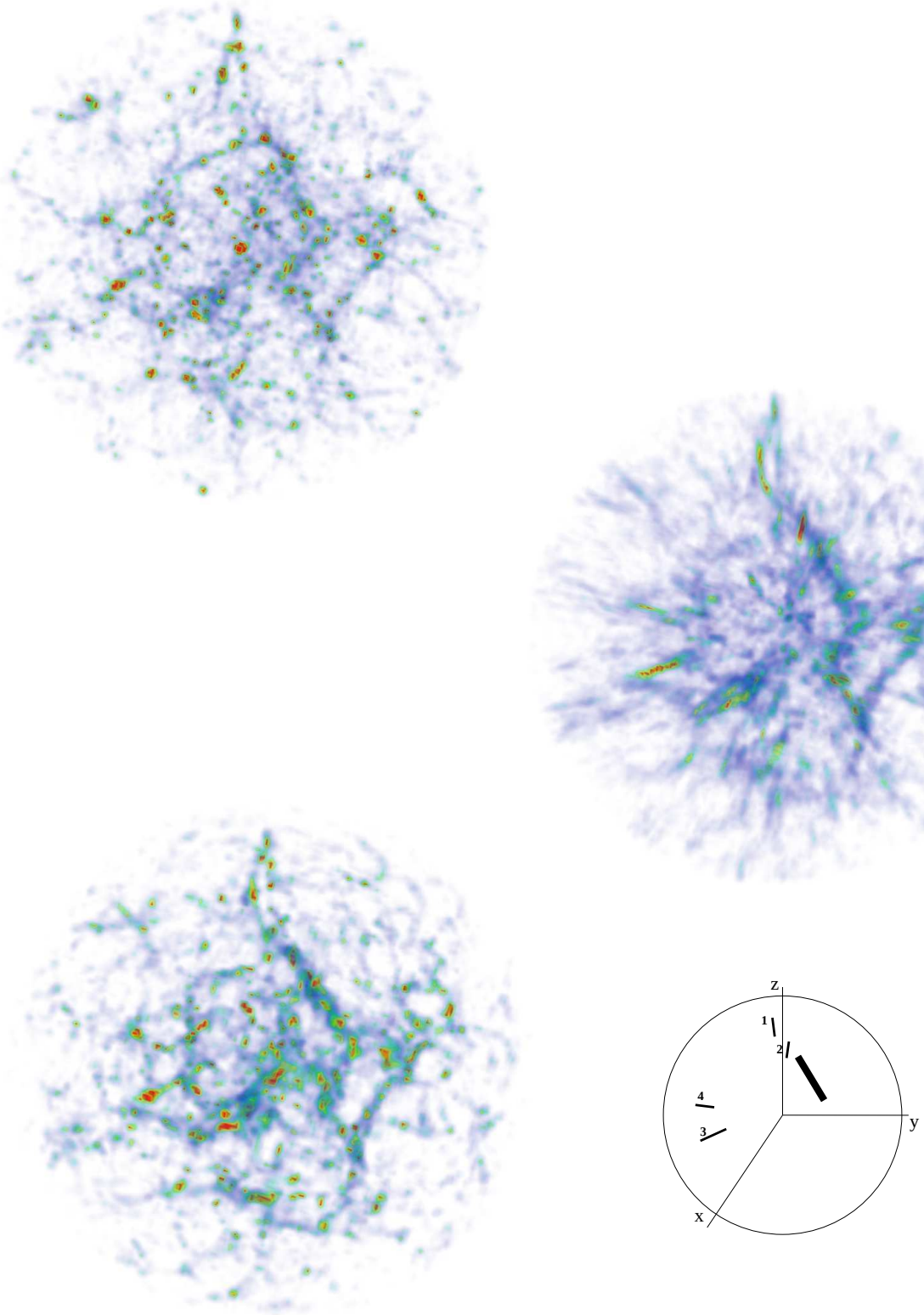

Figure 5.9: Projected 3D reconstructions. **Top:** reconstruction of the density field for the galaxy distribution in real-space without redshift distortions. **Middle:** reconstruction based on the simulated observed galaxy redshift distribution without correcting for the distortions. **Bottom:** Statistically corrected redshift distribution with velocity sampling after 30 iterations. At the bottom on the right we signalize in a scheme some of the most prominent feautures in the reconstructions: four *finger-of-gods* and a *great wall*.

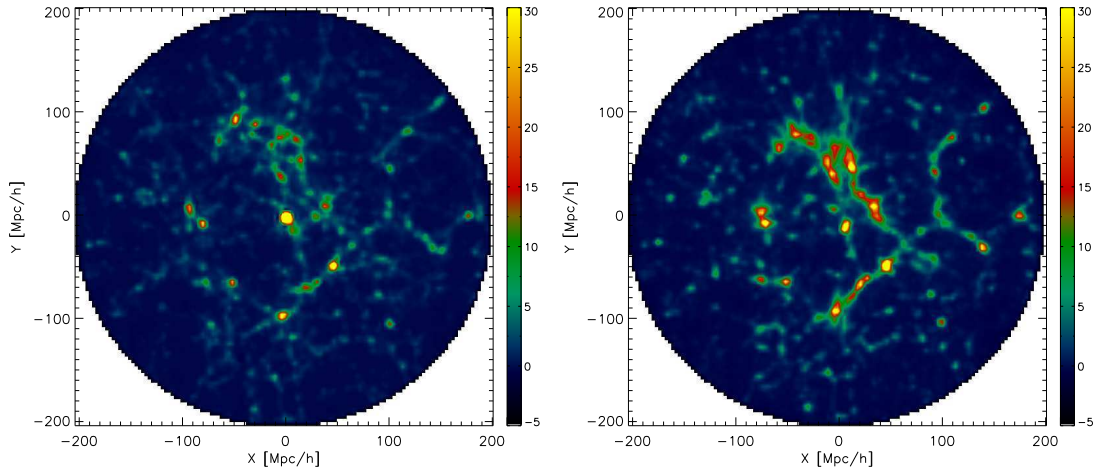

Figure 5.10: Slice through the middle of the reconstructed sphere for a galaxy distribution, which was given in real-space on the left side and for a reconstruction based on a redshift distribution with our redshift-distortions correction sampling scheme on the right side. The slices have a thickness of about 3.2 Mpc/h.

Velocity sampling tests

Let us start with the velocity field in the linear regime. We show in figure (5.5) different slices of a reconstruction with a 64^3 box using the same input data as in the rest of the tests. Over-plotted are the linear velocity fields represented by white arrows. The cosmic flow clearly shows the conglomeration of structures at the right positions when compared to the color-coded over-density. However, it also shows two artificial effects. The first consists in an overestimation of the velocities (by inspection of the values) at high-density regions. This problem can be solved by convolving the reconstructed density field until maximal over-density values of ~ 1. Another approach is to damp the linear velocity term with increasing over-densities. All these methods require further investigation and calibration with numerical simulations. The second artificial effect that we can see in fig. (5.5) is caused by embedding the sphere in a box. The unobserved regions (in the corners of the box) act as empty spaces from which virtual matter flows towards the observed region (see arrows). One way to solve this problem consists of reducing the sample until it fits in a box (see fig. 5.6). This brute force method, however, has the drawback of throwing information away. Moreover, it does not solve the periodic boundary condition which is assumed when using FFTs. One way out of this problem is to sample the cosmic variance in the observed and unobserved regions as we show in the next section with power spectrum estimation. We find our tests, in agreement with Eriksen *et al.* (2004), —for applications in CMB reconstructions— that the cosmic variance is very low in the observed patches (due to missing information) and increases to the large-scale structure fluctuations in the unobserved regions, where basically no information is available. These fluctuating structures compensate the empty spaces and converge statistically to the correct distributions (see section 5.3.2).

Let us ignore the velocity distortions in the linear regime and try to solve the elongation

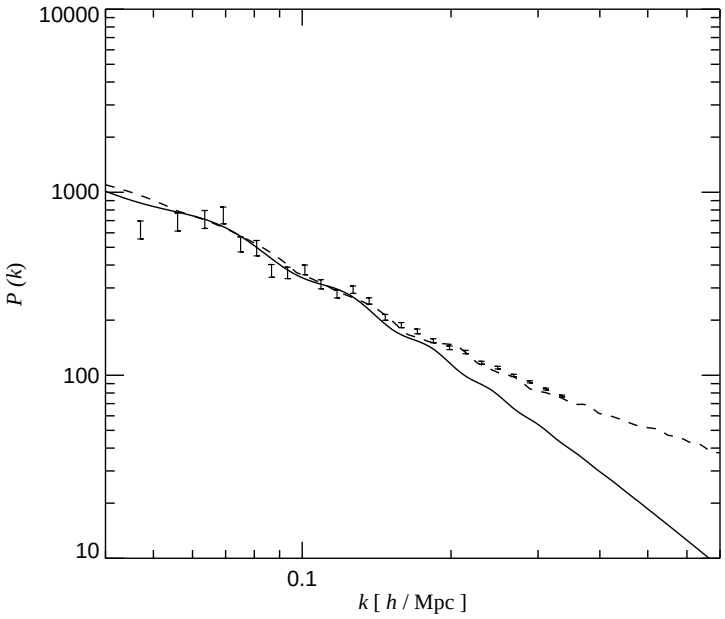

Figure 5.11: Measured power-spectrum from the non-linear reconstruction with data-augmentation. The error bars indicate the power-spectrum measured from the Millenium run at redshift zero (see Springel *et al.*, 2005). The dark line represents the predicted power-spectrum at redshift zero from linear theory. The dashed line shows the power-spectrum of the reconstructed density field, where the reconstruction and augmentation steps were done assuming a non-linear power-spectrum. The volume of the reconstruction was normalized to the volume of the millenium run for a better comparison.

of structures along the line-of-sight. We describe now a partial treatment of the redshift-distortions that affects only structures in high-density regions, which we define as those regions with $\delta > 1$.In our first reconstruction we ignore any correction for the galaxy positions. The following procedure is then iterated until convergence.

The over-density at each galaxy position is interpolated from the reconstruction at the previous iteration. If the over-density is lower than one we skip to the next galaxy, otherwise we proceed. The measured radial position z for the galaxy is taken and its surrounding space is subdivided in cells along the line-of-sight, which are taken as guess positions (see fig. 5.4). Then the over-density at each guess position is interpolated from the reconstruction at the previous iteration. The non-linear contribution is now sampled with a dispersion according to the local over-density for each guess position (see previous section). The velocity is projected along the line-of-sight leading to v_r. This is done for all guesses. Finally, the best guess which minimizes $(r^{\rm guess} + v_r^{\rm guess}) - z$ is taken as true and the new position is evaluated $r^{j+1} = z - v_r^{\rm guess}$. If the new position falls outside the region determined by the cluster then the step is rejected and the whole procedure is repeated again. Note, that the region of the cluster is updated in each iteration. We performed several tests with different definitions of the cluster extension. In the first test, we defined the cluster radius, as the radius given in transversal direction. In the

second test, we defined the cluster extension by looking at the cells in which the over-density is above some threshold. The second definition turned out to be more stable. However, more tests are planned, in which gradients of the density field will eventually be used to determine the cluster region. Once all the galaxies have gone through this scheme, the next reconstruction is performed.

Projections of the reconstructions at different iterations are shown in fig. (5.8). One can see how the elongated structures collapse with the successive reconstructions. Fig. (5.9) shows a comparison between the reconstruction with the galaxy distribution in real-space and in redshift-space. We identify four clearly elongated clusters: two are close to the equator on the lhs of the projection of the sphere and the other two are located close to the polar axis in the northern hemisphere (see scheme in fig. 5.9). Our algorithm manages to collapse those structures in reasonable agreement with the real-space distribution. Also the *great wall* equivalent in this mock data-set becomes sharp. Fig. (5.10) shows a slice through the middle of the reconstructed sphere for the galaxy distribution in real-space and in redshift-space with our redshift-distortions correction scheme. The anisotropic features have disappeared with respect to the plot in fig. (5.2). Some of the elongated clusters have collapsed and others have been divided into several clusters. Finally, the reconstructions using the non-linear Smith *et al.* (2003) power-spectrum show extremely good agreement with the Millenium simulation. Even the first acoustic oscillation peak seems to be resolved. However, one should be careful with these results and sample over the power-spectra to give error estimates. A novel method to sample the joint distribution of the density field and the power-spectrum for the LSS has been developed in collaboration with Jens Jasche, Benjamin Wandelt, Jeremy Blaizot, and Torsten Enßlin. Below we present the basic Gibbs-sampling scheme and some preliminary results.

5.3.2 Joint signal and power-spectrum estimation: sampling the cosmic variance with data augmentation

Now, we want to sample from the joint PDF of the density signal $\boldsymbol{s}$ and its power-spectrum $P(\boldsymbol{s}, \boldsymbol{S}|\boldsymbol{d})$. The following Gibbs-sampling process is iterated until the chain *burns-in*

$$\boldsymbol{s}^{(j+1)} \sim P(\boldsymbol{s} \mid \boldsymbol{S}^{(j)}, \boldsymbol{d}), \tag{5.14}$$

$$\boldsymbol{S}^{(j+1)} \sim P(\boldsymbol{S} \mid \boldsymbol{s}^{(j+1)}). \tag{5.15}$$

The DM signal is sampled with the following PDF (see section 2.5.2)

$$P(\boldsymbol{s} \mid \boldsymbol{S}^{(j)}, \boldsymbol{d}) \propto G\left(\boldsymbol{s} - \boldsymbol{F}_{\rm WF}(\boldsymbol{S}^{(j)})\boldsymbol{d}, \boldsymbol{\sigma}^2_{\rm WF}(\boldsymbol{S}^{(j)})\right). \tag{5.16}$$

The Wiener reconstruction is known to give a biased estimator, which attenuates the power especially for the modes where the noise becomes important, as discussed in section (2.5.3). This filtering effect has to be compensated by adding a fluctuating term with statistics according to the correct covariance (see Wandelt *et al.*, 2004)

$$\boldsymbol{s}^{(j)} = \langle \boldsymbol{s}^{(j)} \rangle_{\rm WF} + \boldsymbol{y}^{(j)}_{\sigma_{\rm WF}}. \tag{5.17}$$

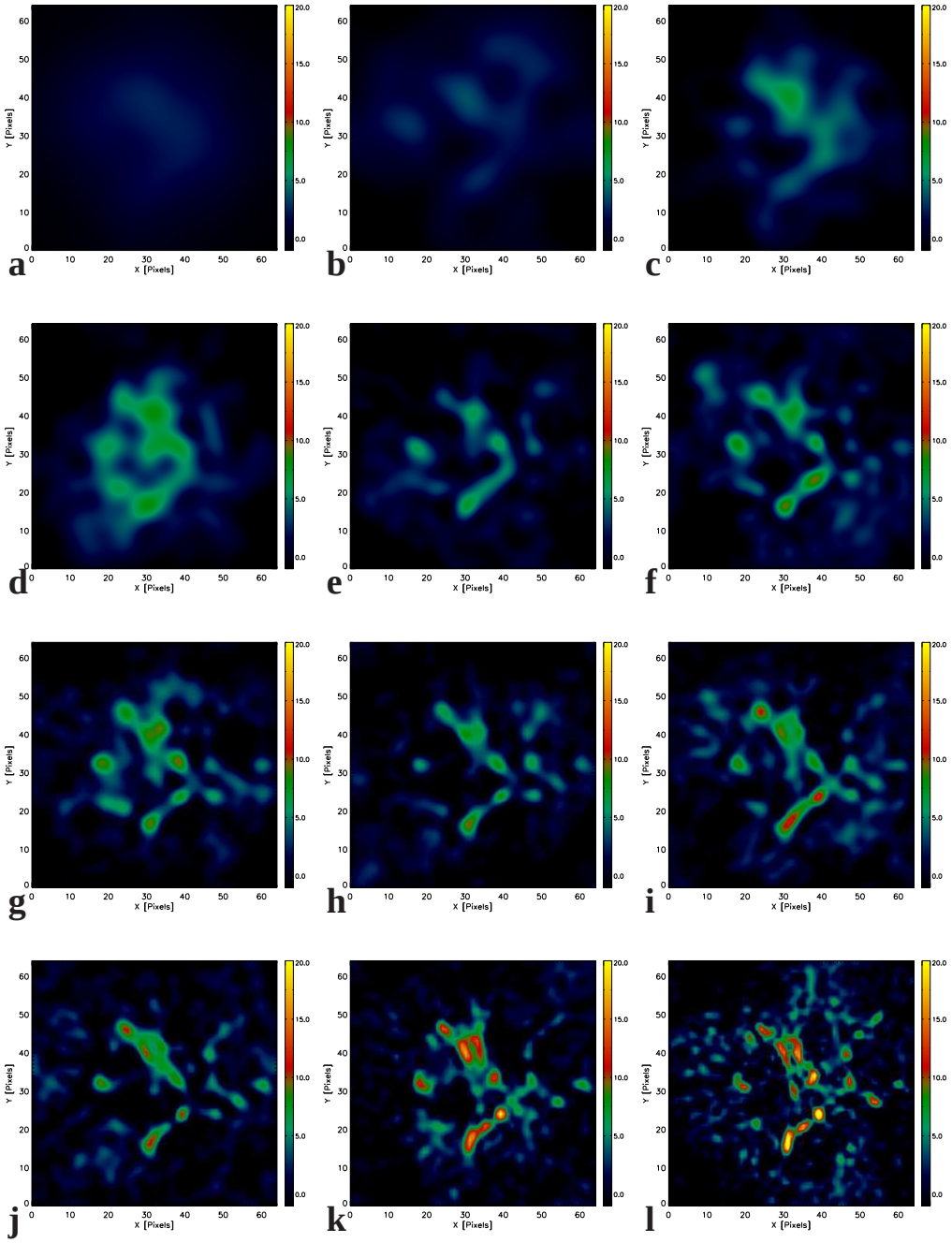

Figure 5.12: Joint signal and power-spectrum reconstruction. We show here the succesive reconstructions of the full-sky SDSS-mock galaxy catalogue. Starting with the first Gibbs-sampling iteration (panel **a**). Also plotted are the iterations: 2, 3, 4, 5, 6, 7, 8, 9, 10, 15, and 30 in panels **b**, **c**, **d**, **e**, **f**, **g**, **h**, **i**, **j**, **k**, and **l**, respectively. These reconstructions correspond to the power-spectra shown in fig. (5.13). The slices have a thickness of about 6.4 Mpc/h.

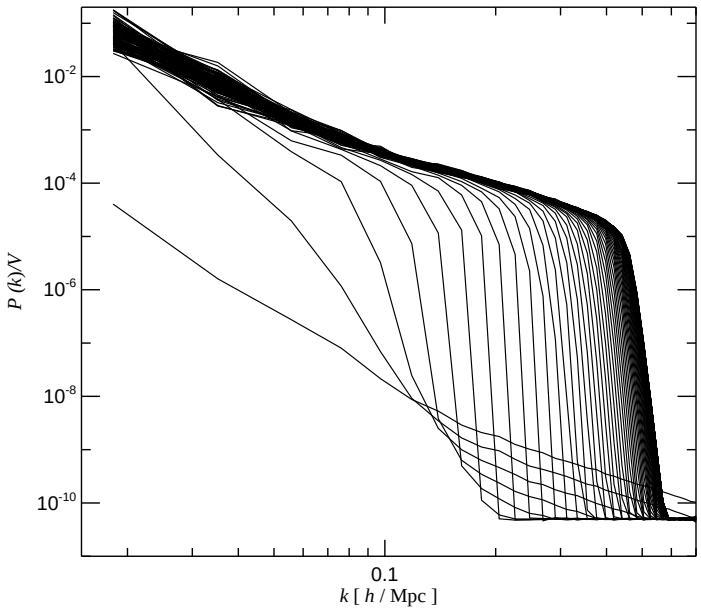

Figure 5.13: Succesive power-spectra for different Gibbs-sampling iterations corresponding to the reconstructions shown in fig. (5.12). The first power-spectrum was assumed to be underestimated by 5 orders of magnitude on purpose, to demonstrate the robust convergence process. The power-spectra grow first at low k-modes and then succesively at higher modes.

To generate the data augmentation $\boldsymbol{y}^{(j)}_{\sigma_{\rm WF}}$ one has to solve the following set of equations (see Eriksen *et al.*, 2007)

$$\boldsymbol{y}^{(j)}_{\sigma_{\rm WF}} = \Big((\boldsymbol{S}^{(j)})^{-1} + \boldsymbol{R}^\dagger \boldsymbol{N}^{-1} \boldsymbol{R} \Big)^{-1} \Big((\boldsymbol{S}^{(j)})^{-1/2} \boldsymbol{x}_{\rm G_1} + \boldsymbol{R}^\dagger \boldsymbol{N}^{-1/2} \boldsymbol{x}_{\rm G_2} \Big), \tag{5.18}$$

where $x_{\rm G_1}$ and $x_{\rm G_2}$ are two independent Gaussian variates. One can show by direct calculation that $\boldsymbol{y}^{(j)}_{\sigma_{\rm WF}}$ has a covariance given by $\boldsymbol{\sigma}^2_{\rm WF}$. To stabilize the inversion Eriksen *et al.* (2007) suggest using the following expression derived from the previous one by factorizing the square-root of the power-spectrum

$$\boldsymbol{y}^{(j)}_{\sigma_{\rm WF}} = (\boldsymbol{S}^{(j)})^{1/2} \Big(\boldsymbol{1} + (\boldsymbol{S}^{(j)})^{1/2} \boldsymbol{R}^\dagger \boldsymbol{N}^{-1} \boldsymbol{R} (\boldsymbol{S}^{(j)})^{1/2} \Big)^{-1} \Big(\boldsymbol{x}_{\rm G_1} + (\boldsymbol{S}^{(j)})^{1/2} \boldsymbol{R}^\dagger \boldsymbol{N}^{-1/2} \boldsymbol{x}_{\rm G_2} \Big). \tag{5.19}$$

Accordingly, the reconstruction step can be done by solving the following set of equations based on the inverse representation of the Wiener-filter (eq 2.21)

$$\boldsymbol{s}^{(j)}_{\rm WF} = (\boldsymbol{S}^{(j)})^{1/2} \Big(\boldsymbol{1} + (\boldsymbol{S}^{(j)})^{1/2} \boldsymbol{R}^\dagger \boldsymbol{N}^{-1} \boldsymbol{R} (\boldsymbol{S}^{(j)})^{1/2} \Big)^{-1} (\boldsymbol{S}^{(j)})^{1/2} \boldsymbol{R}^\dagger \boldsymbol{N}^{-1} \boldsymbol{d}. \tag{5.20}$$

This allows to perform the inversion for the fluctuating term and for the reconstruction in one step. An alternative way, permits us to use the direct representation of the Wiener-filter[1] by

[1]Note, that the direct representation for the covariance (eq. A.20) is not appropriate, due to the inverse of the response operator (see appendix A.3).

generating the fluctuations with a constrained realization (see Bertschinger, 1987; Ganon & Hoffman, 1993; Hoffman & Ribak, 1991)

$$\boldsymbol{y}^{(j)}_{\sigma_{\rm WF}} = \tilde{\boldsymbol{s}}^{(j)} - \boldsymbol{F}_{\rm WF}\tilde{\boldsymbol{d}}^{(j)}, \tag{5.21}$$

using two auxiliary Gaussian random fields $\tilde{s}$ and $\tilde{\epsilon}$ with zero mean and correlation $\langle\tilde{\boldsymbol{s}}\tilde{\boldsymbol{s}}^\dagger\rangle = \boldsymbol{S}$ and $\langle\tilde{\boldsymbol{\epsilon}}\tilde{\boldsymbol{\epsilon}}^\dagger\rangle = \boldsymbol{N}$ respectively. Further we set $\tilde{\boldsymbol{d}} = \boldsymbol{R}\tilde{\boldsymbol{s}} + \tilde{\boldsymbol{\epsilon}}$. This method has the advantage that non-linear reconstructions can be obtained with N-body simulations[1] (see Bistolas & Hoffman, 1998). It can be shown that the term in eq. (5.21) has the appropriate Wiener covariance (see appendix A.4). Each reconstruction step can then be done in one step with the direct Wiener representation by solving the following equations

$$\boldsymbol{s}^{(j)} = \tilde{\boldsymbol{s}}^{(j)} + \boldsymbol{F}_{\rm WF}(\boldsymbol{d} - \tilde{\boldsymbol{d}}^{(j)}). \tag{5.22}$$

The power-spectrum can be sampled by an inverse gamma function, which we derive here for the case of the 3D power-spectrum (see Wandelt *et al.*, 2004, for the analogous CMB case)

$$P(\boldsymbol{S} \mid \boldsymbol{s}) \propto P(\boldsymbol{S})P(\boldsymbol{s} \mid \boldsymbol{S}). \tag{5.23}$$

Assuming a Gaussian signal $\boldsymbol{s}$ (see eq. 2.19) this yields

$$P(P_{\rm S}(\boldsymbol{k}) \mid \boldsymbol{s}^{(j)}) \propto P(P_{\rm S}(\boldsymbol{k}))\prod_{\boldsymbol{k}}\frac{1}{\sqrt{P_{\rm S}(\boldsymbol{k})}}\exp\Big(-\frac{|\boldsymbol{s}^{(j)}(\boldsymbol{k})|^2}{2P_{\rm S}(\boldsymbol{k})}\Big), \tag{5.24}$$

with $\boldsymbol{S} = \mathrm{diag}(P_{\rm S}(\boldsymbol{k}))$. The prior $P(P_{\rm S}(\boldsymbol{k}))$ can be chosen to be flat ($P(P_{\rm S}(\boldsymbol{k})) = \mathrm{const}$) or instead Jeffrey's prior can be used ($P(P_{\rm S}(\boldsymbol{k})) \propto P_{\rm S}(\boldsymbol{k})^{-1}$), see section (2.5.8) and appendix A.9. Note, that the likelihood for the power-spectrum given by eq. (5.24) is clearly non-Gaussian.

Power-spectrum sampling tests

We performed tests varying the initial power-spectrum. The convergence to the right level of the power-spectrum occurs very rapidly whether the power spectrum is overestimated, underestimated, or the assumed shape is completely wrong. The Gibbs-sampling process is shown in the figs. (5.12) and (5.13) with the iterative sampled signal (density-field) and parameter (power-spectrum), respectively. We show in fig. (5.12) a sequence of slices through the middle of the reconstructions with a 64^3 grid assuming a five orders of magnitude underestimated initial power-spectrum. The first reconstruction gives almost zero signal. The signal starts to appear first smoothed out and then successively more resolved. This can be clearly seen in the power-spectra, which gain power first at the low modes and then successively at higher modes (see fig. 5.13). It is also interesting to observe the fluctuating background due to the data augmentation for undetermined signal modes in contrast to the constant features that we can compare with the reconstructions in previous sections.

[1]Note, however, that a Gaussian constrained realization is good enough for power-spectrum estimation especially when one is interested in the traces of the linear regime, like the baryon acoustic oscillations, or the gravitational potential for the ISW-effect. Sampling with constrained N-body reconstructions requires a much deeper development, since the whole cosmological parameter space has to be scanned.

Chapter 6

Summary and outlook

Summary and conclusions

This thesis described a cosmic cartography project. The problem of reconstructing the cosmic matter field from galaxy catalogues was addressed. The necessary concepts, mathematical frame-work, and numerical algorithms were thoroughly analyzed. On that basis a Bayesian software tool was implemented. The resulting ARGO-code allows to investigate the characteristics of the large-scale cosmological structure within the Bayesian methodology with unprecedented fidelity and flexibility. This is achieved by jointly estimating the large-scale density along with a variety of other parameters —such as the cosmic flow, the small-scale peculiar velocity field, and the matter power-spectrum— from the information provided by galaxy redshift surveys. Furthermore, ARGO is capable of dealing with many observational issues like mask-effects, galaxy selection criteria, blurring and noise in a very efficient implementation of an operator based formalism which was carefully derived for that purpose.

The problem of reconstructing the underlying density field requires a statistical approach due to a series of uncertainties, as described in section (1.1). Some of these uncertainties are intrinsic to the nature of the underlying signal (the dark matter) and have a stochastic character, and can be subsumed under the term cosmic variance. Other uncertainties are intrinsic to the nature of the observables. In our case a discrete sample of galaxies leads to uncertainties as for instance the shot noise, the imperfectly known galaxy-bias and the redshift-distortions. Additionally, uncertainties can arise due to the observation process, such as windowing, galaxy criteria selection and blurring effects. Moreover, the mathematical and numerical representation of the data and the reconstructed signal introduces uncertainties that have to be considered, too. All these uncertainties together produce degeneracies between potential reconstructions and therefore require regularization techniques, which should converge to an optimal solution. We discuss the different Bayesian approaches specified by different alternatives for the likelihood and the prior, and see how *natural* regularizations can be performed by the prior-choice (see section 2.5). Moreover, we see how the definition of particular likelihoods and priors define classes of algorithms, each applying to a different problem approach (see table 2.1). Thus, the general Bayesian frame-work adapted here permits one to invent optimized methods for

different situations and to develop more accurate reconstruction algorithms.

Here, we develop new algorithms which account for the discrete nature of a galaxy distribution by taking a Poissonian likelihood. This is done for the case of a Gaussian prior leading to the GAPMAP estimator (see section 2.5.4 and appendix A.5) and for the case of an entropic prior where one gets a maximum entropy estimator (see section 2.5.9 and appendix A.10). The Maximum Entropy method is based on a non-informative prior, which does not assume a particular pattern for the underlying signal. This can be interesting when searching for intrinsic deviations from Gaussianity (see section 2.5.9 and references therein). We also address the possibility of extending such work to determine cosmological parameters and the bias between galaxies and dark matter.

Such goals require a large number of repeated reconstructions, which can only be achieved with highly efficient inverse algorithms. We develop here the necessary numerical schemes in a preconditioned way for linear and non-linear inverse problems (see section 3 and appendix B.1 & B.3). A novel Krylov formula (see section 3.1.5 and appendix B.1) turns out to be superior in terms of performance and fidelity, as we show in section (4). Such iterative schemes acquire their real power only in an operator formalism, which we derive in detail for different Bayesian priors and likelihoods (see section 3.3).

For the case of a Gaussian prior describing the large-scale structures and a Gaussian likelihood with a Poissonian noise covariance matrix representing the galaxy sample, we derive novel algorithms for a joint estimation of the density field, its power-spectrum, and the peculiar velocities of the galaxies (see chapter 5).

Thanks to the achieved high efficiency of ARGO the application of iterative sampling algorithms based on Markov Chain Monte Carlo is possible now. This will ultimately lead to a full description of the matter distribution with all its relevant parameters like velocities, power spectra, galaxy bias, etc., including the associated uncertainties. Some applications are shown, in which such techniques are used. A rejection sampling scheme is successfully applied to correct for the observational redshift-distortions effect, which is especially severe in regimes of non-linear structure formation, causing the so-called *finger-of-god* effect. Also a Gibbs-sampling algorithm for power-spectrum determination is presented and some preliminary results are shown in which the correct level and shape of the power-spectrum is recovered solely from the data.

We conclude that ARGO is capable of performing fast three-dimensional reconstructions of the large-scale structure scaling as $n \log_2 n$ (with n being the total number of grid cells) taking into account a wide variety of the observational and data processing issues. This opens new horizons of possibilities in the field of large-scale structure reconstruction, such as joint parameter and signal estimation, as we could show for some relevant test cases for astronomy. Still, different problems, such as galaxy-bias studies, have to be further analyzed. However, we are confident that the Bayesian perspective elaborated in this thesis can tackle these problems. We hope to have laid the fundament to a precision reconstruction analysis of the large-scale structure. There will be a large number of scientific applications benefiting from this.

Outlook

It is our goal to apply such techniques to reconstruct the underlying density field, the power-spectrum and the peculiar velocities from real galaxy catalogues. This resulting information can be used for a cosmological parameter estimation and for a characterization of the actual large-scale structure.

Parameter estimation

A major goal is to exploit the Bayesian framework and to use ARGO's capability to perform fast and low-cost reconstructions to estimate in a Markov Chain Monte Carlo fashion astrophysical quantities and cosmological parameters, the most important being:

- Power-spectrum of the matter field: We intend to apply the Gibbs-sampling technique presented in this thesis to study the baryon acoustic oscillations that are imprinted in the large-scale structure. Due to the efficiency of ARGO we expect to reach higher accuracy than previous measurements and better error estimates. The novel velocity sampling scheme should improve the estimates on smaller scales.

- Cosmological parameters: These can be sampled together with the power-spectrum or directly extracted from the power-spectrum with fitting formula. The matter content Ω_{m} can be derived by comparison of the redshift-space distribution and the real-space distribution, which can be obtained with ARGO. Matter reconstructions at different redshifs can be used to study the clustering evolution of structures, which depend on the expansion of the Universe, thus constraining dark energy.

Characterization of the large-scale structure

Another very important task is to characterize the large-scale structure. This can help in the understanding of structure formation and gain insight of the physical processes involved. For that purpose a series of projects can be done with ARGO:

- Templates made from the matter reconstructions can be used to study large-scale correlations with the cosmic microwave background and study weak signals that range from the Integrated Sachs-Wolfe effect, over the Sunyaev-Zel'Dovich effect in the diffused gas, to metal absorption lines. Predicted lensing distributions based on a reconstruction, can be used to delense the cosmic microwave background and thereby increase the sensibility for B-mode detection of upcoming cosmic microwave background experiments.

- An interesting further application would be to constrain the bias between luminous and dark matter using reconstructions made by ARGO and correlating them with simulations and reconstructions of the matter distribution coming from other fields. Weak lensing is especially suited for such a study, because it directly traces the dark matter distribution.

- Topological studies could be made from the reconstructed data, leading to a geometrical characterization of the actual large-scale structure.

- The reconstructed structures of a galaxy catalogue can be followed back in time with various methods, like those based on the Zel'Dovich approximation. These early matter density fluctuations can be used as initial conditions for a N-body simulation. The results of such a constrained simulation have a wide application in structure formation theory.

- The methods developed in this thesis could also be applied to study other areas in astrophysics, in which optimal inverse methods are required and where low signal-to-noise ratios demand good error estimates to quantify any results derived from the data. These fields range from weak lensing, over lyman-alpha forest, to the 21 cm line.

In summary, the methods developed in this thesis will allow us to extract a plenitude of information from present and upcoming redshift surveys. This will be a step forward in our detailed understanding of the physical processes leading to a universe filled with structures as we observe today. In this spirit, ARGO will lead us to new horizons to conquer *terra incognita*.

Appendix A

Bayesian estimators

A.1 The Wiener-filter as a Bayesian estimator

Let us recall eq. (2.20) which comes from Bayes theorem assuming a Gaussian prior and a Gaussian likelihood

$$P(\boldsymbol{s} \mid \boldsymbol{d}, \boldsymbol{p}) \propto \exp\left(-\frac{1}{2}\left[\boldsymbol{s}^\dagger \boldsymbol{S}^{-1}\boldsymbol{s} + (\boldsymbol{d}-\boldsymbol{R}\boldsymbol{s})^\dagger \boldsymbol{N}^{-1}(\boldsymbol{d}-\boldsymbol{R}\boldsymbol{s})\right]\right). \tag{A.1}$$

If we just look at the log-posterior distribution we have

$$\begin{aligned} \log P(\boldsymbol{s} \mid \boldsymbol{d}, \boldsymbol{p}) &\propto \boldsymbol{s}^\dagger \boldsymbol{S}^{-1}\boldsymbol{s} + (\boldsymbol{d}-\boldsymbol{R}\boldsymbol{s})^\dagger \boldsymbol{N}^{-1}(\boldsymbol{d}-\boldsymbol{R}\boldsymbol{s}) \\ &= \boldsymbol{s}^\dagger \boldsymbol{S}^{-1}\boldsymbol{s} + \boldsymbol{s}^\dagger \boldsymbol{R}^\dagger \boldsymbol{N}^{-1}\boldsymbol{R}\boldsymbol{s} - \boldsymbol{s}^\dagger \boldsymbol{R}^\dagger \boldsymbol{N}^{-1}\boldsymbol{d} - \boldsymbol{d}^\dagger \boldsymbol{N}^{-1}\boldsymbol{R}\boldsymbol{s} + \boldsymbol{d}^\dagger \boldsymbol{N}^{-1}\boldsymbol{d}. \end{aligned} \tag{A.2}$$

We can combine the first two terms to one term: $\boldsymbol{s}^\dagger(\boldsymbol{\sigma}^2_{\mathrm{WF}})^{-1}\boldsymbol{s}$, with $(\boldsymbol{\sigma}^2_{\mathrm{WF}})^{-1} \equiv (\boldsymbol{S}^{-1} + \boldsymbol{R}^\dagger \boldsymbol{N}^{-1}\boldsymbol{R})$. Since we want to obtain a log-posterior of the form

$$\log P(\boldsymbol{s} \mid \boldsymbol{d}, \boldsymbol{p}) \propto (\boldsymbol{s} - \langle \boldsymbol{s} \rangle_{\mathrm{WF}})^\dagger (\boldsymbol{\sigma}_{\mathrm{WF}}{}^2)^{-1} (\boldsymbol{s} - \langle \boldsymbol{s} \rangle_{\mathrm{WF}}), \tag{A.3}$$

with $\langle \boldsymbol{s} \rangle_{\mathrm{WF}} = \boldsymbol{F}_{\mathrm{WF}}\boldsymbol{d}$, we can identify the third and the fourth term of eq. (A.3) with the corresponding terms in eq. (A.3)

$$-\boldsymbol{s}^\dagger \boldsymbol{R}^\dagger \boldsymbol{N}^{-1}\boldsymbol{d} = -\boldsymbol{s}^\dagger (\boldsymbol{\sigma}^2_{\mathrm{WF}})^{-1}\boldsymbol{F}_{\mathrm{WF}}\boldsymbol{d}, \tag{A.4}$$

and

$$-\boldsymbol{d}^\dagger \boldsymbol{N}^{-1}\boldsymbol{R}\boldsymbol{s} = -\boldsymbol{d}^\dagger \boldsymbol{F}^\dagger_{\mathrm{WF}} (\boldsymbol{\sigma}^2_{\mathrm{WF}})^{-1}\boldsymbol{s}, \tag{A.5}$$

respectively. The remaining term depends only on the data and is thus factorized in the posterior distribution function as part of the evidence. From both eq. (A.4) and eq. (A.5) we conclude that the Wiener-filter has the form

$$\boldsymbol{F}_{\mathrm{WF}} = \boldsymbol{\sigma}^2_{\mathrm{WF}} \boldsymbol{R}^\dagger \boldsymbol{N}^{-1} = (\boldsymbol{S}^{-1} + \boldsymbol{R}^\dagger \boldsymbol{N}^{-1}\boldsymbol{R})^{-1} \boldsymbol{R}^\dagger \boldsymbol{N}^{-1}. \tag{A.6}$$

This is the natural Bayesian representation in contrast to expression (2.24), which is the outcome of a LSQ approach (see appendix A.2). It can be shown that both expressions for the Wiener-filter are mathematically equivalent (see appendix A.3).

A.2 The mapping equation for the Wiener-filter in k-space

Following the concept of minimum variance (e.g. Rybicki & Press, 1992; Zaroubi *et al.*, 1995), we define an action given by the normalized volume integral of the square of the difference between the reconstruction (ψ) and the ensemble of different possible realizations of the density field ($s = \delta_\rho$)

$$\mathcal{A} = \langle \frac{1}{V} \int \mathrm{d}^{N_\mathrm{D}} \boldsymbol{r} \left[\psi(\boldsymbol{r}) - s(\boldsymbol{r}) \right]^2 \rangle_{(\boldsymbol{s},\boldsymbol{\epsilon}|\boldsymbol{p})}. \tag{A.7}$$

From the statistical point of view, the action $\mathcal{A}$ is the loss function that has to be minimized. Note that this action can be expressed as the ensemble average of the squared Euclidean distance between the real density field s and the reconstruction ψ

$$\mathcal{A} = \frac{1}{V} \langle D^2_{\mathrm{Eucl}}(\psi, s) \rangle_{(\boldsymbol{s},\boldsymbol{\epsilon}|\boldsymbol{p})}. \tag{A.8}$$

Transforming expression (A.7) into Fourier space yields

$$\begin{aligned} \mathcal{A} &= \frac{1}{V} \int \frac{\mathrm{d}^{N_\mathrm{D}} \boldsymbol{k}}{(2\pi)^{N_\mathrm{D}}} \Big[\langle \hat{\psi}(\boldsymbol{k}) \overline{\hat{\psi}(\boldsymbol{k})} \rangle_{(\boldsymbol{s},\boldsymbol{\epsilon}|\boldsymbol{p})} + \langle \hat{s}(\boldsymbol{k}) \overline{\hat{s}(\boldsymbol{k})} \rangle_{(\boldsymbol{s},\boldsymbol{\epsilon}|\boldsymbol{p})} - \langle \hat{\psi}(\boldsymbol{k}) \overline{\hat{s}(\boldsymbol{k})} \rangle_{(\boldsymbol{s},\boldsymbol{\epsilon}|\boldsymbol{p})} \\ &- \langle \hat{s}(\boldsymbol{k}) \overline{\hat{\psi}(\boldsymbol{k})} \rangle_{(\boldsymbol{s},\boldsymbol{\epsilon}|\boldsymbol{p})} \Big]. \end{aligned} \tag{A.9}$$

Assuming a linear relation between the reconstruction ψ and the data d

$$\hat{\psi}(\boldsymbol{k}) = \int \frac{\mathrm{d}^{N_\mathrm{D}} \boldsymbol{k'}}{(2\pi)^{N_\mathrm{D}}} \hat{\bar{F}}_{\mathrm{WF}}(\boldsymbol{k}, \boldsymbol{k'}) \hat{d}(\boldsymbol{k'}), \tag{A.10}$$

and statistical homogeneity ($\langle \hat{s}(\boldsymbol{k}) \hat{s}(\boldsymbol{k'}) \rangle_{(\boldsymbol{s},\boldsymbol{\epsilon}|\boldsymbol{p})} = (2\pi)^{N_\mathrm{D}} \delta_\mathrm{D}(\boldsymbol{k} - \boldsymbol{k'}) P_\mathrm{S}(\boldsymbol{k'})$), yields

$$\begin{aligned} \mathcal{A} = \frac{1}{V} \int \frac{\mathrm{d}^{N_\mathrm{D}} \boldsymbol{k}}{(2\pi)^{N_\mathrm{D}}} \int \frac{\mathrm{d}^{N_\mathrm{D}} \boldsymbol{k'}}{(2\pi)^{N_\mathrm{D}}} \Big[\hat{\bar{F}}_{\mathrm{WF}}(\boldsymbol{k}, \boldsymbol{k'}) \int \frac{\mathrm{d}^{N_\mathrm{D}} \boldsymbol{q}}{(2\pi)^{N_\mathrm{D}}} \overline{\hat{\bar{F}}_{\mathrm{WF}}(\boldsymbol{k}, \boldsymbol{q})} \langle \hat{d}(\boldsymbol{k'}) \overline{\hat{d}(\boldsymbol{q})} \rangle_{(\boldsymbol{s},\boldsymbol{\epsilon}|\boldsymbol{p})} \\ + (2\pi)^{N_\mathrm{D}} \delta_D(\boldsymbol{k} - \boldsymbol{k'}) \langle \hat{s}(\boldsymbol{k'}) \overline{\hat{s}(\boldsymbol{k'})} \rangle_{(\boldsymbol{s},\boldsymbol{\epsilon}|\boldsymbol{p})} - \hat{\bar{F}}_{\mathrm{WF}}(\boldsymbol{k}, \boldsymbol{k'}) \langle \hat{d}(\boldsymbol{k'}) \overline{\hat{s}(\boldsymbol{k})} \rangle_{(\boldsymbol{s},\boldsymbol{\epsilon}|\boldsymbol{p})} \\ - \overline{\hat{\bar{F}}_{\mathrm{WF}}(\boldsymbol{k}, \boldsymbol{k'})} \langle \hat{s}(\boldsymbol{k}) \overline{\hat{d}(\boldsymbol{k'})} \rangle_{(\boldsymbol{s},\boldsymbol{\epsilon}|\boldsymbol{p})} \Big]. \end{aligned} \tag{A.11}$$

Now the action is minimized with respect to the linear operator, $\frac{\delta \mathcal{A}}{\delta \hat{\bar{F}}_{\mathrm{WF}}} = 0$, to obtain the following mapping equation

$$\int \frac{\mathrm{d}^{N_\mathrm{D}} \boldsymbol{q}}{(2\pi)^{N_\mathrm{D}}} \hat{\bar{F}}_{\mathrm{WF}}(\boldsymbol{k}, \boldsymbol{q}) \langle \hat{d}(\boldsymbol{q}) \overline{\hat{d}(\boldsymbol{k'})} \rangle_{(\boldsymbol{s},\boldsymbol{\epsilon}|\boldsymbol{p})} = \langle \hat{s}(\boldsymbol{k}) \overline{\hat{d}(\boldsymbol{k'})} \rangle_{(\boldsymbol{s},\boldsymbol{\epsilon}|\boldsymbol{p})}. \tag{A.12}$$

The Wiener Filter can be thus expressed as the correlation matrix between the signal and the data multiplied by inverse of the autocorrelation matrix of the data (see Zaroubi *et al.*, 1995)

$$\boldsymbol{F}_{\mathrm{WF}} = \langle \boldsymbol{s}\boldsymbol{d}^\dagger \rangle \langle \boldsymbol{d}\boldsymbol{d}^\dagger \rangle^{-1}. \tag{A.13}$$

Note that eq. (A.12) allows us to substitute $\boldsymbol{k'}$ by $-\boldsymbol{k'}$, which is equivalent to the conjugation of $\hat{d}(\boldsymbol{k'})$ due to the hermitian redundancy of real numbers

$$\int \frac{\mathrm{d}^{N_\mathrm{D}}\boldsymbol{q}}{(2\pi)^{N_\mathrm{D}}} \hat{\bar{F}}'_{\mathrm{WF}}(\boldsymbol{k},\boldsymbol{q})\langle \hat{d}(\boldsymbol{q})\hat{d}(\boldsymbol{k'})\rangle_{(\boldsymbol{s},\boldsymbol{\epsilon}|\boldsymbol{p})} = \langle \hat{s}(\boldsymbol{k})\hat{d}(\boldsymbol{k'})\rangle_{(\boldsymbol{s},\boldsymbol{\epsilon}|\boldsymbol{p})}. \tag{A.14}$$

The linear operator one obtains in this way is different, but fulfills the same requirements. We compare both cases in section (4). Let us see how one would apply such a filter. The covariance matrix of the data is given by

$$\langle \hat{d}(\boldsymbol{k})\hat{d}(\boldsymbol{k'})\rangle_{(\boldsymbol{s},\boldsymbol{\epsilon}|\boldsymbol{p})} = \langle \hat{\alpha}(\boldsymbol{k})\hat{\alpha}(\boldsymbol{k'})\rangle_{(\boldsymbol{s},\boldsymbol{\epsilon}|\boldsymbol{p})} + \langle \hat{\epsilon}(\boldsymbol{k})\hat{\epsilon}(\boldsymbol{k'})\rangle_{(\boldsymbol{s},\boldsymbol{\epsilon}|\boldsymbol{p})}, \tag{A.15}$$

and its action on some vector by

$$\int \frac{\mathrm{d}^{N_\mathrm{D}}\boldsymbol{k'}}{(2\pi)^{N_\mathrm{D}}} \langle \hat{\alpha}(\boldsymbol{k})\hat{\alpha}(\boldsymbol{k'})\rangle_{(\boldsymbol{s},\boldsymbol{\epsilon}|\boldsymbol{p})}\{\hat{x}(\boldsymbol{k'})\} = \hat{f}_\mathrm{B}\cdot\left[\hat{f}_\mathrm{SM}\circ\left[P_\mathrm{S}\cdot\left[\overline{\hat{f}_\mathrm{SM}}\circ\left[\overline{\hat{f}_\mathrm{B}}\cdot\{\hat{x}\}\right]\right]\right]\right](\boldsymbol{k}), \tag{A.16}$$

and

$$\int \frac{\mathrm{d}^{N_\mathrm{D}}\boldsymbol{k'}}{(2\pi)^{N_\mathrm{D}}} \langle \hat{\epsilon}(\boldsymbol{k})\hat{\epsilon}(\boldsymbol{k'})\rangle_{(\boldsymbol{s},\boldsymbol{\epsilon}|\boldsymbol{p})}\{\hat{x}(\boldsymbol{k'})\} = \hat{f}_\mathrm{SF}\circ\left[P_\mathrm{N}\cdot\left[\overline{\hat{f}_\mathrm{SF}}\circ\{\hat{x}\}\right]\right](\boldsymbol{k}). \tag{A.17}$$

The correlation matrix between the data and the signal applied to that vector yields

$$\int \frac{\mathrm{d}^{N_\mathrm{D}}\boldsymbol{k'}}{(2\pi)^{N_\mathrm{D}}} \langle \hat{s}(\boldsymbol{k})\hat{d}(\boldsymbol{k'})\rangle_{(\boldsymbol{s},\boldsymbol{\epsilon}|\boldsymbol{p})}\{\hat{x}(\boldsymbol{k'})\} = P_\mathrm{S}\cdot\left[\overline{\hat{f}_\mathrm{SM}}\circ\left[\overline{\hat{f}_\mathrm{B}}\cdot\{\hat{x}\}\right]\right](\boldsymbol{k}). \tag{A.18}$$

We see that the difference with respect to the operations derived in section (3.3) resides in the conjugation of certain functions.

A.3 Direct and inverse representations for the Wiener-filter

Here we show the equivalence between the direct and the inverse representations for the Wiener-filter (see section 2.5.3). In a first approach, we start assuming that the inverse of the response operator exists ($\boldsymbol{R}^{-1}$). Then after some operations the equivalence can be shown for both the Wiener-filter

$$\begin{aligned}
\boldsymbol{F}_{\mathrm{WF}} &= (\boldsymbol{S}^{-1}+\boldsymbol{R}^\dagger\boldsymbol{N}^{-1}\boldsymbol{R})^{-1}\boldsymbol{R}^\dagger\boldsymbol{N}^{-1}, \\
&= (\boldsymbol{S}^{-1}(\boldsymbol{R})^{-1}\boldsymbol{N}+\boldsymbol{R}^\dagger)^{-1}, \\
&= \boldsymbol{S}\boldsymbol{R}^\dagger(\boldsymbol{R}\boldsymbol{S}\boldsymbol{R}^\dagger+\boldsymbol{N})^{-1},
\end{aligned} \tag{A.19}$$

and the covariance

$$\begin{aligned}
\boldsymbol{\sigma}^2_{\mathrm{WF}} &= (\boldsymbol{S}^{-1}+\boldsymbol{R}^\dagger\boldsymbol{N}^{-1}\boldsymbol{R})^{-1}, \\
&= \boldsymbol{S}\boldsymbol{R}^\dagger(\boldsymbol{R}+\boldsymbol{R}\boldsymbol{S}\boldsymbol{R}^\dagger\boldsymbol{N}^{-1}\boldsymbol{R})^{-1}, \\
&= \boldsymbol{S}\boldsymbol{R}^\dagger(\boldsymbol{R}\boldsymbol{S}\boldsymbol{R}^\dagger+\boldsymbol{N})^{-1}\boldsymbol{N}(\boldsymbol{R}^\dagger)^{-1}.
\end{aligned} \tag{A.20}$$

Note that the covariance given by eq. (A.20) has limited practical use, since it requires the inverse of the response operator $\boldsymbol{R}$, which is in general a singular matrix. To find a direct representation for the covariance one has to introduce the concept of constrained realizations (see section 5.3.2 and appendix A.4). In order to find a general proof for the equivalence between the direct and the inverse representation of the Wiener-filter, we have to look at the residuals

$$\begin{aligned}\boldsymbol{\sigma}^2_{\mathrm{WF}} &= \langle \boldsymbol{r}\boldsymbol{r}^\dagger \rangle = \langle (\boldsymbol{s} - \boldsymbol{F}_{\mathrm{WF}}\boldsymbol{d})(\boldsymbol{s} - \boldsymbol{F}_{\mathrm{WF}}\boldsymbol{d})^\dagger \rangle \\ &= \boldsymbol{S} - \boldsymbol{S}\boldsymbol{R}^\dagger {\boldsymbol{F}_{\mathrm{WF}}}^\dagger - \boldsymbol{F}_{\mathrm{WF}}\boldsymbol{R}\boldsymbol{S} + \boldsymbol{F}_{\mathrm{WF}}(\boldsymbol{R}\boldsymbol{S}\boldsymbol{R}^\dagger + \boldsymbol{N}){\boldsymbol{F}_{\mathrm{WF}}}^\dagger, \end{aligned} \tag{A.21}$$

where we have done the substitution: $\boldsymbol{d} = \boldsymbol{R}\boldsymbol{s} + \boldsymbol{\epsilon}$ and $\langle \boldsymbol{s}\boldsymbol{\epsilon}^\dagger \rangle = 0$. The first two terms lead to the Wiener covariance, as we show here

$$\begin{aligned}\boldsymbol{S} - \boldsymbol{S}\boldsymbol{R}^\dagger {\boldsymbol{F}_{\mathrm{WF}}}^\dagger &= (\boldsymbol{S}(\boldsymbol{\sigma}^2_{\mathrm{WF}})^{-1} - \boldsymbol{S}\boldsymbol{R}^\dagger {\boldsymbol{F}_{\mathrm{WF}}}^\dagger ({\boldsymbol{\sigma}_{\mathrm{WF}}}^2)^{-1})\boldsymbol{\sigma}^2_{\mathrm{WF}} \\ &= \big(\boldsymbol{S}(\boldsymbol{S}^{-1} + \boldsymbol{R}^\dagger \boldsymbol{N}^{-1}\boldsymbol{R}) - \boldsymbol{S}\boldsymbol{R}^\dagger \boldsymbol{N}^{-1}\boldsymbol{R}\big)\boldsymbol{\sigma}^2_{\mathrm{WF}} \\ &= \boldsymbol{\sigma}^2_{\mathrm{WF}}, \end{aligned} \tag{A.22}$$

where we have used the inverse relation obtained in section (A.1): $\boldsymbol{F}_{\mathrm{WF}} = \boldsymbol{\sigma}^2_{\mathrm{WF}}\boldsymbol{R}^\dagger \boldsymbol{N}^{-1}$. Consequently, the last two terms of eq. (A.21) have to cancel out

$$\begin{aligned} 0 &= -\boldsymbol{F}_{\mathrm{WF}}\boldsymbol{R}\boldsymbol{S} + \boldsymbol{F}_{\mathrm{WF}}(\boldsymbol{R}\boldsymbol{S}\boldsymbol{R}^\dagger + \boldsymbol{N}){\boldsymbol{F}_{\mathrm{WF}}}^\dagger \\ 0 &= \boldsymbol{F}_{\mathrm{WF}}(-\boldsymbol{R}\boldsymbol{S} + (\boldsymbol{R}\boldsymbol{S}\boldsymbol{R}^\dagger + \boldsymbol{N}){\boldsymbol{F}_{\mathrm{WF}}}^\dagger). \end{aligned} \tag{A.23}$$

Now we take the transpose and conjugate of the last equation and factorize the data correlation matrix out (which is always invertible, since the noise covariance matrix is invertible)

$$0 = (\boldsymbol{F}_{\mathrm{WF}} - \boldsymbol{S}\boldsymbol{R}^\dagger(\boldsymbol{R}\boldsymbol{S}\boldsymbol{R}^\dagger + \boldsymbol{N})^{-1})(\boldsymbol{R}\boldsymbol{S}\boldsymbol{R}^\dagger + \boldsymbol{N})\boldsymbol{F}^\dagger_{\mathrm{WF}}. \tag{A.24}$$

The last equation motivates the direct representation of the Wiener-filter without performing least squares, i.e. without demanding the Filter to be optimal ($\partial\boldsymbol{\sigma}^2_{\mathrm{WF}}/\partial\boldsymbol{F}_{\mathrm{WF}} = 0$), which is already imposing some regularity condition on $\boldsymbol{F}_{\mathrm{WF}}$. Note that we also obtain the trivial zero solution ($\boldsymbol{F}_{\mathrm{WF}} = 0$), which is equivalent to $\boldsymbol{R} = 0$ or $\boldsymbol{N} = \infty$ with covariance $\boldsymbol{\sigma}^2 = \boldsymbol{S}$. Since the direct and the inverse representation have the same null-spaces eq. (A.24) already proves the equivalence between the direct and the inverse representations for the Wiener-filter. Nevertheless, let us directly test this equivalence

$$\begin{aligned} \boldsymbol{S}\boldsymbol{R}^\dagger(\boldsymbol{R}\boldsymbol{S}\boldsymbol{R}^\dagger + \boldsymbol{N})^{-1} &\stackrel{?}{=} \boldsymbol{\sigma}^2_{\mathrm{WF}}\boldsymbol{R}^\dagger\boldsymbol{N}^{-1} \\ \boldsymbol{S}\boldsymbol{R}^\dagger &\stackrel{?}{=} \sigma^2_{\mathrm{WF}}\boldsymbol{R}^\dagger\boldsymbol{N}^{-1}(\boldsymbol{R}\boldsymbol{S}\boldsymbol{R}^\dagger + \boldsymbol{N}) \\ \boldsymbol{R}\boldsymbol{S} &\stackrel{?}{=} (\boldsymbol{R}\boldsymbol{S}\boldsymbol{R}^\dagger + \boldsymbol{N})\boldsymbol{N}^{-1}\boldsymbol{R}\boldsymbol{\sigma}^2_{\mathrm{WF}} \\ \boldsymbol{R}\boldsymbol{S} &\stackrel{?}{=} \boldsymbol{R}\boldsymbol{S}\boldsymbol{R}^\dagger\boldsymbol{N}^{-1}\boldsymbol{R}\boldsymbol{\sigma}^2_{\mathrm{WF}} + \boldsymbol{R}\boldsymbol{\sigma}^2_{\mathrm{WF}} \\ \boldsymbol{R}\boldsymbol{S}(\boldsymbol{\sigma}^2_{\mathrm{WF}})^{-1} &\stackrel{?}{=} \boldsymbol{R}\boldsymbol{S}\boldsymbol{R}^\dagger\boldsymbol{N}^{-1}\boldsymbol{R} + \boldsymbol{R} \\ \boldsymbol{R}\boldsymbol{S}(\boldsymbol{S}^{-1} + \boldsymbol{R}^\dagger\boldsymbol{N}^{-1}\boldsymbol{R}) &\stackrel{?}{=} \boldsymbol{R}\boldsymbol{S}\boldsymbol{R}^\dagger\boldsymbol{N}^{-1}\boldsymbol{R} + \boldsymbol{R} \\ \boldsymbol{R} + \boldsymbol{R}\boldsymbol{S}\boldsymbol{R}^\dagger\boldsymbol{N}^{-1}\boldsymbol{R} &\stackrel{?}{=} \boldsymbol{R}\boldsymbol{S}\boldsymbol{R}^\dagger\boldsymbol{N}^{-1}\boldsymbol{R} + \boldsymbol{R}. \end{aligned} \tag{A.25}$$

Since the left-hand-side is equal to the right-hand-side both representations are equivalent. Note that we did not assume the response operator to be invertible. We solely demanded that the inverse of the signal and of the noise covariance matrices can be built ($\exists \boldsymbol{S}^{-1}$ and $\exists \boldsymbol{N}^{-1}$). This implies that the covariance matrix and the inverse of the data autocorrelation matrix exist ($\exists(\boldsymbol{S}^{-1} + \boldsymbol{R}^\dagger \boldsymbol{N}^{-1}\boldsymbol{R})^{-1}$ and $\exists(\boldsymbol{R}\boldsymbol{S}\boldsymbol{R}^\dagger + \boldsymbol{N})^{-1}$), as we required in our proof.

A.4 Covariance of a constrained realization

Following Bistolas & Hoffman (1998); Ganon & Hoffman (1993); Hoffman & Ribak (1991) we can generate a synthetic realization with

$$\boldsymbol{y} = \tilde{\boldsymbol{s}} - \boldsymbol{F}_{\mathrm{WF}}\tilde{\boldsymbol{d}}, \tag{A.26}$$

If the following relations hold[1]: $\langle \tilde{\boldsymbol{s}}\tilde{\boldsymbol{s}}^\dagger\rangle = \boldsymbol{S}$, $\langle \tilde{\boldsymbol{\epsilon}}\tilde{\boldsymbol{\epsilon}}^\dagger\rangle = \boldsymbol{N}$ and $\langle \tilde{\boldsymbol{s}}\tilde{\boldsymbol{\epsilon}}^\dagger\rangle = 0$ then we obtain

$$\begin{aligned}\langle \boldsymbol{y}\boldsymbol{y}^\dagger\rangle &= \langle(\tilde{\boldsymbol{s}} - \boldsymbol{F}_{\mathrm{WF}}\tilde{\boldsymbol{d}})(\tilde{\boldsymbol{s}} - \boldsymbol{F}_{\mathrm{WF}}\tilde{\boldsymbol{d}})^\dagger\rangle \\ &= \boldsymbol{S} - \boldsymbol{S}\boldsymbol{R}^\dagger {\boldsymbol{F}_{\mathrm{WF}}}^\dagger - \boldsymbol{F}_{\mathrm{WF}}\boldsymbol{R}\boldsymbol{S} + \boldsymbol{F}_{\mathrm{WF}}(\boldsymbol{R}\boldsymbol{S}\boldsymbol{R}^\dagger + \boldsymbol{N}){\boldsymbol{F}_{\mathrm{WF}}}^\dagger \end{aligned} \tag{A.27}$$

We can identify these terms with eq. (A.21). Thus, following relation is fulfilled

$$\langle \boldsymbol{y}\boldsymbol{y}^\dagger\rangle = \langle \boldsymbol{r}\boldsymbol{r}^\dagger\rangle = \boldsymbol{\sigma}^2_{\mathrm{WF}}. \tag{A.28}$$

A.5 GAPMAP: MAP with a Gaussian prior and a Poissonian likelihood

Remember $P(\boldsymbol{s} \mid \boldsymbol{d}, \boldsymbol{p}) \propto \mathcal{L}(\boldsymbol{d} \mid \boldsymbol{s}, \boldsymbol{p})P(\boldsymbol{s} \mid \boldsymbol{p})$ to be extremized. First we write the log-likelihood taking the logarithm of eq. (2.11)

$$\log \mathcal{L}(\boldsymbol{s} \mid \boldsymbol{d}, \boldsymbol{p}) = \sum_i \Big[-(\boldsymbol{R}\boldsymbol{s}')_i - c_i + (d'_i + c_i)\log\Big((\boldsymbol{R}\boldsymbol{s}')_i + c_i\Big) - \log\Big((d'_i + c_i)!\Big)\Big]. \tag{A.29}$$

Then we differentiate with respect to the signal to yield

$$\frac{\partial \log \mathcal{L}(\boldsymbol{s} \mid \boldsymbol{d}, \boldsymbol{p})}{\partial s_k} = \sum_i \Big[R_{ik} b\overline{n_{\mathrm{g}}}\Big(-1 + (\sum_j R_{ij}s'_j + c_i)^{-1}(d'_i + c_i)\Big)\Big].$$

The same exercise for the Gaussian prior leads to

$$\frac{\partial \log P(\boldsymbol{s} \mid \boldsymbol{p})}{\partial s_k} = -\sum_j S^{-1}_{kj} s_j. \tag{A.30}$$

Now we demand $0 = \partial \log P(\boldsymbol{s} \mid \boldsymbol{d}, \boldsymbol{p})/\partial s_k$ to get an equation for the MAP estimator. After applying $\boldsymbol{S}$ to the equation we obtain

$$\sum_i \sum_l \Big[S_{kl}R_{il} b\overline{n_{\mathrm{g}}}\Big(-1 + \Big(\sum_m R_{im}\overline{n_{\mathrm{g}}}(1 + bs^j_m) + c_i\Big)^{-1}(d'_i + c_i)\Big)\Big] - s^j_k = 0. \tag{A.31}$$

[1]Note that the realization does not need to be Gaussian distributed, but just fulfill these requirements.

Adding the index $j+1$ and j to $\boldsymbol{s}$ on lhs and rhs respectively, an iteration scheme is formed

$$s_k^{j+1} = \sum_i \sum_l \Big[S_{kl} R_{il} b\overline{n_{\rm g}} \Big(-1 + \Big(\sum_m R_{im} \overline{n_{\rm g}} (1 + b s_m^j) + c_i \Big)^{-1} (d_i' + c_i) \Big) \Big]. \quad \text{(A.32)}$$

Let us simplify this algorithm for positive signals $\boldsymbol{s}'$ in matrix notation

$$\boldsymbol{s}'^{j+1} = \overline{\boldsymbol{s}}'^2 \boldsymbol{S} \boldsymbol{R}^\dagger \Big[-\vec{1} + \mathrm{diag}(\boldsymbol{R}\boldsymbol{s}'^j + \boldsymbol{c})^{-1} (\boldsymbol{d}' + \boldsymbol{c}) \Big] + \overline{\boldsymbol{s}}', \quad \text{(A.33)}$$

where we made following substitutions $b \to 1$ and $\overline{\boldsymbol{n}}_{\rm g} \to \overline{\boldsymbol{s}}'$, with $\overline{\boldsymbol{s}}'$ being the average of the positive signal.

A.6 Poissonian maximum likelihood

The context in which the Richardson-Lucy algorithm is applied has positive intensity signals and the kernel $\boldsymbol{R}$ in eq. (2.1) is understood as a blurring function that can be expressed mathematically as a convolution with the *true* signal $\boldsymbol{s}$. We will further assume no background ($\boldsymbol{c} = 0$) so that the log-likelihood of eq. (2.11) can be written as

$$\log \mathcal{L}(\boldsymbol{s}' \mid \boldsymbol{d}', \boldsymbol{p}) = \sum_i \Big[-(\boldsymbol{R}\boldsymbol{s}')_i + d_i' \log(\boldsymbol{R}\boldsymbol{s}')_i - \log(d_i'!) \Big], \quad \text{(A.34)}$$

differentiating with respect to the signal yields

$$0 = \frac{\partial \log \mathcal{L}(\boldsymbol{s}' \mid \boldsymbol{d}', \boldsymbol{p})}{\partial {s'}_k} = \sum_i \Big[R_{ik} \Big(-1 + (\boldsymbol{R}\boldsymbol{s}')_i^{-1} {d'}_i \Big) \Big]. \quad \text{(A.35)}$$

We can multiply this equation with the signal $\boldsymbol{s}'$ and make an iterative method which coincides with Richardson-Lucy algorithm

$$\boldsymbol{s}'^{j+1} = \mathrm{diag}\Big(\boldsymbol{R}^\dagger \mathrm{diag}(\boldsymbol{R}\boldsymbol{s}'^j)^{-1} \boldsymbol{d}' \Big) \boldsymbol{s}'^j, \quad \text{(A.36)}$$

with $\boldsymbol{R}^\dagger \vec{1} = \vec{1}$ due to the convolution operation.

A.7 COBE-filter

We briefly show here that the COBE-filter is an unbiased estimator only and only if the response matrix is invertible.

$$\begin{aligned} \langle \langle \boldsymbol{s} \rangle_{\rm COBE} \rangle_{(\boldsymbol{d}|\boldsymbol{s},\boldsymbol{p})} &= \langle (\boldsymbol{R}^\dagger \boldsymbol{N}^{-1} \boldsymbol{R})^{-1} \boldsymbol{R}^\dagger \boldsymbol{N}^{-1} \boldsymbol{d} \rangle_{(\boldsymbol{d}|\boldsymbol{s},\boldsymbol{p})} \\ &= (\boldsymbol{R}^\dagger \boldsymbol{N}^{-1} \boldsymbol{R})^{-1} \boldsymbol{R}^\dagger \boldsymbol{N}^{-1} \langle \boldsymbol{R}\boldsymbol{s} + \boldsymbol{\epsilon} \rangle_{(\boldsymbol{d}|\boldsymbol{s},\boldsymbol{p})} \\ &= (\boldsymbol{R}^\dagger \boldsymbol{N}^{-1} \boldsymbol{R})^{-1} \boldsymbol{R}^\dagger \boldsymbol{N}^{-1} \boldsymbol{R}\boldsymbol{s} \\ &= \boldsymbol{s}, \ \text{if } \boldsymbol{R} \text{ is invertible.} \end{aligned} \quad \text{(A.37)}$$

A.8 Linear filters need to be invertible to conserve information

The Fisher information matrix $\boldsymbol{J}$ for a Gaussian distribution[1] with zero mean and covariance matrix $\boldsymbol{C}$ calculated by Vogeley & Szalay (1996) has the form

$$\boldsymbol{J}_{ij} = \frac{1}{2}\mathrm{tr}\,\left(\boldsymbol{G}_i\boldsymbol{G}_j\right), \tag{A.38}$$

with

$$\boldsymbol{G}_i = \boldsymbol{C}^{-1}\boldsymbol{C}_{,i}, \tag{A.39}$$

where the comma notation $\boldsymbol{C}_{,i}$ stands for the derivative with respect to the parameter θ_i: $\mathrm{d}\boldsymbol{C}/\mathrm{d}\theta_i$. Following Tegmark (1997), we calculate the Fisher information matrix $\boldsymbol{J}$ for the filtered and un-filtered signal. Let us assume a linear filter $\boldsymbol{L}$, which provides us with an estimator of the signal

$$\langle\boldsymbol{s}\rangle_{\mathrm{L}} \equiv \boldsymbol{L}\boldsymbol{d}. \tag{A.40}$$

The correlation matrix of the estimator yields

$$\boldsymbol{C}^{\mathrm{est}} = \langle\langle\boldsymbol{s}\rangle_{\mathrm{L}}\langle\boldsymbol{s}\rangle_{\mathrm{L}}^{\dagger}\rangle_{(\boldsymbol{s},\boldsymbol{\epsilon}|\boldsymbol{p})} = \boldsymbol{L}^{\dagger}\left(\boldsymbol{R}\boldsymbol{S}\boldsymbol{R}^{\dagger}+\boldsymbol{N}\right)\boldsymbol{L}. \tag{A.41}$$

We get then

$$\boldsymbol{C}^{\mathrm{est}}_{,i} = \boldsymbol{L}^{\dagger}\left(\boldsymbol{R}\boldsymbol{S}_{,i}\boldsymbol{R}^{\dagger}\right)\boldsymbol{L}, \tag{A.42}$$

$$\boldsymbol{G}^{\mathrm{est}}_{i} = \tilde{\boldsymbol{L}}\left(\boldsymbol{R}\boldsymbol{S}\boldsymbol{R}^{\dagger}+\boldsymbol{N}\right)^{-1}\tilde{\boldsymbol{L}}^{\dagger}\boldsymbol{L}^{\dagger}\left(\boldsymbol{R}\boldsymbol{S}_{,i}\boldsymbol{R}^{\dagger}\right)\boldsymbol{L}, \tag{A.43}$$

where we have denoted the approximate inverse of $\boldsymbol{L}$ as $\tilde{\boldsymbol{L}}$. Doing the same for the data yields

$$\boldsymbol{C}^{\mathrm{data}} = \langle\boldsymbol{d}\boldsymbol{d}^{\dagger}\rangle_{(\boldsymbol{s},\boldsymbol{\epsilon}|\boldsymbol{p})} = \left(\boldsymbol{R}\boldsymbol{S}\boldsymbol{R}^{\dagger}+\boldsymbol{N}\right), \tag{A.44}$$

$$\boldsymbol{C}^{\mathrm{data}}_{,i} = \boldsymbol{R}\boldsymbol{S}_{,i}\boldsymbol{R}^{\dagger}, \tag{A.45}$$

$$\boldsymbol{G}^{\mathrm{data}}_{i} = \left(\boldsymbol{R}\boldsymbol{S}\boldsymbol{R}^{\dagger}+\boldsymbol{N}\right)^{-1}\left(\boldsymbol{R}\boldsymbol{S}_{,i}\boldsymbol{R}^{\dagger}\right). \tag{A.46}$$

If we now insert expression (A.43) in the Fisher matrix (A.38), we get

$$\begin{aligned}\boldsymbol{J}^{\mathrm{est}}_{ij} &= \frac{1}{2}\mathrm{tr}\,\left(\boldsymbol{G}^{\mathrm{est}}_{i}\boldsymbol{G}^{\mathrm{est}}_{j}\right)\\ &= \frac{1}{2}\mathrm{tr}\,\left(\tilde{\boldsymbol{L}}\boldsymbol{C}^{\mathrm{data}-1}\tilde{\boldsymbol{L}}^{\dagger}\boldsymbol{L}^{\dagger}\boldsymbol{C}^{\mathrm{data}}_{,i}\boldsymbol{L}\tilde{\boldsymbol{L}}\boldsymbol{C}^{\mathrm{data}-1}\tilde{\boldsymbol{L}}^{\dagger}\boldsymbol{L}^{\dagger}\boldsymbol{C}^{\mathrm{data}}_{,j}\boldsymbol{L}\right).\end{aligned} \tag{A.47}$$

In general, this will differ from the Fisher matrix of the data. If we assume, however, that the linear operator is invertible ($\exists\boldsymbol{L}^{-1}$), then eq. (A.47) reduces to

$$\boldsymbol{J}^{\mathrm{est}}_{ij} = \frac{1}{2}\mathrm{tr}\,\left(\boldsymbol{L}^{-1}\boldsymbol{G}^{\mathrm{data}}_{i}\boldsymbol{G}^{\mathrm{data}}_{j}\boldsymbol{L}\right). \tag{A.48}$$

[1] Here a Gaussian likelihood is assumed, but the result does not rely on the Gaussianity of the data (see e.g. Seljak, 1998).

Invoking that the trace of a product of matrices is invariant under cyclic permutations, we see that

$$\boldsymbol{J}_{ij}^{\mathrm{est}} = \frac{1}{2}\mathrm{tr}\,\left(\boldsymbol{G}_i^{\mathrm{data}}\boldsymbol{G}_j^{\mathrm{data}}\right) = \boldsymbol{J}_{ij}^{\mathrm{data}}. \tag{A.49}$$

This shows the result that any linear invertible filter conserves information, regardless of the parameters that one wants to estimate. However, one should be careful with this statement because linear filters are, in general, not invertible unless the data and signal space have the same dimension, the noise is non-zero for any frequency, and the $\boldsymbol{R}$- and $\boldsymbol{S}$-matrices are invertible. Usually the data and signal space will differ and the $\boldsymbol{R}$-matrix will not be exactly invertible.

A.9 Jeffrey's prior for the 3-dimensional power spectrum

Let us start by assuming a Gaussian likelihood[1]

$$P(\boldsymbol{s} \mid P_{\mathrm{S}}(\boldsymbol{k})) \propto \prod_{\boldsymbol{k}} \frac{1}{\sqrt{P_{\mathrm{S}}(\boldsymbol{k})}} \exp\left(-\frac{|s(\boldsymbol{k})|^2}{2P_{\mathrm{S}}(\boldsymbol{k})}\right). \tag{A.50}$$

The log-likelihood is then given by

$$\log\left(P(\boldsymbol{s} \mid P_{\mathrm{S}}(\boldsymbol{k}))\right) \propto \sum_{\boldsymbol{k}} \left[\log\left(P_{\mathrm{S}}(\boldsymbol{k})\right) + \frac{|s(\boldsymbol{k})|^2}{P_{\mathrm{S}}(\boldsymbol{k})}\right]. \tag{A.51}$$

We now need the second derivatives of the log-likelihood with respect to the parameter P_{S}

$$\frac{\partial^2}{\partial P_{\mathrm{S}}(\boldsymbol{k})^2}\log\left(P(\boldsymbol{s} \mid P_{\mathrm{S}}(\boldsymbol{k}))\right) \propto \left[-\frac{1}{P_{\mathrm{S}}^2(\boldsymbol{k})} + \frac{2|\,s(\boldsymbol{k})|^2}{P_{\mathrm{S}}^3(\boldsymbol{k})}\right]. \tag{A.52}$$

The next step consists of calculating the Fisher information by performing the integral $\int \mathrm{d}s P(s \mid P_{\mathrm{S}}(\boldsymbol{k}))$ on the above quantity, which is equivalent to performing the following ensemble average (see section 2.2)

$$J(P_{\mathrm{S}}(\boldsymbol{k})) = \langle \frac{\partial^2}{\partial P_{\mathrm{S}}(\boldsymbol{k})^2}\log\left(P(\boldsymbol{s} \mid P_{\mathrm{S}}(\boldsymbol{k}))\right)\rangle_{(\boldsymbol{s}|\boldsymbol{p})} \propto \frac{1}{P_{\mathrm{S}}^2(\boldsymbol{k})}, \tag{A.53}$$

where we have taken into account that $P_{\mathrm{S}}(\boldsymbol{k}) = \langle |s(\boldsymbol{k})|^2\rangle_{(\boldsymbol{s}|\boldsymbol{p})}$. Finally the square-root of the Fisher information leads to Jeffrey's prior

$$P(P_{\mathrm{S}}(\boldsymbol{k})) = \sqrt{J(P_{\mathrm{S}}(\boldsymbol{k}))} \propto P_{\mathrm{S}}(\boldsymbol{k})^{-1}. \tag{A.54}$$

Following Wandelt *et al.* (2004) we can argue in a more intuitive way that $P(P_{\mathrm{S}}(\boldsymbol{k})) \propto P_{\mathrm{S}}(\boldsymbol{k})^{-1}$ is a solution to a measure invariant under scale transformations of the form $P(P_{\mathrm{S}}(\boldsymbol{k}))\mathrm{d}P_{\mathrm{S}}(\boldsymbol{k}) = P(\alpha P_{\mathrm{S}}(\boldsymbol{k}))\alpha\mathrm{d}P_{\mathrm{S}}(\boldsymbol{k})$ (here we have generalized this result to the 3-dimensional power spectrum).

[1] Note that the likelihood for $P_{\mathrm{S}}(\boldsymbol{k})$ is the prior for $\boldsymbol{s}$.

A.10 MEM with Gaussian and Poissonian likelihoods

The quantity to maximize is given by

$$Q^{\mathrm{E}}(\boldsymbol{s} \mid \boldsymbol{p}) = \alpha S^{\mathrm{E}}(\boldsymbol{s} \mid \boldsymbol{p}) + \log \mathcal{L}(\boldsymbol{s} \mid \boldsymbol{d}, \boldsymbol{p}). \tag{A.55}$$

After some calculations we see that the gradient of the entropy for PADs is

$$\nabla S^{\mathrm{E}}_{+}(\boldsymbol{s}' \mid \boldsymbol{p})_i = -\log\left(\frac{s'_i}{m_i}\right), \tag{A.56}$$

and for positive and negative distributions

$$\nabla S^{\mathrm{E}}_{\pm}(\boldsymbol{s} \mid \boldsymbol{p})_i = -\log\left(\frac{w_i + s_i}{m_i}\right). \tag{A.57}$$

We took into account that $\partial w_i/\partial s_j = s_i/w_i\delta_{ij}$. It is then more straightforward to calculate the S^{E} curvature for PADs

$$\nabla\nabla S^{\mathrm{E}}_{+}(\boldsymbol{s}' \mid \boldsymbol{p}) = -\mathrm{diag}(\boldsymbol{s}')^{-1}, \tag{A.58}$$

and for positive and negative distributions,

$$\nabla\nabla S^{\mathrm{E}}_{\pm}(\boldsymbol{s} \mid \boldsymbol{p}) = -\mathrm{diag}(\boldsymbol{w})^{-1}. \tag{A.59}$$

Analogously, we calculate the gradient of the $\log\mathcal{L}(\boldsymbol{s} \mid \boldsymbol{d})$ for the Gaussian case valid for positive ($\boldsymbol{s}'$) and positive and negative signals ($\boldsymbol{s}_{\pm}$)

$$\nabla \log \mathcal{L}_{\mathrm{G}}(\boldsymbol{s} \mid \boldsymbol{d}, \boldsymbol{p})_i = -\frac{1}{2}\nabla\chi^2(\boldsymbol{s})_i = -\Big(\boldsymbol{R}^{\dagger}\boldsymbol{N}^{-1}(\boldsymbol{R}\boldsymbol{s} - \boldsymbol{d})\Big)_i, \tag{A.60}$$

and the corresponding curvature

$$\nabla\nabla \log \mathcal{L}_{\mathrm{G}}(\boldsymbol{s} \mid \boldsymbol{d}, \boldsymbol{p}) = -\frac{1}{2}\nabla\nabla\chi^2(\boldsymbol{s}) = -\boldsymbol{R}^{\dagger}\boldsymbol{N}^{-1}\boldsymbol{R}. \tag{A.61}$$

The Poissonian case leads to

$$\begin{aligned}
\nabla \log \mathcal{L}_{\mathrm{P}}(\boldsymbol{s} \mid \boldsymbol{d}, \boldsymbol{p})_i &= b\overline{n_{\mathrm{g}}} \sum_k \Big[R_{ki}\Big(-1 + (\sum_j R_{kj}{s'}_j + c_k)^{-1}({d'}_k + c_k)\Big)\Big] \\
&= b\overline{n_{\mathrm{g}}}\Big[\boldsymbol{R}^{\dagger}\Big(-\vec{1} + \mathrm{diag}\Big((\boldsymbol{R}\boldsymbol{s}') + \boldsymbol{c}\Big)^{-1}(\boldsymbol{d}' + \boldsymbol{c})\Big)\Big]_i,
\end{aligned}$$

and

$$\begin{aligned}
\nabla\nabla \log \mathcal{L}_{\mathrm{P}}(\boldsymbol{s} \mid \boldsymbol{d}, \boldsymbol{p})_{ij} &= -b^2\overline{n_{\mathrm{g}}}^2 \sum_k \Big[R_{ki}(\sum_l R_{kl}{s'}_l + c_k)^{-2}R_{kj}({d'}_k + c_k)\Big] \\
&= -b^2\overline{n_{\mathrm{g}}}^2\Big[\boldsymbol{R}^{\dagger}\Big(\mathrm{diag}\Big((\boldsymbol{R}\boldsymbol{s}') + \boldsymbol{c}\Big)^{-2}\boldsymbol{R}^{\dagger}(\boldsymbol{d}' + \boldsymbol{c})\Big)\Big]_{ij}.
\end{aligned}$$

Note that when dealing with over-density fields one should do the following substitution: ${\boldsymbol{s}'}_i = \overline{n_{\mathrm{g}}}(1 + b\boldsymbol{s}_i)$ in the last two expressions.

Summing up, we have the following gradient of Q^{E} for PADs

$$\nabla Q^{\mathrm{E}}_{+}(\boldsymbol{s}' \mid \boldsymbol{p})_i = -\alpha \log\left(\frac{s'_i}{m_i}\right) + \nabla \log \mathcal{L}(\boldsymbol{s}' \mid \boldsymbol{d}, \boldsymbol{p})_i, \tag{A.62}$$

and for positive and negative distributions

$$\nabla Q^{\mathrm{E}}_{\pm}(\boldsymbol{s} \mid \boldsymbol{p})_i = -\alpha \log\left(\frac{w_i - s_i}{m_i}\right) + \nabla \log \mathcal{L}(\boldsymbol{s} \mid \boldsymbol{d}, \boldsymbol{p})_i, \tag{A.63}$$

and the corresponding curvatures

$$\nabla\nabla Q^{\mathrm{E}}_{+}(\boldsymbol{s}' \mid \boldsymbol{p}) = -\alpha \mathrm{diag}(\boldsymbol{s}')^{-1} + \nabla\nabla \log \mathcal{L}(\boldsymbol{s}' \mid \boldsymbol{d}, \boldsymbol{p}), \tag{A.64}$$

$$\nabla\nabla Q^{\mathrm{E}}_{\pm}(\boldsymbol{s} \mid \boldsymbol{p}) = -\alpha \mathrm{diag}(\boldsymbol{w})^{-1} + \nabla\nabla \log \mathcal{L}(\boldsymbol{s} \mid \boldsymbol{d}, \boldsymbol{p}). \tag{A.65}$$

The corresponding likelihood (Gaussian or Poissonian) has to be inserted in each of the expressions for the gradient or curvature of Q^{E}. For the choice of an optimal regularization constant α see e.g. Maisinger *et al.* (1997) and Hobson *et al.* (1998).

Appendix B

Inverse and regularization methods

B.1 Krylov methods: Conjugate Gradients

B.1.1 Orthogonality between the residuals and the searching vectors

Eq. (3.30) tells us that each error vector $\boldsymbol{\eta}^{j+1}$ is $\boldsymbol{A}$-orthogonal to the previous searching vector $\boldsymbol{M\mu}^{j}$. Since all different searching vectors $\boldsymbol{M\mu}^{i}$ are $\boldsymbol{A}$-orthogonal to each other by construction, and the error vectors are given by the linear combination of the previous error vector and the previous searching vector (eq. (3.27)), it follows that each error vector $\boldsymbol{\eta}^{j+1}$ is $\boldsymbol{A}$-orthogonal to all previous searching vectors $\boldsymbol{\mu}^{i}$, i.e. for $i \leq j$,

$$\langle \boldsymbol{\eta}^{j+1} | \boldsymbol{M\mu}^{i} \rangle_{\boldsymbol{A}} = 0. \tag{B.1}$$

Using eq. (3.28) we can write eq. (B.1) as

$$\langle \boldsymbol{\xi}^{j+1} | \boldsymbol{M\mu}^{i} \rangle = 0, \tag{B.2}$$

being $i \leq j$.

$\boldsymbol{A}$pplying the inner product between the searching vectors $\boldsymbol{M\mu}^{i}$ and the recurrent formula for the residuals (eq. 3.29), we get

$$\langle \boldsymbol{\xi}^{j+1} | \boldsymbol{M\mu}^{i} \rangle = \langle \boldsymbol{\xi}^{j} | \boldsymbol{M\mu}^{i} \rangle - \tau^{j} \langle \boldsymbol{M\mu}^{j} | \boldsymbol{M\mu}^{i} \rangle_{\boldsymbol{A}}. \tag{B.3}$$

For $i \neq j$ this equation reduces to

$$\langle \boldsymbol{\xi}^{j+1} | \boldsymbol{M\mu}^{i} \rangle = \langle \boldsymbol{\xi}^{j} | \boldsymbol{M\mu}^{i} \rangle. \tag{B.4}$$

From eq. (B.2) and eq. (B.4) we conclude that for $i < j$,

$$\langle \boldsymbol{\xi}^{j} | \boldsymbol{M\mu}^{i} \rangle = 0. \tag{B.5}$$

B.1.2 The set of residuals as a basis of linearly independent vectors

Taking the Gram-Schmidt orthogonalization scheme (eq. 3.33) and multiplying it with the residuals, we obtain

$$\langle \boldsymbol{\xi}^i | \boldsymbol{M}\boldsymbol{\mu}^j \rangle = \langle \boldsymbol{\xi}^i | \boldsymbol{M}\boldsymbol{\xi}^j \rangle + \sum_{k=0}^{j-1} \beta^{kj} \langle \boldsymbol{\xi}^i | \boldsymbol{M}\boldsymbol{\mu}^k \rangle. \tag{B.6}$$

Using the result obtained in the appendix B.1.1 (eq. B.5), one shows the orthogonality (strictly orthogonal, if $\boldsymbol{M} = \boldsymbol{I}$) between any different residuals (for $i \neq j$)[1]

$$\langle \boldsymbol{\xi}^i | \boldsymbol{M}\boldsymbol{\xi}^j \rangle = 0. \tag{B.7}$$

For $i = j$ by combining (B.5) and (B.6) we get the relation we used in equation (3.32)

$$\langle \boldsymbol{\xi}^i | \boldsymbol{M}\boldsymbol{\mu}^i \rangle = \langle \boldsymbol{\xi}^i | \boldsymbol{M}\boldsymbol{\xi}^i \rangle. \tag{B.8}$$

B.1.3 Formulae for the β-factor

From the scalar product between eq. (3.29) and the residual $\boldsymbol{\xi}^i$

$$\langle \boldsymbol{\xi}^{j+1} | \boldsymbol{M}\boldsymbol{\xi}^i \rangle = \langle \boldsymbol{\xi}^j | \boldsymbol{M}\boldsymbol{\xi}^i \rangle - \tau^j \langle \boldsymbol{M}\boldsymbol{\mu}^j | \boldsymbol{M}\boldsymbol{\xi}^i \rangle_{\boldsymbol{A}}, \tag{B.9}$$

it is clear that the β-factors are all zero except for one. Notice that the denominator in β, given by $\langle \boldsymbol{M}\boldsymbol{\mu}^j | \boldsymbol{M}\boldsymbol{\xi}^i \rangle_{\boldsymbol{A}}$ cancels out if neither $i = j+1$ nor $i = j$. The latter is excluded according to the definition of β (see eqs. 3.33 and 3.35). Gram-Schmidt orthogonalization thus simplifies to eq. (3.36), with

$$\beta^{j+1}_{\mathrm{EXP}} = -\frac{\langle \boldsymbol{M}\boldsymbol{\xi}^{j+1} | \boldsymbol{M}\boldsymbol{\mu}^j \rangle_{\boldsymbol{A}}}{\langle \boldsymbol{M}\boldsymbol{\mu}^j | \boldsymbol{M}\boldsymbol{\mu}^j \rangle_{\boldsymbol{A}}}. \tag{B.10}$$

Other expressions for this factor can be derived by replacing $i = j+1$ in eq. (B.9)

$$\langle \boldsymbol{M}\boldsymbol{\mu}^j | \boldsymbol{M}\boldsymbol{\xi}^{j+1} \rangle_{\boldsymbol{A}} = -\frac{1}{\tau^j} \langle \boldsymbol{\xi}^{j+1} | \boldsymbol{M}\boldsymbol{\xi}^{j+1} \rangle. \tag{B.11}$$

Substituting this expression in eq. (3.35) and using the formula for τ^j (eq. 3.32) one obtains the Fletcher-Reeves equation

$$\beta^{j+1}_{\mathrm{FR}} = \frac{\langle \boldsymbol{\xi}^{j+1} | \boldsymbol{M}\boldsymbol{\xi}^{j+1} \rangle}{\langle \boldsymbol{\xi}^j | \boldsymbol{M}\boldsymbol{\xi}^j \rangle}. \tag{B.12}$$

Polak-Ribières formula can now be obtained trivially by taking expression (B.7) into account. Let us do an invariant operation by adding $-\langle \boldsymbol{\xi}^{j+1} | \boldsymbol{M}\boldsymbol{\xi}^j \rangle$ to the nominator in Fletcher-Reeves formula

$$\langle \boldsymbol{\xi}^{j+1} | \boldsymbol{M}\boldsymbol{\xi}^{j+1} \rangle - \langle \boldsymbol{\xi}^{j+1} | \boldsymbol{M}\boldsymbol{\xi}^j \rangle = \langle \boldsymbol{\xi}^{j+1} | \boldsymbol{M}(\boldsymbol{\xi}^{j+1} - \boldsymbol{\xi}^j) \rangle, \tag{B.13}$$

[1] This result is at first glance only valid for $i < j$. However, with the additional requirement that the matrix $\boldsymbol{M}$ be self-adjoint, the generalization to $i \neq j$ is trivial.

which immediately leads to Polak-Ribières expression

$$\beta_{\mathrm{PR}}^{j+1} = \frac{\langle \boldsymbol{\xi}^{j+1} | \boldsymbol{M}(\boldsymbol{\xi}^{j+1} - \boldsymbol{\xi}^{j}) \rangle}{\langle \boldsymbol{\xi}^{j} | \boldsymbol{M}\boldsymbol{\xi}^{j} \rangle}. \tag{B.14}$$

In order to get Hestenes-Stiefels formula one has to consider eqs. (B.8) and (B.5) in the denominator of β_{PR}

$$\langle \boldsymbol{\xi}^{j} | \boldsymbol{M}\boldsymbol{\xi}^{j} \rangle = \langle \boldsymbol{\mu}^{j} | \boldsymbol{M}\boldsymbol{\xi}^{j} \rangle - \langle \boldsymbol{\mu}^{j} | \boldsymbol{M}\boldsymbol{\xi}^{j+1} \rangle = \langle \boldsymbol{\mu}^{j} | \boldsymbol{M}(\boldsymbol{\xi}^{j} - \boldsymbol{\xi}^{j+1}) \rangle, \tag{B.15}$$

resulting in the following expression

$$\beta_{\mathrm{HS}}^{j+1} = -\frac{\langle \boldsymbol{\xi}^{j+1} | \boldsymbol{M}(\boldsymbol{\xi}^{j+1} - \boldsymbol{\xi}^{j}) \rangle}{\langle \boldsymbol{\mu}^{j} | \boldsymbol{M}(\boldsymbol{\xi}^{j+1} - \boldsymbol{\xi}^{j}) \rangle}. \tag{B.16}$$

Due to the relations derived in this appendix other equivalent formulae for β (summarized in table 3.1) can be found, which differ in their numerical behavior. Note that from the 16 possible schemes presented here, only 3 are discussed in the literature.

B.1.4 Preconditioned non-linear time step

The function under consideration is expanded until the second order around $\tau^j \boldsymbol{M}\boldsymbol{\mu}^j$ according to eq. (3.26)

$$Q_{\boldsymbol{A}}(\boldsymbol{\psi}^j + \tau^j \boldsymbol{M}\boldsymbol{\mu}^j) \simeq Q_{\boldsymbol{A}}(\boldsymbol{\psi}^j) + \tau^j \langle \nabla Q_{\boldsymbol{A}}(\boldsymbol{\psi}^j) | \boldsymbol{M}\boldsymbol{\mu}^j \rangle + \frac{\tau^{j2}}{2} \langle \boldsymbol{M}\boldsymbol{\mu}^j | \boldsymbol{M}\boldsymbol{\mu}^j \rangle_{\nabla\nabla Q_{\boldsymbol{A}}(\boldsymbol{\psi}^j)}. \tag{B.17}$$

Then the derivative with respect to the searching vector is done to find the extremum

$$\frac{\mathrm{d}}{\mathrm{d}\tau^j} Q_{\boldsymbol{A}}(\boldsymbol{\psi}^j + \tau^j \boldsymbol{M}\boldsymbol{\mu}^j) \simeq \langle \nabla Q_{\boldsymbol{A}}(\boldsymbol{\psi}^j) | \boldsymbol{M}\boldsymbol{\mu}^j \rangle + \tau^j \langle \boldsymbol{M}\boldsymbol{\mu}^j | \boldsymbol{M}\boldsymbol{\mu}^j \rangle_{\nabla\nabla Q_{\boldsymbol{A}}(\boldsymbol{\psi}^j)}. \tag{B.18}$$

By setting this equation to zero, one finds an expression for the time step

$$\tau^j = -\frac{\langle \nabla Q_{\boldsymbol{A}}(\boldsymbol{\psi}^j) | \boldsymbol{M}\boldsymbol{\mu}^j \rangle}{\langle \boldsymbol{M}\boldsymbol{\mu}^j | \boldsymbol{M}\boldsymbol{\mu}^j \rangle_{\nabla\nabla Q_{\boldsymbol{A}}(\boldsymbol{\psi}^j)}}. \tag{B.19}$$

Note that the last equation can be rewritten using relation (B.8) as

$$\tau^j = -\frac{\langle \nabla Q_{\boldsymbol{A}}(\boldsymbol{\psi}^j) | \boldsymbol{M} \nabla Q_{\boldsymbol{A}}(\boldsymbol{\psi}^j) \rangle}{\langle \boldsymbol{M}\boldsymbol{\mu}^j | \boldsymbol{M}\boldsymbol{\mu}^j \rangle_{\nabla\nabla Q_{\boldsymbol{A}}(\boldsymbol{\psi}^j)}}. \tag{B.20}$$

B.2 Bayes, Tikhonov, asymptotic regularization and learning algorithms

We want to solve eq. (3.3) from a Bayesian perspective. Let us assume a Gaussian likelihood with covariance $\boldsymbol{I}$

$$\mathcal{L}(\boldsymbol{\psi} \mid \boldsymbol{f}, \boldsymbol{p}) = G(\boldsymbol{f} - \boldsymbol{A}\boldsymbol{\psi}, \boldsymbol{I}), \tag{B.21}$$

which is a fair assumption in the absence of noise (eq. (3.3) is equivalent to eq. (2.2) without noise, $\boldsymbol{\epsilon} = 0$). Let us further assume a Gaussian prior around a prior solution $\boldsymbol{\psi}^*$ with covariance $\tau\tilde{\boldsymbol{M}}^{-1}$

$$P(\boldsymbol{\psi} \mid \boldsymbol{p}) = G(\boldsymbol{\psi} - \boldsymbol{\psi}^*, \tau\tilde{\boldsymbol{M}}^{-1}). \tag{B.22}$$

We can now calculate the MAP which coincides in this case with the mean of the posterior. Let us look at the quantity given by the $\log$-posterior PDF

$$||\boldsymbol{f} - \boldsymbol{A}\boldsymbol{\psi}||^2 + \tau||\boldsymbol{\psi} - \boldsymbol{\psi}^*||^2_{\tilde{\boldsymbol{M}}}, \tag{B.23}$$

which is a generalization of Tikhonov regularization. Minimizing the negative $\log$-posterior yields the following equation for the Bayesian estimator $\langle\boldsymbol{\psi}\rangle_{\mathrm{B}}$

$$\boldsymbol{A}^\dagger(\boldsymbol{A}\langle\boldsymbol{\psi}\rangle_{\mathrm{B}} - \boldsymbol{f}) + \tau^{-1}\tilde{\boldsymbol{M}}(\langle\boldsymbol{\psi}\rangle_{\mathrm{B}} - \boldsymbol{\psi}^*) = 0. \tag{B.24}$$

If we now choose $\tilde{\boldsymbol{M}} = \boldsymbol{A}^\dagger\boldsymbol{M}^{-1}$ ($\boldsymbol{M}$ is an invertible matrix) we get

$$\boldsymbol{A}^\dagger\left(\boldsymbol{M}^{-1}(\boldsymbol{\psi}^* - \langle\boldsymbol{\psi}\rangle_{\mathrm{B}}) + \tau(\boldsymbol{f} - \boldsymbol{A}\langle\boldsymbol{\psi}\rangle_{\mathrm{B}})\right) = 0, \tag{B.25}$$

This equation will be fulfilled if the following equality holds

$$\langle\boldsymbol{\psi}\rangle_{\mathrm{B}} = \boldsymbol{\psi}^* + \tau\boldsymbol{M}(\boldsymbol{f} - \boldsymbol{A}\langle\boldsymbol{\psi}\rangle_{\mathrm{B}}). \tag{B.26}$$

The estimator $\langle\boldsymbol{\psi}\rangle_{\mathrm{B}}$ for the solution to the inverse problem (eq. (3.3)) is expressed in eq. (B.26) as the prior solution $\boldsymbol{\psi}^*$ plus a correction term given by the residual $\boldsymbol{f} - \boldsymbol{A}\langle\boldsymbol{\psi}\rangle_{\mathrm{B}}$. Since only the residual based on the prior solution is known, the following substitution must be done on the right-hand-side (rhs) $\langle\boldsymbol{\psi}\rangle_{\mathrm{B}} \to \psi^*$ leading to

$$\langle\boldsymbol{\psi}\rangle_{\mathrm{B}} \simeq \boldsymbol{\psi}^* + \tau\boldsymbol{M}(\boldsymbol{f} - \boldsymbol{A}\boldsymbol{\psi}^*). \tag{B.27}$$

This can be interpreted as an iterative scheme, in which the estimator is the update $j+1$ ($\langle\boldsymbol{\psi}\rangle_{\mathrm{B}} \to \boldsymbol{\psi}^{j+1}$ on the left-hand-side (lhs)) of the estimator at the previous step j ($\boldsymbol{\psi}^* \to \boldsymbol{\psi}^j$ on the rhs)

$$\boldsymbol{\psi}^{j+1} = \boldsymbol{\psi}^j + \tau\boldsymbol{M}(\boldsymbol{f} - \boldsymbol{A}\boldsymbol{\psi}^j). \tag{B.28}$$

In this way, we have found the general iterative method (eq. 3.14) derived with the asymptotic regularization in section (3.1.2). From the Bayesian point of view, this scheme could be interpreted as a learning algorithm, in which the estimator of the solution to the inverse problem is calculated from the prior solution and becomes itself the prior solution for the subsequent iteration.

B.3 Preconditioning

We can enhance the convergence of the iteration methods by multiplying the matrix we want to invert by another matrix that is close to its inverse

$$\boldsymbol{MA\psi} = \boldsymbol{Mf}, \tag{B.29}$$

with $\boldsymbol{M} \sim \boldsymbol{A}^{-1}$. Let us show this by deriving eq. (3.14) in a different way. We can invert $\boldsymbol{MA}$ using the Neumann expansion for the inverse of an operator

$$\boldsymbol{\psi} = (\boldsymbol{MA})^{-1}\boldsymbol{Mf} = \sum_{i=0}^{\infty}(\boldsymbol{I} - \boldsymbol{MA})^i\boldsymbol{Mf}. \tag{B.30}$$

This iteration scheme will converge if $||\boldsymbol{I} - \boldsymbol{MA}|| < 1$. Let us introduce the following notation

$$\boldsymbol{\psi} \equiv \sum_{i=0}^{\infty}\boldsymbol{\psi}[i], \tag{B.31}$$

$$\boldsymbol{\psi}^j \equiv \sum_{i=0}^{j}\boldsymbol{\psi}[i], \tag{B.32}$$

with

$$\boldsymbol{\psi}[i] \equiv (\boldsymbol{I} - \boldsymbol{MA})^i\boldsymbol{Mf}. \tag{B.33}$$

It follows that

$$\boldsymbol{\psi}[i+1] = (\boldsymbol{I} - \boldsymbol{MA})\boldsymbol{\psi}[i], \tag{B.34}$$

and summing over i we get

$$\sum_{i=0}^{j}\boldsymbol{\psi}[i+1] = \sum_{i=0}^{j}\boldsymbol{\psi}[i] - \sum_{i=0}^{j}\boldsymbol{MA\psi}[i]. \tag{B.35}$$

Manipulating the indices, we see that

$$\sum_{i=0}^{j}\boldsymbol{\psi}[i+1] = \sum_{i=0}^{j+1}\boldsymbol{\psi}[i] - \boldsymbol{\psi}[0]. \tag{B.36}$$

Combining the last two equations we obtain eq. (3.14)[1]

$$\boldsymbol{\psi}^{j+1} = \boldsymbol{\psi}^j + \boldsymbol{M}(\boldsymbol{f} - \boldsymbol{A\psi}^j), \tag{B.37}$$

with

$$\boldsymbol{\psi}[0] = \boldsymbol{\psi}^0 = \boldsymbol{Mf}. \tag{B.38}$$

The meaning of the preconditioning matrix $\boldsymbol{M}$ is clear when we look at eq. (B.30). There it can be seen that a much more rapid convergence is obtained if $(\boldsymbol{I} - \boldsymbol{MA})$ is close to zero, that is if $\boldsymbol{M}$ is close to the inverse of $\boldsymbol{A}$.

[1] The iteration time step τ has been absorbed here in the matrix $\boldsymbol{M}$.

Appendix C

Poissonian distributions

C.1 Properties of Poissonian distributions

We derive here some of the properties for Poissonian distributions $P(n|\lambda) = \lambda^n \mathrm{e}^{-\lambda}/n!$ that we use in chapter (5).

- Mean for the Poissonian distribution

$$\langle n \rangle_n = \sum_{n=0}^{\infty} n\, P(n|\lambda) = \sum_{n=0}^{\infty} \frac{\lambda^{n-1}\mathrm{e}^{-\lambda}}{(n-1)!}\lambda = \lambda. \tag{C.1}$$

- Variance for the Poissonian distribution

$$\begin{aligned} \langle n^2 \rangle_n &= \sum_{n=0}^{\infty} n^2 P(n|\lambda) = \sum_{n=0}^{\infty} (n-1+1)\frac{\lambda^{n-1}\mathrm{e}^{-\lambda}}{(n-1)!}\lambda = \lambda(\lambda+1) \\ \langle (n - \langle n \rangle_n)^2 \rangle_n &= \langle n^2 \rangle_n - \langle n \rangle_n^2 = \lambda(\lambda+1) - \lambda^2 = \lambda = \langle n \rangle_n \\ \langle n^2 \rangle_n &= \langle n^2 \rangle_n - \langle n \rangle_n^2 + \langle n \rangle_n^2 = \langle n \rangle_n + \langle n \rangle_n^2. \end{aligned} \tag{C.2}$$

- Flat prior assumption with a Poissonian likelihood

  Bayes theorem states

$$P(\lambda|n) = \frac{P(n|\lambda)P(\lambda)}{P(n)}. \tag{C.3}$$

  The flat prior is defined as: $P(\lambda) = \mathrm{c}$, with c being a constant. The evidence is then given by

$$P(n) = \int_0^{\infty} \mathrm{d}\lambda\, P(n|\lambda)c = c, \tag{C.4}$$

  since

$$\int_0^{\infty} \mathrm{d}\lambda\, P(n|\lambda) = \int_0^{\infty} \mathrm{d}\lambda\, \frac{\lambda^n \mathrm{e}^{-\lambda}}{(n)!} = \frac{\Gamma(n+1)}{n!} = 1. \tag{C.5}$$

Consequently, we obtain

$$P(\lambda|n) = P(n|\lambda). \tag{C.6}$$

- Estimator for the mean under a flat prior assumption

$$\int_0^\infty \mathrm{d}\lambda\, \lambda\, P(\lambda|n) = \int_0^\infty \mathrm{d}\lambda\, \frac{\lambda^{n+1}\mathrm{e}^{-\lambda}}{(n+1)!}(n+1) = n+1. \tag{C.7}$$

- Variance for the mean under a flat prior assumption

$$\begin{aligned}
&\langle(\lambda - \langle\lambda\rangle_\lambda)^2\rangle_\lambda = \langle\lambda^2\rangle_\lambda - \langle\lambda\rangle_\lambda^2 \\
&\langle\lambda^2\rangle_\lambda = \int_0^\infty \mathrm{d}\lambda\, \lambda^2 \frac{\mathrm{e}^{-\lambda}\lambda^n}{n!} = \int_0^\infty \mathrm{d}\lambda\, \frac{\mathrm{e}^{-\lambda}\lambda^{n+2}}{(n+2)!}(n+2)(n+1) = (n+2)(n+1) \\
&\langle\lambda^2\rangle_\lambda - \langle\lambda\rangle_\lambda^2 = (n+1)(n+2-(n+1)) = n+1.
\end{aligned} \tag{C.8}$$

C.2 Noise covariance-matrix for a Poissonian distribution on a grid

The convolution produced by gridding the galaxy field is given by the following transformation

$$n'_{\mathrm{g}}(\boldsymbol{r}_g) = \int \mathrm{d}\boldsymbol{r}'\, W(\boldsymbol{r}_g - \boldsymbol{r}')\, n_{\mathrm{g}}(\boldsymbol{r}'). \tag{C.9}$$

The number density values n'_{g} should only be evaluated on the grid positions $\boldsymbol{r}_g$[1]. In order to have a representation of the grid into continuous space we define according to Hockney & Eastwood (1981)

$$\tilde{n}_{\mathrm{g}}(\boldsymbol{r}) \equiv \Pi\big(\frac{\boldsymbol{r}}{H}\big) \int \mathrm{d}\boldsymbol{r}'\, W(\boldsymbol{r} - \boldsymbol{r}')\, n_{\mathrm{g}}(\boldsymbol{r}'), \tag{C.10}$$

with $\Pi(\boldsymbol{r}) = \sum_{\boldsymbol{n}\in\mathbb{Z}} \delta_{\mathrm{D}}(\boldsymbol{r} - \boldsymbol{n})$ and H being the grid-spacing.

The expected number of galaxies on the grid is given by

$$\langle\tilde{n}_{\mathrm{g}}(\boldsymbol{r})\rangle_{n_{\mathrm{g}}} = \Delta V\, \Pi\big(\frac{\boldsymbol{r}}{H}\big) \int \mathrm{d}\boldsymbol{r}'\, W(\boldsymbol{r} - \boldsymbol{r}')\, \rho_{\mathrm{g}}(\boldsymbol{r}') = \Delta V \tilde{\rho}_{\mathrm{g}}(\boldsymbol{r}). \tag{C.11}$$

Let us now use the property for Poissonian likelihoods: $\langle n_{\mathrm{g}}^2\rangle_{n_{\mathrm{g}}} = \langle n_{\mathrm{g}}\rangle_{n_{\mathrm{g}}}^2 + \langle n_{\mathrm{g}}\rangle_{n_{\mathrm{g}}}$ to find an expression for the noise covariance-matrix (see eq. C.2 in appendix C.1). Using this property we can write

$$\langle n_{\mathrm{g}}(\boldsymbol{r}) n_{\mathrm{g}}(\boldsymbol{r}')\rangle_{n_{\mathrm{g}}} = \Delta V^2 \rho_{\mathrm{g}}(\boldsymbol{r})\rho_{\mathrm{g}}(\boldsymbol{r}') + \Delta V \rho_{\mathrm{g}}(\boldsymbol{r}')\delta^{\mathrm{K}}_{\boldsymbol{r},\boldsymbol{r}'}. \tag{C.12}$$

Using definition (C.10) we obtain

$$\begin{aligned}
&\langle\tilde{n}_{\mathrm{g}}(\boldsymbol{r}_1)\tilde{n}_{\mathrm{g}}(\boldsymbol{r}_2)\rangle_{n_{\mathrm{g}}} \\
&= \Pi\big(\frac{\boldsymbol{r}_1}{H}\big)\Pi\big(\frac{\boldsymbol{r}_2}{H}\big) \int \mathrm{d}\boldsymbol{r}'_1 \int \mathrm{d}\boldsymbol{r}'_2\, W(\boldsymbol{r}_1 - \boldsymbol{r}'_1) W(\boldsymbol{r}_2 - \boldsymbol{r}'_2) \langle n_{\mathrm{g}}(\boldsymbol{r}'_1) n_{\mathrm{g}}(\boldsymbol{r}'_2)\rangle_{n_{\mathrm{g}}} \\
&= \Delta V^2\, \tilde{\rho}_{\mathrm{g}}(\boldsymbol{r}_1)\tilde{\rho}_{\mathrm{g}}(\boldsymbol{r}_2) + \Delta V\, \Pi\big(\frac{\boldsymbol{r}_1}{H}\big)\Pi\big(\frac{\boldsymbol{r}_2}{H}\big) \int \mathrm{d}\boldsymbol{r}'_1\, W(\boldsymbol{r}_1 - \boldsymbol{r}'_1) W(\boldsymbol{r}_2 - \boldsymbol{r}'_1) \rho_{\mathrm{g}}(\boldsymbol{r}'_1) \\
&= \langle\tilde{n}_{\mathrm{g}}(\boldsymbol{r}_1)\rangle_{n_{\mathrm{g}}} \langle\tilde{n}_{\mathrm{g}}(\boldsymbol{r}_2)\rangle_{n_{\mathrm{g}}} + \Pi\big(\frac{\boldsymbol{r}_1}{H}\big)\Pi\big(\frac{\boldsymbol{r}_2}{H}\big) \int \mathrm{d}\boldsymbol{r}'_1\, W(\boldsymbol{r}_1 - \boldsymbol{r}'_1) W(\boldsymbol{r}_2 - \boldsymbol{r}'_1) \langle n_{\mathrm{g}}(\boldsymbol{r}'_1)\rangle_{n_{\mathrm{g}}}.
\end{aligned} \tag{C.13}$$

[1] We note $W \geq 0$ and $\int \mathrm{d}\boldsymbol{r}\, W(\boldsymbol{r}) = 1$.

Accordingly, we can define the (relative) noise covariance-matrix as

$$\begin{aligned}\boldsymbol{N}(\boldsymbol{r}_1,\boldsymbol{r}_2) &\equiv \frac{1}{\overline{n}^2}\left(\langle\tilde{n}_{\rm g}(\boldsymbol{r}_1)\tilde{n}_{\rm g}(\boldsymbol{r}_2)\rangle_{n_{\rm g}} - \langle\tilde{n}_{\rm g}(\boldsymbol{r}_1)\rangle_{n_{\rm g}}\langle\tilde{n}_{\rm g}(\boldsymbol{r}_2)\rangle_{n_{\rm g}}\right)\\ &= \frac{1}{\overline{n}^2}\,\Pi(\frac{\boldsymbol{r}_1}{H})\Pi(\frac{\boldsymbol{r}_2}{H})\int {\rm d}\boldsymbol{r}_1'\,W(\boldsymbol{r}_1-\boldsymbol{r}_1')W(\boldsymbol{r}_2-\boldsymbol{r}_1')\langle n_{\rm g}(\boldsymbol{r}_1')\rangle_{n_{\rm g}}, \quad \text{(C.14)}\end{aligned}$$

where we have normalized the result, dividing by $\overline{n}^2$, in order to express the result for galaxy over-densities instead for counts.

We conclude from this calculation that the gridding Kernel has to be taken into account, similarly to the shot noise term found by Jing (2005). In appendix (C.21) we work out the relation between both noise expressions.

C.3 Model for the expected number count of galaxies

The formula that we have derived for the noise covariance in the previous section requires an estimate for $\lambda^g \equiv \langle n_{\rm g}^g\rangle_{n_{\rm g}}$. We suggest here to take the estimate of λ^g conditioned on the observations, which is then given by (see eq. C.7 in appendix C.1)

$$\langle\lambda^g\rangle_\lambda = \int_0^\infty {\rm d}\lambda^g\,\lambda^g P(\lambda^g|n^g) = n_{\rm g}^g + 1, \quad \text{(C.15)}$$

where we have assumed a flat prior (see eq. C.6 in appendix C.1) and the number of galaxy counts in the cell is given by $n_{\rm g}^g$. Note that the error on λ^g is precisely (see eq. C.8 in appendix C.1)

$$\langle(\lambda^g - \langle\lambda^g\rangle_\lambda)^2\rangle_\lambda = n_{\rm g}^g + 1. \quad \text{(C.16)}$$

C.4 Power-spectrum with a Poissonian galaxy model on a grid

We develop here the relation between the Poissonian noise covariance-matrix and the *true* power-spectrum. The essence of this relation lies on the additional ensemble average one has to introduce for the cosmic variance of the underlying density field. In the linear bias model one assumes that the expected number of galaxies within a volume element ΔV is related to the dark matter density field by $\langle n_{\rm g}(\boldsymbol{r})\rangle_{n_{\rm g}} = \Delta V\rho_{\rm g}(\boldsymbol{r}) = \overline{n}_{\rm g}(1+b\delta(\boldsymbol{r}))$, where in general one has to take into account a redshift dependence: $\overline{n}_{\rm g} = \overline{n}_{\rm g}(z)$ and $b = b(z)$. Note, that for the actual observed galaxy distribution we can therefore introduce with $\delta_{\rm g} = b\delta$: $n_{\rm g}(\boldsymbol{r}) = \overline{n}_{\rm g}(1+\delta_{\rm g}(\boldsymbol{r}))$. Substituting these relations in eq. (C.13) and performing the ensemble average over the different density field realizations we find for the lhs of eq. (C.13)

$$\begin{aligned}&\langle\langle\tilde{n}_{\rm g}(\boldsymbol{r}_1)\tilde{n}_{\rm g}(\boldsymbol{r}_2)\rangle_{n_{\rm g}}\rangle_\delta\\ &= \langle\langle\Pi(\frac{\boldsymbol{r}_1}{H})\Pi(\frac{\boldsymbol{r}_2}{H})\int {\rm d}\boldsymbol{r}_1'\int {\rm d}\boldsymbol{r}_2'\,W(\boldsymbol{r}_1-\boldsymbol{r}_1')\,W(\boldsymbol{r}_2-\boldsymbol{r}_2')\,\overline{n}_{\rm g}(1+\delta_{\rm g}(\boldsymbol{r}_1))\overline{n}_{\rm g}(1+\delta_{\rm g}(\boldsymbol{r}_2))\rangle_{n_{\rm g}}\rangle_\delta\\ &= \overline{n}_{\rm g}^2\Pi(\frac{\boldsymbol{r}_1}{H})\Pi(\frac{\boldsymbol{r}_2}{H})\int {\rm d}\boldsymbol{r}_1'\int {\rm d}\boldsymbol{r}_2'\,W(\boldsymbol{r}_1-\boldsymbol{r}_1')W(\boldsymbol{r}_2-\boldsymbol{r}_2') + \overline{n}_{\rm g}^2\langle\langle\tilde{\delta}_{\rm g}(\boldsymbol{r}_1)\tilde{\delta}_{\rm g}(\boldsymbol{r}_2)\rangle_{n_{\rm g}}\rangle_\delta, \quad \text{(C.17)}\end{aligned}$$

with the definition $\tilde{\delta}_{\rm g}(\boldsymbol{r}) \equiv \Pi(\frac{\boldsymbol{r}}{H}) \int {\rm d}\boldsymbol{r}'\, W(\boldsymbol{r}-\boldsymbol{r}')\delta_{\rm g}(\boldsymbol{r}')$, and for the rhs of eq. (C.13)

$$\begin{aligned}
&\Delta V^2\langle\tilde{\rho}_{\rm g}(\boldsymbol{r}_1)\tilde{\rho}_{\rm g}(\boldsymbol{r}_2)\rangle_\delta + \Delta V\langle\Pi(\frac{\boldsymbol{r}_1}{H})\Pi(\frac{\boldsymbol{r}_2}{H})\int {\rm d}\boldsymbol{r}_1'\, W(\boldsymbol{r}_1-\boldsymbol{r}_1')W(\boldsymbol{r}_2-\boldsymbol{r}_1')\rho_{\rm g}(\boldsymbol{r}_1')\rangle_\delta \\
&= \Delta V^2\Pi(\frac{\boldsymbol{r}_1}{H})\Pi(\frac{\boldsymbol{r}_2}{H})\langle\int {\rm d}\boldsymbol{r}_1'\, W(\boldsymbol{r}_1-\boldsymbol{r}_1')\rho_{\rm g}(\boldsymbol{r}_1')\int {\rm d}\boldsymbol{r}_2'\, W(\boldsymbol{r}_2-\boldsymbol{r}_2')\rho_{\rm g}(\boldsymbol{r}_2')\rangle_\delta \\
&\quad +\langle\Pi(\frac{\boldsymbol{r}_1}{H})\Pi(\frac{\boldsymbol{r}_2}{H})\int {\rm d}\boldsymbol{r}_1'\, W(\boldsymbol{r}_1-\boldsymbol{r}_1')W(\boldsymbol{r}_2-\boldsymbol{r}_1')\overline{n}_{\rm g}(1+b\delta(\boldsymbol{r}_1))\rangle_\delta \\
&= \overline{n}_{\rm g}^2\Pi(\frac{\boldsymbol{r}_1}{H})\Pi(\frac{\boldsymbol{r}_2}{H})\int {\rm d}\boldsymbol{r}_1'\int {\rm d}\boldsymbol{r}_2'\, W(\boldsymbol{r}_1-\boldsymbol{r}_1')W(\boldsymbol{r}_2-\boldsymbol{r}_2') \\
&\quad +\overline{n}_{\rm g}^2 b^2\Pi(\frac{\boldsymbol{r}_1}{H})\Pi(\frac{\boldsymbol{r}_2}{H})\int {\rm d}\boldsymbol{r}_1'\int {\rm d}\boldsymbol{r}_2'\, W(\boldsymbol{r}_1-\boldsymbol{r}_1')W(\boldsymbol{r}_2-\boldsymbol{r}_2')\langle\delta(\boldsymbol{r}_1')\delta(\boldsymbol{r}_2')\rangle_\delta \\
&\quad +\overline{n}_{\rm g}\Pi(\frac{\boldsymbol{r}_1}{H})\Pi(\frac{\boldsymbol{r}_2}{H})\int {\rm d}\boldsymbol{r}_1'\, W(\boldsymbol{r}_1-\boldsymbol{r}_1')W(\boldsymbol{r}_2-\boldsymbol{r}_1'). \qquad \text{(C.18)}
\end{aligned}$$

Combining the last two equations (eqns. C.17 and C.18) we obtain

$$\begin{aligned}
\langle\langle\tilde{\delta}_{\rm g}(\boldsymbol{r}_1)\tilde{\delta}_{\rm g}(\boldsymbol{r}_2)\rangle_{n_{\rm g}}\rangle_\delta &= b^2\Pi(\frac{\boldsymbol{r}_1}{H})\Pi(\frac{\boldsymbol{r}_2}{H})\int {\rm d}\boldsymbol{r}_1'\int {\rm d}\boldsymbol{r}_2'\, W(\boldsymbol{r}_1-\boldsymbol{r}_1')W(\boldsymbol{r}_2-\boldsymbol{r}_2')\langle\delta(\boldsymbol{r}_1')\delta(\boldsymbol{r}_2')\rangle_\delta \\
&\quad +\frac{V}{N}\Pi(\frac{\boldsymbol{r}_1}{H})\Pi(\frac{\boldsymbol{r}_2}{H})\int {\rm d}\boldsymbol{r}_1'\, W(\boldsymbol{r}_1-\boldsymbol{r}_1')W(\boldsymbol{r}_2-\boldsymbol{r}_1'), \qquad \text{(C.19)}
\end{aligned}$$

being $\overline{n}_{\rm g} \equiv N/V$. If we take the Fourier transform of this expression using

$$\Pi(\boldsymbol{k}) = \frac{1}{V}\int {\rm d}\boldsymbol{r}\, {\rm e}^{i\boldsymbol{k}\cdot\boldsymbol{r}}\,\Pi(\frac{\boldsymbol{r}}{H}) = \sum_{\boldsymbol{n}\in\mathbb{Z}}\delta^{\rm K}_{\boldsymbol{k},2\,{\rm diag}(\boldsymbol{k}_{Ny})\boldsymbol{n}} \qquad \text{(C.20)}$$

with $\boldsymbol{k}' = \boldsymbol{k} + 2\,{\rm diag}(\boldsymbol{k}_{Ny})\boldsymbol{n}$ and $\boldsymbol{k}_{Ny} = [k_{Nyx}, k_{Nyy}, k_{Nyz}]$ the Nyquist frequencies in x, y and z direction, we get

$$\langle\langle\tilde{\delta}_{\rm g}(\boldsymbol{k}_1)\overline{\tilde{\delta}_{\rm g}(\boldsymbol{k}_2)}\rangle_{n_{\rm g}}\rangle_\delta = \sum_{\boldsymbol{n}_1,\boldsymbol{n}_2}\Big[|W(\boldsymbol{k}_1')|^2 b^2 P(\boldsymbol{k}_1')\delta^{\rm K}_{\boldsymbol{k}_1',\boldsymbol{k}_2'} + \frac{1}{N}|W(\boldsymbol{k}_1')|^2\delta^{\rm K}_{\boldsymbol{k}_1',\boldsymbol{k}_2'}\Big]. \qquad \text{(C.21)}$$

For $\boldsymbol{k}_1 = \boldsymbol{k}_2$ we have

$$\langle\langle|\tilde{\delta}_{\rm g}(\boldsymbol{k})|^2\rangle_{n_{\rm g}}\rangle_\delta = \sum_{\boldsymbol{n}}\Big[|W(\boldsymbol{k}')|^2 b^2 P(\boldsymbol{k}') + \frac{1}{N}|W(\boldsymbol{k}')|^2\Big]. \qquad \text{(C.22)}$$

The formula we have obtained here is deduced in Jing (2005) with minor changes. Let us point them out. Since we have made the difference between the galaxy over-density $\delta_{\rm g}$ and the underlying over-density δ, we obtain a squared bias factor. Then we have made the generalization to a box with different side-lengths in each direction leading to three different Nyquist frequencies for each direction. Finally, we have clarified the underlying statistical model for this formula. This is composed by two ensemble averages: a Poissonian process for the galaxies, and a statistical homogeneous process for the underlying density field. We have distinguished between them through the notation in the ensemble average: $\langle\rangle_{n_{\rm g}}$ or $\langle\rangle_\delta$. We confirm that the approach by Peebles of introducing a gridding step on a hyperfine grid in which either zero or one galaxy is found —this approach is chosen also by Jing (2005)— implicitly assumes a Poissonian likelihood for galaxy formation.

Appendix D

Redshift-distortions treatment

D.1 Angular-averaged redshift-space real-space transformation

Let us start recalling the formula given by Zaroubi *et al.* (1995) to transforms the data from redshift-space into the reconstructed signal in real-space

$$\langle s(\boldsymbol{r})\rangle_{\rm WF} = \langle s(\boldsymbol{r})d^\dagger(\boldsymbol{z})\rangle\langle d(\boldsymbol{z})d^\dagger(\boldsymbol{z})\rangle^{-1}d(\boldsymbol{z}). \tag{D.1}$$

The non-linear power spectrum in redshift-space is then expressed by

$$P^z_{\rm NL}(k,\mu) = P^r_{\rm NL}(k,\mu)K(\mu)D(k,\mu), \tag{D.2}$$

see section (5.2.3). Erdoğdu *et al.* (2004) suggest to take the angular-average of eq. (D.2) defined as

$$P^z_{\rm NL}(k) = P^r_{\rm NL}(k)K_D(k), \tag{D.3}$$

with $K_D(k) = \frac{1}{2}\int_{-1}^{1}{\rm d}\mu K(\mu)D(k,\mu)$. They find

$$K_D(k) = \frac{4(\sigma_{\rm p}^2k^2-\beta)\beta}{\sigma_{\rm p}^4k^4} + \frac{2\beta^2}{3\sigma_{\rm p}^2k^2} + \frac{\sqrt{2}(k^2\sigma_{\rm p}^2-2\beta)^2\arctan(k\sigma_{\rm p}/\sqrt{2})}{k^5\sigma_{\rm p}^5}. \tag{D.4}$$

Accordingly, they define the correlation matrix of the signal and the data in their respective spaces as

$$\langle s(\boldsymbol{r})d^\dagger(\boldsymbol{z})\rangle = P^r_{\rm NL}(k,\mu)\sqrt{K(\mu)}\sqrt{D(k,\mu)}. \tag{D.5}$$

This matrix is then approximated by the following angular averaged expression

$$\langle s(\boldsymbol{r})d^\dagger(\boldsymbol{z})\rangle \approx P^r_{\rm NL}(k)\overline{K_D(k)}, \tag{D.6}$$

where $\overline{K_D(k)} = \frac{1}{2}\int_{-1}^{1}{\rm d}\mu\sqrt{K(\mu)}\sqrt{D(k,\mu)}$ is found to be

$$\overline{K_D(k)} = \frac{1}{2k^2\sigma_{\rm p}^2}\ln\left[k^2\sigma_{\rm p}^2\left(1+\sqrt{1+1/k^2\sigma_{\rm p}^2}\right)\right] + \frac{\beta}{k^2\sigma_{\rm p}^2}\sqrt{1+k^2\sigma_{\rm p}^2} + \frac{\beta}{k^3\sigma_{\rm p}^3}{\rm arcsinh}(k^2\sigma_{\rm p}^2). \tag{D.7}$$

D.2 Detailed-balance velocity rejection-sampling

We present here a velocity Bayesian-sampling algorithm based on a detailed balance rejection-sampling scheme. We recall the expected galaxy density in real-space: $\rho_{\rm g}(r) = \overline{\rho_{\rm g}}(1 + b\delta(r))$.

Let us define the probability to find a galaxy, which is located at r, at redshift $z = r + v_r$ with a Gaussian likelihood: $P(z|r) = G(z - r - v_r(r), \sigma_v(r))$. Further we assume that the prior for a galaxy to be positioned at r is: $P(r) \propto \rho_{\rm g}(r) \propto 1 + b\delta(r)$. Consequently, the posterior of a galaxy observed at z according to Bayes theorem is given by

$$P(r|z) = \frac{P(z|r)P(r)}{P(z)}, \tag{D.8}$$

and the posterior ratio of two possible locations r_1 and r_2 of a galaxy with redshift z reads

$$\frac{P(r_1|z)}{P(r_2|z)} = \frac{P(z|r_1)P(r_1)}{P(z|r_2)P(r_2)} = \frac{G(z - r_1 - v_r(r_1), \sigma_v(r_1))(1 + b\delta(r_1))}{G(z - r_2 - v_r(r_2), \sigma_v(r_2))(1 + b\delta(r_2))}. \tag{D.9}$$

We can now define a procedure for the position sampling. A galaxy with redshift z is assumed at step j to be located at $r = r^j$. We pick a new trial position $r' \sim G(r^j - r', \sigma_{\rm s}(r^j))$ and accept r' as r^{j+1} with probability $P_{\rm accept}(r \to r')$ so that $P(r \to r') = G(r - r', \sigma_{\rm s}(r))P_{\rm accept}(r \to r')$. We have introduced the sampling dispersion $\sigma_{\rm s}$, which is different from the physical determined dispersion σ_v and in contrast to it can be chosen freely, but should be tuned towards efficient sampling (over-relaxation). In order to find out the acceptance scheme we demand detailed balance

$$P(r|z)P(r \to r') = P(r'|z)P(r' \to r). \tag{D.10}$$

Assuming this we find for the following probability ratio

$$\begin{aligned} \frac{P_{\rm accept}(r \to r')}{P_{\rm accept}(r' \to r)} &= \frac{G(r' - r, \sigma_{\rm s}(r'))P(r'|z)}{G(r - r', \sigma_{\rm s}(r))P(r|z)} \\ &= \frac{G(r' - r, \sigma_{\rm s}(r'))G(z - r' - v_r(r'), \sigma_v(r'))\rho_{\rm g}(r')}{G(r - r', \sigma_{\rm s}(r))G(z - r - v_r(r), \sigma_v(r))\rho_{\rm g}(r)}. \end{aligned} \tag{D.11}$$

Defining a probability function given by

$$f(r \to r') \equiv G(r - r', \sigma_v(r'))G(z - r' - v_r(r'), \sigma_v(r'))\rho_{\rm g}(r'), \tag{D.12}$$

we deduce the following acceptance criterion from eq. (D.11)

$$P_{\rm accept}(r \to r') = \begin{cases} 1 & : \quad f(r \to r') > f(r' \to r) \\ \frac{f(r \to r')}{f(r' \to r)} & : \quad \text{otherwise} \end{cases}. \tag{D.13}$$

If the trial position r' is accepted with this rejection rule then detailed balance is fulfilled and the distribution of accepted galaxy positions converges versus the position of the galaxy position given the measured redshift information ($P(r|z)$).

Note that although Gaussians are used here, other distribution functions could be assumed without any change of the structure of the formalism.

References

ALBRECHT, A. & STEINHARDT, P.J. (1982). Cosmology for grand unified theories with radiatively induced symmetry breaking. *Physical Review Letters*, **48**, 1220–1223.

ASTER, R.A., BROCHERS, B. & THURBER, C.H. (2005). *Parameter estimation and inverse problems*. Elsevier Academic Press, London.

BAKUSHINSKII, A.B. (1992). The problem of the convergence of the iteratively regularized Gauss-Newton method. *Compt.Math.Phy.*, **32**, 1353–1359.

BALLINGER, W.E., PEACOCK, J.A. & HEAVENS, A.F. (1996). Measuring the cosmological constant with redshift surveys. *MNRAS*, **282**, 877–+.

BARDEEN, J.M., STEINHARDT, P.J. & TURNER, M.S. (1983). Spontaneous creation of almost scale-free density perturbations in an inflationary universe. *Phys. Rev. D*, **28**, 679–693.

BARDEEN, J.M., BOND, J.R., KAISER, N. & SZALAY, A.S. (1986). The statistics of peaks of Gaussian random fields. *ApJ*, **304**, 15–61.

BERGER, J.O. & BERNARDO, J.M. (1992). On the development of the reference prior method. In J.O. Berger, J.M. Bernardo, A.P. Dawid & A.F.M. Smith, eds., *Bayesian Statistics 4*, 35–60, Oxford University Press, Oxford.

BERNARDEAU, F. & VAN DE WEYGAERT, R. (1996). A new method for accurate estimation of velocity field statistics. *MNRAS*, **279**, 693–+.

BERTSCHINGER, E. (1987). Path integral methods for primordial density perturbations - Sampling of constrained Gaussian random fields. *ApJ*, **323**, L103–L106.

BERTSCHINGER, E. & DEKEL, A. (1989). Recovering the full velocity and density fields from Large-Scale redshift-distance samples. *ApJ*, **336**, L5–L8.

BERTSCHINGER, E. & DEKEL, A. (1991). Mapping Large-Scale Flows in Three Dimensions: Method. In D.W. Latham & L.A.N. da Costa, eds., *ASP Conf. Ser. 15: Large-Scale Structures and Peculiar Motions in the Universe*, 67–+.

BERTSCHINGER, E., DEKEL, A., FABER, S.M., DRESSLER, A. & BURSTEIN, D. (1990). Potential, velocity, and density fields from redshift-distance samples: Application - Cosmography within 6000 kilometers per second. *ApJ*, **364**, 370–395.

BISTOLAS, V. & HOFFMAN, Y. (1998). Nonlinear Constrained Realizations of the Large-Scale Structure. *ApJ*, **492**, 439–+.

BLAIZOT, J. (2007). personal communication.

BLAIZOT, J., WADADEKAR, Y., GUIDERDONI, B., COLOMBI, S.T., BERTIN, E., BOUCHET, F.R., DEVRIENDT, J.E.G. & HATTON, S. (2005). MoMaF: the Mock Map Facility. *MNRAS*, **360**, 159–175.

BLASCHKE, B., NEUBAUER, A. & SCHERZER, O. (1997). On convergence rates for the iteratively regularized Gauss-Newton method. *IMA Journal of Numerical Analysis*, **17**, 421–436.

BOND, J.R. & EFSTATHIOU, G. (1984). Cosmic background radiation anisotropies in universes dominated by nonbaryonic dark matter. *ApJ*, **285**, L45–L48.

BOTZLER, C.S., SNIGULA, J., BENDER, R. & HOPP, U. (2004). Finding structures in photometric redshift galaxy surveys: an extended friends-of-friends algorithm. *MNRAS*, **349**, 425–439.

BRANCHINI, E. & PLIONIS, M. (1996). Reconstructing Positions and Peculiar Velocities of Galaxy Clusters within 25,000 Kilometers pe r Second: The Cluster Real Space Dipole. *ApJ*, **460**, 569–+.

BRANCHINI, E., PLIONIS, M. & SCIAMA, D.W. (1996). Reconstructing Positions and Peculiar Velocities of Galaxy Clusters within 25,000 Kilometers pe r Second: The Bulk Velocity. *ApJ*, **461**, L17+.

BRENIER, Y., FRISCH, U., HÉNON, M., LOEPER, G., MATARRESE, S., MOHAYAEE, R. & SOBOLEVSKIĬ, A. (2003). Reconstruction of the early Universe as a convex optimization problem. *MNRAS*, **346**, 501–524.

BUNN, E.F. & SUGIYAMA, N. (1995). Cosmological Constant Cold Dark Matter Models and the COBE Two-Year Sky Maps. *ApJ*, **446**, 49–+.

BUNN, E.F., FISHER, K.B., HOFFMAN, Y., LAHAV, O., SILK, J. & ZAROUBI, S. (1994). Wiener filtering of the COBE Differential Microwave Radiometer data. *ApJ*, **432**, L75–L78.

CARASSO, A.S. (1999). Linear and nonlinear image deblurring: a documented study. *SIAM Journal on Numerical Analysis*, **36**, 1657–2689.

COORAY, A. & SHETH, R. (2002). Halo models of large scale structure. *Physics Reports*, **372**, 1.

CROFT, R.A.C. & GAZTANAGA, E. (1997). Reconstruction of cosmological density and velocity fields in the Lagrangian Zel'dovich approxi mation. *MNRAS*, **285**, 793–805.

DEKEL, A. & LAHAV, O. (1999). Stochastic Nonlinear Galaxy Biasing. *ApJ*, **520**, 24–34.

DEKEL, A., BERTSCHINGER, E. & FABER, S.M. (1990). Potential, velocity, and density fields from sparse and noisy redshift-distance samples - Method. *ApJ*, **364**, 349–369.

DORÉ, O., TEYSSIER, R., BOUCHET, F.R., VIBERT, D. & PRUNET, S. (2001). MAPCUMBA: A fast iterative multi-grid map-making algorithm for CMB experiments. *Astr.Astrophy.*, **374**, 358–370.

DOROSHKEVICH, A.G., GOTTLOBER, S. & MADSEN, S. (1997). The accuracy of parameters determined with the core-sampling method: Application to Voronoi tessellations. *Astr.Astrophy.Suppl.*, **123**, 495–506.

EBELING, H. & WIEDENMANN, G. (1993). Detecting structure in two dimensions combining Voronoi tessellation and percolation. *Phys. Rev. E*, **47**, 704–710.

EKE, V. (2001). A speedy pixon image reconstruction algorithm. *MNRAS*, **324**, 108–118.

ENßLIN, T. (2007). personal communication.

ERDOĞDU, P., LAHAV, O., ZAROUBI, S. & ET AL. (2004). The 2dF Galaxy Redshift Survey: Wiener reconstruction of the cosmic web. *MNRAS*, **352**, 939–960.

ERDOĞDU, P., LAHAV, O., HUCHRA, J. & ET AL. (2006). Reconstructed density and velocity fields from the 2MASS Redshift Survey. *MNRAS*, **373**, 45–64.

ERIKSEN, H.K., O'DWYER, I.J., JEWELL, J.B., WANDELT, B.D., LARSON, D.L., GÓRSKI, K.M., LEVIN, S., BANDAY, A.J. & LILJE, P.B. (2004). Power Spectrum Estimation from High-Resolution Maps by Gibbs Sampling. *.Rev.Astrn.Astrophys.*, **155**, 227–241.

ERIKSEN, H.K., HUEY, G., SAHA, R., HANSEN, F.K., DICK, J., BANDAY, A.J., GÓRSKI, K.M., JAIN, P., JEWELL, J.B., KNOX, L., LARSON, D.L., O'DWYER, I.J., SOURADEEP, T. & WANDELT, B.D. (2007). A Reanalysis of the 3 Year Wilkinson Microwave Anisotropy Probe Temperature Power Spectrum and Likelihood. *ApJ*, **656**, 641–652.

FISHER, K.B., SCHARF, C.A. & LAHAV, O. (1994). A spherical harmonic approach to redshift distortion and a measurement of Omega(0) from the 1.2-Jy IRAS Redshift Survey. *MNRAS*, **266**, 219–+.

FISHER, K.B., LAHAV, O., HOFFMAN, Y., LYNDEN-BELL, D. & ZAROUBI, S. (1995). Wiener reconstruction of density, velocity and potential fields from all-sky galaxy redshift su rveys. *MNRAS*, **272**, 885–908.

FLETCHER, R. & REEVES, C.M. (1964). Function Minimization by Conjugate Gradients. *Computer Journal*, **7**, 163–168.

FOSTER, M. (1961). An application of the Wiener-Kolmogorov smoothing theory to matrix inversion. *J. SIAM*, **9**, 387–392.

FRIEDEN, B.R. (1972). Restoring with Maximum Likelihood and Maximum Entropy. *Journal of the Optical Society of America (1917-1983)*, **62**, 511–518.

FRISCH, U., MATARRESE, S., MOHAYAEE, R. & SOBOLEVSKI, A. (2002). A reconstruction of the initial conditions of the Universe by optimal mass transportation. *Nature*, **417**, 260–262.

GANON, G. & HOFFMAN, Y. (1993). Constrained realizations of Gaussian fields - Reconstruction of the Large-Scale structure. *ApJ*, **415**, L5–L8.

GELMAN, A., CARLIN, J.B., STERN, H.S. & RUBIN, D. (2004). *Bayesian data analysis*. Chapman & Hall/CRC, Boca Raton, Florida.

GEMAN, S. & GEMAN, D. (1984). Stochastic Relaxation, Gibbs Distributions, and the Bayesian Restoration of Images. *IEEE Transactions on Pattern Analysis and Machine Intelligence*, **6**, 721–741.

GOLDBERG, D.M. (2001a). Using Perturbative Least Action to Reconstruct Redshift-Space Distortions. *ApJ*, **552**, 413–426.

GOLDBERG, D.M. (2001b). Using Perturbative Least Action to Reconstruct the Local Group. *ApJ*, **550**, 87–93.

GOLDBERG, D.M. & SPERGEL, D.N. (2000a). Using Perturbative Least Action to Recover Cosmological Initial Conditions. *ApJ*, **544**, 21–29.

GOLDBERG, D.M. & SPERGEL, D.N. (2000b). Using Perturbative Least Action to Run N-Body Simulations Back in Time. In S. Courteau & J. Willick, eds., *ASP Conf. Ser. 201: Cosmic Flows Workshop*, 282–+.

GORDON, R. (1974). Tutorial on algebraic reconstruction technique. *IEEE Trans NS*, **21**, 78–92.

GOTTLÖBER, S., KERSCHER, M., KRAVTSOV, A.V., FALTENBACHER, A., KLYPIN, A. & MÜLLER, V. (2002). Spatial distribution of galactic halos and their merger histories. *Astr.Astrophy.*, **387**, 778–787.

GRAMANN, M. (1993). An improved reconstruction method for cosmological density fields. *ApJ*, **405**, 449–458.

GULL, S.F. (1989). Developments in Maximum Entropy data analysis. In J. Skilling, ed., *Maximum Entropy and Bayesian Methods*, 53–71, Kluwer Academic Publishers, Dordtrecht.

GULL, S.F. & DANIELL, G.J. (1978). Image reconstruction from incomplete and noisy data. *Nature*, **272**, 686–690.

GULL, S.F. & SKILLING, J. (1990). *The MEMSYS5 User's Manual*. Maximum Entropy Data Consultants Ltd, Royston.

GUTH, A.H. (1981). Inflationary universe: A possible solution to the horizon and flatness problems. *Phys. Rev. D*, **23**, 347–356.

GUTH, A.H. & PI, S.Y. (1982). Fluctuations in the new inflationary universe. *Physical Review Letters*, **49**, 1110–1113.

HAMILTON, A.J.S. (1998). Linear Redshift Distortions: a Review. In D. Hamilton, ed., *The Evolving Universe*, vol. 231 of *Astrophysics and Space Science Library*, 185–+.

HANKE, M. (1997). A regularizing Levenberg-Marquardt scheme with applications to inverse groundwater filtration problems. *Inverse Problems*, **13**, 75–95.

HANKE, M., NEUBAUER, A. & SCHERZER, O. (1995). A convergence analysis of the Landweber iteration for nonlinear ill-posed problems. *Numerische Mathematik*, **72**, 21–37.

HASTINGS, W.K. (1970). Monte Carlo Sampling Methods Using Markov Chains and Their Applications. *Biometrika*, **57**, 97–109.

HAWKING, S.W. (1982). The unpredictability of quantum gravity. *Communications in Mathematical Physics*, **87**, 395–415.

HAWKINS, E., MADDOX, S., COLE, S., LAHAV, O., MADGWICK, D.S., NORBERG, P., PEACOCK, J.A., BALDRY, I.K., BAUGH, C.M., BLAND-HAWTHORN, J., BRIDGES, T., CANNON, R., COLLESS, M., COLLINS, C., COUCH, W., DALTON, G., DE PROPRIS, R., DRIVER, S.P., EFSTATHIOU, G., ELLIS, R.S., FRENK, C.S., GLAZEBROOK, K., JACKSON, C., JONES, B., LEWIS, I., LUMSDEN, S., PERCIVAL, W., PETERSON, B.A., SUTHERLAND, W. & TAYLOR, K. (2003). The 2dF Galaxy Redshift Survey: correlation functions, peculiar velocities and the matter density of the Universe. *MNRAS*, **346**, 78–96.

HESTENES, M.R. & STIEFEL, E. (1952). Methods of Conjugate Gradients for Solving Linear Systems. *Journal of Research of the National Bureau of Standards*, **49**, 6.

HOBSON, M.P. & MCLACHLAN, C. (2003). A Bayesian approach to discrete object detection in astronomical data sets. *MNRAS*, **338**, 765–784.

HOBSON, M.P., JONES, A.W., LASENBY, A.N. & BOUCHET, F.R. (1998). Foreground separation methods for satellite observations of the cosmic microwave background. *MNRAS*, **300**, 1–29.

HOCKNEY, R.W. & EASTWOOD, J.W. (1981). *Computer Simulation Using Particles*. Computer Simulation Using Particles, New York: McGraw-Hill, 1981.

HOERL, A.E. (1962). Application of ridge analysis to regression problems, Chemical Engineering Progress. *Chemical Engineering Progress*, **58**, 54–59.

HOERL, A.E. & KENNARD, R.W. (1970). Ridge regression: Biased estimation for nonorthogonal problems. *Technometrics*, **12**, 55–67.

HOFFMAN, Y. (1994). Wiener Reconstruction of the Large-Scale Structure in the Zone of Avoidance. In C. Balkowski & R.C. Kraan-Korteweg, eds., *ASP Conf. Ser. 67: Unveiling Large-Scale Structures Behind the Milky Way*, 185–+.

HOFFMAN, Y. & RIBAK, E. (1991). Constrained realizations of Gaussian fields - A simple algorithm. *ApJ*, **380**, L5–L8.

ICKE, V. & VAN DE WEYGAERT, R. (1991). The galaxy distribution as a Voronoi foam. *QJRAS*, **32**, 85–112.

JANSSEN, M.A. & GULKIS, S. (1992). Mapping the sky with the COBE differential microwave radiometers. In M. Signore & C. Dupraz, eds., *NATO ASIC Proc. 359: The Infrared and Submillimetre Sky after COBE*, 391–408.

JASCHE, J. (2007). personal communication.

JAYNES, E.T. (1963). Information Theory and Statistical Mechanics. In K. Ford, ed., *Statistical Physics*, 181, Benjamin, New York.

JAYNES, E.T. (1968). Prior Probabilities. *IEEE Trans. on Systems Science and Cybernetics*, **SSC-4**, 227.

JEWELL, J., LEVIN, S. & ANDERSON, C.H. (2004). Application of Monte Carlo Algorithms to the Bayesian Analysis of the Cosmic Microwave Background. *ApJ*, **609**, 1–14.

JING, Y.P. (2005). Correcting for the Alias Effect When Measuring the Power Spectrum Using a Fast Fourier Transform. *ApJ*, **620**, 559–563.

KAISER, N. (1987). Clustering in real space and in redshift space. *MNRAS*, **227**, 1–21.

KAISER, N. & STEBBINS, A. (1991). Reconstructing the Density Field from Peculiar Velocities: A Maximum Probability Technique. In D.W. Latham & L.A.N. da Costa, eds., *ASP Conf. Ser. 15: Large-Scale Structures and Peculiar Motions in the Universe*, 111–+.

KEIHÄNEN, E., KURKI-SUONIO, H. & POUTANEN, T. (2005). MADAM- a map-making method for CMB experiments. *MNRAS*, **360**, 390–400.

KIBBLE, T.W.B. (1976). Topology of cosmic domains and strings . *Journal of Physics A Mathematical General*, **9**, 1387–1398.

KIM, R., STRAUSS, M., BAHCALL, N., GUNN, J.E., LUPTON, R.H., VOGELEY, M.S., SCHLEGEL, D. & THE SDSS COLLABORATION (2000). Finding Clusters of Galaxies in the Sloan Digital Sky Survey using Voronoi Tessellation. In A. Mazure, O. Le Fèvre & V. Le Brun, eds., *Clustering at High Redshift*, vol. 200 of *Astronomical Society of the Pacific Conference Series*, 422–+.

KITAURA, F.S. & ENßLIN, T.A. (2007). Bayesian reconstruction of the cosmological large-scale structure: methodology, inverse algorithms and numerical optimization. *ArXiv e-prints*, **705**.

KOMATSU, E., KOGUT, A., NOLTA, M.R., BENNETT, C.L., HALPERN, M., HINSHAW, G., JAROSIK, N., LIMON, M., MEYER, S.S., PAGE, L., SPERGEL, D.N., TUCKER, G.S., VERDE, L., WOLLACK, E. & WRIGHT, E.L. (2003). First-Year Wilkinson Microwave Anisotropy Probe (WMAP) Observations: Tests of Gaussianity. .*Rev.Astrn.Astrophys.*, **148**, 119–134.

KUDLICKI, A., CHODOROWSKI, M., PLEWA, T. & RÓŻYCZKA, M. (2000). Reconstructing cosmic peculiar velocities from the mildly non-linear density field. *MNRAS*, **316**, 464–472.

LAHAV, O. (1994). Wiener Reconstruction of All-Sky Spherical Harmonic Maps of the Large-Scale Structure. In C. Balkowski & R.C. Kraan-Korteweg, eds., *ASP Conf. Ser. 67: Unveiling Large-Scale Structures Behind the Milky Way*, 171–+.

LAHAV, O. & GULL, S.F. (1989). Distances to clusters of galaxies by Maximum Entropy method. *MNRAS*, **240**, 753–763.

LAHAV, O., FISHER, K.B., HOFFMAN, Y., SCHARF, C.A. & ZAROUBI, S. (1994). Wiener Reconstruction of All-Sky Galaxy Surveys in Spherical Harmonics. *ApJ*, **423**, L93+.

LARSON, D.L., ERIKSEN, H.K., WANDELT, B.D., GÓRSKI, K.M., HUEY, G., JEWELL, J.B. & O'DWYER, I.J. (2007). Estimation of Polarized Power Spectra by Gibbs Sampling. *ApJ*, **656**, 653–660.

LINDE, A.D. (1982). A new inflationary universe scenario: A possible solution of the horizon, flatness, homogeneity, isotropy and primordial monopole problems. *Physics Letters B*, **108**, 389–393.

LUCY, L.B. (1974). An iterative technique for the rectification of observed distributions. *AJ*, **79**, 745–+.

MAISINGER, K., HOBSON, M.P. & LASENBY, A.N. (1997). A maximum entropy method for reconstructing interferometer maps of fluctuations in the cosmic microwave background radiation. *MNRAS*, **290**, 313–326.

MARCHUK, G.I. (1982). *Methods of numerical mathematics*. Springer-Verlag, New York.

MARTEL, H. (2005). Generation of Gaussian Density Fields. *ArXiv Astrophysics e-prints*.

MATHIS, H., LEMSON, G., SPRINGEL, V., KAUFFMANN, G., WHITE, S.D.M., ELDAR, A. & DEKEL, A. (2002). Simulating the formation of the local galaxy population. *MNRAS*, **333**, 739–762.

METROPOLIS, N., ROSENBLUTH, A.W., ROSENBLUTH, M.N., TELLER, A.H. & TELLER, E.T. (1953). Equations of State Calculations by Fast Computing Machines. *Journal of Chemical Physics*, **21**, 1087–1092.

MEURS, E.J.A. & WILKINSON, M.I. (1999). Large-scale structure assessed with Voronoi techniques. In G. Giuricin, M. Mezzetti & P. Salucci, eds., *Observational Cosmology: The Development of Galaxy Systems*, vol. 176 of *Astronomical Society of the Pacific Conference Series*, 333–+.

MOHAYAEE, R. & TULLY, R.B. (2005). The Cosmological Mean Density and Its Local Variations Probed by Peculiar Velocities. *ApJ*, **635**, L113–L116.

MOHAYAEE, R., FRISCH, U., MATARRESE, S. & SOBOLEVSKII, A. (2003). Back to the primordial Universe by a Monge-Ampère-Kantorovich optimization scheme. *Astr.Astrophy.*, **406**, 393–401.

MOHAYAEE, R., TULLY, B. & FRISCH, U. (2004). Reconstruction of Large-Scale peculiar velocity fields. *ArXiv Astrophysics e-prints*.

MOHAYAEE, R., MATHIS, H., COLOMBI, S. & SILK, J. (2006). Reconstruction of primordial density fields. *MNRAS*, **365**, 939–959.

MOLINA, R., NUNEZ, J., CORTIJO, F.J. & MATEOS, J. (2001). Image restoration in astronomy: a Bayesian perspective. *Signal Processing Magazine, IEEE*, **18**, 11–19.

NARAYAN, R. & NITYANANDA, R. (1986). Maximum Entropy image restoration in astronomy. *Ann.Rev.Astrn.Astrophys.*, **24**, 127–170.

NARAYANAN, V.K. & CROFT, R.A.C. (1999). Recovering the Primordial Density Fluctuations: A Comparison of Methods. *ApJ*, **515**, 471–486.

NARAYANAN, V.K. & WEINBERG, D.H. (1998). Reconstruction Analysis of Galaxy Redshift Surveys: A Hybrid Reconstruction Method. *ApJ*, **508**, 440–471.

NATOLI, P., DE GASPERIS, G., GHELLER, C. & VITTORIO, N. (2001). A Map-Making algorithm for the Planck Surveyor. *Astr.Astrophy.*, **372**, 346–356.

NEAL, R.M. (1993). Probabilistic Inference Using Markov Chain Monte Carlo Methods. In *Technical Report CRG-TR-93-1*, Dept. of Computer Science, University of Toronto.

NUSSER, A. & DAVIS, M. (1994). On the prediction of velocity fields from redshift space galaxy samples. *ApJ*, **421**, L1–L4.

NUSSER, A. & DEKEL, A. (1992). Tracing Large-Scale fluctuations back in time. *ApJ*, **391**, 443–452.

NUSSER, A., DEKEL, A., BERTSCHINGER, E. & BLUMENTHAL, G.R. (1991). Cosmological velocity-density relation in the quasi-linear regime. *ApJ*, **379**, 6–18.

O'DWYER, I.J., ERIKSEN, H.K., WANDELT, B.D., JEWELL, J.B., LARSON, D.L., GÓRSKI, K.M., BANDAY, A.J., LEVIN, S. & LILJE, P.B. (2004). Bayesian Power Spectrum Analysis of the First-Year Wilkinson Microwave Anisotropy Probe Data. *ApJ*, **617**, L99–L102.

O'SULLIVAN, F. (1990). Convergence characteristics of methods of regularization estimators for nonlinear operator equations. *SIAM J. Numer. Anal.*, **27**, 1635–1649.

PANKO, E. & FLIN, P. (2004). Application of the Voronoi tessellation technique for galaxy cluster search in the Münster Red Sky Survey. In A. Diaferio, ed., *IAU Colloq. 195: Outskirts of Galaxy Clusters: Intense Life in the Suburbs*, 245–247.

PEACOCK, J.A. (1999). Book Review: Cosmological physics / Cambridge U Press, 1999. *The Observatory*, **119**, 296–+.

PEACOCK, J.A. & DODDS, S.J. (1994). Reconstructing the Linear Power Spectrum of Cosmological Mass Fluctuations. *MNRAS*, **267**, 1020–+.

PEEBLES, P.J.E. (1980). *The large-scale structure of the universe*. Research supported by the National Science Foundation. Princeton, N.J., Princeton University Press, 1980. 435 p.

PEEBLES, P.J.E. (1989). Tracing galaxy orbits back in time. *ApJ*, **344**, L53–L56.

PEEBLES, P.J.E. (1990). The gravitational instability picture and the formation of the Local Group. *ApJ*, **362**, 1–13.

PEN, U.L. (1998). Reconstructing Nonlinear Stochastic Bias from Velocity Space Distortions. *ApJ*, **504**, 601–+.

PERCIVAL, W.J. (2005). Markov chain reconstruction of the 2dF Galaxy Redshift Survey real-space power spectrum. *MNRAS*, **356**, 1168–1176.

PIERPAOLI, E. & ANTHOINE, S. (2005). Finding SZ clusters in the ACBAR maps. *Advances in Space Research*, **36**, 757–761.

PRESS, W.H., TEUKOLSKY, S.A., VETTERLING, W.T. & FLANNERY, B.P. (1992). *Numerical recipes in C. The art of scientific computing*. Cambridge: University Press, —c1992, 2nd ed.

PUETTER, R.C. & PINA, R.K. (1993). The pixon and Bayesian image reconstruction. In A.M. Fowler, ed., *Proc. SPIE Vol. 1946, p. 405-416, Infrared Detectors and Instrumentation, Albert M. Fowler; Ed.*, 405–416.

RAMELLA, M., BOSCHIN, W., FADDA, D. & NONINO, M. (2001). Finding galaxy clusters using Voronoi tessellations. *Astr.Astrophy.*, **368**, 776–786.

RICHARDSON, W.H. (1972). Bayesian-based iterative method of image restoration. *Journal of the Optical Society of America (1917-1983)*, **62**, 55–59.

ROBERT, C.P. (2001). *The Bayesian choice*. Springer-Verlag, New York.

ROBINSON, D.R.T. (1991). Maximum Entropy with Poissonian statistics. In W.T. Grandy & L.H. Schick, eds., *Maximum Entropy and Bayesian methods*, 337–341.

RYBICKI, G.B. & PRESS, W.H. (1992). Interpolation, realization, and reconstruction of noisy, irregularly sampled data. *ApJ*, **398**, 169–176.

SCHAAP, W.E. & VAN DE WEYGAERT, R. (2000). Continuous fields and discrete samples: reconstruction through Delaunay tessellations. *Astr.Astrophy.*, **363**, L29–L32.

SCHMOLDT, I.M., SAAR, V., SAHA, P., BRANCHINI, E., EFSTATHIOU, G.P., FRENK, C.S., KEEBLE, O., MADDOX, S., MCMAHON, R., OLIVER, S., ROWAN-ROBINSON, M., SAUNDERS, W., SUTHERLAND, W.J., TADROS, H. & WHITE, S.D.M. (1999). On Density and Velocity Fields and beta from the IRAS PSCZ Survey. *ApJ*, **118**, 1146–1160.

SCOCCIMARRO, R. (2004). Redshift-space distortions, pairwise velocities, and nonlinearities. *Phys. Rev. D*, **70**, 083007–+.

SELJAK, U. (1998). Cosmography and Power Spectrum Estimation: A Unified Approach. *ApJ*, **503**, 492–+.

SELJAK, U. & ZALDARRIAGA, M. (1996). A Line-of-Sight Integration Approach to Cosmic Microwave Background Anisotropies. *ApJ*, **469**, 437–+.

SHANNON, C.E. (1948). *A mathematical theory of communication*, vol. 27. Bell System Technical Journal.

SHAYA, E.J., PEEBLES, P.J.E. & TULLY, R.B. (1995). Action Principle Solutions for Galaxy Motions within 3000 Kilometers per Second. *ApJ*, **454**, 15–+.

SHEPP, L.A. & VARDI, Y. (1982). Maximum likelihood reconstruction for emission tomography. *IEEE Trans. Med. Imaging*, **1**, 113–122.

SHETH, R.K. (1995). Constrained realizations and minimum variance reconstruction of non-Gaussian random fields. *MNRAS*, **277**, 933–944.

SHEWCHUK, J.R. (1994). *An Introduction to the Conjugate Gradient Method Without the Agonizing Pain*. published in the web.

SKILLING, J., ed. (1989). *Maximum Entropy and Bayesian methods : 8 : 1988*.

SMITH, R.E., PEACOCK, J.A., JENKINS, A., WHITE, S.D.M., FRENK, C.S., PEARCE, F.R., THOMAS, P.A., EFSTATHIOU, G. & COUCHMAN, H.M.P. (2003). Stable clustering, the halo model and non-linear cosmological power spectra. *MNRAS*, **341**, 1311–1332.

SPRINGEL, V., WHITE, S.D.M., JENKINS, A., FRENK, C.S., YOSHIDA, N., GAO, L., NAVARRO, J., THACKER, R., CROTON, D., HELLY, J., PEACOCK, J.A., COLE, S., THOMAS, P., COUCHMAN, H., EVRARD, A., COLBERG, J. & PEARCE, F. (2005). Simulations of the formation, evolution and clustering of galaxies and quasars. *Nature*, **435**, 629–636.

STAROBINSKY, A.A. (1982). Dynamics of phase transition in the new inflationary universe scenario and generation of perturbations. *Physics Letters B*, **117**, 175–178.

STOMPOR, R., BALBI, A., BORRILL, J.D., FERREIRA, P.G., HANANY, S., JAFFE, A.H., LEE, A.T., OH, S., RABII, B., RICHARDS, P.L., SMOOT, G.F., WINANT, C.D. & WU, J.H.P. (2002). Making maps of the cosmic microwave background: The MAXIMA example. *Phys. Rev. D*, **65**, 022003–+.

SUTTON, E.C. & WANDELT, B.D. (2006). Optimal Image Reconstruction in Radio Interferometry. *.Rev.Astrn.Astrophys.*, **162**, 401–416.

TANNER, M.A. (1996). *Tools for statistical inference*. Springer-Verlag, New York.

TEGMARK, M. (1997). Cmb mapping experiments: A designer's guide. *Phys. Rev. D*, **56**, 4514–4529.

TEGMARK, M. (1997). How to Make Maps from Cosmic Microwave Background Data without Losing Information. *ApJ*, **480**, L87+.

TEGMARK, M. & BROMLEY, B.C. (1999). Observational evidence for stochastic biasing. *The Astrophysical Journal*, **518**, L69.

TIKHONOV, A.N. (1963). Solution of incorrectly formulated problems and the regularization method. *Soviet Math Dokl*, **4**, 1035–1038.

VALENTINE, H., SAUNDERS, W. & TAYLOR, A. (2000). Reconstructing the IRAS Point Source Catalog Redshift Survey with a generalized PIZA. *MNRAS*, **319**, L13–L17.

VAN DE WEYGAERT, R. & SCHAAP, W. (2001). Tessellation Reconstruction Techniques. In A.J. Banday, S. Zaroubi & M. Bartelmann, eds., *Mining the Sky*, 268–+.

VOGELEY, M.S. & SZALAY, A.S. (1996). Eigenmode Analysis of Galaxy Redshift Surveys. I. Theory and Methods. *ApJ*, **465**, 34–+.

WANDELT, B.D., LARSON, D.L. & LAKSHMINARAYANAN, A. (2004). Global, exact cosmic microwave background data analysis using Gibbs sampling. *Phys. Rev. D*, **70**, 083511–+.

WEBSTER, M., LAHAV, O. & FISHER, K. (1997). Wiener reconstruction of the IRAS 1.2-Jy galaxy redshift survey: cosmographical implications. *MNRAS*, **287**, 425–444.

WEINBERG, D.H. (1992). Reconstructing primordial density fluctuations. I - Method. *MNRAS*, **254**, 315–342.

YAHIL, A., STRAUSS, M.A., DAVIS, M. & HUCHRA, J.P. (1991). A redshift survey of IRAS galaxies. II - Methods for determining self-consistent velocity and density fields. *ApJ*, **372**, 380–393.

YVON, D. & MAYET, F. (2005). Mirage: A new iterative map-making code for CMB experiments. *Astr.Astrophy.*, **436**, 729–739.

ZANINETTI, L. (1995). Dynamical Voronoi tessellation. V. Thickness and incompleteness. *Astr.Astrophy.Suppl.*, **109**, 71–77.

ZANINETTI, L. (2006). On the Large-Scale Structure of the Universe as given by the Voronoi Diagrams. *Chinese Journal of Astronomy and Astrophysics*, **6**, 387–395.

ZAROUBI, S. (2002a). Cosmic Flows: Review of Recent Developments. *ArXiv Astrophysics e-prints*.

ZAROUBI, S. (2002b). Unbiased reconstruction of the Large-Scale structure. *MNRAS*, **331**, 901–908.

ZAROUBI, S., HOFFMAN, Y., FISHER, K.B. & LAHAV, O. (1995). Wiener Reconstruction of the Large-Scale Structure. *ApJ*, **449**, 446–+.

ZAROUBI, S., HOFFMAN, Y. & DEKEL, A. (1999). Wiener Reconstruction of Large-Scale Structure from Peculiar Velocities. *ApJ*, **520**, 413–425.

ZEL'DOVICH, Y.B. (1970). Gravitational instability: an approximate theory for large density perturbations. *Astr.Astrophy.*, **5**, 84–89.

II

Appendix: Gravitational collapse and subsequent neutrino-driven explosion of the low-mass end of core-collapse Supernovae

We present results of simulations of stellar collapse and explosions in spherical symmetry and in two spatial dimensions for progenitor stars in the 8–10 $M_\odot$ range with an O-Ne-Mg core. The simulations were continued until nearly one second after core bounce and were performed with the PROMETHEUS/VERTEX code and its extension to the multi-dimensional version of the code (MUDBATH) with a variable Eddington factor solver for the neutrino transport, including a state-of-the-art treatment of neutrino-matter interactions. Particular effort was made to implement nuclear burning and electron capture rates with sufficient accuracy to ensure a smooth continuation, without transients, from the progenitor evolution to core collapse. Using two different nuclear equations of state (EoSs), a soft version of the Lattimer & Swesty EoS and the significantly stiffer Wolff & Hillebrandt EoS, we found no prompt explosions, but instead delayed explosions, powered by neutrino heating and the neutrino-driven baryonic wind which sets in about 200 ms after bounce. The models eject little nickel ($< 0.015 M_\odot$), explode with an energy of $\gtrsim 0.1 \times 10^{51}$ erg, and leave behind neutron stars (NSs) with a baryonic mass near $1.36\,M_\odot$. Different from previous models of such explosions, the ejecta during the first second have a proton-to-baryon ratio of $Y_\mathrm{e} \gtrsim 0.46$, which suggests a chemical composition that is not in conflict with galactic abundances. No low-entropy matter with $Y_\mathrm{e} \ll 0.5$ is ejected. This excludes such explosions as sites of a low-entropy r-process. The convective behaviour above the proto-neutron star found in our 2D simulation, slightly enhances the explosion energy remaining at the same order of magnitude. This result stays in contrast to previous work, in which convection was treated approximately and leads to significantly more energetic explosions. We do not find a coupling between the convection below the neutrino-sphere and the shock expansion, as is observed for more massive stars, which develop low-mode instabilities. The low explosion energy and nucleosynthetic implications are compatible with the observed properties of the Crab supernova, and the small nickel mass supports the possibility that our models explain some subluminous Type II-P supernovae.

The following supernova part contains material produced by the author that has been partially published in Janka, Marek & Kitaura (2007), Kitaura, Janka & Hillebrandt (2006), Janka, Buras, Kitaura et al. (2005), Janka, Buras, Kitaura et al. (2004) and Kitaura (2003). All the computer simulations and figures presented here have been made by the author.

Contents

List of Figures

LIST OF FIGURES

Chapter 1

Introduction

We came from the stars so they say, now it's time to go back.

Jerome, Gattaca

1.1 The Crab Nebula and the low mass end of core-collapse supernovae

When Chinese and Arab astronomers watched the sky in the spring of the year 1054 A.D., they discovered a new star in the constellation of Taurus. According to their historical records, the "guest star" became brighter during several weeks and could be observed by July for 23 days even in the daytime. It remained visible to the naked eye for about two years.

Now we know that they observed the birth of the Crab Nebula by a gigantic supernova explosion. After millions of years of quiet evolution, a massive star had exhausted its supply of nuclear fuel, whose burning had provided the energy and pressure to stabilize the star against the pull of its own gravity. When the nuclear flame in its center died, the stellar core collapsed within fractions of a second to a neutron star, a compact object with more mass than the Sun but a diameter of only 20 kilometers. This neutron star is visible as the famous pulsar in the Crab Nebula, which sends periodic pulses of radiation as it spins around its axis 33 times per second.

Most of the star, however, was ejected in a violent explosion with an energy roughly equal to what the Sun has radiated in 5 billion years of its life. The hot stellar debris flashed up as the new star reported by the Chinese and Arab astronomers, and is nowadays visible as the filamentary gas cloud of the Crab Nebula measuring six light-years across and still expanding with a velocity of 1500 kilometers per second. It contains not only the chemical elements which the star has built up in a sequence of nuclear burning stages — first fusing hydrogen to helium, then helium to carbon, and then carbon to neon, magnesium, and oxygen — but also material like radioactive nickel, which was freshly assembled during the explosion. The helium richness of the nebula and the low abundances of carbon and oxygen were interpreted as hints that the exploding star had a mass of only about 8 to 10 solar masses, just sufficient to end its

life as a supernova.

But how did the star blow up? What was the reason why the star was disrupted? Neutrinos reveal to be the driving force behind the explosion. These elementary particles are produced in huge numbers in the very hot and extremely dense interior of the newly formed neutron star, mainly by reactions of electrons and positrons with protons and neutrons, the constituents of atomic nuclei. Having made their way to the surface of the neutron star, most of these neutrinos stream off and carry away more than 99 percent of the energy liberated during the neutron star formation. Less than one percent of the neutrinos, however, is captured in the stellar gas surrounding the neutron star before being able to escape. The energy transfer by these neutrinos heats the gas and makes it boiling like the fluid in a pressure cooker. The rising pressure finally accelerates the overlying stellar material and leads to the outburst of the supernova.

Although this theory for the onset of the explosion is 25 years old, proving its viability with detailed computer models turned out to be extremely difficult. Now at least for stars near the lower end of the mass range of supernova progenitors the models lend support to the theoretical idea as we show in this work. The new exploding models agree nicely with observations that the energy of the Crab explosion was only about one tenth of that of a typical supernova. Different from previous simulations they also predict only small amounts of ejected carbon, oxygen, and nickel. Moreover, the strong enrichment of the chemical composition of the remnant with exotic elements is absent and thus a conflict of the older models with the observed abundances of rare elements in the Milky Way Galaxy. Since the disrupted star had a rather low mass and the explosion was sub-energetic with little production of radioactive material, other Crab-like supernovae must be expected to be fairly dim and therefore difficult to discover at great distances, although they could account for one third of all supernovae.

1.2 Motivation and previous work

Recent observations of subluminous Type II-P supernovae (SNe) like 2005cs, 2003gd, 1999br and 1997D, have renewed attention to stars near the lower end of the mass range of core-collapse SN progenitors, i.e. to stars with about 8–10 $M_{\odot}$, which develop O-Ne-Mg cores. A possible link between both has been suggested because of the low ^{56}Ni and ^{16}O ejecta masses and low progenitor luminosities (e.g., Chugai & Utrobin 2000, Hendry et al. 2005). However, due to many uncertainties this connection is far from being clear (e.g., Pastorello et al. 2004, 2005; Hamuy 2003; Zampieri et al. 2003, and refs. therein). Also the Crab Nebula's progenitor was proposed to be in this mass window (Gott et al. 1970, Arnett 1975, Woosley et al. 1980, Hillebrandt 1982). The observed composition of the Crab remnant (small C and O abundances, He overabundance) was interpreted as a strong indication that the Crab Nebula comes from a collapsing and exploding progenitor with an O-Ne-Mg core (Davidson et al. 1982, Nomoto et al. 1982, Nomoto 1983).

Moreover, these stars were considered as possible sites for a low entropy r-process (for example, Hillebrandt 1978, Wheeler et al. 1997, Sumiyoshi et al. 2001, Wanajo et al. 2003) based on the assumption that they explode by the prompt bounce-shock mechanism, which Hillebrandt et al. (1984) found to work in a numerical simulation, taking Nomoto's O-Ne-Mg

core model (Nomoto 1984, 1987). Such explosions are characterized by the direct propagation of the shock out of the core, the formation of a mass cut, and the continuous acceleration of the material outside of the mass cut to high velocities. They are expected to eject relatively large amounts of neutron-rich matter with low $Y_{\rm e}$ ($\sim$0.2) and low entropies ($\sim 10 k_{\rm B}$ per nucleon). However, several groups could not confirm the viability of the prompt explosion mechanism (Burrows & Lattimer 1985, Baron et al. 1987, Mayle & Wilson 1988). Mayle & Wilson (1988) continued their simulations in the post-bounce phase for a longer time and obtained instead a so-called neutrino-driven, delayed explosion (Bethe & Wilson 1985) with a low production of ^{56}Ni (approximately 0.002 $M_\odot$) in agreement with subluminous Type II-P SNe as mentioned above, but with a vast overproduction of neutron-rich material (at least 0.02 $M_\odot$ of ejecta with $Y_{\rm e} \lesssim 0.41$). The latter finding is inconsistent with the chemical composition of our galaxy, which allows for no more than 10^{-3} $M_\odot$ of material with $Y_{\rm e} < 0.42$ being ejected per SN (Hartmann et al. 1985). Moreover, the explosion energies of both studies, around 2×10^{51}erg in Hillebrandt et al.'s (1984) model and between 0.6 and 1.2 $\times 10^{51}$erg in Mayle & Wilson's (1988) simulations, would be inconsistent with the long plateau phase of the above mentioned subluminous SNe, if their H-envelope masses were $\lesssim 8 M_\odot$.

It was suggested that the reason for the discrepant results in the SN simulations of O-Ne-Mg cores (prompt explosions, delayed explosions, no explosions) could be explained by the different nuclear EoSs used by the groups (Fryer et al. 1999). Having in mind that the different approximations in the neutrino transport in previous calculations introduced additional uncertainties, we revisit this topic with a state-of-the-art neutrino transport treatment together with a careful description of weak interactions and including relevant nuclear burning reactions. We additionally make a comparison of collapse and post-bounce calculations with different nuclear EoSs.

Finally, our 2D calculation permits us to investigate the role of convection in the proto-neutron star and in the region between the gain-radius and the shock, where the neutrino energy is deposited and study its effect on the explosion energy.

Chapter 2

Numerical techniques and input physics

2.1 Hydrodynamics-Boltzmann code

The transport of neutrinos and antineutrinos of all flavors is done with the energy-dependent solver for the coupled set of moments equations and Boltzmann equation called VERTEX. It is described in detail in Rampp & Janka (2002). For the two-dimensional simulation we use the MUDBATH code described in Buras et al. (2005, 2006). The equations of hydrodynamics are integrated with the Newtonian finite-volume code PROMETHEUS, which uses a third-order, time-explicit Godunov scheme. This code is a direct implementation of the Piecewise Parabolic Method (PPM), based on a Riemann solver. General relativistic gravity is taken into account approximately by an "effective relativistic potential" according to Marek et al. (2005). Gravitational redshift and time dilation effects are included in the neutrino transport (see Rampp & Janka 2002). In appendix A we recall the basic equations as described in Rampp & Janka (2002) and in appendix B we present a corrected description of the iteration procedure with a revised flow-chart of the VERTEX-code with respect to Kitaura (2003).

2.2 Microphysics and nuclear burning

The code is augmented with improved microphysics as described in Buras et al. (2005). It includes also the improved treatment of electron captures on a large variety of nuclei in nuclear statistical equilibrium (NSE), based on shell model Monte Carlo calculations, as described by Langanke et al. (2003). In addition, electron captures on certain important nuclei in the non-NSE regime, in particular ^{20}Ne and ^{24}Mg, are implemented according to Takahara et al. (1989) (see appendix C).

A simplified treatment of nuclear burning accounts for the main reactions of seven symmetric nuclei (He, C, O, Ne, Mg, Si, Ni). Details about the implemented microphysics are described in appendix (D). The nuclear burning reactions considered by Hillebrandt et al. (1984) ($^{12}\mathrm{C}+^{12}\mathrm{C}$, $^{16}\mathrm{O}+^{16}\mathrm{O}$, $^{12}\mathrm{C}+^{16}\mathrm{O}$) are all included, taking into account different reaction channels.

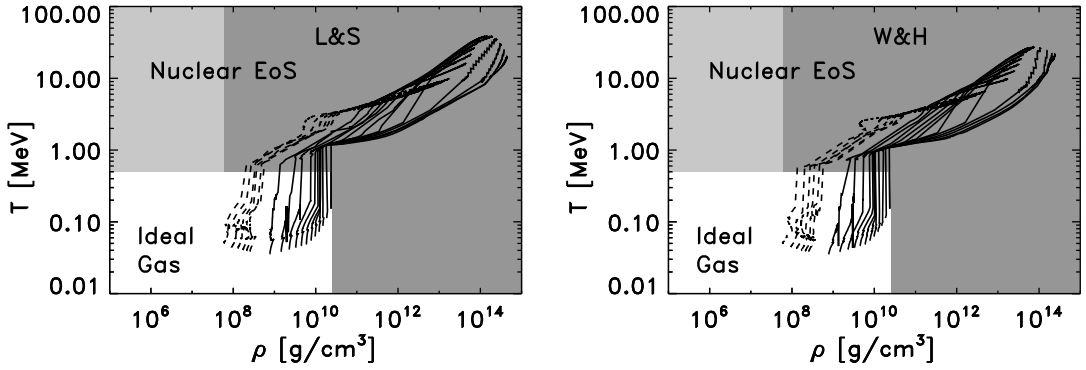

Figure 2.1: Panels **a b** show the evolution of the collapsing mass shell trajectories in a temperature-density diagram during the collapse and postbounce phase for our 1D simulations with the L&S and W&H EoSs. We see that the trajectories converge to a high density region with also high temperatures, where the proto-neutron star is forming. The dark region stands for the high-density nuclear EoS, the bright-grey region represents the low-density region, and the white region is the low-temperature region.

2.3 The equations of state

To describe matter in NSE, we use two different nuclear EoSs in separate simulations, the Wolff & Hillebrandt (W&H) EoS (Hillebrandt et al. 1984), which is based on Hartree Fock calculations, and the Lattimer & Swesty (L&S) EoS (1991), which is a finite-temperature compressible liquid-drop model and has a compressibility modulus of 180 MeV.

This permits us to compare our models with those of Hillebrandt et al. (1984), in which the Wolff and Hillebrandt EoS was used and which produced prompt explosions. The low-temperature and low-density EoS outside of the NSE regime is described by an ideal gas of nuclei and nucleons, electrons, positrons, and photons (Janka 1999). Figure 2.1 shows the evolution of the collapsing mass shell trajectories in a temperature-density diagram during the collapse and postbounce phase for our 1D simulations with the L&S and W&H EoSs. The trajectories show a smooth behavior in the region interfaces. This permits us to switch between NSE and non-NSE in a density- and temperature-dependent manner. Coulomb lattice corrections in the low-density EoS were not included in order to accomplish better agreement with Nomoto's initial data which were obtained with a different equation of state.

2.4 The initial data

The initial model is the same as the one used in previous SN calculations of O-Ne-Mg cores by Hillebrandt et al. (1984) and Mayle & Wilson (1988). It is a 2.2 $M_\odot$ He core that corresponds to a progenitor with a main sequence mass of $\sim$8.8$M_\odot$ (Nomoto 1984, 1987). Figure (2.2) shows the profile of the progenitor. Prior to collapse it has an O-Ne-Mg core with $\sim$1.3$M_\odot$, surrounded by a C-O shell of about $0.08M_\odot$. We take, however, the initial data at a time when the central density is $\sim 4\times10^{10}$ g/cm^3 and only $\sim$0.1 solar masses at the center of the core have

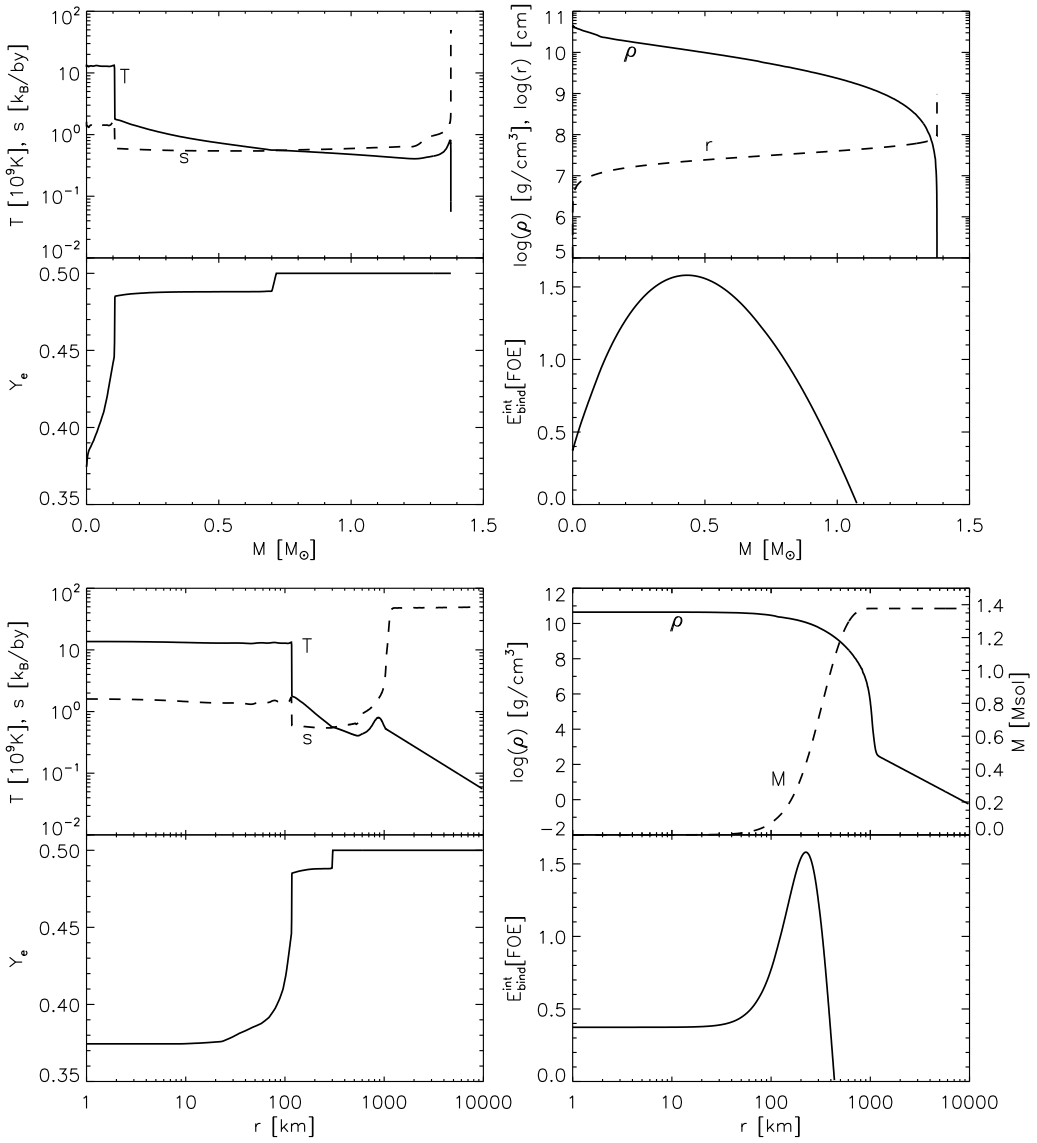

Figure 2.2: The core profile corresponding to a 8.8 solar mass progenitor taken as initial model for our calculations. We extended the profile to an outer radius of 10^5 km assuming a power-law for the temperature profile and hydrostatical equilibrium at the H-He outer atmosphere. The temperature, the entropy, the density, the electron fraction and the binding energy at the onset of gravitational collapse are plotted against the stellar mass in the upper panel and against the stellar radius in the lower one.

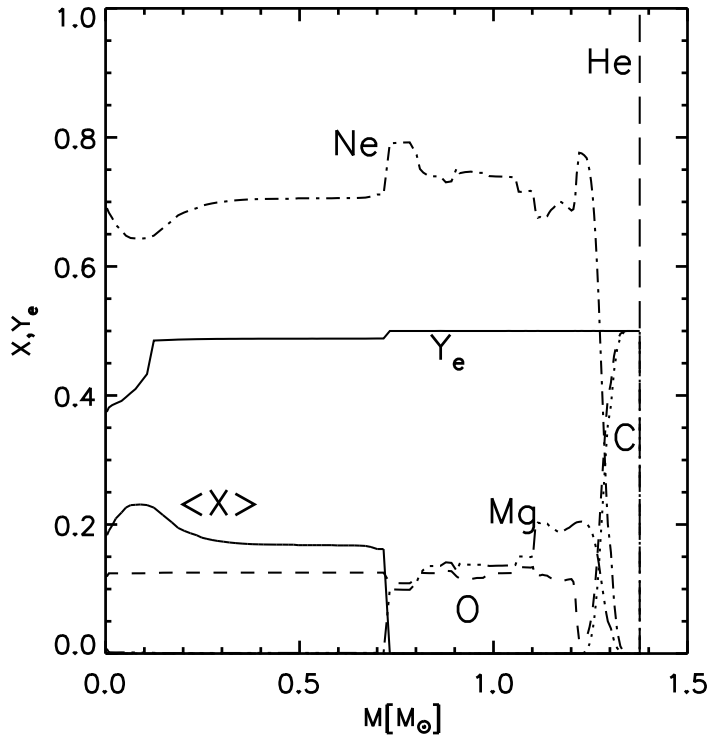

Figure 2.3: Composition of the O/Ne/Mg core plus the C/O layer interior to the helium burning shell at the time where $\rho_{\rm c} = 4.425 \cdot 10^{10}$ g cm^{-3}. The fraction of the average heavy nucleus representing the neutron rich species is given by $< X >$. The initial electron fraction $Y_{\rm e}$ is also represented.

reached nuclear statistical equilibrium (NSE). This is earlier than the starting configuration taken by other groups, where the core had already a central density of $\sim 3 \times 10^{11}$ g/cm^3 and where around 0.3 solar masses were in NSE. Our earlier initial model allows us to trace the evolution of the core towards collapse. The initial composition of the O-Ne-Mg core can be seen in fig. (2.3).

We added a helium atmosphere of about $10^{-4} M_\odot$ around the O-Ne-Mg and C-O core, so that we could move the outer boundary of our Eulerian grid from the core radius of about 1100 km to 100 000 km. For the He-shell profile we adopted a power-law like behavior of the temperature ($T \propto r^{-1}$) from a 10.2 $M_\odot$ progenitor of A. Heger (private communication), and constructed the density profile by assuming hydrostatic equilibrium, a mass fraction of 100% He, and using the EoS for the low-density regime. We employ in our simulations a very fine mesh in order to resolve the steep density gradient at the outer boundary of the C-O layer, with 1600 nonequidistant zones for the hydrodynamics part. The neutrino transport is done with 235 nonequidistant radial zones.

Chapter 3

Results

3.1 Core-collapse

Our results show a very smooth transition from the preceding progenitor evolution to core-collapse. Since O-Ne-Mg cores are gravitationally less bound than more massive stellar progenitors and can release more energy due to nuclear burning, a temperature- and density-dependent treatment of all relevant nuclear burning reactions had to be included, combined with a detailed description of the important electron capture rates. Only that ensured that the progenitor evolution continued towards gravitational collapse without numerical transients. We could therefore confirm that the neutrinos produced by electron captures carry away efficiently the energy that is released by nuclear burning (Miyaji et al. 1980, Miyaji & Nomoto 1987, Hashimoto & Nomoto 1993). A cruder burning treatment, or omission of the improved electron capture rates on nuclei, can have the consequence that the core expands instead of collapsing to a NS, as we verified in test calculations. fig. (3.1) shows how the mass shells in the inner region during the first milliseconds start contracting towards the center. The collapse of the core proceeds to higher central densities and when the density of nuclear matter is reached, the EoS "stiffens", and the inner homologous core bounces.

3.2 Shock formation and post-bounce evolution

3.2.1 Prompt-shock

The supersonically falling outer layers collide with this central core and a hydrodynamic shock is formed as can be seen in fig. (3.1), where this discontinuity in the fluid flow becomes visible by sharp kinks of the mass shell trajectories. This happens after 59 ms of collapse for the calculation with the W&H EoS and after 78 ms in the calculation with the softer L&S EoS. The shock formation radius is at 1.40×10^6 cm, corresponding to an enclosed mass of $0.475M_\odot$ in the former case, and at 1.15×10^6 cm with an enclosed mass of $0.425M_\odot$ in the second model. This so-called prompt bounce shock produces initially positive velocities in the post-shock matter. However, the energy of the shock is insufficient to cause a prompt explosion, and

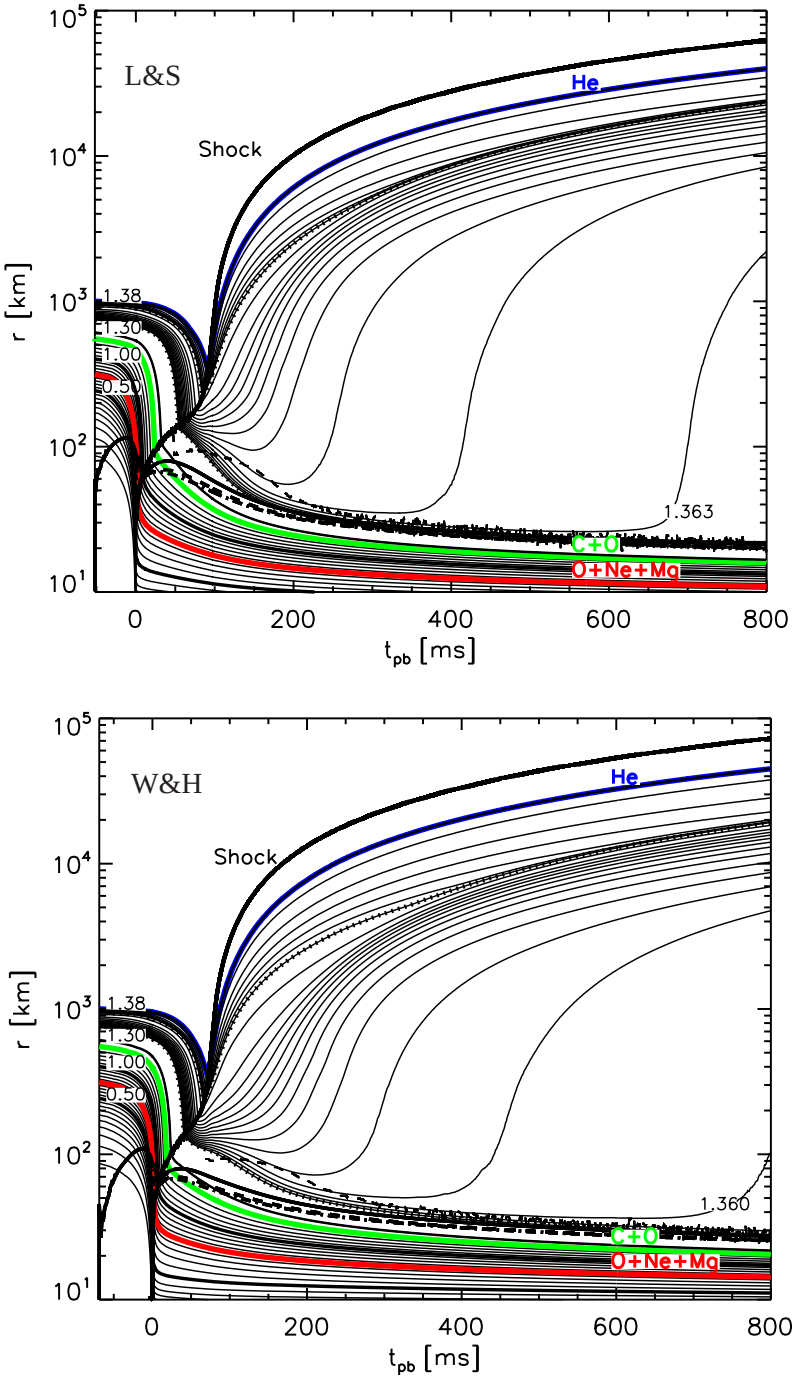

Figure 3.1: Mass trajectories for the simulations with the L&S EoS and the W&H EoS as a function of post-bounce time (t_{pb}). Also plotted: shock position (thick solid line starting at time zero and rising to the upper right corner), gain radius (thin dashed line), and neutrinospheres (ν_e: thick solid; $\bar{\nu}_e$: thick dashed; ν_μ, $\bar{\nu}_\mu$, ν_τ, $\bar{\nu}_\tau$: thick dash-dotted). In addition, the composition interfaces are plotted with different bold, labelled lines: the inner boundaries of the O-Ne-Mg layer at $\sim$0.77 $M_\odot$, of the C-O layer at $\sim$1.26 $M_\odot$, and of the He layer at 1.3769 $M_\odot$. The two dotted lines represent the mass shells where the mass spacing between the plotted trajectories changes. An equidistant spacing of $5 \times 10^{-2} M_\odot$ was chosen up to $1.3579 M_\odot$, between that value and $1.3765 M_\odot$ it was $1.3 \times 10^{-3} M_\odot$, and $8 \times 10^{-5} M_\odot$ outside.

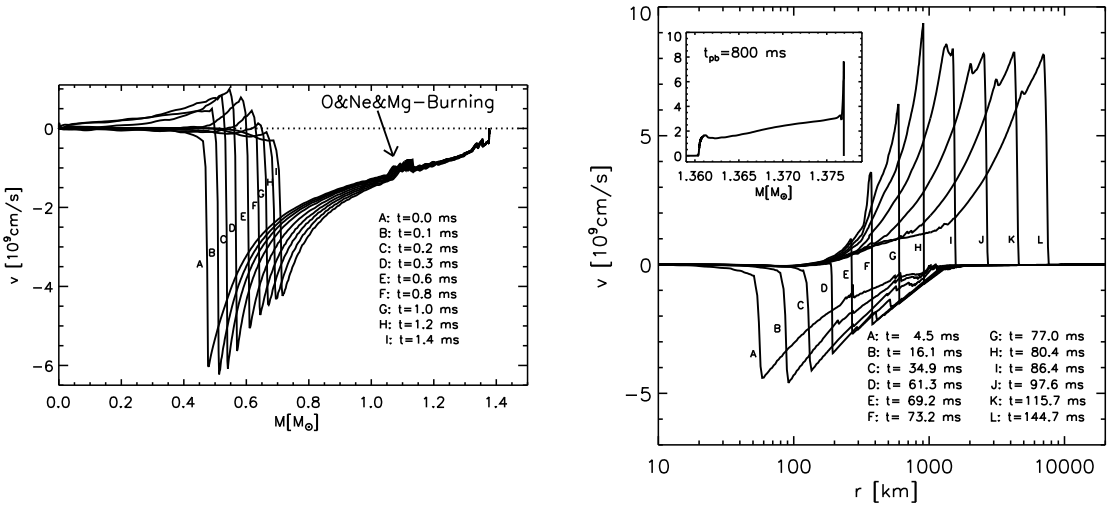

Figure 3.2: **Left:** Velocity profiles vs. enclosed mass at different times for the model with the W&H EoS. Times are normalized to core bounce. **Right:** Velocity profiles as functions of radius for different post-bounce times for the simulation with the W&H EoS. The insert shows the velocity profile vs. enclosed mass at the end of our simulation.

the photodisintegration of nuclei consumes such amounts of energy that the shock is quickly damped and that within only $\sim$1.2 ms after shock formation the velocities are negative everywhere (see fig. (3.2) for the case of the W&H EoS). Therefore, the prompt shock mechanism fails, independent of the employed nuclear EoS.

3.2.2 Explosion-mechanism

The subsequent expansion of the shock is supported by a combination of different effects. Initially very high mass accretion rates cause the material to pile up between neutrinosphere and shock as it is also observed in the early post-bounce accretion phase of more massive progenitor stars (see, for example, Buras et al. 2005). Second, the rapid decrease of the mass accretion rate contributes to ensure ongoing expansion (see right plot in fig. 3.4), because even for quasi-stationary conditions the accretion shock adjusts to a larger radius for smaller mass accretion rates. Finally, as soon as the shock reaches the outer edge of the C-O shell, a very steep density decline leads to an outward acceleration of the shock. The last two aspects are linked to the specific structure of O-Ne-Mg cores and discriminate SN progenitors with such cores from more massive stars. However, despite the shock expansion the material behind the shock has initially still negative velocities and is accreted onto the forming NS (figs. 3.1,3.2). Note that when the matter right behind the shock starts to expand with the shock, the gas accreted by the shock is gravitationally bound and remains so in passing through the shock. However, $p\mathrm{d}V$ work excerted from below and to a minor extent energy input by neutrino heating can convert the accretion into an explosion, accelerating a tiny amount of matter ($\ll 10^{-3}\,M_{\odot}$) to move outward with the shock.

While the shock reaches larger radii, the temperature and density behind the shock de-

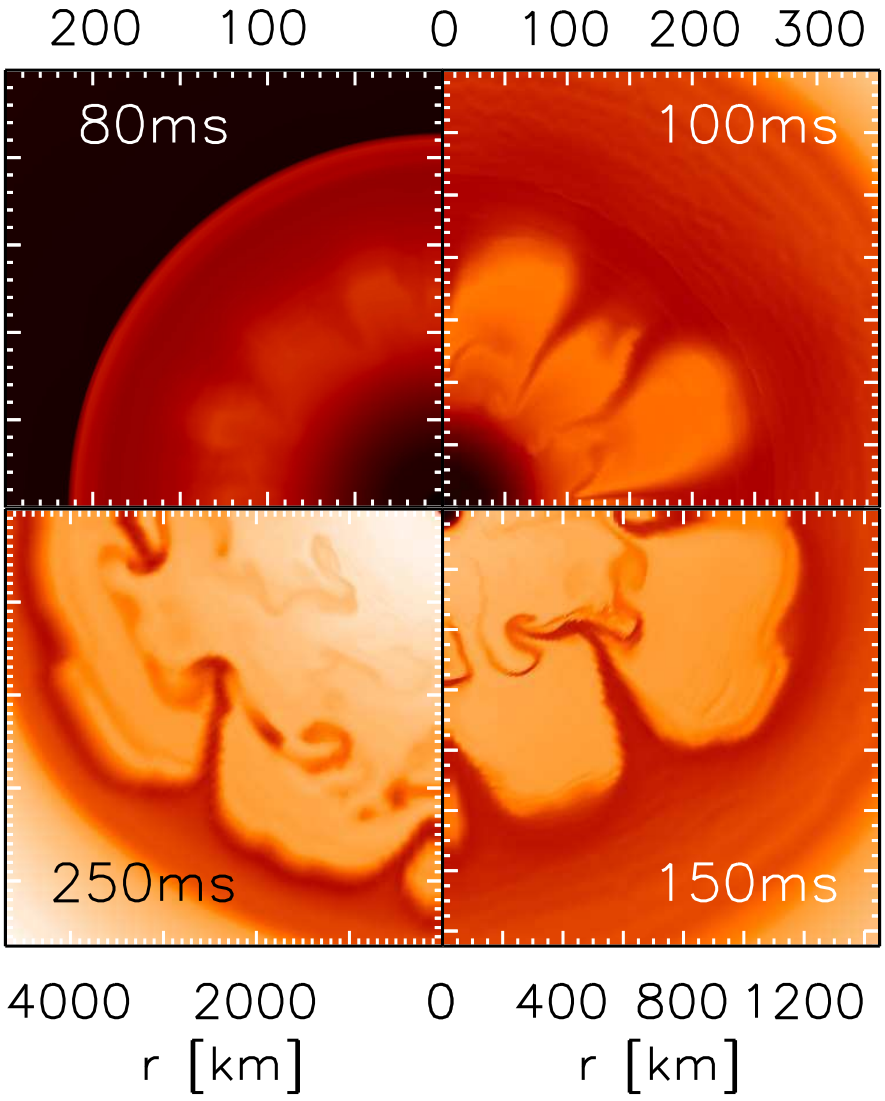

Figure 3.3: Four snapshots of the explosion of an 8–10 $M_\odot$ star in a two-dimensional (2D) simulation, which was performed in a $\pm 45^\circ$ wedge around the equatorial plane, using periodic boundary conditions. Time is normalized to bounce. The color coding represents the entropy per nucleon with black corresponding to values of $\lesssim 7\,k_\mathrm{B}$, red to 10–15 k_B, orange to 15–20 k_B, and white to about 25 k_B. The supernova shock is visible as sharp red/black discontinuity at about 210 km in the upper left panel, while it is already far outside the displayed region at all other times (the corresponding shock radii are roughly 900 km, 5600 km, and 15000 km).

crease. High-energy electron neutrinos and antineutrinos, which stream off from their neutrinospheres (represented by the thick solid, dashed, and dash-dotted lines in fig. (3.1)) begin to deposit energy behind the shock mainly by absorption on nucleons. This leads to the formation of a "gain radius" (thin dashed line in fig. (3.1)) which separates a layer of neutrino cooling

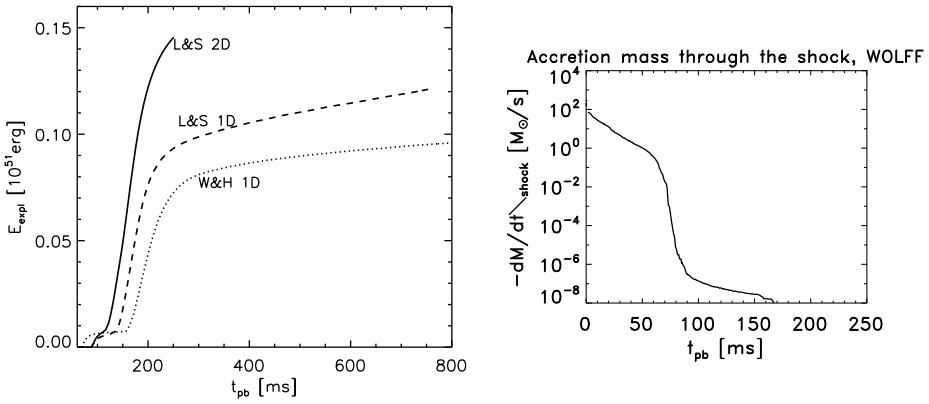

Figure 3.4: **Left:** Explosion energy as a function of time for the 2D simulation of the left figure compared to two runs in spherical symmetry (1D) with a soft ("L&S") and a stiff ("W&H") nuclear equation of state. The steep increase of the explosion energy in the 1D models after about 150 ms is caused by the onset of the expansion of neutrino-heated matter away from the gain radius. Convective overturn leads to more efficient neutrino heating of a larger mass and to an earlier rise of the explosion energy in the 2D simulation. The energy is defined as the volume integral of the total gas energy (internal plus kinetic plus gravitational) in regions where the latter is positive. **Right:** The mass accretion rate of the collapsing ONeMg core at a function of time after bounce, measured just outside of the supernova shock.

around the neutrinosphere from the energy "gain layer" behind the shock (Bethe & Wilson 1985). The neutrino emission evolution can be nicely seen in the luminosty plots shown in fig. (3.6). Four phases characterise the evolution: the collapse phase, in which neutrinos are trapped, the prompt burst of electron neutrinos, the accretion phase, and finally the explosion phase, which we explain below.

About 80 ms after bounce for the L&S EoS and about 60 ms for the W&H EoS, the neutrino heating timescale, defined by the total energy in the gain layer divided by the neutrino heating rate in that region, gets smaller than the advection timescale (see fig. 3.5). The latter is given as the time the accreted matter needs for being advected from the shock to the gain radius. Since the increasing shock radius leads to smaller and smaller postshock velocities, the duration of the deposition of energy via neutrino absorption in the shocked matter increases. The continuous input of energy raises the total energy of the gain layer to a value near zero within roughly 100 ms, unbinding the matter in the gravitational field of the forming NS. The fluid velocity in the layer close to the gain radius therefore starts to become positive (see fig. (3.1) and the right plot in fig. (3.2)) and the explosion energy shows a rapid increase (left plot in fig. 3.4).

The cooling region then becomes more and more narrow as the gain radius retreats towards the neutrinosphere, so that neutrinos diffusing out of the contracting protoneutron star begin to heat the layers right above the neutrinosphere. Gas is thus ablated from the NS surface, and the so-called neutrino-driven wind phase sets in at $t \gtrsim 200$ ms after bounce. Several of the mass shells depicted in fig. (3.1) clearly show this process.

At this time the energy in the expanding postshock matter has increased to about 0.1×10^{51}

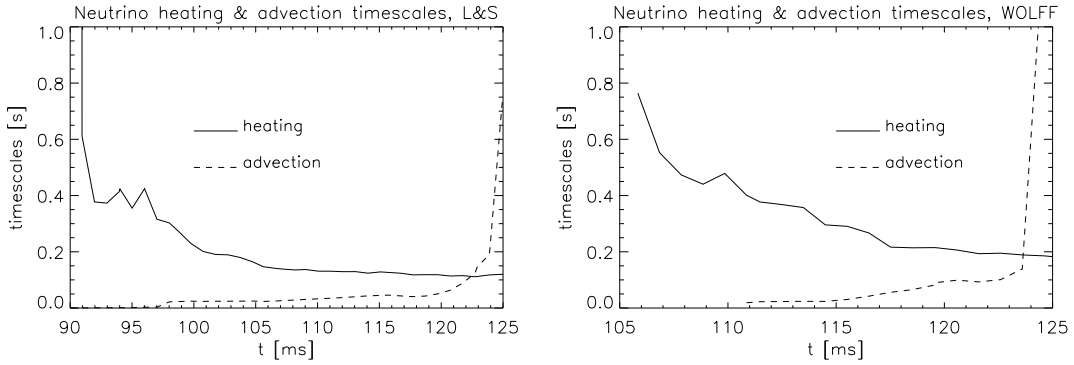

Figure 3.5: Neutrino heating and advection timescales for the L&S and for the W&H EoS. The physical time is not normalized to bounce, but starts with the onset of collapse, where the simulation was initiated.

erg, rising further due to the power input by the neutrino-driven wind. We extrapolate that the final energy of the explosion will be slightly larger than 0.1×10^{51} erg for the calculation with the W&H EoS and might be about 50% higher in case of the L&S EoS. This is roughly a factor of 10 lower than the canonical SN value, in contrast to the findings in previous explosion models of O-Ne-Mg cores (Hillebrandt et al. 1984, Mayle & Wilson 1988).

At the end of our simulation the mass cut, and therefore the baryon mass of the protoneutron star, is around 1.360 $M_\odot$ for the W&S EoS (fig. 3.1) and about $1.365\ M_\odot$ for the L&S EoS (see figure 3.8). The NS mass will only slightly decrease further because of the ongoing mass loss in the neutrino-driven wind. The mass of the ejecta lies therefore between 0.014 and 0.017 $M_\odot$. The ejected gas has an electron fraction, Y_e, between 0.46 and 0.53 and entropy values between 10 and 40 k_B per nucleon for both EoSs (see fig. (3.7) for the case with the W&H EoS). Since only about one third of the ejected matter has a Y_e value very close to 0.5, the mass of ejected ^{56}Ni is certainly smaller than $\sim$0.015$M_\odot$. The Y_e values in our models are higher than those in previous simulations of SNe from O-Ne-Mg cores (Mayle & Wilson 1988). This points to important differences in the neutrino treatment. Spectral Boltzmann transport calculations have recently found early ejecta with Y_e around 0.5 and higher also in (artificial) explosions of more massive progenitors (Buras et al. 2005, Fröhlich et al. 2005). The reason for this difference compared to the older models is a refined description of neutrino spectra formation and in particular of charged-current neutrino-nucleon interactions, including the weak magnetism corrections that were pointed out to be relevant by Horowitz (2002).

3.3 Multi-dimensional effects

Multi-dimensional effects are not crucial for obtaining neutrino-driven explosions of progenitors with the structure of the considered $\sim 9\,M_\odot$ model. Nevertheless, a simulation performed in two dimensions (2D; i.e., assuming axial symmetry) shows that convective overturn in the neutrino-heated layer between the gain radius (at 90 km) and the shock becomes strong about 80 ms after bounce and has fully developed 20 ms later (see fig. 3.3, upper panels of left plot). It carries cooler matter in narrow downdrafts from larger distances to locations closer to the gain

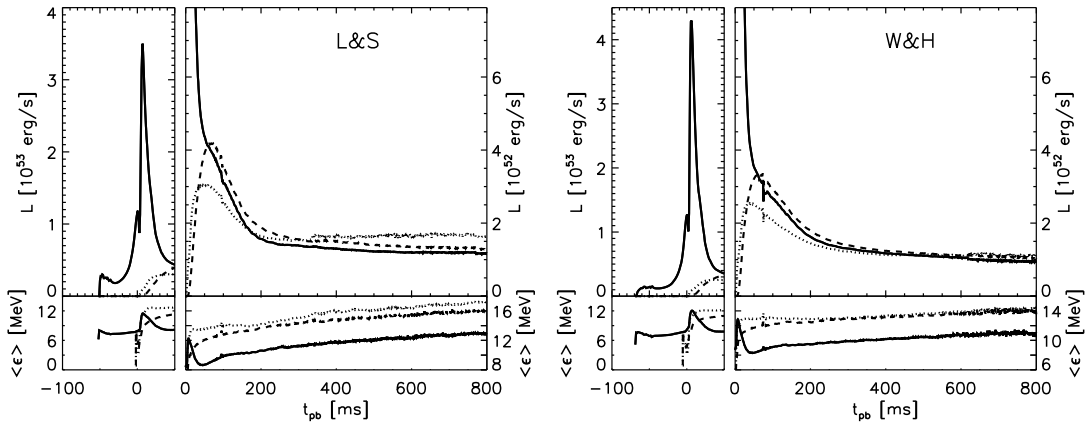

Figure 3.6: Neutrino luminosities for the L&S (left) and for the W&H (right) EoSs for an observer at rest at 400 km. The solid line is for electron neutrinos (ν_e), the dashed line is for the electron antineutrinos ($\overline{\nu_e}$) and the dotted line is for the rest of flavours, μ and τ neutrinos and antineutrinos. In the lower panel, the average energies of the emitted neutrinos are plotted.

radius, where the gas is exposed to more efficient neutrino heating. Therefore a larger gas mass absorbs energy from neutrinos before it accelerates outward in rising high-entropy plumes. This leads to a considerably higher energy of the explosion than in the corresponding 1D simulations (left plot in fig. 3.4), but has essentially no effect on the propagation of the supernova shock during this phase, because the shock is already far outside of the convective region. After about 150 ms of post-bounce evolution the radial propagation of the neutrino-heated layers has become so fast that the mixing motions freeze out and the corresponding fluid pattern with characteristic Rayleigh-Taylor mushrooms expands self-similarly with high velocity (fig. 3.3, lower panels). The 2D simulation also shows that convection inside the nascent neutron star does not lead to any significant increase of the neutrino luminosities and thus of the neutrino heating behind the shock. In agreement with recent simulations with spectral neutrino transport (Bruenn et al 2007) we also observe convective-like fluid motions below the neutrino-sphere confined to a layer between 10 and 30 km (see figs. 3.9 and 3.10). This convection is initiated promptly after bounce (around 8 ms post-bounce time) and fades away within less than 15 ms. Mezzacappa et al (2007) also report about this Ledoux convection and claim that it is driven by the negative entropy gradient left behind by the weakening post-bounce shock. Around 50 ms after bounce the convective behavior is reinitiated below the neutrinosphere and stays until the end of our simulation ($\sim$250 ms). Figure (3.9) shows the four stages: the upper-left pannel for both plots shows a rather spherical symmetric pattern, where convection is just about to start 4 ms after bounce. The upper-right pannels show the strongest convective features in the first convective phase at around 10 ms. The lower-right pannels show the behavior in the interval between 20 ms and 50 ms (the snapshot is taken at 48 ms), where convection is suppressed. Finally, the lower left pannels show the typical pattern when convection has restarted (the snapshots are taken at 150 ms). We have depicted in fig. (3.10) the typical cycle of a bubble which is transported by convection in an outflow till the turn-over radius is reached and falls back in a downflow. This process occurs within less than 10 ms.

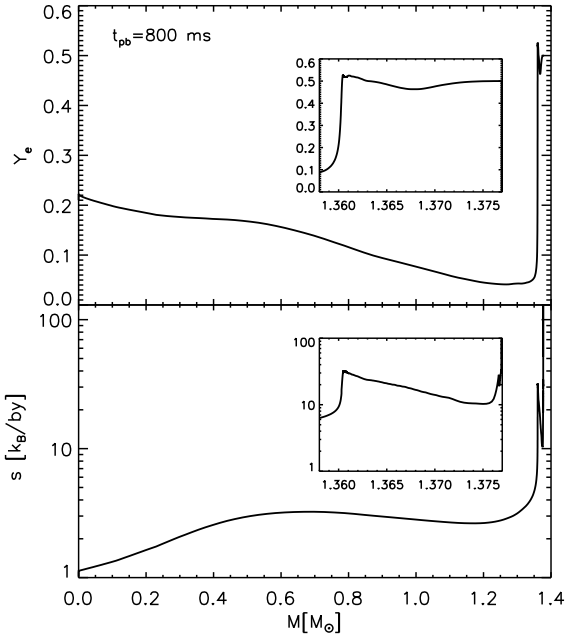

Figure 3.7: Profiles of the electron fraction $Y_{\rm e}$ and entropy s as functions of enclosed mass at the end of our simulation with the W&H EoS.

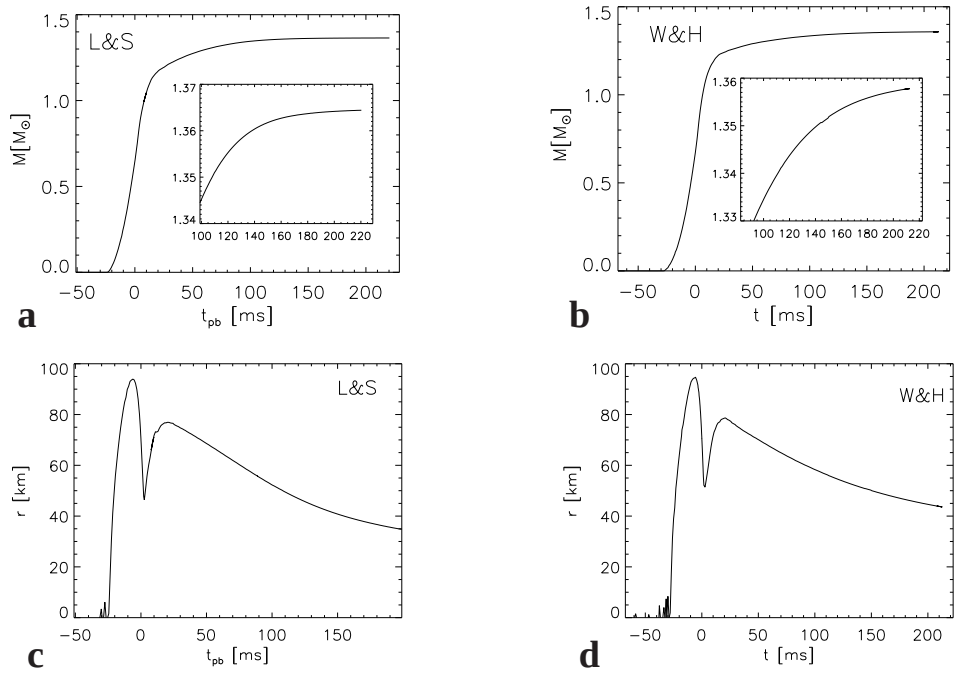

Figure 3.8: Neutron star mass (panels **a** and **b**) and neutron star radius (panels **c** and **d**) for the L&S and for the W&H EoSs respectively. Here the layer with a density of 10^{11} g/cc was followed in time.

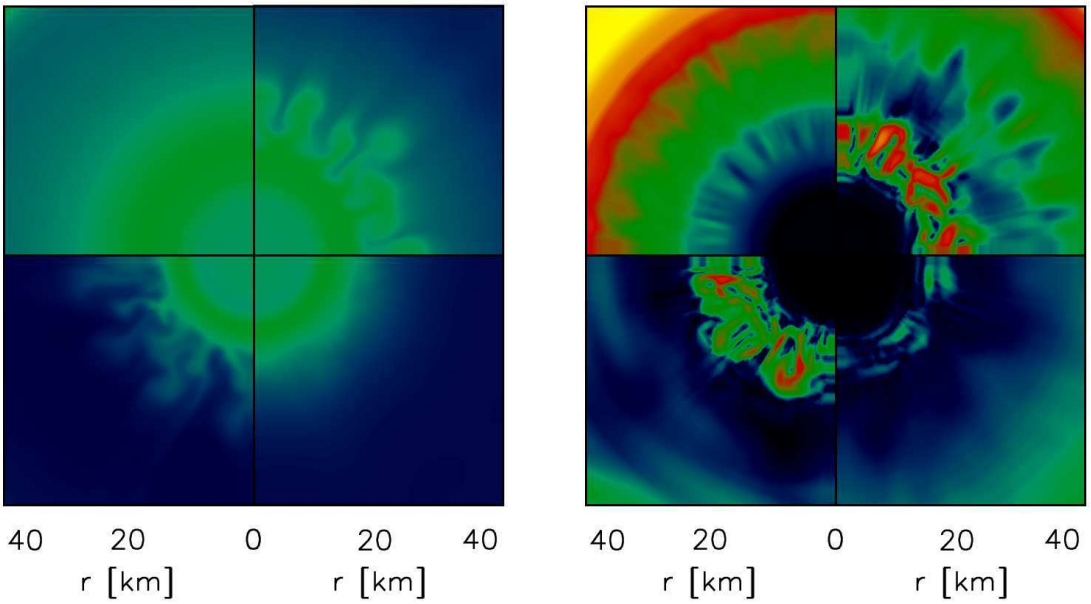

Figure 3.9: Neutron star convection at different post-bounce times represented by the electron fraction in the left plot and by the velocity modulus in the right plot. The snapshots are taken at 4 ms (upper-left), at 10 ms (upper-right), at 48 ms (lower-left), and at 150 ms (lower-right).

The enhanced explosion energy is merely a consequence of the convective activity behind the supernova shock. This is clearly different from the simulations by Mayle & Wilson (1988), who obtained models with larger explosion energy by assuming that the neutrino luminosities were boosted by neutron-finger convection below the neutrinosphere.

The rapid outward acceleration also has the consequence that the convective pattern never develops dominant power on the largest scales. The expansion of the gain layer happens so quickly that the convective plumes have no time to merge to structures with lateral wavelengths of more than about 45°. Since the shock radius grows continuously with time, also the SASI (stationary accretion shock instability) has no possibility to grow (for more details, see Blondin et al 2003, Scheck et al 2007). Such a situation disfavors the development of a large global asymmetry of the small amount of material that is accelerated during the early stages of the explosion. Therefore the pulsar kick velocities must be expected to remain rather small (roughly $\lesssim 100$ km/s) in case of the O-Ne-Mg core collapse events.

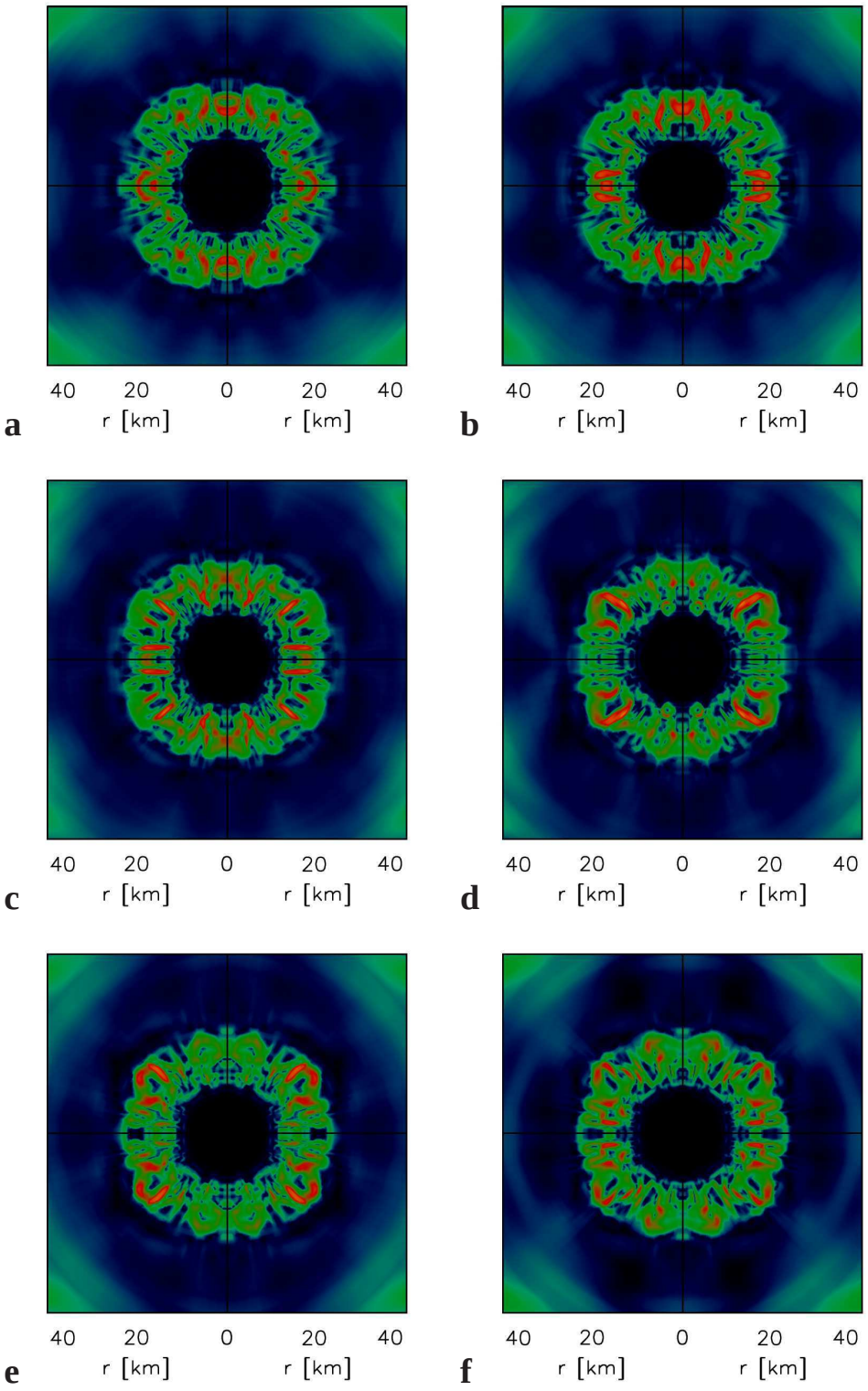

Figure 3.10: Neutron star convection represented by the velocity modulus for 6 snapshots starting at 100 ms post-bounce time with each subsequent snapshot taken with an interval of 1 ms. The $\pm 45^{\circ}$ wedge around the equatorial plane has been reproduced in each of the 4 quadrants for visualization purpose.

Chapter 4

Conclusions

Our 1D and 2D simulations of SN explosions from the collapse of O-Ne-Mg cores suggest that such SNe are powered by neutrino heating and by the neutrino-driven wind of the newly formed NS, similar to what Woosley & Baron (1992) found in case of the accretion-induced collapse of white dwarfs to NSs. Such events have a low explosion energy ($\sim 0.1\times10^{51}$ erg) and produce little ^{56}Ni ($\lesssim 10^{-2}\,M_\odot$). Most of the ejecta expand initially with velocities of 2–4$\times10^4$ km s^{-1}, a small fraction has nearly 10^5 km s^{-1}. This is significantly faster than in SNe of more massive progenitors. Of course, sweeping up the matter of the stellar mantle and envelope, the shock will decelerate, and the ejecta velocities after shock breakout from the stellar surface will be correspondingly lower. During the first second of the explosion, the ejected matter has $0.46 \lesssim Y_\mathrm{e} \lesssim 0.53$ and modest entropies ($10 \lesssim s/(k_\mathrm{B}/\mathrm{by}) \lesssim 40$). Such conditions exclude that r-process elements are formed in this matter during this early phase of the explosion of O-Ne-Mg cores: Y_e is too large for the "classical" low-entropy r-process and s is too low for high-entropy r-processing. The ejecta in our models, however, do not show the vast overproduction of some very neutron-rich, rare isotopes like ^{87}Kr, which was made in low-Y_e material ($Y_\mathrm{e} \lesssim 0.44$) in previous simulations (Mayle & Wilson 1988), and which was interpreted as a severe constraint to the rate of such events. Our models yield considerably less energetic explosions than previous simulations and show other significant differences in the dynamics and explosion characteristics. These are probably mainly linked to the improved treatment of neutrino transport and neutrino-matter interactions.

The small explosion energy obtained in our simulations is more consistent than previous explosion models of O-Ne-Mg cores with the low present expansion velocities (~ 1500 km s^{-1}) of the filaments of the Crab remnant of SN 1054 (Davidson & Fesen 1985), corresponding to a low kinetic energy of 0.6–1.5$\times10^{50}$ erg for an ejecta mass of $4.6 \pm 1.8\,M_\odot$ in ionized and neutral gas (Fesen et al. 1997). The energy could be even somewhat larger if there were several solar masses of material in an undetected, extended halo.

While our simulations are spherically symmetric, we do not expect any qualitative changes in the multi-dimensional case, and probably only a modest increase of the explosion energy. Since very fast outflow develops on a relatively short timescale after core bounce, nonradial hydrodynamic instabilities are unlikely to have time to merge and grow to very large structures

or global asymmetry before the anisotropic pattern freezes out in the accelerating expansion (Scheck et al. 2006, in preparation). Therefore the recoil velocity of the NS due to anisotropic mass ejection should remain fairly small (see Scheck et al. 2004), in agreement with speculations by Podsiadlowski et al. (2004). Corresponding 2D simulations are in progress.

Our models have also an important bearing on the nuclear EoS constraints deduced by Podsiadlowski et al. (2005) from the low-mass Pulsar B of the double pulsar J0737-3039, which has a gravitational mass of $M_{\rm G} = 1.249 \pm 0.001\,M_\odot$. Provided the progenitor model we use is valid, the mass loss of the collapsing O-Ne-Mg core during the explosion leaves the neutron star with a baryonic mass of $M_0 = 1.36 \pm 0.002\,M_\odot$. The error range accounts approximately for variations associated with the employed EoS and the wind ablation after our simulations are terminated. Our value implies a systematic left shift and reduction of the "acceptance rectangle" in fig. (3) of Podsiadlowski et al. (2005). Combined with the recent measurement of a pulsar of $2.1\pm0.2\,M_\odot$ in PSR J0751+1807 (Nice et al. 2005), which is the largest well determined NS mass so far, this lends viability only to a limited number of NS EoSs which allow for a sufficiently large maximum mass and whose $M_{\rm G}/M_0$-curves pass through the acceptance rectangle.

Based on our findings one might speculate that (B-) stars around $9\,M_\odot$ are also the progenitors of some of the subluminous Type II-P supernovae mentioned in the introduction. In fact, their peculiarities would be explained in a very natural way. The low peak luminosity and extended plateau phase could result from the combination of a low hydrogen envelope mass ($\simeq 6\,M_\odot$) with low expansion velocities ($\lesssim$ 3000 km/s). The small mass of radioactive ^{56}Ni would explain the low tail-luminosity of these objects. An alternative interpretation of subluminous Type II-P supernovae is the explosion of rather massive stars with extended envelopes, but otherwise more "normal" explosion energies. This connection is supported by the long duration of the plateau phase of many of these events (cf. Pastorello et al. 2004, and refs. therein). Provided the observations cover the full duration of the plateau, SN 1997D and 2003gd may still be viable cases for explosions of stars with main sequence masses around $9\,M_\odot$ (Hendry et al. 2005). There is a clear difference between such stars and more massive supernova progenitors. The former eject very little amounts (some $10^{-3}\,M_\odot$?) of oxygen only, like SN 1997D (Chugai & Utrobin 2000), whereas the latter produce up to a solar mass or more. Therefore one might be able to distinguish between the two scenarios on the basis of observations by measuring the oxygen lines in the late nebular spectra.

Appendix A

The equations of neutrino hydrodynamics

The simulation of the dynamics of stellar core-collapse and supernova explosion requires the description of the evolution of the coupled physical system that contains "neutrinos" and stellar plasma or "fluid".

"Fluid" is called a system of particles that admits a hydrodynamical description. For this it is necessary that the mean free path between interactions of those particles is very small compared to the scales of macroscopic variations in the system. It has to be also fulfilled, that the forces between particles saturate or are of "short range", because otherwise collective effects must be taken into account. Formally, the energy per particle has to remain constant with the number of particles going towards infinite. Gravity and electromagnetic forces which both scale as $\sim r^{-1}$, are non-saturating forces. Hence, gravity must be included in the hydrodynamic equations as a macroscopic external force. Electromagnetic forces however saturate in electrically neutral systems due to screening. The stellar fluid can be assumed to contain nucleons and nuclei, charged leptons and photons, since mean free paths of these particles are determined by electromagnetic and strong interactions and are thus very short. These particles are therefore in thermodynamic equilibrium unless nuclear reactions play a role.

For densities $\rho \leq 10^{12}$ g cm^{-3}, the mean free paths of neutrinos are comparable to the radius of the core, so that neutrinos are not in equilibrium with the stellar plasma and also the condition for a hydrodynamical description is not fulfilled. Neutrinos have to be treated separately by solving transport equations, because weak interactions cannot establish equilibrium. Since a star has regions which are opaque, semitransparent or transparent for neutrinos, the neutrino transport can neither be described by a diffusion equation nor by simply using source terms that account for local sinks of energy and lepton number. An accurate treatment of neutrino transport by solving the Boltzmann equation in connection with hydrodynamical simulations has only been achieved recently (see Mezzacappa et al. 2001, Rampp 2000, Rampp & Janka 2000, 2002, Thomson, Burrows & Pinto 2003).

A.1 Hydrodynamics

Fluid elements are considered to contain a number of particles that is sufficiently large to introduce mean quantities on a macroscopic scale like a mean mass density, mean momentum density, mean internal energy density etc. These mean quantities are treated as continuous functions of the space coordinates, without referring explicitly to the physical state of individual particles which constitute the fluid elements. The properties of a fluid element are described mathematically by moments of a particle distribution function over momentum space. It is therefore possible to derive the equations of hydrodynamics from statistical mechanics by constructing moments of the Boltzmann equation over momentum space and truncating the system on a certain level (see e.g. Mihalas & Mihalas 1984, §30.) For a classical derivation based on conservation laws see e.g. Landau & Lifschitz (1991).

For an ideal fluid characterized by the mass density ρ, the Cartesian components of the velocity vector $(v_1, v_2, v_3)^T$, the specific energy density $\varepsilon = e + \frac{1}{2}v^2$ and the gas pressure p, the Eulerian, nonrelativistic equations of hydrodynamics in Cartesian coordinates read with sum over i implied (see e.g. Rampp & Janka 2002):

$$\partial_t \rho + \partial_i(\rho v_i) = 0 \quad , \tag{A.1}$$

$$\partial_t(\rho v_k) + \partial_i(\rho v_i v_k + \delta_{ik} p) = -\rho \partial_k \Phi^{\rm Newt} + Q_{{\rm M}k} \quad , \tag{A.2}$$

$$\partial_t(\rho\varepsilon) + \partial_i(\{\rho\varepsilon + p\}v_i) = -\rho v_i \partial_i \Phi^{\rm Newt} + Q_{\rm E} + v_i Q_{{\rm M}i} \quad , \tag{A.3}$$

where $\Phi^{\rm Newt}$ denotes the Newtonian gravitational potential of the fluid, which can be determined from the Poisson equation

$$\partial_i \partial^i \Phi^{\rm Newt} = 4\pi G\rho \quad , \tag{A.4}$$

where G is Newton's constant. $Q_{\rm M}$ and $Q_{\rm E}$ are the neutrino source terms for momentum transfer and energy exchange, respectively, δ_{ik} is the Kronecker symbol, and $\partial_i := \partial/\partial x^i$ is an abbreviation for the partial derivative with respect to the coordinate x^i. In order to describe the evolution of the chemical composition of the (electrically neutral) fluid, the hydrodynamic equations are supplemented by a continuity equation for the electron fraction $Y_{\rm e}$ (number density of electrons minus positrons divided by the number density of baryons),

$$\partial_t(\rho Y_{\rm e}) + \partial_i(\rho Y_{\rm e} v_i) = Q_{\rm N} \quad , \tag{A.5}$$

where the source term $Q_{\rm N}$ describes the change of the net electron number density (i.e. the density of electrons minus that of positrons) due to emission and absorption of electron-flavour neutrinos. Unless nuclear statistical equilibrium (NSE) holds, an equation like (A.5) has to be solved for the mass fraction X_k of each of the $N_{\rm nuc}$ nuclear species. In NSE $X_k = X_k(\rho, T, Y_{\rm e})$ is determined by the Saha equations.

An equation of state is invoked in order to express the pressure as a function of the independent thermodynamical variables, i.e., $p = p(\rho, T, Y_{\rm e})$, if NSE holds,

or $p = p(\rho, T, Y_{\rm e}, \{X_k\}_{k=1\ldots N_{\rm Nuc}})$ otherwise.

A.2 Neutrino transport

A.2.1 Boltzmann equation

The physical state of a statistical ensemble of particles with given statistics (bosons, fermions) is described by the particle distribution function $f(t,\boldsymbol{r},\boldsymbol{p})$ in phase space.

Then $g/h^3 \cdot f(t,\boldsymbol{r},\boldsymbol{p})\mathrm{d}^3\boldsymbol{r}\mathrm{d}^3\boldsymbol{p}$ is the number of particles occupying the phase-space volume $d^3\boldsymbol{r}d^3\boldsymbol{p}$ at $(\boldsymbol{r},\boldsymbol{p})$, g denotes the statistical weight of the particles; e.g. $g = 1$ for Dirac neutrinos, g=2 for photons; $h = 2\pi\hbar$ is Planck's constant. The temporal evolution of the distribution function is governed by the Boltzmann equation

$$\frac{\partial}{\partial t}f + \frac{\partial \boldsymbol{r}}{\partial t}\nabla_{\boldsymbol{r}} f + \frac{\partial \boldsymbol{p}}{\partial t}\nabla_{\boldsymbol{p}} f = \left(\frac{\mathrm{d}f}{\mathrm{d}t}\right)^{\mathrm{coll.}} \quad . \tag{A.6}$$

Eq. A.6 assumes flat spacetime (Minkowski) and thus disregards general relativistic effects. Particles with vanishing rest mass, usually referred to as "radiation" in the classical sense, then move along straight rays with the speed of light, hence $\mathrm{d}\boldsymbol{r}/\mathrm{d}t = \boldsymbol{n}\mathrm{c} \equiv \boldsymbol{p}/|\boldsymbol{p}|\ c$. If, in addition, no external forces are present ($\dot{\boldsymbol{p}} \equiv 0$), eq. (A.6) simplifies to (ignoring for the moment, e.g. effects due to motion of the medium that carries the target particles for radiation or neutrino interactions):

$$\frac{1}{c}\frac{\partial}{\partial t}f + \boldsymbol{n}\nabla_{\boldsymbol{r}} f = B \quad . \tag{A.7}$$

The Boltzmann eq. (A.7) is a hyperbolic partial differential equation. In particular, for a given source term B, eq. (A.7) is a linear advection equation with characteristic speed c: Along a line element of length $\Delta s = \boldsymbol{n}\Delta\boldsymbol{r}$ and within the time interval $\Delta t = \Delta s/c$, the change of the distribution function of particles entering at one end (s,t) and emerging at the other end $(s + \Delta s,\ t + \Delta t)$ results as given by the collision term B. Introducing the "emissivity" $\tilde{\eta}$ and the opacity χ, which is the inverse of the mean free path, the collision term can be written as (scattering processes can be considered as absorptions with subsequent emissions)

$$B := \frac{1}{c}\left(\frac{\mathrm{d}f}{\mathrm{d}t}\right)^{coll.} \equiv \tilde{\eta} - \chi f \quad . \tag{A.8}$$

Introducing the monochromatic specific intensity

$$\mathcal{I} := \left(\frac{\epsilon}{hc}\right)^3 c \cdot f \quad , \tag{A.9}$$

and the emissivity

$$\eta := \left(\frac{\epsilon}{hc}\right)^3 c \cdot \tilde{\eta} \quad , \tag{A.10}$$

the Boltzmann equation (A.7) reads

$$\frac{1}{c}\frac{\partial}{\partial t}\mathcal{I} + \boldsymbol{n}\nabla_{\boldsymbol{r}}\mathcal{I} = C \equiv \eta - \chi\mathcal{I} \quad , \tag{A.11}$$

where ϵ is the energy of the neutrinos. Rewriting the momentum-space part of a phase-space volume element as ($\mathrm{d}\Omega$ denotes the solid angle element)

$$\mathrm{d}^3\boldsymbol{p} = \epsilon^2/c^3 \mathrm{d}\epsilon \mathrm{d}\Omega \ , \tag{A.12}$$

the quantities $\mathcal{I}(t,\boldsymbol{r},\epsilon,\boldsymbol{n})\mathrm{d}\Omega\mathrm{d}\epsilon\ \boldsymbol{n}\boldsymbol{r}/|\boldsymbol{r}|\mathrm{d}A\mathrm{d}t$ and $\epsilon^{-1}\mathcal{I}(t,\boldsymbol{r},\epsilon,\boldsymbol{n})\mathrm{d}\Omega\mathrm{d}\epsilon\boldsymbol{n}\boldsymbol{r}/|\boldsymbol{r}|\mathrm{d}A\mathrm{d}t$ can be interpreted as the amount of energy and particle number, respectively, which during the time $\mathrm{d}t$ is carried by radiation within the frequency interval $h^{-1}[\epsilon, \epsilon+\mathrm{d}\epsilon]$ through the surface element $\mathrm{d}A$ (with the outwardly directed normal $\boldsymbol{r}/|\boldsymbol{r}|$) into the solid angle $\mathrm{d}\Omega$ about the direction $\boldsymbol{n}$. The source term $C := (\epsilon/hc)^3 c \cdot B \equiv \eta - \chi\mathcal{I}$ is interpreted as the amount of radiation energy in a unit frequency interval contained within the unit solid angle around the direction $\boldsymbol{n}$ that is exchanged with a material element of unit volume per unit time interval.

A.2.2 Angular moments

The angular moments of the monochromatic specific intensity are defined as the following integrals over all angular directions

$$\begin{aligned}
J(t,\boldsymbol{r},\epsilon) &:= \frac{1}{4\pi}\int \mathrm{d}\Omega\, \mathcal{I}(t,\boldsymbol{r},\epsilon,\boldsymbol{n}) = \frac{c}{4\pi}E(t,\boldsymbol{r},\epsilon), && \text{(A.13)}\\
H_i(t,\boldsymbol{r},\epsilon) &:= \frac{1}{4\pi}\int \mathrm{d}\Omega\, n_i\mathcal{I}(t,\boldsymbol{r},\epsilon,\boldsymbol{n}) = \frac{1}{4\pi}F_i(t,\boldsymbol{r},\epsilon), && \text{(A.14)}\\
K_{ij}(t,\boldsymbol{r},\epsilon) &:= \frac{1}{4\pi}\int \mathrm{d}\Omega\, n_i n_j\mathcal{I}(t,\boldsymbol{r},\epsilon,\boldsymbol{n}) = \frac{c}{4\pi}P_{ij}(t,\boldsymbol{r},\epsilon), && \text{(A.15)}\\
&\vdots \quad ,
\end{aligned}$$

where $E(t,\boldsymbol{r},\epsilon)$ denotes the (monochromatic) neutrino energy-density, $\boldsymbol{F}$ the density of the (monochromatic) energy flux (the momentum density is given by $1/c^2\boldsymbol{F}$), and P_{ij} are the components of the stress tensor P. Moments of higher order do not admit an immediate physical interpretation.

A.2.3 Moment equations

Forming angular moments of the Boltzmann equation (A.11) one obtains the hierarchical set of monochromatic moment equations:

$$\begin{aligned}
\frac{1}{c}\frac{\partial}{\partial t}J + \nabla\cdot\boldsymbol{H} &= C^{(0)} \qquad (0^{th}\text{-order moment equation}), && \text{(A.16)}\\
\frac{1}{c}\frac{\partial}{\partial t}\boldsymbol{H} + \nabla\cdot\boldsymbol{K} &= \boldsymbol{C}^{(1)} \qquad (1^{st}\text{-order moment equation}), && \text{(A.17)}\\
&\vdots
\end{aligned}$$

with the corresponding source terms being defined as

$$C^{(0)}(t,\boldsymbol{r},\epsilon) := \frac{1}{4\pi}\int \mathrm{d}\Omega\, C(t,\boldsymbol{r},\epsilon,\boldsymbol{n}), \tag{A.18}$$

$$\boldsymbol{C}^{(1)}(t,\boldsymbol{r},\epsilon) := \frac{1}{4\pi}\int \mathrm{d}\Omega\, \boldsymbol{n}C(t,\boldsymbol{r},\epsilon,\boldsymbol{n}), \tag{A.19}$$

$$\vdots$$

The angular moments admit a very straightforward physical interpretation up to second order, the angular moment equations up to first order. It is usual to truncate the infinite system of moment equations (A.16, A.17, ...) at a certain level for solving the equations. This is done at the first order in the moment equations, i.e. at the level of the neutrino momentum equation.

In order to further reduce the dimensionality of the radiative transfer problem we assume spherical symmetry, i.e. that the spatial variation of all quantities can be described by only one coordinate, i.e. the radius r. In this case, it can be shown that in addition to this spatial coordinate r, the time t and the frequency $h^{-1}\epsilon$, the specific intensity depends only on one angular coordinate Θ. In spherical coordinates Θ is measured as the angle between the radial direction $\boldsymbol{r}$ (with $r :=|\boldsymbol{r}|$) and the direction of propagation $\boldsymbol{n}$ of the neutrinos:

$$\mu := \cos\Theta := \frac{\boldsymbol{r}\cdot\boldsymbol{n}}{r} \quad . \tag{A.20}$$

Spherical symmetry furthermore implies that the energy flux points into the radial direction

$$\boldsymbol{F} = 4\pi\frac{\boldsymbol{r}}{r}H \quad , \tag{A.21}$$

and that only relevant quantity of the stress tensor is the 33-component, which is identified with the scalar "radiation pressure"

$$P = \frac{4\pi}{c}K_{33} \equiv \frac{4\pi}{c}K \quad . \tag{A.22}$$

A.3 Neutrino hydrodynamics

The system of eqs. (A.16-A.17) is coupled to the evolution equations of the fluid (eqs. A.1-A.3 and A.5), since the source terms appearing on the rhs. of the monochromatic moment equations (A.16, A.17) are defined as the rate of net-energy and net-momentum exchange (per unit frequency interval and unit volume) between the fluid and neutrinos. By conservation of total energy (i.e. energy of the fluid plus neutrinos) and momentum (i.e. momentum of the fluid plus neutrinos), the fluid's energy density and momentum density has to change by exactly the opposite amount of the changes of the quantities for neutrinos. Summing over all frequencies the source terms therefore are

$$Q_{\mathrm{E}} = -4\pi\int_0^\infty d\epsilon\, C^{(0)}(\epsilon) \quad , \tag{A.23}$$

$$Q_{\rm M} = -\frac{4\pi}{c}\int_0^\infty d\epsilon\, C^{(1)}(\epsilon) \quad . \tag{A.24}$$

Due to the total electron-lepton number conservation there is an additional continuity equation for the number density of electrons minus positrons in the fluid plus the number density of electron neutrinos minus electron antineutrinos. Thus, the net source term (electron neutrinos minus electron antineutrinos) that enters the continuity equation for the net electron number (electrons minus positrons, eq. A.5) must read:

$$Q_{\rm N} = -4\pi m_B \int_0^\infty d\epsilon\, \mathcal{C}^{(0)}(\epsilon) \quad , \tag{A.25}$$

where $m_{\rm B}$ denotes the baryonic mass, and $\mathcal{C}^{(0)}(\epsilon) := \epsilon^{-1} C^{(0)}(\epsilon)$.

Appendix B

Numerical implementation

An operator splitting approach (see e.g. LeVeque 1998) is applied in order to decouple the neutrino hydrodynamics into a hydrodynamics part and a neutrino transport part. This allows one to solve independently in subsequent ("fractional") steps the equations of neutrino hydrodynamics.

The Newtonian finite volume code PROMETHEUS (**PRO**gram for **M**ulti dimensional **E**ulerian **T**hermonuclear **H**ydrodynamics with **E**xplicit **U**pwind **S**econd order Differencing) developed by Bruce Fryxell and Ewald Müller is used for the integration of the equations of hydrodynamics (Fryxell, Müller, & Arnett 1989). PROMETHEUS is a direct Eulerian, time explicit implementation of the Piecewise Parabolic Method (PPM) of Colella & Woodward (1984), which is a second-order Godunov scheme (see e.g. Godunov 1999) employing a Riemann solver, i.e. PPM achieves second order accuracy in space and time for the homogeneous equations of hydrodynamics. One of the numerous advantages Godunov schemes have is that they account for the nature of the equations of hydrodynamics being conservation laws for mass, momentum and energy. By employing Riemann-solvers, the hyperbolic character of the equations is explicitly taken into account. Such kinds of schemes are particularly well suited to follow discontinuities in the fluid flow like shocks or composition interfaces.

The version of PROMETHEUS used here was provided by Keil (1997). It offers an optional generalization of the Newtonian gravitational potential that includes general relativistic corrections. The hydrodynamics code was considerably updated and augmented by K.Kifonidis who added a simplified version of the "Consistent Multifluid Advection"-method (CMA) proposed by Plewa & Müller (1999) which ensures the accurate advection of individual chemical components of the fluid.

The neutrino transport is done with the Boltzmann solver scheme described in much detail by Rampp & Janka (2002). The integro-differential character of the Boltzmann equation is tamed by applying a so-called variable Eddington factor method. The moments of the neutrino distribution function and the energy and lepton number exchange with the stellar medium are determined by iteratively solving the zeroth and first order moment equations in combination with a model Boltzmann equation. Interaction kernels on rhs. of Boltzmann equations can be wined in terms of moments $J, H, ...$ The latter is discretized on a grid of tangent rays.

The variable Eddington factor is determined from the solution of the Boltzmann equation and the system of Boltzmann equation and its moment equations is iterated until convergence is achieved. The neutrino transport contains gravitational redshift and time dilation, but ignores the difference between coordinate radius and proper radius. This simplification is necessary for coupling the transport code to the basically Newtonian hydrodynamics. These approximations are reasonably good as long as there are only moderate deviations ($\sim$10-20%) of the metric coefficients from unity and the infall velocities do not reach more than 10-20% of the speed of light (Janka, Buras & Rampp 2002, Liebendörfer, Rampp, Janka, Mezzacappa 2003).

The operator-splitting structure of the code is represented in fig. B.1.3 with each important step numbered and explained in the next section.

B.1 Iteration procedure

Since the neutrino transport part is solved with an implicit method and the hydrodynamics part is handled with an explicit scheme they have different numerical requirements. The hydrodynamics part is in general more restrictive concerning the timestep length due to the CFL condition (eq. B.2), while the neutrino part is computationally much more expensive. This is the reason why a transport step is divided into a number of hydrodynamics substeps ($N^n_{\rm Hyd}$). Moreover the hydrodynamics part and the transport part work on different spatial grids, so that a conservative mapping procedure (the energy density, e, the density, ρ, momentum and lepton number have to be conserved quantities) between both grids is employed when quantities that are defined on one grid are required on the other.

B.1.1 Hydrodynamics

One hydrodynamics step is calculated as follows. The initial hydrodynamical state is the one at the old time level $(\rho^n, e^n, Y_{\rm e}^n, v^n)$ (H1). First the PPM algorithm computes a solution of the hydrodynamics equation laws (eqs. A.1-A.3) together with the continuity equations for $Y_{\rm e}$ and the nuclear composition (eq. A.5) (H2,H3). With the updated density the Poisson equation (H4) is solved to calculate the gravitational potential (H5). The neutrino source terms ($Q_{\rm E}$, $Q_{\rm N}$, $Q_{\rm M}$) together with the gravitational source term (gravitational potential Φ) (H6) are then applied to the total energy equation (eq. A.3) and the momentum equation (eq. A.2). The effects of the neutrino source terms are taken into account by using the source term of the old timestep. The neutrino pressure $Q_{\rm M}$ for example is taken into account in each individual hydrodynamic substep in the following way: $[\rho v]^{n+\varepsilon} = Q^n_{\rm M}\cdot\Delta t_{\rm Hyd}$. The effects of the source terms for energy and lepton number are treated in an analogous way. Finally, the nuclear effects, i.e. burning, are computed (H8). NSE is evaluated automatically whenever EoS is called. This completes the hydrodynamic substep $n+\varepsilon$, $\varepsilon \in [1/N^n_{\rm Hyd}, 2/N^n_{\rm Hyd}, ..., N^n_{\rm Hyd}/N^n_{\rm Hyd}]$ with the size $\Delta t^n_{\rm Hyd}$. Since the PPM algorithm uses an explicit integration the time step is limited by the CFL-condition (Courant-Friedrichs-Lewy condition)

$$\Delta t \leq \Delta t_{\rm CFL} \equiv \min_i \frac{\Delta r_i}{c_{{\rm s}i} + |v_i|} \quad , \tag{B.1}$$

where Δr_i is the grid spacing, $c_{\mathrm{s},i}$ is the local sound speed and $|v_i|$ is the flow velocity of zone i. This ensures that information is able to travel not more than one zone within a single time step (see e.g. Müller 1998). By performing a total of N^n_{Hyd} substeps the hydrodynamical state is evolved from the time level t^n to the new transport time level t^{n+1} given by

$$t^{n+1} = t^n + \Delta t^n = t^n + \Delta t^n_{\mathrm{Hyd}} \cdot N^n_{\mathrm{Hyd}} \ , \tag{B.2}$$

where $N^n_{\mathrm{Hyd}} \in \mathbb{N}$ is determined by the condition $\Delta t^n \leq \Delta t^{\max}_{\mathrm{Tr}}$ (Def. see Sect. 4.1.2). This leads to a partially updated hydrodynamical state $(\rho^{n+1}, \tilde{e}^{n+1}, \tilde{Y}^{n+1}_{\mathrm{e}}, \tilde{v}^{n+1})$ (H10) which includes the effects due to hydrodynamical fluid motions and the acceleration by gravitational forces, neutrino momentum transfer, neutrino energy and lepton number source terms. However, neutrino effects are only taken into account in an "explicit" way up to this point. Since we want "implicit" corrections the state variables are then mapped onto the transport grid and the quantities e, Y_{e} and v denoted with " ˜ " have to be updated using the solution of the current transport timestep (see coupling neutrinos with hydrodynamics).

B.1.2 Neutrinos

The maximum size of the transport time step $\Delta t^{\max}_{\mathrm{Tr}}$ is chosen so that the local hydrodynamical and neutrino variables change within chosen limits during the timestep.

The transport part starts with guess values for J, H, $\mathcal{J}$, $\mathcal{H}$, e, Y_{e} and v (T1). The thermodynamic state is determined by the quantities e, Y_{e} and the density ρ. The EoS then gives the temperature, chemical potentials, pressure, and NSE composition. These, together with J and H are used to evaluate the rhs. of the Boltzmann equation (T3) with the neutrino rates (T2). First the Legendre coefficients associated with an expansion of the collision integral as needed for non-isoenergetic scattering and pair processes are calculated from the corresponding rates (initial rates,T2). In the subsequent iterations only the absorption opacities $\kappa_{\mathrm{a}*}$ (T5) as needed for neutrino absorption and emission are calculated from the rates (T4) (Bruenn 1985 and Mezzacappa & Bruenn 1993). Now the formal solution of the Boltzmann equation can be computed (T6) in which the emissivities and the opacities are assumed to be known (for a detailed explanation see Rampp & Janka 2002). The Eddington factors (T7) that can be obtained from the formal solution are then fed into the system of moment equations which are solved together with the source term equations (T8) to obtain improved values for J, H, e and Y_{e} (T9).

The source-term equations, i.e. the evolution equations for the electron fraction and internal energy of the stellar medium in response to neutrino absorption and emission, are given by

$$\frac{\delta}{\delta t} e = -\frac{4\pi}{\rho} \int_0^\infty d\epsilon \sum_{\nu \in \{\nu_{\mathrm{e}}, \bar{\nu}_{\mathrm{e}}, \ldots\}} C^{(0)}_\nu(\epsilon) \tag{B.3}$$

$$\frac{\delta}{\delta t} Y_{\mathrm{e}} = -\frac{4\pi m_{\mathrm{B}}}{\rho} \int_0^\infty d\epsilon \left(\mathcal{C}^{(0)}_{\nu_{\mathrm{e}}}(\epsilon) - \mathcal{C}^{(0)}_{\bar{\nu}_{\mathrm{e}}}(\epsilon) \right) \ . \tag{B.4}$$

The notation $\delta/\delta t$ indicates that for exmaple eq. (A.5) is split into the equations $\partial_t(\rho Y_{\mathrm{e}}) + r^{-2}\partial_r(r^2 \rho Y_{\mathrm{e}} v) = 0$ and $\delta_t Y_{\mathrm{e}} = Q_N/\rho$.

The iteration procedure between T4 and T9 is continued until numerical convergence is achieved. Until this time the neutrino number density $\mathcal{J}$ and the flux density $\mathcal{H}$ are conventionally replaced by $\epsilon^{-1}J$ and $\epsilon^{-1}H$. With the Eddington factors being known from the described iteration procedure, the complete system of source-term and moment equations for neutrino energy and number (T10) is solved (once) in order to accomplish lepton number conservation. In this step $\mathcal{J}$ and $\mathcal{H}$ are treated as additional variables (T11). This yields the neutrino source terms (T12).

B.1.3 Coupling neutrino transport with hydrodynamics

We map the source terms from the transport grid to the hydrodynamics grid by a conservative procedure and then update the electron number density and the total energy density on the hydrodynamics grid (H11) according to

$$[\rho\varepsilon]^{n+1} = \rho^{n+1}\tilde{\varepsilon}^{n+1} + (Q_{\mathrm{E}}^{n+1} + v^{n+1}Q_{\mathrm{M}}^{n+1}) \cdot \Delta t^{n} \quad , \tag{B.5}$$

$$[\rho Y_{\mathrm{e}}]^{n+1} = \rho^{n+1}\tilde{Y}_{\mathrm{e}}^{n+1} + Q_{\mathrm{N}}^{n+1} \cdot \Delta t^{n} \quad . \tag{B.6}$$

Eqs. (B.5) and (B.6) express the effective influence of the source terms $Q_{\mathrm{E}} + vQ_{\mathrm{M}}$ over the time of a transport step, but in fact we apply the corresponding sources (as given at the old time level) during each substep of the hydrodynamics. The quantities $\tilde{e}^{n+1}$ and $\tilde{Y}_{\mathrm{e}}^{n+1}$ as needed for the transport part of the code, are recovered a posteriori by subtracting the accumulated effects of the neutrino sources again. The momentum equation of the stellar fluid is treated in a similar way. Accounting for the momentum transfer (acceleration) by neutrinos after each individual hydrodynamics substep (by using the old momentum source term Q_{M}^{n}), however, is of crucial importance here. The fluid velocity $\tilde{v}^{n+1}$ used in the transport step includes the effects due to the acceleration by neutrinos.

After the transport time step has been completed, the new neutrino stress Q_{M}^{n+1} is used for correcting $\tilde{v}^{n+1}$ to give the new velocity v^{n+1} at the time level t^{n+1}:

$$[\rho v]^{n+1} = \rho^{n+1}\tilde{v}^{n+1} + (Q_{\mathrm{M}}^{n+1} - Q_{\mathrm{M}}^{n}) \cdot \Delta t^{n} \quad . \tag{B.7}$$

The final output (H12) contains the coupled hydrodynamics-transport effects after one step. The whole process shown in fig. (B.1.3) is then iterated to follow the systems time evolution.

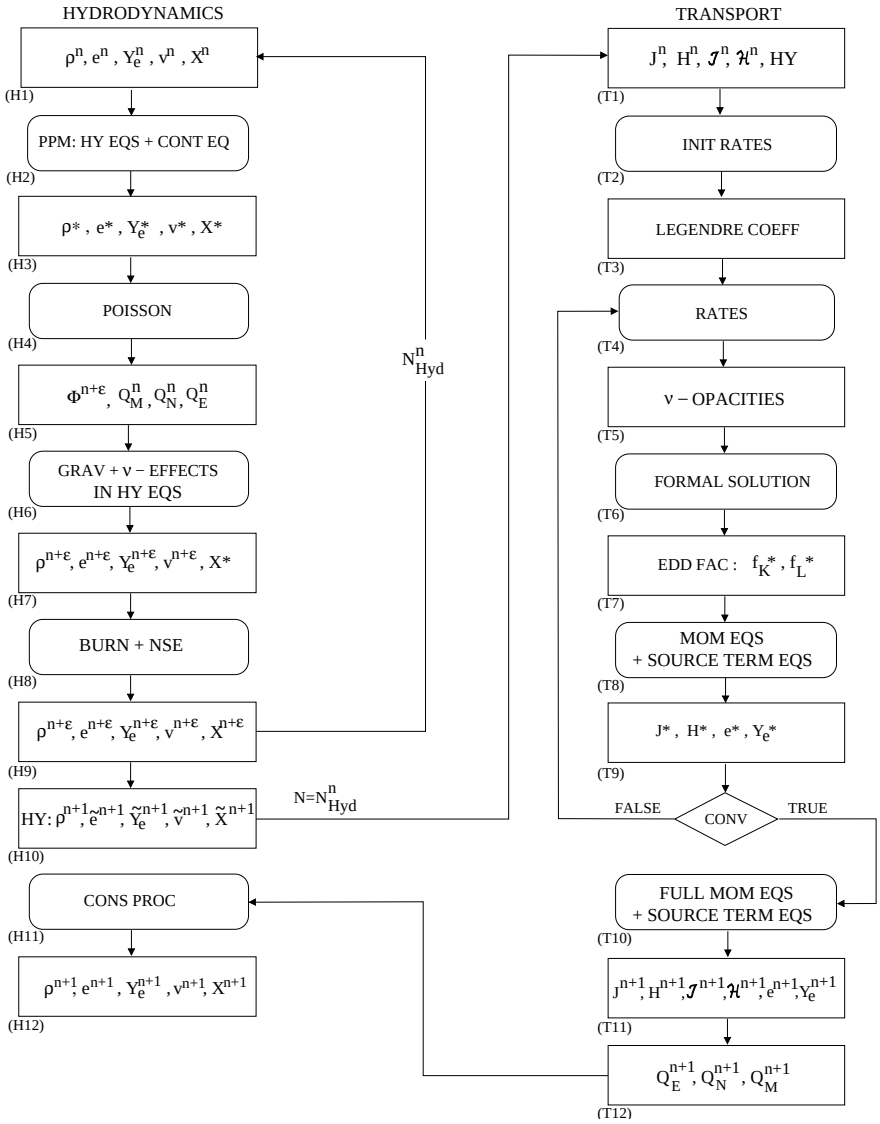

Figure B.1: Simplified flowchart of the code representing the evolution from the time level t^n to the new time level t^{n+1}. The code is basically divided into two parts according to an operator-splitting approach: the hydrodynamics part (left hand side) and the neutrino transport part (right hand side). Both parts are coupled so that the interaction of the neutrinos with matter is taken into account in each hydrodynamics substep using the source terms of the previous timestep and correcting their influence with the current transport timestep once at the end. The quantities on the left hand side are defined on the hydro-grid, whereas the ones on the right hand side are defined on the transport-grid. The tables for the EoS for different regimes are used throughout the code to derive other quantities that are required (e.g. the temperature and pressure are given through the EoS entering ρ, e and Y_e plus composition in non-NSE).

Appendix C

Electron capture rates and neutrino loss rates

The degenerate core of a progenitor with about 9 solar masses grows initially through hydrogen and helium double-shell burning. When the mass interior to the helium burning shell, i.e. the O/Ne/Mg core plus a C/O layer, reaches 1.38 $M_{\odot}$, the central density reaches 4 x 10^9 g cm^{-3}, for which the Fermi energy of degenerate electrons exceeds the threshold for the electron capture, ^{24}Mg(e$^-$, ν)^{24}Na (see Miyaji, Nomoto, Yokoi, 1980; Nomoto, 1987; Miyaji, Nomoto, 1987):

$$^{24}\mathrm{Mg} + e^- \rightarrow \nu + ^{24}\mathrm{Na} \ . \tag{C.1}$$

At first an electron is captured to form the isomeric state of ^{24}Na, which decays to its ground state by emitting gamma-rays with $E_\gamma = 0.2$ MeV. Electron capture processes according to ^{24}Na(e$^-$, ν)^{24}Ne and ^{20}Ne(e$^-$, ν)^{20}F(e$^-$, ν)^{20}O begin when ρ_{c} exceeds 5 x 10^9 and 9 x 10^9 g cm^{-3}, respectively:

$$^{24}\mathrm{Na} + e^- \rightarrow \nu + ^{24}\mathrm{Ne} \ , \tag{C.2}$$

$$^{20}\mathrm{Ne} + e^- \rightarrow \nu + ^{20}\mathrm{F} \ , \tag{C.3}$$

$$^{20}\mathrm{F} + e^- \rightarrow \nu + ^{20}\mathrm{O} \ . \tag{C.4}$$

As Y_{e} decreases, the value of the Chandrasekhar mass is reduced, and thus the core contraction is accelerated. The rapid contraction of the core ignites the oxygen deflagration at a stage with central density $\rho_{\mathrm{c}} > 10^{10}$ g cm^{-3}, and the material undergoes transformation into nuclear statistical equilibrium (NSE) at the oxygen deflagration front. The collapse of the core is accelerated owing to the rapid electron capture onto NSE elements. The oxygen deflagration front advances in mass to increase the mass of the NSE core. The calculations done by Nomoto for this work were stopped at $\rho_{\mathrm{c}} = 4.425 \cdot 10^{10}$ g cm^{-3}.

For the further evolution of the core (collapse, and post-bounce phase) we implemented the rates provided by Takahara et al. (1989), who used improved shell model calculations.

We assumed that the composition of $^{20}\mathrm{Ne}$ and $^{24}\mathrm{Mg}$ does not change, but took into account in each iteration the electron fraction decrease according to

$$dY_{\mathrm{e}} = -\sum_j \lambda_j^{\mathrm{ec}} \frac{X_j}{A_j} dt \quad , \tag{C.5}$$

and the energy loss by

$$de = -\sum_j \langle E_\nu \rangle_j \frac{X_j}{\mathrm{m_u}} dt \quad , \tag{C.6}$$

with the corresponding electron capture rates (λ_{e}) and neutrino loss rates ($\langle E_\nu \rangle$) for the species j ($^{20}\mathrm{Ne}$ or $^{24}\mathrm{Mg}$) with their corresponding mass fraction (X) and atomic mass number (A) and $\mathrm{m_u}$ the atomic mass unit.

Appendix D

Nuclear burning description

Here we present a simplified nuclear reaction network carrying seven symmetric elements (He, C, O, Ne, Mg, Si, Ni), that accomplishes charge and mass conservation. However, the effects of burning reactions involving free neutrons, free protons and neutron poor or ionized nuclei are also taken into account, with the aim to give a reallystic description of the energy transformation due to nuclear burning (see the main nuclear reactions section). The complete reaction network would give a detailed description of the quantitative evolution of the nuclear species, which is not attempted here.

D.1 Basic equations

The nuclear abundances $Y_i = n_i/(\rho\ N_A)$ (where n_i are the number densities of the species i, ρ is the density, and N_A is the Avogadro number) in an astrophysical plasma can change basically due to three categories of reaction mechanisms: single, double and triple particle reactions. The reaction network is described by the following set of differential equations

$$\begin{aligned}\frac{\mathrm{d}}{\mathrm{d}t}Y_i &= \sum_j N_j^i \lambda_j Y_j + \sum_{j,k} N_{j,k}^i\ \rho\ N_A < \sigma v >_{j,k} Y_j Y_k \\ &\quad + \sum_{j,k,l} N_{j,k,l}^i\ \rho^2\ N_A^2 < \sigma v >_{j,k,l} Y_j Y_k Y_l\ , \end{aligned} \tag{D.1}$$

where the first term represents the single particle reactions, i.e. decays, photodisintegrations, electron and positron captures and neutrino induced reactions, and the second and the third term, two and three particles reactions, respectively. The individual N^i coefficients are given by: $N_j^i = \pm N_i$, $N_{j,k}^i = \pm N_i/(N_j!N_k!)$ and $N_{j,k,l}^i = \pm N_i/(N_j!N_k!N_l!)$, where N_i is an absolute number indicating how many particles i are created (+) or destroyed (-) in a reaction, and $N_i!$ prevents double counting for reactions involving identical particles. The single interaction rate is represented by λ, whereas the two and three particles reactions rates are represented by $N_A < \sigma v >$. An accurate description of the time evolution of nuclear abundances would require solving the full set of equations at once implicitly. Since we are only interested in

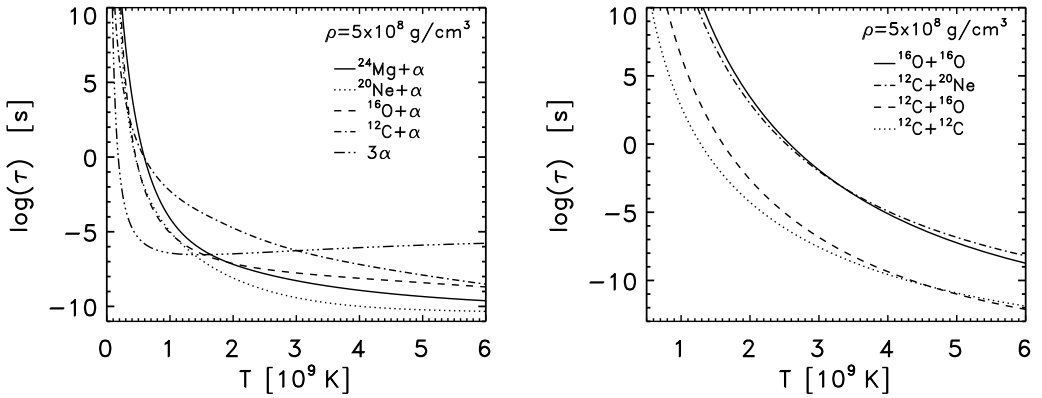

Figure D.1: Relevant burning rates for an intermediate density of 5×10^8 g/cc defined as $\tau_i = |\frac{Y_i}{\dot{Y}_i}|$ for the fuel Y_i, assuming 100 % fuel mass fraction or 50 % mass fraction for the case of two particle reactions with different fuels (see Thielemann et al. 1998). For the plot on the right the effective burning rate was computed as the sum of the burning rates for the different channels (see section D.2).

the energy changes, it is sufficient to take the main reactions and solve each corresponding equation separately in an explicit scheme. This also allows for a low computational cost.

The single particle reactions of the form:

$$Y_{\rm a} \rightarrow Y_{\rm b} + Y_{\rm c} + \dots \quad , \tag{D.2}$$

can be solved trivially. The corresponding differential equation:

$$\mathrm{d}Y_{\rm a}/\mathrm{d}t = -\lambda_1 \, Y_{\rm a} \quad , \tag{D.3}$$

with $\lambda_1 \equiv \lambda$, can be integrated formally:

$$Y_{{\rm a}f} = Y_{{\rm a}i} \exp\left\{-\lambda_1 \, \Delta t\right\} \quad , \tag{D.4}$$

with $\Delta t \equiv t_f - t_i$.

The two particles reactions we have to deal with are of two types, those with only one fuel:

$$Y_{\rm a} + Y_{\rm a} \rightarrow Y_{\rm b} + Y_{\rm c} \quad , \tag{D.5}$$

and those with two fuels:

$$Y_{\rm d} + Y_{\rm e} \rightarrow Y_{\rm f} + Y_{\rm g} \quad . \tag{D.6}$$

It is possible to solve both cases analytically. The first one leads to a single differential equation:

$$\mathrm{d}Y_{\rm a}/\mathrm{d}t = -\lambda_2 \, Y_{\rm a}^2 \quad , \tag{D.7}$$

with $\lambda_2 \equiv \; N_{j,k}^i \rho \, N_A < \sigma v >_{j,k}$, which solution is simply:

$$Y_{{\rm a}f} = Y_{{\rm a}i}/(1 + Y_{{\rm a}i} \lambda_2 \, \Delta t) \quad . \tag{D.8}$$

The mass fractions ($X = A\,Y$, with A the atomic number) for the different species change as follow:

$$X_{\mathrm{a}f} = X_{\mathrm{a}i}/(1 + \lambda_2\,\Delta t\,X_{\mathrm{a}i}/A_{\mathrm{a}}) \ , \tag{D.9}$$

$$X_{\mathrm{b}f} = X_{\mathrm{b}i} + \frac{1}{2}\Delta X_{\mathrm{a}} A_{\mathrm{b}}/A_{\mathrm{a}} \ , \tag{D.10}$$

and

$$X_{\mathrm{c}f} = X_{\mathrm{c}i} + \frac{1}{2}\Delta X_{\mathrm{a}} A_{\mathrm{c}}/A_{\mathrm{a}} \ , \tag{D.11}$$

with $\Delta X_{\mathrm{a}} \equiv X_{\mathrm{a}i} - X_{\mathrm{a}f}$. The reaction with two fuels (D.20) gives a set of two differential equations:

$$\mathrm{d}Y_{\mathrm{d}}/\mathrm{d}t = -\lambda_2\,Y_{\mathrm{d}}Y_{\mathrm{e}} \ , \tag{D.12}$$

and

$$\mathrm{d}Y_{\mathrm{e}}/\mathrm{d}t = -\lambda_2\,Y_{\mathrm{d}}Y_{\mathrm{e}} \ . \tag{D.13}$$

In order to solve this set exactly we have to take into account a second set of equations that states number conservation, i.e. : $-\mathrm{d}Y_{\mathrm{d}}/\mathrm{d}t = -\mathrm{d}Y_{\mathrm{e}}/\mathrm{d}t = \mathrm{d}Y_{\mathrm{f}}/\mathrm{d}t = \mathrm{d}Y_{\mathrm{g}}/\mathrm{d}t$. We can define the quantity: $z = Y_{\mathrm{d}} + Y_{\mathrm{e}}$ and obtain then a single differential equation,

$$\mathrm{d}^2z/\mathrm{d}t^2 = -\lambda_2\,z\,\mathrm{d}z/\mathrm{d}t \ , \text{ which solution is given by :} \tag{D.14}$$

$$z_f = z_i/(1 + z_i\lambda_2\,\Delta t/2) \ . \tag{D.15}$$

The mass fractions are then:

$$X_{\mathrm{d}f} = X_{\mathrm{d}i} - \frac{1}{2}\Delta z\,A_{\mathrm{d}} \ , \tag{D.16}$$

$$X_{\mathrm{e}f} = X_{\mathrm{e}i} - \frac{1}{2}\Delta z\,A_{\mathrm{e}} \ , \tag{D.17}$$

$$X_{\mathrm{f}f} = X_{\mathrm{f}i} + \frac{1}{2}\Delta z\,A_{\mathrm{f}} \ , \tag{D.18}$$

and

$$X_{\mathrm{g}f} = X_{\mathrm{g}i} + \frac{1}{2}\Delta z\,A_{\mathrm{g}} \ . \tag{D.19}$$

One can see that the solutions accomplish mass conservation ($\sum X = 1$), by recalling $2A_{\mathrm{a}} = A_{\mathrm{b}} + A_{\mathrm{c}}$ and $A_{\mathrm{d}} + A_{\mathrm{e}} = A_{\mathrm{f}} + A_{\mathrm{g}}$.

Let us also consider the triple reaction for the case of only one fuel:

$$Y_{\mathrm{a}} + Y_{\mathrm{a}} + Y_{\mathrm{a}} \rightarrow Y_{\mathrm{b}} \ . \tag{D.20}$$

We get the following differential equation:

$$\mathrm{d}Y_{\mathrm{a}}/\mathrm{d}t = -\lambda_3\,Y_{\mathrm{a}}^3 \ , \tag{D.21}$$

with $\lambda_3 \equiv\ N^i_{j,k,l}\,\rho^2\,N_A^2 < \sigma v >_{j,k}$ and which solution is simply:

$$Y_{\mathrm{a}f} = Y_{\mathrm{a}i}/\sqrt{(1 + Y^2_{\mathrm{a}i}\lambda_3\,\Delta t)}\ . \tag{D.22}$$

The mass fractions for the fuel and the product are given by:

$$X_{\mathrm{a}f} = X_{\mathrm{a}i}/\sqrt{(1 + \lambda_3\,\Delta t\,X^2_{\mathrm{a}i}/A^2_{\mathrm{a}})}\ , \tag{D.23}$$

$$X_{\mathrm{b}f} = X_{\mathrm{b}i} + \frac{1}{3}\Delta X_{\mathrm{a}} A_{\mathrm{b}}/A_{\mathrm{a}}\ . \tag{D.24}$$

One can see that mass conservation is fulfilled by recalling that $3A_{\mathrm{a}} = A_{\mathrm{b}}$.

D.2 The main nuclear reactions

The initial composition is assumed to consist of 5 symmetric nuclei (He, C, O, Ne, Mg). All of them undergo a series of reaction chains producing in an intermediate step mainly silicon (^{28}Si,^{29}Si, ^{30}Si) and sulphur (^{31}S,^{32}S) (see, for example, Chieffi et al 1998 and fig. D.2). These heavier nuclei continue burning until iron group elements are produced. In this last step the reactions occur so rapidly at high temperatures, that explosive burning can be assumed, i.e. a transformation of the composition, which is instantaneous on the hydrodynamical relevant timescales. We take the symmetric element ^{28}Si as the representative nucleus before explosive burning sets in, and assume the transition from ^{28}Si to ^{56}Ni to take place at a temperature of $T = 4.5 \times 10^9$ K. The main goal of the treatment of nuclear burning described here, is to give an adequate approximation for the reaction steps which ultimately lead to the formation of iron group elements.

Oxygen burning has three channels that give silicon, sulphur and phosphor. The latter only needs a proton capture to convert to silicon or sulphur. Since we just want to consider ^{28}Si, we take only the channel involving this nucleus, but with an effective rate given by the sum of all the rates for the different channels. We do the same for the reaction involving carbon and neon. For the rest of reactions with carbon we take only the channel involving αs and use the corresponding effective rate. However, the products now, represented by neon and magnesium, are lighter than the nuclei at which we expect explosiv burning. Reactions with α particles will lead to silicon.

Neon and magnesium burning depend crucially on the presence of α particles. Neon nuclei can capture α particles to produce magnesium. Magnesium on the other hand can react with α particles to give silicon. Therefore the mass fraction of αs plays an important role in the whole burning process, having a great influence on the global burning timescale. However, the proportion of αs is negligible inside the stellar core. The dissociation processes produce αs, but are clearly slower than oxygen and carbon burning in the whole density range of interest, except for neon dissociation, that is comparable to oxygen burning. Since neon dissociation produces also oxygen, it is the oxygen burning rate which will determine the timescale at which all neon is transformed to silicon. The speed could be enhanced under the presence of carbon. However, since the mass fraction of oxygen dominates in the interior of the core over that of

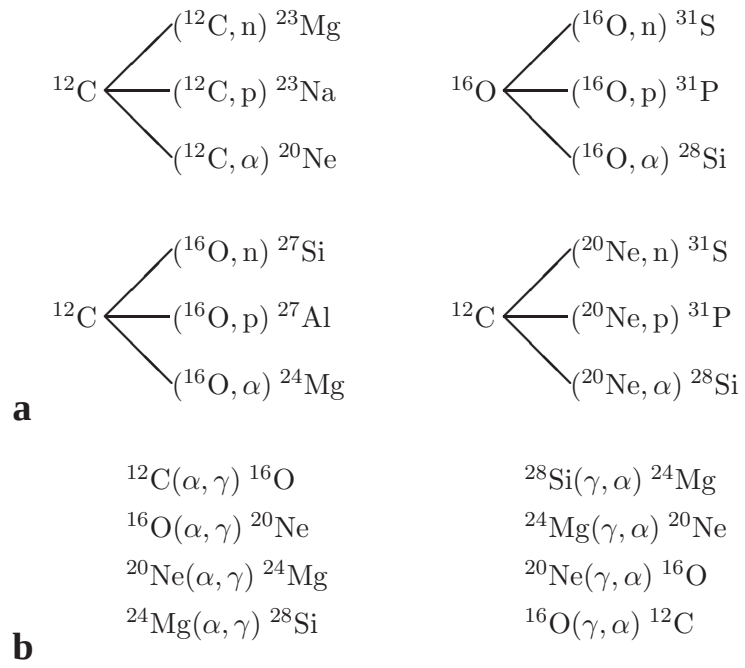

Figure D.2: Relevant nuclear burning reactions that take place in the collapse and explosion of an O-Ne-Mg core. Panel **a** shows the different channels for the reactions: ^{12}C+^{12}C, ^{12}C+^{16}O, ^{12}C+^{20}Ne, and ^{16}O +^{16} O. Panel **b** shows the reactions involving alpha particles.

carbon, we take the burning rate for oxygen to describe neon burning and magnesium burning, each as a two particle reaction with one fuel. In the outer atmosphere, where helium dominates completely the composition, tripple α burning becomes important. It is the fastest reaction we consider at low temperatures (see fig. D.1). The reactions are computed in the right order in each hydrodynamcal timestep according to their rates.

References

ARNETT, W.D. (1975). Supernova Remnants and Presupernova Models. *ApJ*, **195**, 727–733.

BARON, E., COOPERSTEIN, J. & KAHANA, S. (1987). Collapse of 9 $M_{\odot}$ Stars. *ApJ*, **320**, 300–303.

BETHE, H.A. & WILSON, J.R. (1985). Revival of a stalled supernova shock by neutrino heating. *ApJ*, **295**, 14–23.

BLONDIN, J.M., MEZZACAPPA, A. & DEMARINO, C. (2003). Stability of Standing Accretion Shocks, with an Eye toward Core-Collapse Supernovae. *ApJ*, **584**, 971–980.

BRUENN, S.W., DIRK, C.J., MEZZACAPPA, A., HAYES, J.C., BLONDIN, J.M., HIX, W.R. & MESSER, O.E.B. (2007). Modeling core collapse supernovae in 2 and 3 dimensions with spectral neutrino transport. *ArXiv e-prints*, **709**.

BURAS, R., JANKA, H.T., RAMPP, M. & KIFONIDIS, K. (2006a). Two-dimensional hydrodynamic core-collapse supernova simulations with spectral neutrino transport. II. Models for different progenitor stars. *Astr.Astrophy.*, **457**, 281–308.

BURAS, R., RAMPP, M., JANKA, H.T. & KIFONIDIS, K. (2006b). Two-dimensional hydrodynamic core-collapse supernova simulations with spectral neutrino transport. I. Numerical method and results for a 15 Mȯ star. *Astr.Astrophy.*, **447**, 1049–1092.

BURROWS, A. & LATTIMER, J. (1985). The prompt mechanism of type ii supernovae. *ApJ*, **299**, L19–L22.

CHIEFFI, A., LIMONGI, M. & STRANIERO, O. (1998). The Evolution of a 25 Msun Star from the Main Sequence Up to the Onset of the Iron Core Collapse. *ApJ*, **502**, 737–+.

CHUGAI, N.N. & UTROBIN, V.P. (2000). The nature of SN 1997D: low-mass progenitor and weak explosion. *Astr.Astrophy.*, **354**, 557–566.

DAVIDSON, K. & FESEN, R.A. (1985). Recent developments concerning the Crab Nebula. *Ann.Rev.Astrn.Astrophys.*, **23**, 119–146.

DAVIDSON, K., GULL, T.R., MARAN, S.P., STECHER, T.P., FESEN, R.A., PARISE, R.A., HARVEL, C.A., KAFATOS, M. & TRIMBLE, V.L. (1982). The ultraviolet spectrum of the Crab Nebula. *ApJ*, **253**, 696–706.

FESEN, R.A., SHULL, J.M. & HURFORD, A.P. (1997). An Optical Study of the Circumstellar Environment Around the Crab Nebula. *AJ*, **113**, 354–363.

FRÖHLICH, C., HAUSER, P., LIEBENDÖRFER, M., MARTÍNEZ-PINEDO, G., THIELEMANN, F.K., BRAVO, E., ZINNER, N.T., HIX, W.R., LANGANKE, K., MEZZACAPPA, A. & NOMOTO, K. (2006). Composition of the Innermost Core-Collapse Supernova Ejecta. *ApJ*, **637**, 415–426.

FRYER, C.L., BENZ, W., HERANT, M. & COLGATE, S. (1999). What can the Accretion-induced Collpase of White Dwarfs really explain? *ApJ*, **516**, 892–899.

GOTT, J.R.I., GUNN, J.E. & OSTRIKER, J.P. (1970). Runaway Stars and the Pulsars Near the Crab Nebula. *ApJ*, **160**, L91+.

HAMUY, M. (2003). Properties of core-collapse supernovae. *ApJ*, **582**, 905–914.

HARTMANN, D., WOOSLEY, S.E. & EL EID, M.F. (1985). Nucleosynthesis in neutron-rich supernova ejecta. *ApJ*, **297**, 837–845.

HASHIMOTO, M., IWAMOTO, K. & NOMOTO, K. (1993). Type II Supernovae from 8-10 $M_{\odot}$ Asymptotic Giant Branch Stars. *ApJ*, **414**, L105–L108.

HENDRY, M.A., SMARTT, S.J., MAUND, J.R., PASTORELLO, A., ZAMPIERI, L., BENETTI, S., TURATTO, M., CAPPELLARO, E., MEIKLE, W.P.S., KOTAK, R., IRWIN, M.J., JONKER, P.G., VERMAAS, L., PELETIER, R.F., VAN WOERDEN, H., EXTER, K.M., POLLACCO, D.L., LEON, S., VERLEY, S., BENN, C.R. & PIGNATA, G. (2005). A study of the Type II-P supernova 2003gd in M74. *MNRAS*, **359**, 906–926.

HILLEBRANDT, W. (1978). The rapid neutron-capture process and the synthesis of heavy and neutron-rich elements. *Space Science Reviews*, **21**, 639–702.

HILLEBRANDT, W. (1982). An exploding 10 solar mass star - A model for the Crab supernova. *Astr.Astrophy.*, **110**, L3–L6.

HILLEBRANDT, W., NOMOTO, K. & WOLFF, R.G. (1984). Supernova explosions of massive stars - the mass range 8 to 10 $m_{\odot}$. *Astr.Astrophy.*, **133**, 175–184.

HOROWITZ, C.J. (2002). Weak magnetism for antineutrinos in supernovae. *Phys. Rev. D*, **65**, 043001–1–12.

JANKA, H.., BURAS, R., KITAURA JOYANES, F.S., MAREK, A. & RAMPP, M. (2004). Core-Collapse Supernovae: Modeling between Pragmatism and Perfectionism. *ArXiv Astrophysics e-prints*.

JANKA, H.T. (1999). unpublished.

JANKA, H.T., BURAS, R., KITAURA JOYANES, F.S., MAREK, A., RAMPP, M. & SCHECK, L. (2005). Neutrino-driven supernovae: An accretion instability in a nuclear physics controlled environment. *Nuclear Physics A*, **758**, 19–26.

JANKA, H.T., MAREK, A. & KITAURA, F.S. (2007). Neutrino-Driven Explosions Twenty Years After SN 1987A. In *American Institute of Physics Conference Series*, vol. 937 of *American Institute of Physics Conference Series*, 144–154.

KITAURA, F. (2003). Hydrodynamical simulation of core-collapse supernovae with o-ne-mg cores. *Master-thesis, TUM*.

KITAURA, F.S., JANKA, H.T. & HILLEBRANDT, W. (2006). Explosions of O-Ne-Mg cores, the Crab supernova, and subluminous type II-P supernovae. *Astr.Astrophy.*, **450**, 345–350.

LANGANKE, K., MARTINEZ-PINEDO, G., SAMPAIO, J.M., DEAN, D.J., HIX, W.R., MESSER, O.E.B., MEZZACAPPA, A., LIEBENDÖRFER, M., JANKA, H.T. & RAMPP, M. (2003). Electron capture rates on nuclei and implications for stellar core collapse. *Phys. Rev. Lett.*, **90**, 241102.

LATTIMER, J. & SWESTY, F. (1991). A generalized equation of state for hot, dense matter. *Nucl. Phys. A*, **535**, 331–376.

MAREK, A., DIMMELMAYER, H., JANKA, H.T., MÜLLER, E. & BURAS, R. (2005). . *Astr.Astrophy.*, astro-ph/0502161, in the press.

MAYLE, R. & WILSON, J.R. (1988). Supernovae from collapse of oxygen-magnesium-neon cores. *ApJ*, **334**, 909–926.

MEZZACAPPA, A., BRUENN, S.W., BLONDIN, J.M., HIX, W.R. & BRONSON MESSER, O.E. (2007). Ascertaining the Core Collapse Supernova Mechanism: An Emerging Picture? In *American Institute of Physics Conference Series*, vol. 924 of *American Institute of Physics Conference Series*, 234–242.

MIYAJI, S. & NOMOTO, K. (1987). On the Collapse of 8-10 $M_\odot$ Stars due to Electron Capture. *ApJ*, **318**, 307–315.

MIYAJI, S., NOMOTO, K., YOKOI, K. & SUGIMOTO, D. (1980). Supernova Triggered by Electron Captures. *Astron.Soc.Jap.*, **32**, 303–329.

NOMOTO, K. (1983). Presupernova evolution of 8-12 $m_\odot$ stars and the crab nebula's progenitor. *Int.Astron.U.*, **101**, 139N.

NOMOTO, K. (1984). Evolution of 8-10 $m_\odot$ stars toward electron capture supernovae. i. formation of electron-degenerate o+ne+mg cores. *ApJ*, **277**, 791–805.

NOMOTO, K. (1987). Evolution of 8-10 $m_\odot$ stars toward electron capture supernovae. ii. collapse of an o+ne+mg core. *ApJ*, **322**, 206–214.

NOMOTO, K., SPARKS, W.M., FESEN, R.A., GULL, T.R., MIYAJI, S. & SUGIMOTO, D. (1982). The crab nebula's progenitor. *Nature*, **299**, 803–805.

PASTORELLO, A., ZAMPIERI, L., TURATTO, M., CAPPELLARO, E., MEIKLE, W.P.S., BENETTI, S., BRANCH, D., BARON, E., PATAT, F., ARMSTRONG, M., ALTAVILLA, G., SALVO, M. & RIELLO, M. (2004). Low-luminosity Type II supernovae: spectroscopic and photometric evolution. *MNRAS*, **347**, 74–94.

PASTORELLO, A., ARETXAGA, I., ZAMPIERI, L., MUCCIARELLI, P. & BENETTI, S. (2005). Spectroscopic and Photometric Observations of SN IIn 1995N. *ArXiv Astrophysics e-prints*.

RAMPP, M. & JANKA, H.T. (2002). Radiation hydrodynamics with neutrinos. Variable Eddington factor method for core-collapse supernova simulations. *Astr.Astrophy.*, **396**, 361–392.

SCHECK, L., JANKA, H.., FOGLIZZO, T. & KIFONIDIS, K. (2007). Multidimensional supernova simulations with approximative neutrino transport. II. Convection and the advective-acoustic cycle in the supernova core. *ArXiv e-prints*, **704**.

SUMIYOSHI, K., TERASAWA, M., MATHEWS, G.J., KAJINO, T., YAMADA, S. & SUZUKI, H. (2001). r-Process in Prompt Supernova Explosions Revisited. *ApJ*, **562**, 880–886.

TAKAHARA, M., HINO, T., ODA, T., MUTO, K., WOLTERS, A.A. & GLAUDEMANS, P.W.M. (1989). Microscopic Calculation of the Rates of Electron Captures which induce the Collapse of O+Ne+Mg Cores. *Nucl. Phys. A*, **504**, 167–192.

WANAJO, S., TAMAMURA, M., NAOKI, I., NOMOTO, K., YUHRI, I., BEERS, T. & NOZAWA, S. (2003). The r-Process in Supernovae Explosions from the Collapse of O-Ne-Mg Cores. *ApJ*, **593**, 968–979.

WHEELER, J.C., COWAN, J.J. & HILLEBRANDT, W. (1997). The r-Process in Collapsing O/Ne/Mg Cores. *ApJ*, **493**, L101–L104.

WOOSLEY, S.E. & BARON, E. (1992). The Collapse of White Dwarfs to Neutron Stars. *ApJ*, **391**, 228–235.

WOOSLEY, S.E., WEAVER, T.A. & TAAM, R.E. (1980). Models for Type I supernovae. In J.C. Wheeler, ed., *Texas Workshop on Type I Supernovae*, 96–112.

ZAMPIERI, L., PASTORELLO, A., TURATTO, M., CAPPELLARO, E., BENETTI, S., ALTAVILLA, G., MAZZALI, P. & HAMUY, M. (2003). Peculiar, low-luminosity Type II supernovae: low-energy explosions in massive progenitors? *MNRAS*, **338**, 711–716.

Acknowledgements

Wähntest du etwa,
ich sollte das Leben hassen,
in Wüsten fliehen,
weil nicht alle
Knabenmorgenblütenträume reiften?

Johann Wolfgang von Goethe, Prometheus

Studying and working on physics and astrophysics has been a great experience for me in which I could realize one of the dreams of my life. I want to thank my parents for supporting me in this adventure.

I was eleven years old when my godfather Luis came for a visit to Madrid and gave me the book *A brief history of time* by Stephen Hawking and with his grave voice said: *smart boys get never bored*. I remember a little boy feeling under pressure to read that book and who could hardly read the first eighty pages, for the text being *somewhat* difficult, but was completely amazed by its contents. I was astonished, how human-beings could just start to think after observing the sky and come up with theories about the whole Universe like Olbers paradox, I remember. There I decided to study physics. I want to thank Luis for influencing my life in this way.

When I was about to finish my studies at the Universidad Complutense de Madrid and at the Technische Universität in Munich I went to the Max Planck Institute looking for a Master-thesis with the aim to work in cosmology. I was introduced to different people. After entering Simon White's room, he showed me a movie of a simulation and said: *Look, that are numerical simulations with many particles using only Newtonian Gravity.* Only Newtonian Gravity! I immediately decided to look for something else and ended up in the Supernova group with Thomas Janka doing simulations with many neutrinos... However, I am happy that I found my way back to cosmology and started the thesis precisely in Simon's group. Simon is one of the scientists I most admire. Having scientific conversations with him was great and I am very greatful to his advices. I want thank Thomas for the very

nice collaboration from whom I learned a lot. Bringing a star to explode was one of the most exciting experiences in my life (even though it only happened in a computer). Let me thank here also Wolfgang Hillebrandt and Kenichi Nomoto for their support and scientific collaboration.

However, my dream of working in cosmology would have not come true, if my supervisor Torsten Enßlin would not have given me the chance to do my thesis coming from an exploding star. I thank him also because I learned from him not to fear any calculation and jump to the black-board and just write equations. How much fun! I thank him so much for his support and advices.

I thank my collaborators Benjamin Wandelt and Jeremy Blaizot for being so good in their respective fields plus nice persons. Work makes so much fun that way. I want to thank Gerard Lemson and Ben Metcalf for very useful discussions.

Several persons have contributed a lot to make each day at the Max Planck funny and interesting so that I could really enjoy astrophysics. I thank Robert Buras for his friendship and scientific support in supernova. From that group let me also thank Leonhard Scheck, Almudena Arcones and Rohland Oechslin. Let me also thank Shinja Wanajo and Bernhard Mueller for the collaboration on Supernovae. I thank Antonella Maselli for so many things, but especially for our scientific and literature and cheese and wine conversations. I thank Jens Jasche for being such a nice smart guy. Let me say here that it was a honor to be his guide in large-scale structure reconstructions and Bayesian stuff. I thank him for his valueable scientific contribution. Now, I am learning from him. Let me now thank Daniel Sauer for being such a nice room-mate and helping me with computational issues. He is a crack. Also Martin Reinecke helped me dealing with software problems. Rainer Moll helped with Amira. Thanks. Special thanks to Sheridon Sauer and Pilar Esquej for proof-reading my manuscripts. Kei Kotake, Keiichi Maeda domo arigatoo. I also thank the Aikido group in Spain (Ametsuchi-dojo) and in Munich for their support. I want to thank my WG for their support and friendship. I also want to thank my family in Spain and Japan and my friends around the world for having patience with me and encourage me to continue my work. Thank you Heike. Danke Frau Wölbing. Thank you Nacho, Pampa, Juan, Amada, Kiyoshi, Dani, Marc, Teo, Christoph, Justo, Jan, Seb, Kassu, Tuula, Marta, Ricardo, Natalie, Pabloo, Anna, Elena, Philipp, Pollo. Mercedes, Antonio, Isra, gracias. Seigo, Tomi, Yuri, Yukari, Masayuki, Takayuki, domo arigatoo.